Technical University of Denmark

DTU

Vascularization of soft tissue engineering constructs

Pimentel Carletto, Rodrigo; Dufva, Martin; Larsen, Layla Bashir; Okkels, Fridolin

[Link back to DTU Orbit](#)

DTU Library
Technical Information Center of Denmark

Vascularization of Soft Tissue Engineering Constructs

Rodrigo Pimentel Carletto
PhD Thesis June 2017

Vascularization of Soft Tissue Engineering Constructs
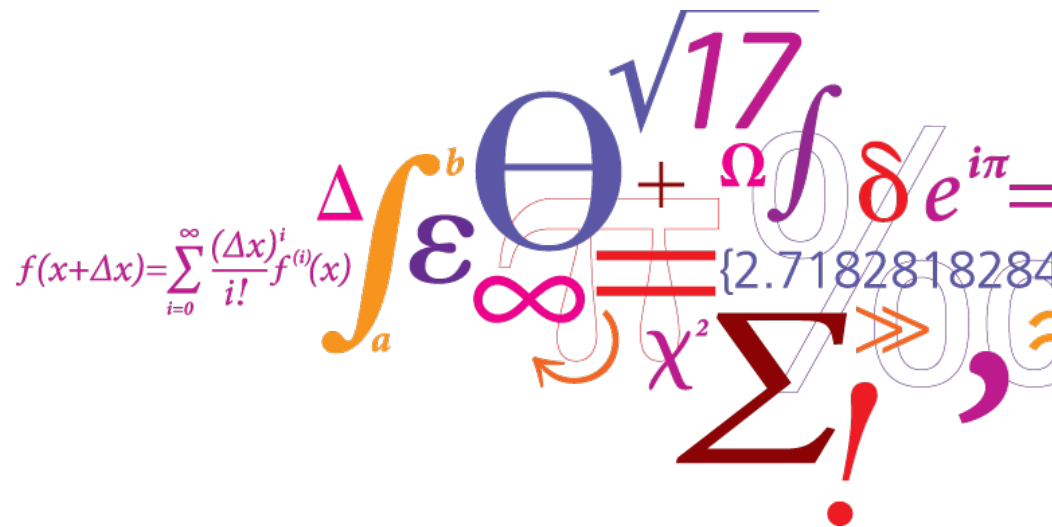
Rodrigo Pimentel C.

$$f(x+\Delta x)=\sum_{i=0}^{\infty}\frac{(\Delta x)^i}{i!}f^{(i)}(x)$$

x

A mamae e papai,
a quem tudo devo.

ABSTRACT

Vascularization is recognized to be the biggest challenge for the fabrication of tissues and finally, organs in vitro. So far, several fabrication techniques have been proposed to create a perfusable vasculature within hydrogels, however, the vascularization and perfusion of hydrogels with mechanical properties in the range of soft tissues has not been fully achieved.

My project focused on the fabrication and the active perfusion of hydrogel constructs with multi-dimensional vasculature and controlled mechanical properties targeting soft tissues. Specifically, the initial part of the research has focused on: (1) the fabrication and characterization of gelatin constructs with 2D and 3D perfusable vasculature and (2) the development of a fluidic platform to allow the direct perfusion of the fabricated constructs. Throughout the developed technology, it was possible to fabricate and perfuse densely populated constructs integrating a 3D vasculature. Also, it was possible to fabricate and test a hydrogel-based fluidic system integrating sensors capable of simulating a barrier environment.

ACKNOWLEDGEMENTS

CONTENT

PREFACE

This thesis is presented as a partial requirement for obtaining a Ph.D. degree from the Technical University of Denmark (DTU). The research was financed by the EU Commission within the framework of the FP7 project "NanoBio4Trans" ("A new nanotechnology-based paradigm for engineering vascularised liver tissue for transplantation", Grant No: 304842), the Danish National Research Foundation and Villum Foundation's Center for Intelligent Drug delivery and sensing Using microcontainers and Nanomechanics, IDUN, (Danish National Research Foundation (DNRF122), and the Department of Micro- and Nanotechnology (DTU Nanotech). The research was carried out at DTU Nanotech in the period from February 2014 to April 2017. The Ph.D. project was supervised by Associate Professor Martin Dufva, leader of the Fluidic Array System Technologies (FAST) group, and co-supervised by Associate Professor Fridolin Okkels.

Kgs. Lyngby,

17st April 2017

Rodrigo Pimentel C.

LIST OF SUBMITTED MANUSCRIPTS

The following manuscripts represents the core of this thesis and they will define chapters 2 to 5 of this thesis.

I.   **Hepatic Differentiation of Human Induced Pluripotent Stem Cell Derived Definitive Endoderm Cells under Flow Conditions for Liver Tissue Engineering**

Viktoriia Starokozhko, Mette Hemmingsen, Layla Larsen, Soumyaranjan Mohanty, Marjolijn Merema, **Rodrigo Pimentel C.**, Anders Wolff, Jenny Emnéus, Anders Aspegren, Geny Groothuis, and Martin Dufva

Manuscript submitted to the Journal of Tissue Engineering and Regenerative Medicine

II. **Fabrication of cell laden soft hydrogels perforated with a 3D channels network interfaced to a perfusion system**

Rodrigo Pimentel C., Mette Hemmingsen, Anders Wolff, Fridolin Okkels, Anders Aspegren, Jenny Emnéus, and Martin Dufva

Manuscript submitted to Biofabrication

III. **Three-dimensional fabrication of thick and densely populated soft constructs with complex and actively perfused vasculature**

Rodrigo Pimentel C., Suk Kyu Ko, Claudia Caviglia, Jenny Emnéus, Stephan Sylvest Keller and Martin Dufva

Manuscript submitted to Biomaterials

IV. **Fabrication of a hydrogel-based fluidic system with integrated sensors capable of simulating physiological barriers**

Rodrigo Pimentel C., Claudia Caviglia, Maria Luisa Marini, Stephan Sylvest Keller and Martin Dufva

Manuscript to be submitted to Biosensors and Bioelectronics

MY CONTRIBUTION TO THE PAPERS

I.   I performed the imaging acquisition and analysis, especially, the confocal microscopy acquisition as well as the 3D reconstruction. The theoretical analysis (i.e., numerical simulations) was carried out by me.

II.   I designed, planned and performed the experiments. I designed and fabricated all the hardware parts employed (3D printing characterization, CAD modelling, electronic part) as well as wrote the software for controlling the pumps. The cellular part was performed together with Mette Hemmingsen and I did the imaging acquisition and analysis. I evaluated the results and wrote the paper.

III.   I designed, planned and performed the experiments. Part of the experiments (3D printing fabrication) was performed by a bachelor student supervised by me (Suk Kyu Ko). I performed all the cellular experiments in collaboration with Claudia Caviglia, I did the imaging acquisition and analysis, performed the theoretical analysis (i.e., numerical simulations), evaluated the results and wrote the paper.

IV.   I designed and planned the experiments. The experimental part, except some CAD modelling and fabrication, was performed together with Claudia Caviglia and a master student supervised by me (Maria Luisa Marini). I did the imaging acquisition and analysis, and the electrical analysis was made in collaboration with Claudia Caviglia. and I evaluated the results and I wrote the paper.

LIST OF PUBLICATIONS NOT INCLUDED IN THIS THESIS

The following papers were the results of collaborations during my Ph.D., and they are not included at this thesis.

I. **Calibration of a numerical model for heat transfer and fluid flow in an extruder**

    Thomas Hofstätter, David Bue Pedersen, Jakob Skov Nielsen, **Rodrigo Pimentel C.**, Michael Mischkot and Hans Nørgaard Hansen

    International Journal of Rapid Manufacturing, 2016, Vol 6, No.1, p. 1-16

II. **Simulation of a downsized fused deposition modelling (FDM) nozzle**

    Thomas Hofstätter, **Rodrigo Pimentel C.**, David Bue Pedersen, Michael Mischkot and Hans Nørgaard Hansen

    Proceedings, COMSOL Conference 2015

LIST OF CONFERENCE CONTRIBUTIONS

I. **Indirect fabrication of three-dimensional hydrogel constructs for tissue engineering applications**

   Rodrigo Pimentel C., Layla Larsen, A. Wolff, M. Dufva, J. Emnéus and F. Okkels

   EMBS Micro and Nanotechnology in Medicine Conference (MNMC 2014)

   December 8-12, 2014, Hawaii, USA

   (POSTER)

II. **Towards a new generation of organs-on-chip: the scaffold reactor approach**

   Rodrigo Pimentel C., J. Emnéus, Anja Boisen and M. Dufva

   19th NanoBioTech-Montreux Conference

   November 16-18, 2015, Montreaux, Switzerland

   (POSTER)

III. **Towards a new generation of organs-on-chip: the scaffold reactor approach**

   Rodrigo Pimentel C., Suk Kyu Ko, Claudia Caviglia, Jenny Emnéus, Anja Boisen and Martin Dufva

   EMBS Micro and Nanotechnology in Medicine Conference (MNMC 2016)

   December 12-16, 2016, Hawaii, USA

   (POSTER)

IV. **3D *in vitro* system for bone cell studies**

   Claudia Caviglia, Stefania de Roni, **Rodrigo Pimentel C.**, Gaetano Panagia, Yasmin Mohamed Hassan, Suhith Hernanth, Martin Dufva and Stephan Sylvest Keller

   EMBS Micro and Nanotechnology in Medicine Conference (MNMC 2016)

   December 12-16, 2016, Hawaii, USA

   (POSTER)

V. **Three-dimensional sensing scaffold for bone cells studies**

Claudia Caviglia, Stefania de Roni, **Rodrigo Pimentel C.**, Suhith Hernanth, Yasmin Mohamed Hassan, Gaetano Panagia, Martin Dufva and Stephan Sylvest Keller

BioSensor 2017

March 20-23, 2016, Potsdam, Germany

(ORAL)

CHAPTER 1

INTRODUCTION

Tissue engineering (TE) has emerged to address the major issues concerning organs transplantation, such as the absence of available organs for the patients in the waiting list and the problems related to the immune response of the patient organism after the donated organ [1–4]. In this context, it was necessary to design and fabricate functional and living tissues using living cells, which are usually associated with a support matrix to guide tissue development [5]. Although in the last 30 years there have been extensive progress in the TE field, the fabrication of engineered thick tissues and organs such as the heart, kidney, and liver remains a challenge [3,6]. One of the major problem concerning the fabrication of thick engineered tissues, and finally organs, rely on the absence of a perfusable vasculature [6–18]. The absence of a perfusable vasculature means that the three-dimensional (3D) engineered tissue construct will not have sufficient oxygen, nutrients, waste removal and gas exchange needed for its maturation in time [7,11]. In the normal TE approach bioreactors are responsible to induce the transport of oxygen and nutrients by means of the fluid flow [19–32] whereas scaffolds, which are responsible to give a temporal extracellular matrix (ECM) for the cells, are most of the times porous structures that can be perfused [1,24,33–40]. This combination could partially overcome the limitations of the absence of a perfusable vasculature when fabricating large and tick tissue constructs [12,24,25,35,36,41–44]. However, a 3D porous scaffold is not able to produce the characteristic 3D cell-cell cell-ECM interaction presented *in vivo* [27,45–50]. By contrast, if the scaffold is just a combination of cells encapsulated in a hydrogel material (e.g., cell-laden hydrogel) capable to present a more *in vivo* like environment, the bioreactor is not sufficient anymore to guarantee the appropriate level of nutrients and oxygen while extracting metabolic waste from the cells in the inner core of the a thick construct [27,29,51–54]. Cell-laden hydrogels without a network of channels are unable to provide physiological cues such as oxygen nutrient and growth factors (essentially all para and autocrine factors) required to the cells for growing, and fusing together to form large functional tissues and ultimately organs [18,55]. By contrast, at the organ level, the cells are 3D distributed around a vascular branch responsible to guarantee the physiological factors required for the cells to maintain their homeostasis [4,12].

Despite the advances in the biofabrication technology, it is still challenging to fabricate thick, functional and densely populated engineer constructs with an integrated vascular network [7,55]. In addition, the available fabrication techniques don't allow the

fabrication of tissue engineer constructs with multi-scale vascular network, able to resemble the human vascular anatomy [55]. Moreover, while fabricating the construct, it is still difficult to control at the same time the mechanical properties of the ECM used to simulate the bulk where the cells are encapsulated and to control the complexity of the vasculature within the ECMs [7,55]. Finally, the success of the tissue constructs relies on the time needed for its maturation [25]. This means that the construct should stay in a controlled environment (e.g., temperature, pH, O2, CO2) to give time for the cells to grow to remodel the ECM with which continuously interacts, to form tissues and finally organs. Therefore, not only is crucial the ability to fabricate constructs with perfusable vasculature but it is also crucial to induce these constructs to be actively perfused to ensure the cells encapsulated within the construct to be metabolically functional and to mature in a more complex and functional construct [51,56].

1.1 Background

Many TE approaches involve the use of cells cultured *in vitro* on a biomaterial scaffold to generate functional tissue constructs [20,25,57]. However, it is not sufficient to generate functional constructs, since the *in vivo* biophysical environment is dynamically more complex than a static culture of cells on a scaffold [8,58–60]. It is also well understood that traditional two-dimensional (2D) culture techniques cannot recapitulate the microenvironment experienced by the cells and tissues [47,61] In a 2D environment the cells are not able to experience the typical cell-cell, cell-ECM interaction and temporal chemical gradients in a 3D configuration as it happens in a tissue. Therefore, the control of the *in vitro* environment represents one of the key challenges to produce 3D constructs able to resemble the *in vivo* milieu [27,62,63] (Figure 1.1).
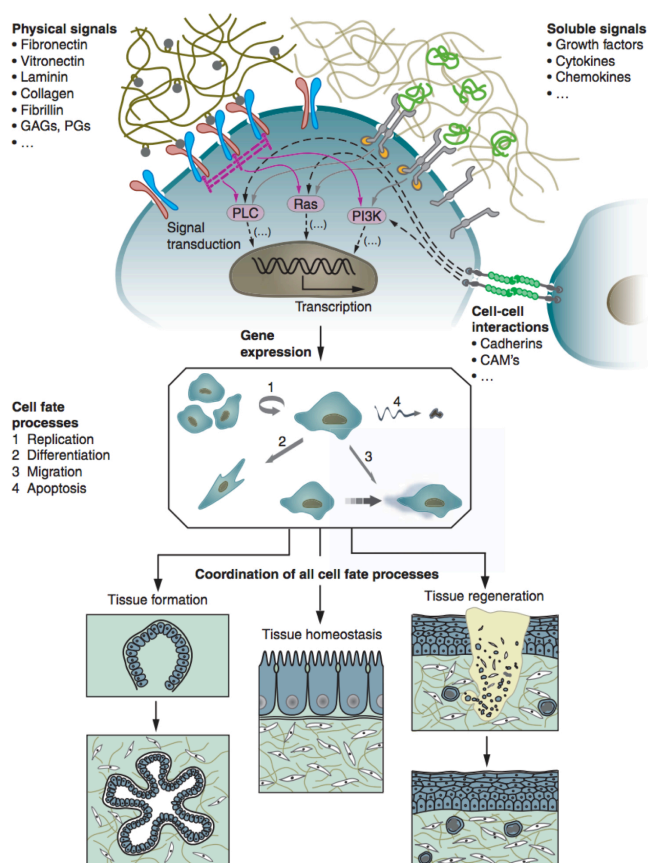
Figure 1.1. The behavior of individual cells and the dynamic behavior of multicellular tissues is regulated by complex bidirectional molecular interactions between cells and the 3D ECM. This ECM is a hydrated protein and proteoglycan-based gel network that comprise soluble and physically bound signals and signals originating from cell-cell interactions. The specific binding of these signaling cues with the cell-surface receptors induces complex intracellular signaling cascades that converge to regulate gene expression, establish cell phenotype and direct tissue formation, homeostasis and regeneration. The image is reprinted from [64].

In particular, the working hypothesis is that the precise control of the *in vitro* culture conditions would have a significant influence in the control of the structure, composition, biochemical and biological function and mechanical properties of the engineered tissues [19,20,25]. The main constituents that are responsible for defining the *in vitro* culture conditions or model are: 3D tissue-engineering scaffold systems, bioreactors, growth factors, and mechanical conditioning regimens that control cell behavior and functional tissue assembly [19,20,25,65]. Therefore, the general strategy used to engineer functional tissues *in vitro* rely on four main building blocks: cells, scaffolds, bioreactors and growth factors Figure 1.1).
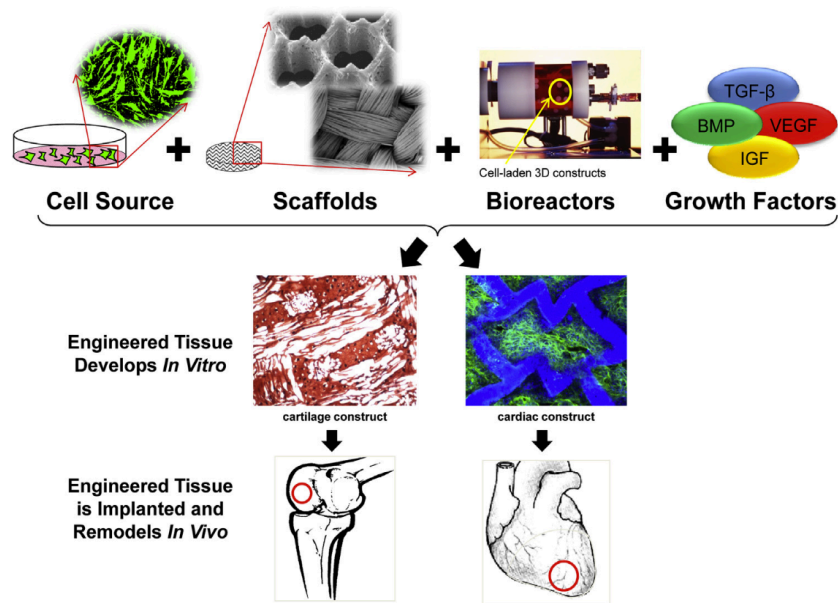
Figure 1.2. Cells, scaffolds, bioreactors and growth factors are the four building blocks required for the fabrication of functional tissues *in vitro*. The image is reprinted from [25].

There have been several reports in the last decade where describing how to manipulate the cell environment using scaffolds, bioreactors, and signals together for guiding the cell behavior to create functional tissue engineered constructs able to resemble the *in vivo* complexity. As an example, there have been an extensive research on the creation of tissue engineered constructs for the cartilage [66–68], bladder [69–72], bone [73–77], and human skin [78–81]. In addition, there have been attempts to engineer more complex organs such as the heart [65,82–85], the kidney [86–88] and the liver [30,89–92]. Despite that great success for simple organs (i.e., cartilage, the bladder, and the skin) both from a research point of view and from translational point of view with the artificial skin (e.g., Derma graft®, Alloderm®) and blood vessel substitutes (e.g., Goretex®, Dacron®), the same didn't occurred for the more complex ones [3,60]. The simple organs were easier to engineer because they are characterized by simple and small geometries, small demand for blood vessels, and small cell consumption rate. By contrast, it was extremely complex to engineer thick and functional tissues or organs, mainly because of the absence of an efficient media exchanger to guarantee an adequate level of oxygen and nutrients while removing the waste [12,93]. The absence of an efficient media exchanger caused a nonhomogeneous cell distribution and limited cell activity.

1.2 Fabrication of tissue engineered constructs

The basics behind the tissue engineering process involves: a cellular or several cellular candidates depending on the final application, cellular incubation and proliferation (when is possible), design and fabrication of a 3D biomaterial scaffold, scaffold seeding with the incubated cells, construct cultivation by means of a bioreactor, tissue generation and implantation (Figure 1.2) [20,25]. The bioreactor, and the scaffold plays the decisive role in manipulating the cell environment and guiding the cell behavior [51,77,94]

1.2.1 Cells

When fabricating functional tissue engineer constructs with relevant dimensions, one of the critical aspects resides in the type of the utilized cells, the available amount and available source of them. In general, cells can be extracted from various sites and sources (e.g., solid tissues, or fluidic ones such as bone marrow or blood) [95]. Once the cells are divided by source categories, generally they are grouped into: autologous cells, allogenic cells, xenogeneic cells. Every group comprises primary cells, cell lines and stem cells. Recently many researchers have started to favour the use of autologous cells in 3D cultures applications. This is because autologous cells are seen as a more relevant tool for studying human biology and also in review of a possible clinical application. As an example, a previous study showed chondrocyte cells isolated from a small and healthy biopsy of the cartilage. The isolated chondrocyte were seed onto a poly(lactic acid) (PLA) scaffold creating 3D constructs that were implanted in 12 different patients. The implanted constructs were able to form new cartilage tissue showing the success of the application [96]. However, autologous cells are difficult to be isolated from the tissue source, and most of the time they are not available. In addition, once the primary cells are cultivated in vitro they lose the ability to proliferate limiting therefore the available number of cells at disposable for the fabrication of densely populate constructs. On the contrary, allogenic cells can be used in clinical application but it must be considered complications regarding the immune incompatibility. Xenogeneic cells were used for clinical purposes where was necessary to supply or to remove chemicals within a tissue or organ. As an example, xenogeneic cells where used to fabricated a bioartificial liver (BAL). Here, the developed BAL consisted on a bioreactor with porcine hepatocytes that populates non-woven polyester matrix. Patient plasma flows through the bioreactor into direct contact with the

porcine hepatocytes without provoking any downsides moving the BAL to phase one trial [97].

Stem cells are also used as an alternative of primary cells since they represent a new source of cells. In addition, stem cells are capable of proliferate and they have the capacity to be self-renewal [98,99]. This means that once proliferated, the resulting daughter cells continues to be unspecialized, like the parent stem-cells. Remarkable advances have been made in isolation, expansion, characterization [4,100–104]. In fact, the number of sites available for stem cells isolation comprises: embryonic stem cells (ES) from discarded human embryos [105], induced pluripotent stem (IPs) cells by genetic reprogramming of somatic cells [106], and adult stem cells (so named regardless of sourcing, from fetal, neonatal, pediatric or adult) either autologous or allogeneic (Figure 1.3) [107]. Stem cells are called multipotent (ES, IPs) or, if constrained to a single fate, unipotent (adult stem cells) [108,109].
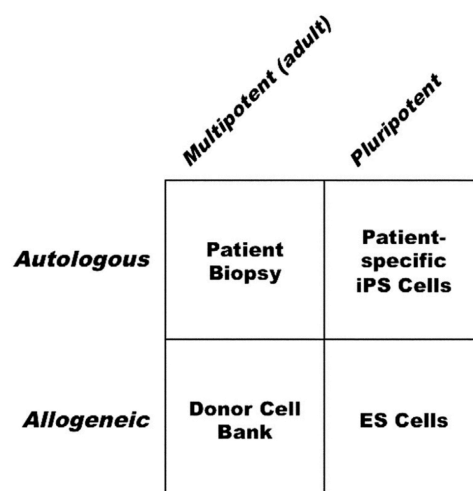
Figure 1.3. Stem cells source used in TE application. Adult stem cells can be isolated from a patient biopsy (autologous) or can be isolated from tissue donors. By contrast, pluripotent stem cells can be used to achieve potentially any desired cell line by reprogramming to pluripotency cells from the available cells obtained from biopsy. Allogeneic cells can be sourced form tissue donors. The image is reprinted from [4].

Despite the theoretical possibility to drive stem cell differentiation towards any cellular lineage, there is a still a challenge in direct the differentiation with accuracy towards an intended phenotype. (46,47). As an example, Engler et al., demonstrated that when

mesenchymal stem cells (MSCs) are cultured in a hydrogel with control mechanical properties with the presence of soluble induction factors, the MSCs differentiate towards the lineage specified by the matrix elasticity (Figure 1.4).
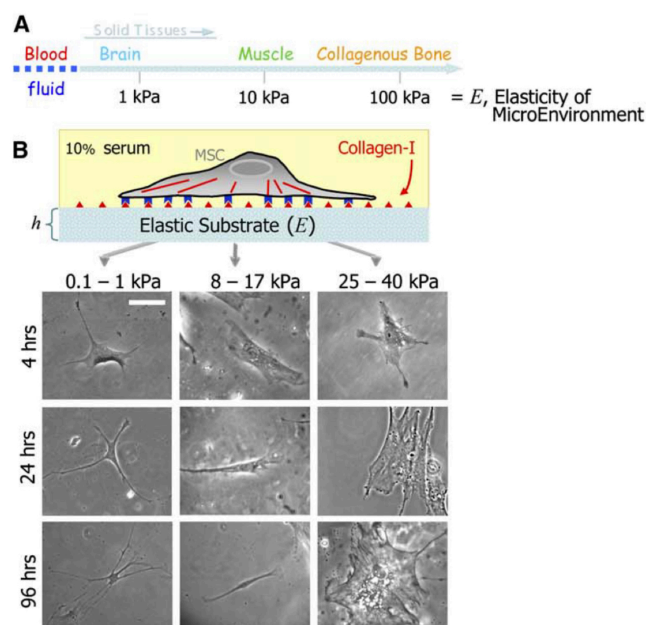
Figure 1.4. (A) Solid tissues exhibit different mechanical properties, as measure by the elastic modulus (i.e., E) and (B) The mechanical properties of the hydrogel are controlled trough crosslinking and the control of cell adhesion is mediated by using collagen-I. The mechanical properties of the gel system were capable to guide the MSCs differentiation towards the brain (0.1-1 kPa), muscle (8-17 kPa) and the bone (25-40 kPa), after 96 hours of culture. The image is reprinted from [110].

1.2.2 Bioreactors

The bioreactor is responsible to initiate, maintain and direct cell growth and tissue development in a well-defined, closed and controlled culture conditions (e.g., pH, temperature, pressure, nutrient supply and waste removal) [21]. Bioreactors have been successfully used to overcome the limitations associated with oxygen and nutrient transport that are often observed in tissues cultured in static environments. , and to enhance matrix synthesis and mechanical properties by biophysical stimulation of the fabricated constructs [19,111,112]. In fact, static cell culture techniques are unable to support 3D cultures or tissues because they depend on diffusional transport mechanisms that are efficient only through a thin superficial layer in contact with the medium culture (in most cases only within

~100-200 μm) [113]. In addition, as the cell density increase, so does the nutrient requested by the cells. As consequence, nutrients are depleted over short distances leading the cells positioned further from the source of nutrients and oxygen to die [113–116]. Different bioreactors have been designed and developed to increase the mass transport between the cells within the scaffolds and the culture medium (Figure 1.4) [21,26,117]. Spinner flask bioreactors create an undulating motion of the culture medium to limit the size of the stagnant cell layer present at the surfaces of tissue constructs. Spinner flask have been used to culture 3D constructs [118]. The medium stirring generate by the bioreactor enhances external mass-transfer but also generates turbulent at the edges that could be damaging for the development of the tissue (Figure 1.5(A)). Rotating-wall bioreactors provide a dynamic culture environment to the constructs, with low shear stresses and high mass-transfer rates. The bioreactor rotates at a rate that induces the drag force (F_d), centrifugal force (F_c) and net gravitational force (F_g) on the construct to be balanced to guarantee that the construct remains in a free-fall state within the culture medium. (Figure 1.5(B)) [26,114]. A possible drawback of associated with the spinner flask and the rotating bioreactors resides on the generation of shear stresses that could cause cell differentiation [119]. Also, the size and viability of the tissue constructs is strictly depended on the internal diffusion of nutrients, since there is no perfusion throughout the construct. Another configuration of bioreactor used is the hollow-fiber (Figure 1.5(C)). It is used to enhance the mass transport of highly metabolic and sensitive type of cells, like the hepatocyte. In fact it is the preferred configuration used in the design of BAL [120]. Finally, the perfusion bioreactor represents the best configuration in terms of mass transport since the medium is pumped through the 3D constructs (Figure 1.5(D)). In fact, the easiest way to increase the transport of mass in a scaffold is to increase the diffusion using the convection [116]. The medium pumped through the scaffold is capable to provide nutrients and oxygen, removing waste, in the inner areas of the porous construct that wouldn't be reached by means of simple diffusion. Perfusion bioreactor were successfully used for the culture of 3D constructs [121,122]. As an example, Figallo et al. developed a perfusion micro-bioreactor able to perfuse porous 3D scaffolds and thin layers of hyaluronic acid hydrogel (HA) using different flow configurations [121].
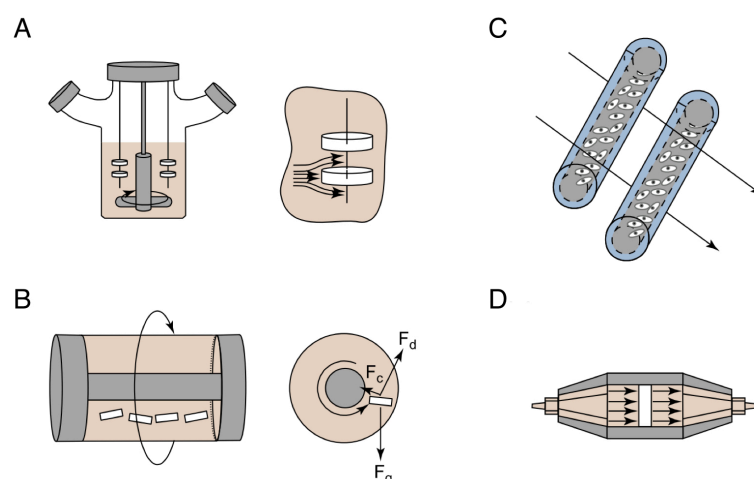
Figure 1.5. Bioreactors used in TE applications to enhance the mass transport: (A) spinner flask bioreactor., (B) rotating-wall bioreactor, (C) hollow fiber bioreactors and (d) direct perfusion bioreactors. The image is reprinted from [114].

1.2.3 Scaffolds

The scaffold is not only a temporary "support" for the cultured cells to growth and proliferate, but it is a complex 3D matrix with suitable physical (e.g., stiffness and mass transfer) and chemical (e.g., employed material type and degradation rate) properties [35,51,123–126]. It has been demonstrated that cells are capable to sense and to interpret the information coming from the ECM [127–132]. The topography, mechanical properties (e.g., stiffness, viscosity and elasticity), molecules presented by the ECM, and the concentration gradients of soluble growth factors represents some of the characteristics presented by the scaffold [34,40,57,123,133]. Therefore, the cells receive and process a multiple combination of physicochemical and biological cues always within a spatiotemporal context by reorganizing themselves via cell–cell contacts [134] and cell–ECM interactions [135]. As an example, it has been show that using gel matrices with well-controlled elasticity, and non-limiting ligand density, all cells were found to adhere, to spread and to anchor more strongly to stiff substrates compared to soft ones (Figure 1.6(A-B)) [136]. Dolega et al. demonstrated that spheroids grown under isotropic compression presented reduced proliferation capacities within the center in comparison to the ones grown in normal conditions (Figure 1.6(C)) [137]. Finally, it has been shown that the cell-ECM interaction can be a more potent cue of differentiation for MSCs than standard induction methods. In particular, human MSCs encapsulated in poly(ethylene glycol) (PEG)

functionalized with various small molecules were induced to proliferate towards osteogenic and adipogenic pathways. Benoit et al. demonstrated that by controlling the 3D environment using tethered small-molecule chemical functional group dispersed within the hydrogel material it was possible to control the induction of multiple MSCs lineage [138].
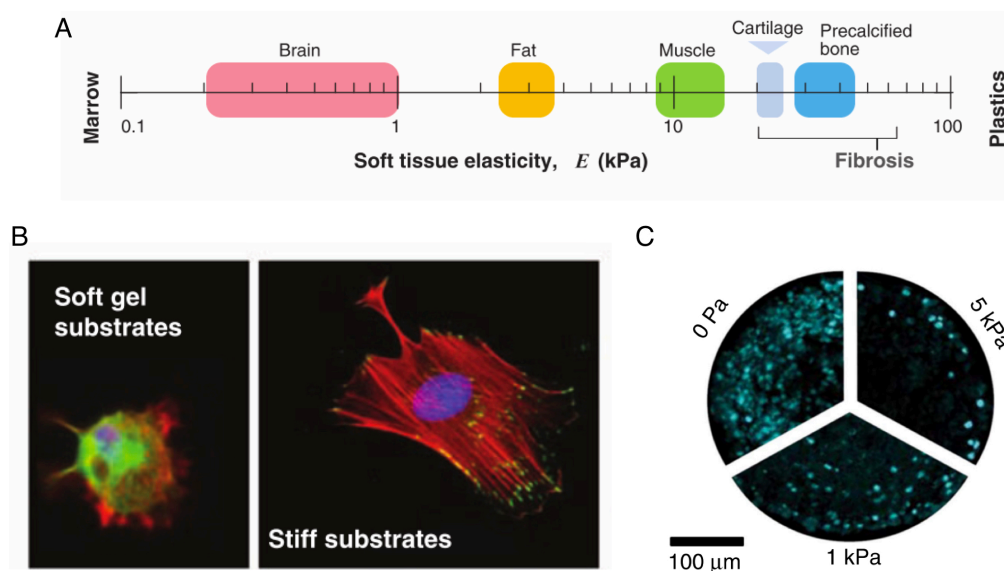
Figure 1.6. Soft tissue elasticity scale ranging from soft brain, fat, striated muscle to stiff cartilage and precalcified bone. (B) In vitro substrates mimicking soft and stiff tissue microenvironments: cells anchor more strongly to stiff substrates, whereas for softer substrates the force of adhesion is weaker. The images are reprinted from [127]. (C) Cellular proliferation along the radius of a spheroid grown under a mechano-osmotic stress of 1 and 5 kPa in respect to the control (0 kPa). The images is reprinted from [137] .

All these considerations are crucial when choosing the biomaterial and the fabrication technique employed to fabricate the scaffold [139,140]. From an engineering stand-point, it is important that the scaffold integrates all the regulatory functions and properties within the scaffold design in a reproducible and controlled way. This is crucial because the design of the scaffold would be primarily responsible to induce and control the tissue formation in a stepwise manner [64,141] (Figure 1.7).
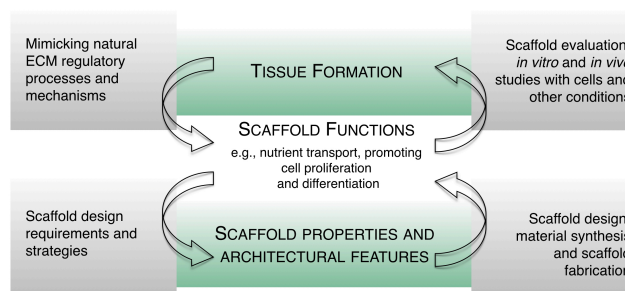
Figure 1.7. Breakdown of the processes necessary to understand the design principles and the enabling technologies to design and fabricate a scaffold. Adapted from [142]
.

1.2.3.1 Biomaterials

The two main classes of biomaterials used to fabricate TE scaffolds are biologically derived and synthetic polymers [143]. Biologically derived polymers are materials created by living organisms whereas synthetic polymers are man-made.

1.2.3.1.1   Biologically derived polymers: collagen and gelatin

One important class of biologically derived materials are the proteins [50,143,144]. Proteins are polymers derived from naturally occurring a-L-amino acids, where the connection of the amino acids are obtained through hydrolytically stable amide bonds. This means that these materials are degraded through enzymatic mechanisms. The main limitations connected to protein polymers are represented by their inherent immunogenicity, their lack of 'processibility' and their mechanical properties for their use as medical implants [143]. The immunogenicity is because proteins carries the risk of being recognized as foreign by the patient's immune system since they are created by living organisms. The lack of 'processibility' is the major shortcoming of proteins as starting materials of the fabrication of medical implants. The 'processibility' means the ability of creating a shaped device by any of the conventional processing technologies used in the plastic industry: compression molding, extrusion, injection molding and fiber spinning. Finally, their weak mechanical properties make the proteins the worse candidate to fabricate medical devices. By contrary, the outstanding biological properties presented by the proteins makes them the perfect candidate for designing polymers with controlled biological activities. Two of the main used proteins in TE applications are collagen and gelatin [145].

Collagen represents the richest protein in the human body (~ 30%) as well as the main component of the ECM of many tissues. Fibroblasts and osteoblast cells are the ones that mostly synthetizes collagen [146]. So far, fourteen types of collagen have been identified [147]. Among all, collagen I is the most abundant since is extracted from several tissues (e.g., skin, ligaments, bones) by acid and enzymatic treatments [148]. In addition, thanks to its unique physical and biological properties, collagen I has been extensively used in the formulation of biomedical materials [146]. The structure of type I collagen has been extensively investigated, and it consist of a triple helical structure extending over a large portion of the molecule [149]. The helices are organized in complex supramolecular structures and every third amino acid of the helix chain is a glycine [150]. The remaining (~ one third) amino acids presented in the helix chain are proline and hydrosyproline with their side chains pointing towards the outer region of the helix [150]. Because of the well-conserved primary sequence and its helical structure collagen I is only partially immunoreactive [151]. Collagen can be fast biodegraded in via collagenases and metalloproteinases enzyme to yield the corresponding amino acids. The free amines on lysine residues on collagen can be used for crosslinking to increase the mechanical properties of type I collagen and to modulate the rate of degradation [152]. It has been recognized that substrate attachment sites are crucial for growth, differentiation, replication, and metabolic activity of most cell types in culture [153]. Collagen represents a perfect candidate since it presents integrin-binding domains (e.g., arginine glycine-aspartic acid (RGD) sequences). As an example, fibroblast grown on a 2D collagen matrices differentiate in ways that resembles the in vivo cellular activity exhibiting almost identical morphology and metabolism [150]. In addition, when cultured in collagen matrices, chondrocytes are capable of maintain their phenotype and cellular activity [154]. These results show that type I collagen represents a good candidate for the fabrication of tissue engineer scaffolds for almost any number of cell constructs. Moreover, collagen has been used in several TE applications [155], such as cartilage repair [156], bone regeneration [76] and the most common clinically used biomaterial for skin repair [78].

Gelatin is the product of the rupture of the collagen triple helix into single-strain molecules [157]. Two different types of gelatin can be obtained by two different collagen treatments. The first type of gelatin can be obtained by the hydrolysis of the amide groups of asparagine and glutamine carboxyl groups whereas the second type of gelatin is obtained from an acid treatment. This means that the variations in the collagen treatment allows the gelatin to bind with either positively or negatively charged molecules [158]. In

contrast to collagen, gelatin exhibits limited antigenicity due to heat denaturation [145]. In addition, the important bioactive sequences presented by the collagen (e.g., RGD peptides) for cell attachment and matrix metalloproteinase (MMP)- sensitive degradation sites are retained in the gelatin backbone [159]. This is extremely important because critical cellular functions like migration, proliferation, and differentiation, can be modulated via integrin mediated cell adhesion and cell-mediated enzymatic degradation [144,160,161]. Gelatin is thermo-responsive hydrogel: this means that gelatin undergoes into a reversible sol-gel transition by decreasing the temperature below 37 °C, while liquefies by heating at physiological temperatures. To stabilize gelatin at physiological temperatures, gelatin can be chemically or enzymatically cross linked with different crosslinking agents (e.g., glutaraldehyde [162], formaldehyde [163], genipin [164], microbial transglutaminase (TG) [126,165]) [166,167]. As an example, TG was used to fabricate gelatin scaffolds with tunable degradation rates. Yung et al. showed that HEK 293 cells encapsulated in TG crosslinked gelatin were capable of proliferate forming spheroids that increased in size in time. They also showed that the construct was stable a physiological temperature and showed that proteolytic degradation was controlled by surface erosion [126]. Gelatin has been chemically modified, where methacrylate groups were added to the its lateral chains creating a photo-crosslinkable gelatin-methacryloyl (gelMA) [144]. GelMA has been extensively used as a bioink for fabricating bioprinted constructs [144].

1.2.3.1.2   Synthetic polymers: poly(lactic acid) (PLA) and poly(vinyl alcohol) (PVA)

PLA is an aliphatic polyester widely used in the fabrication of porous scaffolds for TE applications [168]. PLA is biocompatible, biodegradable, highly hydrophobic with limited water uptake and soluble in organic solvents (e.g., choloroform) [169]. PLA with different molecular weight has been produced by a multistep process where, firstly the cyclic dimer of the lactic acid is produced and isolated and secondly the isolated product is used as monomers ring-opening polymerization [170]. Considering that PLA is made by a lactic acid, which is a chiral molecule, it exists in two stereoisomeric forms that give rise to four morphologically distinct polymers. The first two are D-PLA and L-PLA, which are the stereoregular polymers; the second two are D,L- PLA, which is the racemic polymer obtained from a mixture of D- and L-lactic acid, and meso-PLA can be obtained from D,L-lactide [143]. The differences in the crystallinity of D,L- PLA and L-PLA have important practical considerations. On one hand, D,L- PLA is usually considered for application such

drug delivery since is an amorphous polymer [169]. On the other hand, the semi-crystalline L-PLA is employed in application where high mechanical strength is required (e.g., sutures and orthopaedic devices) [171,172]. In fact, L-PLA (PLLA) is a rigid material that has a glass transition temperature (T_g) of approximately 60 °C, and a melting point temperature (T_m) of 180 °C. The PLLA Young's modulus is close to 3.5 GPa while its stress at break is 65 MPa and a maximum break elongation smaller than 6 % [173,174]. PLLA polymers degrade by hydrolysis: the degradation starts with upper uptake followed by random cleavage of the ester bonds in the polymer chain. The degradation is throughout the bulk of the material [175]. During the degradation of semi-crystalline PLLA, the crystallinity of the residual material increases because the degradation takes place initially in the amorphous domains [176]. By contrary. the final degradation and resorption of the PLLA implants involves inflammatory responses. Although this late-stage inflammatory response can have a deleterious effect on some healing events, PLLA has been successfully employed as matrices for cell transplantation and tissue regeneration [177,178].

PVA is a synthetic polymer produced via partial or full hydrolysis of the poly(vinyl acetate) [179]. The physical, chemical and mechanical properties of the PVA it is dependent from the degree of hydrolysis [180]. The resulting PVA polymer is highly soluble in water but resistant to most organic solvents [179]. PVA is a vinyl polymer in which the main chains are joined by only carbon-carbon links [181]. The resistance of the PVA against organic solvents as well as the aqueous solubility made PVA a suitable material for several applications. In fact, PVA is commonly used for food packaging, textile industries, and paper products manufacturing [182,183]. PVA is also used as a biomaterial since is biocompatible, nontoxic, noncarcinogenic. In addition, the PVA swelling properties, bioadhesive characteristics, and biodegradability made PVA a perfect candidate material for the fabrication of medical devices as well as for TE applications [178,184,185]. PVA is a biodegradable polymer, and its degradability is enhanced through hydrolysis because of the presence of hydroxyl groups on the carbon atoms. PVA is manly used to create hydrogels [183]. PVA hydrogels and membranes have been developed for biomedical applications such as contact lenses [186], artificial pancreases [187,188], hemodialysis [189], and synthetic vitreous humor [190], as well as for implantable medical materials to replace cartilage [191–193] and meniscus tissues [194,195].It is an attractive material for these applications because of its biocompatibility and low protein adsorption properties resulting in low cell adhesion compared with other hydrogels [179,185]. PVA hydrogels have been also investigated as artificial cartilage replacements due to their rubber elastic physical properties, and because

the hydrogels can be manufactured to have tensile strength in the cartilage range of 1–17 MPa [179]. Moreover, PVA implants have been used in meniscus replacements. Kobayashi studied PVA hydrogel for the replacement of meniscus using a rabbit model. The PVA hydrogel implants were placed in the lateral compartment of one knee of female rabbits. Five rabbits were examined after 2 year and the postoperative follow-up showed that the PVA hydrogel implants were intact, with no wear or dislocation seen [194,195].

1.2.3.2 Fabrication methods

To date, several technologies have been employed to fabricate scaffolds for TE applications. Porous random scaffolds with a limited control of scale have been fabricated using freeze-drying [196–198], electrospinning [75,199,200], solvent casting/particulate leaching [201–203], whereas scaffolds with controlled 3D architectures were fabricated using additive manufacturing technologies (AM) [204–207]. In particular, fused deposition modelling (FDM) has been used to fabricate, via layer-by-layer, porous and complex 3D scaffolds with resolution of 100-200 µm [34]. However due to the rigidity of the biopolymers used (e.g., PLA, poly(caprolactone) (PCL)) in FDM the fabricated scaffolds were mainly used to engineer the bone [39,74,205]. FDM has been also used to 3D print poly(vinyl alcohol) (PVA)sacrificial structures [202,208] (Figure 1.8(A-C)). The fabricated 3D printed structures were used as sacrificial templates to create thick and 3D elastomeric scaffolds with controlled 3D architecture (Figure 1.8(D-R)). The 3D scaffolds were seeded with HepG2 and were kept in culture for 12 days. Mohanty et al. demonstrated that the 3D architecture of the scaffold was sufficient to ensure an adequate transport of oxygen and nutrients to maintain a good cell activity and viability (Figure 1.8(S)). Although the constructs could maintain good cell viability, the elastomeric material employed does not represent a suitable material choice for the fabrication of scaffolds for TE applications since it is not degradable. In addition, the initial seeding was not homogenous throughout the scaffold showing the difficulties of the tissue scaffolding approach.
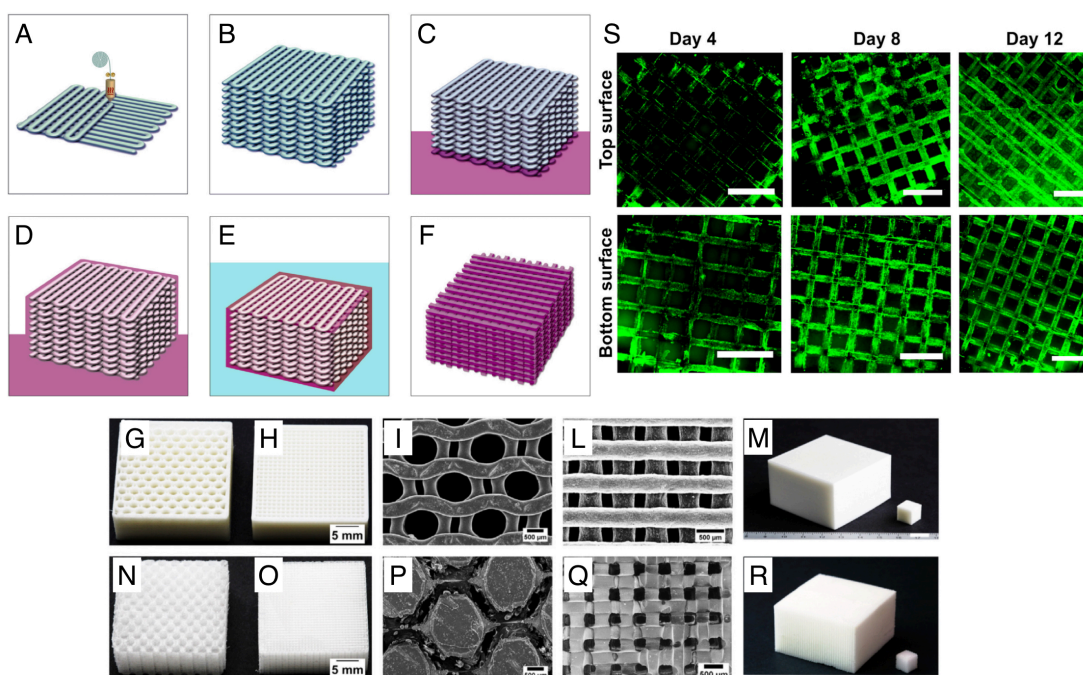
Figure 1.8. (A-F) Schematic illustration of the steps required to fabricate structured porous elastomeric scaffolds. (G-R) Photographs of the molds and the fabricated scaffolds with (G, N) hexagonal and (H, O) lattice-like structures; SEM images of the sacrificial templates and the fabricated scaffolds having (I,P) hexagonal and (L,P) lattice-like; (I-J) Photographs of the sacrificial templates 3D printed with 50 (1 cc cube) and 150 (75 cc cube) layers and (J) the fabricated elastomeric scaffold using the sacrificial templates in I. (Scale bars: 1cm.) (S) Live/dead staining of HepG2 cells grown on the top and bottom surface of elastomeric PDMS scaffold at day 4, 8 and 12 (Scale bars: 1 mm). The image is reprinted from [208].

Another AM technology used to fabricate porous scaffolds is the sterelitography. Stereolitography is a solid freeform fabrication technique where a photocurable resin placed in a reservoir is crosslinked by a laser controlled in X-Y. A vertically controlled stage is immersed at the surface of the resin reservoir and the laser starts the polymerization at the resin surface. Every layer the stage move up and the polymerization proceeds thus creating a 3D structures. The resolution of the stereolitographyc process can me tuned by focusing the laser as well as increasing the laser power. In addition, the stereolitography fabrication technique can achieved extremely high resolutions. Traditionally, stereolitography has been used to fabricate 3D cell-free scaffolds, but with the development of more biocompatible resins, the potential for the stereolitography to be used for TE increased [209–211]. As an example, Hang Lin et al. fabricate 3D hydrogel scaffolds with specific shapes and internal architectures by using stereolitography. They showed that human adipose-derived stem

cells (hADSCs) encapsulated in a hydrogel composed by PEGDA and lithium phenyl-2,4,6-trimethylbenzoylphosphinate (LAP) as photo-initiator were capable of stay alive for 7 days thanks to the 3D architecture of the fabricated scaffolds [212]. Although the fabrication of porous scaffold was beneficial to enhance the mass transport properties, there is still a lack of understanding of tissue and organ formation leading to the limitation in fabricating constructs through tissue scaffolding [25]. In tissue scaffolding is still difficult to include and to homogeneously seed high densities of cells within a porous scaffold, particularly when the goal is the scaling up of the final construct [25]. In addition, higher cell densities might require an optimized media exchanger to guarantee the necessary supply of oxygen and nutrients required to the cells to maintain their metabolic activity [52].

Another possible approach used to generate engineered construct is to use natural or synthetic hydrogels as scaffold candidate material [213]. Cells within a tissue interact with neighboring cells and with the ECM throughout 3D interactions establishing a 3D communication network that maintains the specificity and homeostasis of the tissue [58,62,135]. Hydrogels are able to resemble the nature of most tissues due to their high water content and the presence of pores that facilitate the free diffusion of oxygen, nutrients and growth factors, morphogens, etc. [135] [18,23]. In addition, hydrogels have been employed to encapsulate cells to create 3D cell cultures: such cultures are able to re-establish such physiological cell–cell and cell–ECM interactions that can mimic the specificity of real tissues better than conventional two-dimensional (2D) cultures [213,214]. 3D cultures platforms are currently used in several biological applications, including tumor biology [46,215,216], cell migration and cell adhesion [217–219]. As an example, a recent study showed that collagen crosslinking-induced ECM stiffening supports the invasive phenotype by enhancing integrin signaling [220]. By using glutaraldehyde as a crosslinker to increase the stiffness of collagen gels independently from pore size or collagen concentration, Lang et al. showed that 3D invasion is dependent on pore size; while increased matrix stiffness promotes 3D invasion in gels with large pores (small steric hindrance), increased matrix stiffness hinders cell invasion in gels with small pores (large steric hindrance) [221]. Although encapsulated cells within hydrogels could potentially mimic artificial ''mini'' organs [32,222] or be used to create more complex tumors models [46], the absence of adequate perfusion limits the final scalability of the construct.

Finally, a third possible approach used in TE to fabricate 3D constructs does not require a solid scaffold structure. It consists in the belief that the tissue is a cell-generated material and therefore the direct manipulation and the control of cells is more important that

the provision of the structural, mechanical and chemical cues via the intermediary of a scaffold [223]. In such approach, cells are encapsulated in hydrogels forming clusters or aggregates that are manipulated or positioned into 3D cellular constructs in a bottom-up approach using bioprinting technology [7,224–226]. These aggregates are used as single bricks that are deposited in controlled positions in the 3D space generating constructs with more *in vivo* like cellular conditions [223] (Figure 1.9).

Figure 1.9. From 2D cell culture to bioprinting of tissues. The image is reprinted from [144].

Recentely, Kesti et al. designed two different inks for the fabrication of cartilaginous graft structures. The first ink, a combination of gellan gum, alginate, HA (hyaluronic acid) particles and cells, was responsible for defining the tissue graft. The second ink, Pluronic F127, was used as support material for the dual printing of complex structures. They were capable of bioprinting different cartilaginous grafts with different complexities such as the ear, meniscus, intervertebral disk, and a nose [226]. Although the bottom-up approach has a number of hidden advantages over the scaffold fabrication approach, the mechanical strength of the final construct is not sufficient to guarantee the long-term stability of the constructs during maturation, and the assembly of large structures is still limited by the transport of oxygen and nutrients until a vascular system is developed [7,60].

All the proposed approaches have been currently used to fabricate TE constructs with different degree of complexities trying to recapitulate the whole complexity of the

native tissue. However, many authors agree on the fact that high levels of complexity are not necessary for many applications, since many tissues and organs are capable of remodeling and regeneration, and a correctly designed engineered construct could take advantage of this capacity [51,227]. In fact, cells enclosed within 3D matrices rapidly remodel their microenvironment depositing their ECM molecules [51,61]. For this reason, it is possible to atone the absence of such complexity with artificial systems capable of inducing desired effects in a more efficient and rational way to the hosted cells [227]. In addition, when designing and fabricating tissue constructs with relevant dimensions the absence of a network of perfusable channels and finally the lack of an existing vasculature is still the limiting factor to the fabrication of thick and dense tissues and finally organs.

1.3 Strategies for the vascularization of tissue constructs

The ability to fabricate tissues constructs with a network of perfusable channels represents one of the main challenges that TE is facing today. In fact, the lack of an efficient way to exchange media rate ensuring oxygen and nutrients and at the same removing waste is the limiting factor for the fabrication of complex and dense tissues. Nonhomogeneous cell distribution and limited metabolic activities are often observed, since seeded cells cannot get enough oxygen, growth factors, and nutrients for metabolic activities that are needed for maturation during perfusion [6,18,228]. Moreover, the biomaterial employed plays an important role since it is responsible to transport and release bioactive molecules, while meeting regulatory biocompatibility and biodegradability standards together with a network of molecules important for the cellular adhesion [6]. The currently strategies employed to fabricate vascularized tissue constructs are: microfluidic system integration, 3D sacrificial molding, direct bioprinting and the combination between bioprinting and sacrificial moulding using fugitive inks.

1.3.1 Microfluidic system integration

Several methods to fabricate microfluidic systems have been employed to fabricate vascularized constructs. These methods comprises soft lithography [54,228–231], and laser-based technologies [232–238]. However, each of the above-mentioned fabrication techniques had its own advantages and disadvantages. Soft lithography represents a popular method in vasculature network fabrication due to its accuracy, reproducibility, and low cost. Using soft lithography technology, Zheng et al. fabricated a microfluidic network in

a collagen matrix, that was populated by human umbilical vein endothelial (Huvec) cells [229]. The micro vasculature was actively perfused and the huvec cells formed a confluent monolayer within the collagen channels showing the differences in the channel permeability in response to the presence of the cells (Figure 1.10 (A-B)).
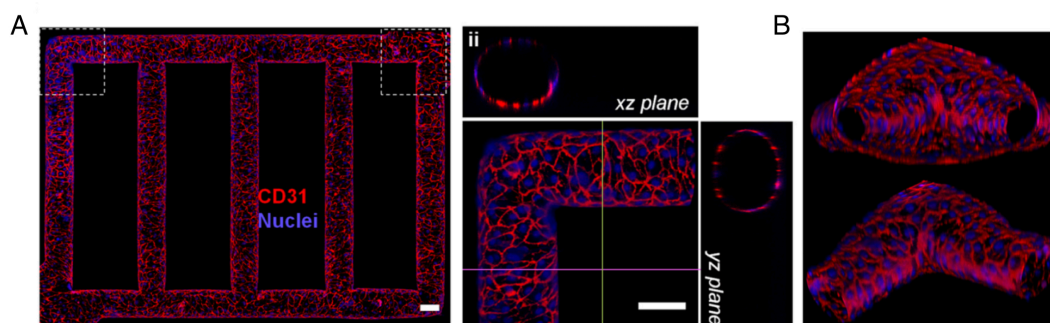
Figure 1.10. Endothelialized micro- fluidic vessels: (A-B) huvec cells are culture within a vascular network creting vascular channels with changed permeability. Red, CD31; blue, nuclei (Scale bar: 100 µm.) The image is reprinted from [229].

Cuchiara et al. developed a soft lithography process to fabricate a microfluidic network by using poly(ethylene glycol) diacrylate hydrogel. They demonstrated that by having an active perfusion, encapsulated mammalian cells where able to maintain a high viability within the hydrogel [230]. However, soft lithograph does not represent the best approach for fabricating complex 3D constructs due to cumbersome procedures. Despite their superior accuracy and repeatability, laser-based methods may not be suitable for fabricating thick tissue constructs because of their limited light-penetrating depths in precursor solution and because of the chemical residuals released during the reaction that might affected the cell culture. Ovsianikov et al. proposed a two photon polymerization to fabricate poly(ethylene glycol) (PEG) microstructures (300 µm height) with arbitrary shapes [238].

1.3.2 3D molding technique

The 3D molding technique consist of (i) the fabrication of a rigid 3D template, used as a negative mold to define the network of the microfluidic architecture, (ii) the casting of the 3D template into a suitable material and (iii) the sacrifice the template revealing a microfluidic architecture in the bulk material. Therriault et al. was able to use the 3D molding technique to fabricate microvascular networks. A fugitive ink was direct printed to fabricate the 3D lattice network. The 3D lattice network was casted into an epoxy resin, and the

epoxy resin was cured and finally, the 3D network was extracted from inside the cured resin revealing the complex microfluidic architecture. The fabricated scaffolds had 3D microvascular networks with geometric complexity and where able to generate complicated flow patterns. However, the 3D sacrificial molding required the use of processing conditions, for either removing the sacrificial filaments or casting the surrounding material, that could not be accomplished with aqueous-based ECMs or in the presence of living cells [239]. By the contrary, Miller et al. was the first one that coupled the 3D sacrificial molding with ECMs and living cells (Figure 1.11(A)). They used FDM to fabricate 3D sacrificial lattice-like templates using a glass carbohydrate material (Figure 1.11(B)). The peculiarity of their 3D printed templates was that the glass carbohydrate material used to fabricate the 3D templates were water soluble. Then different ECMs (e.g., agarose, alginate, PEG, fibrin and matrigel) with encapsulated cells were casted around the 3D printed structures starting the dissolution and subsequently the removal of the sacrificial templates. They demonstrated that the presence of a perfusable network of channels was essential to deliver sufficient nutrients to the encapsulated cells, and higher cell viability resulted in regions closer to the vasculature network [240] (Figure 1.11(C-D)).
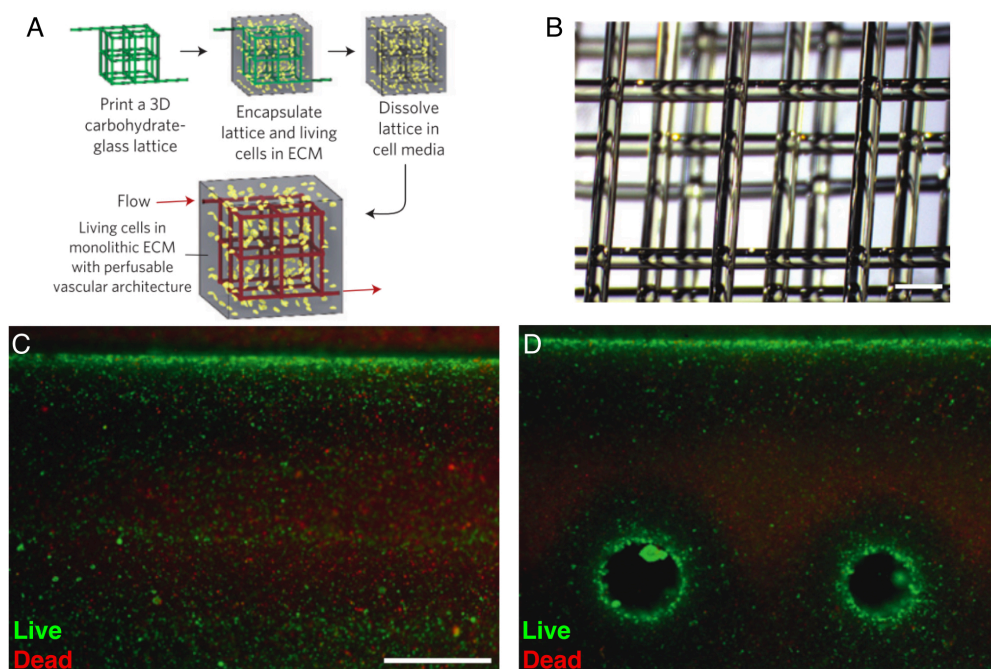
Figure 1.11. (A) An open interconnected, self-supporting sacrificial template is printed for the casting of 3D vascular network. The sacrificial template is encapsulated in ECM with cells, and then the sacrificial structure is dissolved in minutes in media. The process allows the creation of a tissue construct with a vascular network that matches the original lattice. (B) Printed multilayered carbohydrate-glass lattice

(scale bar, 1mm.) (C-D) Live/Dead images of primary rat hepatocytes and stabilizing stromal fibroblast encapsulated in agarose gels (slab versus channeled) after eight days in culture (scale bar, 1mm.) The image is reprinted from [240].

Sacrificial templates have been fabricated also by using alginate bioprinted structures. Bertassoni et al. showed that by bioprinting agarose, it was possible to create complex microchannels within methacrylated gelatin (GelMA), star poly(ethylene glycol-co-lactide) acrylate (SPELA), poly(ethylene glycol) dimethacrylate (PEGDMA) and poly(ethylene glycol) diacrylate (PEGDA) hydrogels (Figure 1.12(A-B)). In addition, GelMa was used to demonstrate the importance of a single channel in maintaining good cell viability in the encapsulated cells as wells to deliver signals to guide cell activities [241] (Figure 1.12(C-F)).
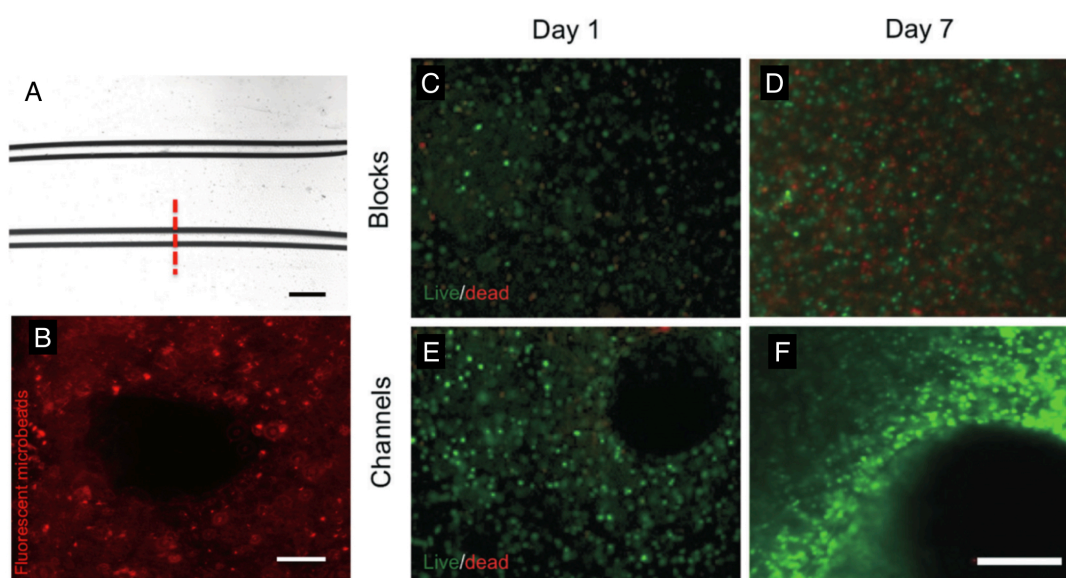
Figure 1.12. (A) Bioprinted agarose template fibers and respective microchannels. (scale bar 1 mm.) (B) Cross-section (indicated by red dotted-line) of a fluorescent microbead GelMA hydrogel indicating the rounded shape of the lumen (scale bar 250 μm.) Viability of MC3T3 cells encapsulated in 10% GelMA hydrogels comparing constructs with (E-F) fabricated microchannel versus a slab-hydrogel (C-D) at day one and day 7. (scale bar 700 μm.) The image is reprinted from [241].

By contrary, Nam Chan et al. used stereolitography to fabricate complex 3D molds. A photocrosslinked resin was used to 3D print the negative mold for the subsequent fabrication of the sacrificial templates. Then, the sacrificial templates were embedded in 10% agarose hydrogel encapsulated with HepG2 to form the vascular channels. Although

their constructs had a complex vasculature network, the encapsulated cells didn't present signs of proliferation after 3 days in perfusion. In addition, the overall fabrication consisted in several steps, requiring the use of toxic solvents for the dissolution of the 3D printed resin mold.

Several fabrication techniques such as molding [242,243], FDM [240,244,245], bioprinting [241], and stereolitography [246,247] have been used to fabricate sacrificial molds with a plethora of different sacrificial materials (e.g., carbohydrate glass, sodium alginate, PVA) as well as complexities. However, in some cases the sacrificial templates employed to fabricate the constructs with encapsulated cells were rather simple, based on single or parallel planar microchannels [240–243,245]. In others, the complex sacrificial templates were achieved by several fabrication steps [244,246,247] and the final constructs didn't have a clear strategy of active perfusion [240–242,245].

1.3.3 Direct bioprinting

The direct bioprinting fabrication technique was employed to fabricate vascular tissue constructs by a layer by layer deposition of hydrogels and cells at the same time [7,28,55,84,225,226,248,249]. Gao et al. presented a bioprinting technique with a coaxial nozzle where they fabricated vascular conducts made by alginate filament (Figure 1.13(A)). They demonstrated that the bioprinted conducts could fuse together creating a construct of fused conducts with different geometries where the cells encapsulated nearby the channel could survive during 7 days (Figure 1.13(B-D)) [250].
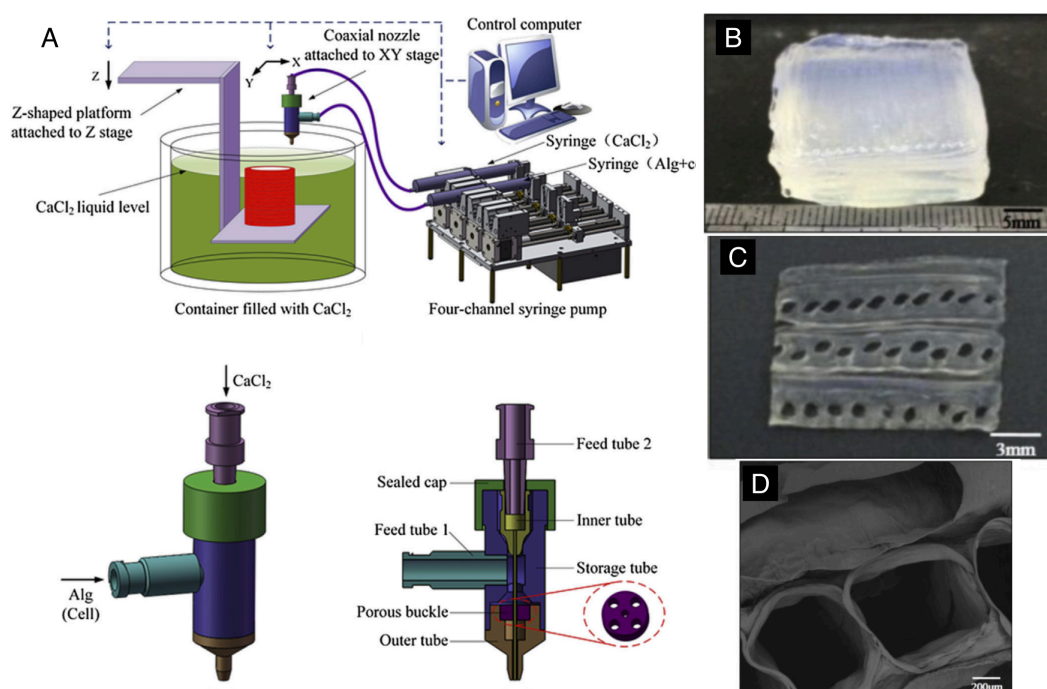
Figure 1.13. (A) Schematic showing the coaxial nozzle-assisted 3D bioprinting system along with details about the modified coaxial nozzle. (B) Photographs of the fused adjacent alginate hollow filaments in a printed cuboid structure consisting of 6 layers of hollow filaments. (C) Macroscopic view of the cross section of the printed cuboid structure. (D) SEM image of fused filaments in the printed cuboid structure. The image is reprinted from [250].

By contrary, Colosi et al. showed the fabrication of a bioprinted 3D lattice-like structures using an engineered blend ink based on a mixture of gelatin methacroyl (GelMA), alginate, photoinitiator and cells (Figure 1.14(A-B)). The ink was bioprinted using a coaxial needle to generate 3D vascularized constructs with huvecs lining in the inner regions of the lattice-like structure (Figure 1.14(C-F)). They also showed that the spatial deposition control of the ink was obtained using the bioprinting fabrication techniques and they were capable of cast cardiomyocytes encapsulated on a hydrogel to create a co-culture of a vascularized cardiac tissue (Figure 1.14(G-J)) [251].
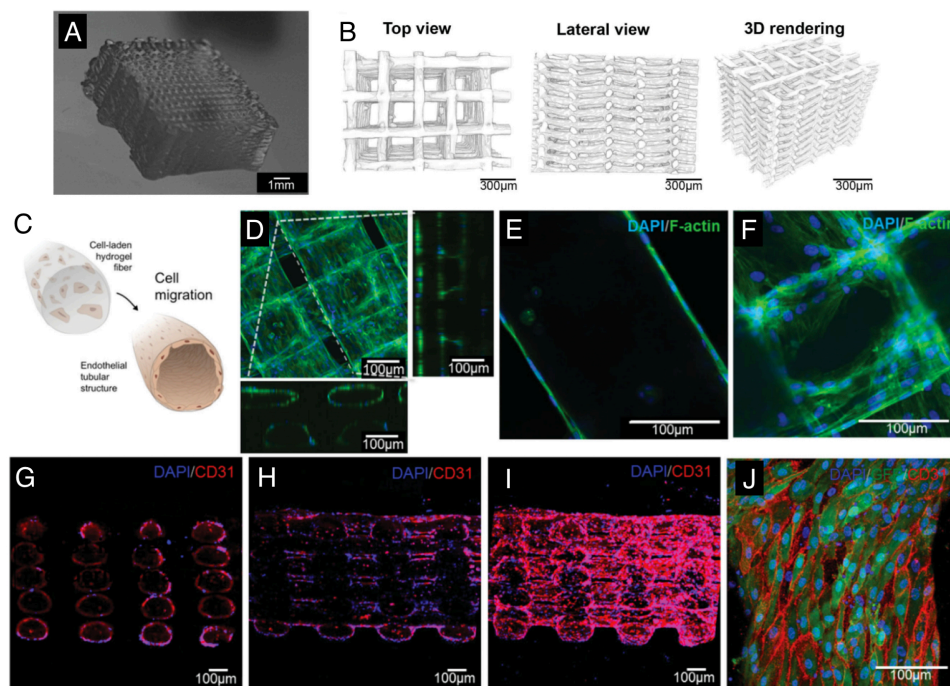
Figure 1.14. (A) Photograph of the 3D printed construct (30 layers). (B) 3D μCT reconstructions of the top and view of the lateral and 3D μCT final bioprinted structure. (C) Schematic of the migration to outer regions of the encapsulated HUVECs in the bioprinted fibers after 10 days of culture. (D-F) Confocal microscopy images showing the (D) top view, (E) cross section and (F) fiber junctions showing interconnected structures. (G-J) Confocal microscopy images of a 1 mm thick lattice-like structure showing (G) the transversal cross-section, (H) the longitudinal cross-section, (I) outer surface of the construct. (J) Top view of a single fiber immunostained for CD31 (red) and DAPI (blue). The image is reprinted from [251].

Also, Another study has been shown a bioprinted 3D construct using an engineered blend ink based three different hydrogels: gelatin methacryloyl (GelMA), sodium alginate, and 4-arm poly(ethylene glycol)-tetra-acrylate (PEGTA). The ink was bioprinted using a tri-layered coaxial nozzle to generate perfusable structures with cells encapsulated on it. Jia et al. showed that the spatial deposition control of the ink was obtained using the bioprinting fabrication techniques by creating 2D structures with different shapes, and by creating also 3D lattice-like structures with encapsulated cells on it [252]. Finally, Zhu et al. presented a pre-vascularized construct fabricated with a microscale continuous optical bioprinting (μCOB). In one case, A mixture of GelMA and LAP were used to encapsulate HepG2. In the other, Huvecs cell and supportive 10T1/2 cells were encapsulated in the same hydrogel composition to form pre-vascularized constructs. They have showed that their fabrication technique was fast (~1min) and was able to have good cell viability (~80%). In addition, the

pre-vascularized constructs were implanted *in vivo* for 2 weeks showing a formation of an endothelial network [253]. Although bioprinting could represent the future for the fabrication of thick tissue constructs, there are some technological challenges, such as material printability, special nozzle requirement, printing time and complexity of the forms that can be printed without the presence of a support structure underneath [254].

1.3.4 Direct bioprinting and sacrificial molding

Direct bioprinting and 3D molding were coupled to fabricate several complex TE construct. It consists on printing different inks at the same time, where one of the inks represents a "fugitive ink". The fugitive ink is characterized from a viscosity that changes in function of the temperature. For certain ranges of temperature, the viscosity of the fugitive ink is enough to be printed whereas for other ranges of temperature the viscosity of the fugitive is small enough to be removed from inside the ECM without causing damages to the printed construct. Several studies have been used fugitive inks in combination with the bioprinting technology to fabricate vascularized tissue constructs [87,255–259]. As an example, a recent study used gelatin hydrogel as a fugitive ink to fabricate vascularized constructs. The tissue construct was fabricated by a multi-step approach: first collagen was bioprinted for defining the construct bottom. Then gelatin was bioprinted to define the internal channels followed by the deposition of a mixture of fibrinogen, thrombin, huvecs and normal human lung fibroblast (NHLS) cells. Then, another layer of collagen was bioprinted on top of the structure finalizing the construct. Finally, the gelatin was removed from within the construct leaving behind the open channels and Huvecs were seeded within the channels to form the vasculature (Figure 1.15(A)). Lee et al. demonstrate that the perfusion of the channels and the composition of the ECMs as well as the presence of the cells where able to induce the formation of micro-capillaries (Figure 1.15(B-F)) able to increase the diffusion of fluorescence molecules within a hydrogel construct [259] (Figure 1.15(H)).
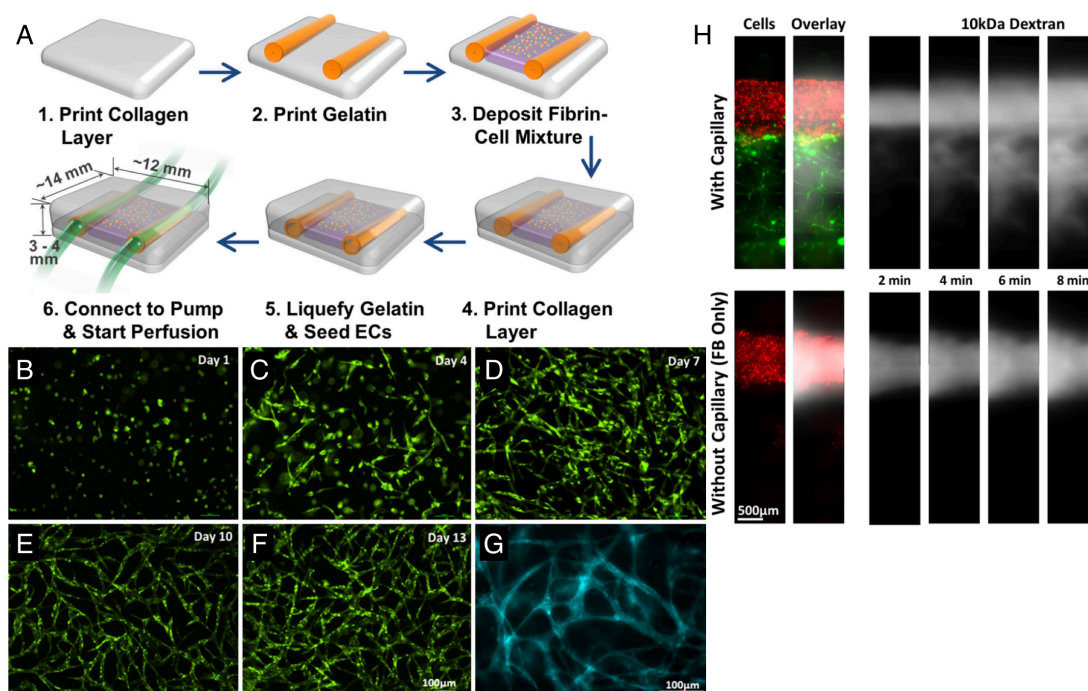
Figure 1.15. (A) Fabrication steps of the 3D printed construct using 3D bio-printer. (B-F) Capillary network formation of GFP-huvecs within thirteen days and (G) CD31 staining on Day 14. (H) Time-lapse fluorescence images of 10 kDa dextran diffusion in structure with capillary network (top panel) and structure without capillary network (bottom panel). The image is reprinted from [259].

In another study, Pluronic F127 has been used as fugitive ink to fabricate micro-channels. Kang et al. developed a fabrication technique called integrated tissue–organ printer (ITOP) (Figure 1.16(A)). It basically consists on printing several materials at the same time with different purposes: bioinks made by ECMs with cells encapsulated are used to define the location of the cells whereas pluronic F127 is used to create a network of micro-channels with the purpose to enhance the transport of oxygen and nutrients. To increase the mechanical properties of the final fabricated tissue construct, PCL was also printed together with the other inks. They showed that they could fabricated large constructs with different sizes and morphologies. Moreover, they demonstrated that the different fabricated engineer constructs (Figure 1.16(C-F)) where able to be implanted *in vivo* regenerating the damaged tissue without any host immune response [257].
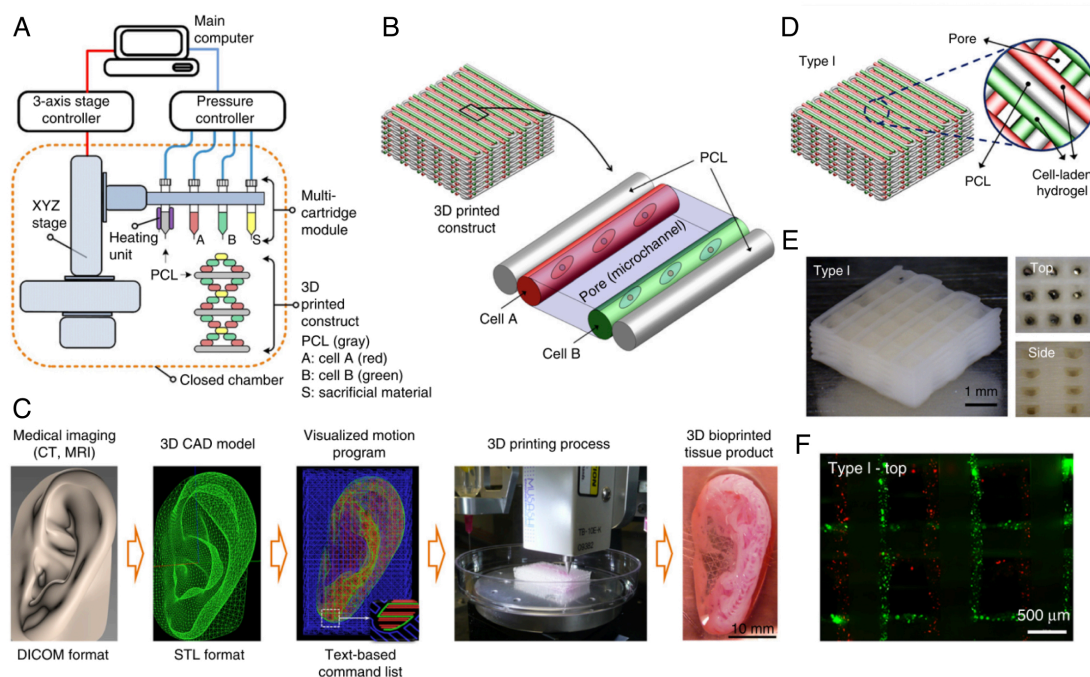
Figure 1.16. (A) The ITOP system. (B) Illustration of basic patterning of 3D architectures with several hydrogels, PCL and pluronic F127. (C) Steps necessary to fabricate TE constructs: from the conversion of medical data to the conversion in the STL format, the generation of the machine instructions and the fabrication of the 3D vascular constructs. The image is reprinted from [257].

By contrast, Kolesky et al. has been shown the fabrication of vascularized tissue constructs using a combination of bioprinting with the moulding approach together with the 3D moulding approach. They bioprinted a lattice-like structure with two different inks at the same time: the first ink used was pluronic F127, which was the sacrificial material responsible for defining the vascular channels. The second ink was a mixture of cells and suitable ECM that was made by a blend of gelatin and fibrinogen, which was direct printed in the positions along the vascular channels. The fabricated structure was used as mold and another mixture of gelatin and fibrinogen cross-linked by a dual-enzymatic strategy by using thrombin and transglutaminase (TG) was casted around the direct printed structure to give mechanical stability on the final printed construct. Then, the pluronic was removed from inside the fabricated construct leaving behind the open vasculature network (Figure 1.17(A)). Finally, the construct was connected to a pump and was perfused for up to 6 weeks (Figure 1.17(B-D)). They demonstrated that their fabricated constructs where able to be actively perfused with growth factors to differentiate human mesenchymal stem cells (hMSCs) toward an osteogenic lineage in situ [256] (Figure 1.17(E-F)).
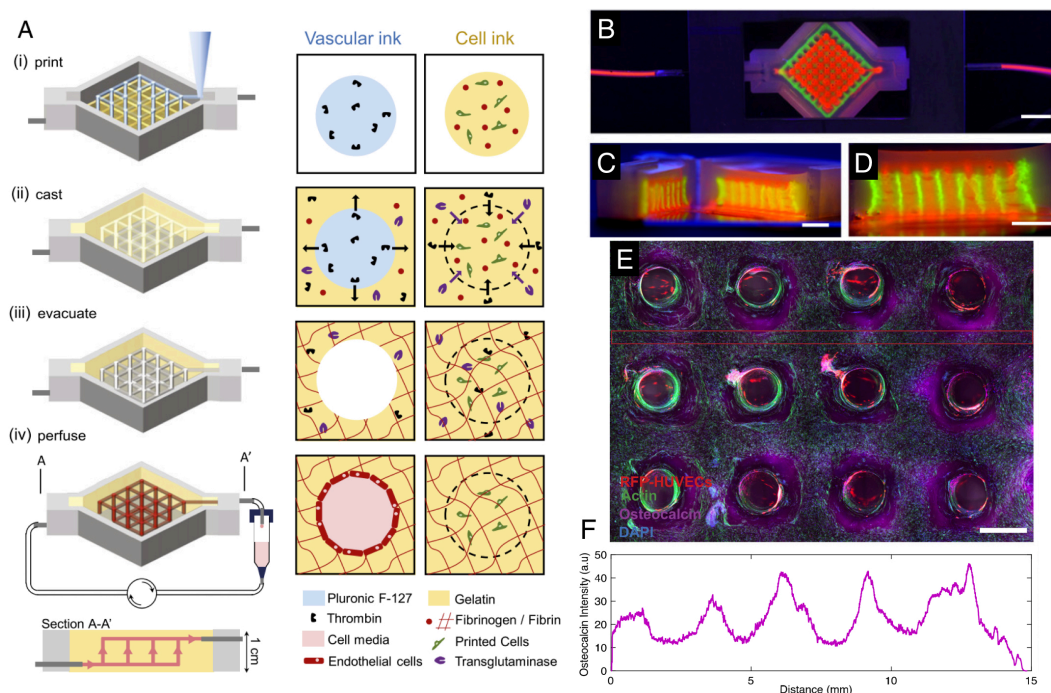
Figure 1.17. (A) Schematic illustration of the tissue Manufacturing process. (B-D) Photographs of a printed construct within a perfusion chamber. (Scale bars: 5 mm.) E) Confocal microscopy trough a cross section of 1cm thick construct after 30 days of perfusion showing the osteogenic differentiation. (Scale bar: 1.5 mm.) (F) Osteocalcin intensity within the fabricated construct inside the dotted red lines in C.

Despite all the presented works were a huge step forward in the field, especially in fabricating thick tissue constructs, there are still some aspects that needs to be addressed. From a mechanical point of view, the fabricated constructs are mechanically weak, and in some cases they required the use of biopolymers to stabilize the structure [227]. In other cases, the bioprinted structure needed a cast of a hydrogel mixture to mechanically stabilize the construct [256]. Nevertheless, it still an open question if pluronic F127 can be used in TE applications due to its poor cell compatibility [260].

1.4 Research strategy

1.4.1 Problem definition

Despite several technologies have been used to engineer vascular constructs, the biofabrication of a perfusable branch network in thick engineer constructs remains a challenge. The majority of the proposed constructs only presented a single or a built-in planar vasculature and the constructs that showed a more complex one are based on 2D

lattice-like structures [28,87,240–243,251,252,255,256]. A natural blood vessel network, on the other hand, is a complex hierarchical organization, where tubular vessels branch into smaller-scale vessels up to capillary scale. In addition, in some cases, the majority of ECMs employed in the bioprinting technique are based on synthetic hydrogels that require initiators to be photocrosslinked, and the byproducts released during the fabrication process are usually toxic or acidic, which further devastates the cell culture environment. In other cases, the ECMs are based on natural hydrogels that have exceptional biocompatibility and biodegradability providing an ideal substrate for cell encapsulation. However, the inks based on natural hydrogels are intrinsically weak, and therefore the final mechanical properties of the fabricated construct are rather limited. Finally, to engineer constructs with some functionality, it is necessary to have different cells populations encapsulated within the same ECM to guide the tissue towards the proper maturation, and a continuous perfusion to ensure the adequate level of oxygen and nutrients to the fabricated tissue construct.

1.4.2 Research objectives

The objective of this thesis is to contribute to the knowledge of how to fabricate TE tissue constructs having: (1) relevant sizes, (2) targeted mechanical properties, (3) relevant number of cells, and (4) perfusable 3D vasculature.

More precisely, it investigates how to use FDM and 3D molding technique to fabricate thick constructs with a built-in network of channels and controlled mechanical properties that can be actively perfused. The presented method has greater flexibilities compared to existing strategies in the literature. The offered advantages are: (1) it uses natural hydrogels (e.g., gelatin) and (2) it allows the fabrication of complex 3D shapes (e.g., 2D, and full 3D structures) using a cheap and commercial layer-by-layer printed process.

The proposed method allows the fabrication of thick (e.g., 1 cm) tissue constructs with an integrated vasculature that supports the perfusion media, including nutrients, water, and oxygen, and the removal of waste.

1.4.3 Thesis outline

This thesis comprises two theoretical and four experimental chapters. **Chapter 2** includes a discussion regarding stem cells differentiation, together with a description of an *in vitro* system used to differentiate hiPSC-derived DE cells towards mature hepatocytes by

the effect of the fluid flow. A tissue engineering bioreactor platform was used to perfuse a 3D tissue scaffold, having different 3D architecture, at two different flow rates for long term periods (> 21 days). Hepatic differentiation and functionality of hiPSC-derived hepatocytes are assessed using freshly obtained human liver as an ex vivo liver representative model.

Chapter 3 introduce the methods used to fabricate TE constructs with a built-in network of microchannels. The constructs are made by gelatin hydrogel with tunable mechanical properties (e.g., 2-8 kPa), and are fabricated by a 3D molding approach. It is illustrated how 2D and 3D sacrificial templates are manufactured using the FDM technology. Besides, it is also showed how the sacrificial structures are cast in the hydrogel material to fabricate constructs with embedded vasculature and with encapsulated cells. **Chapter 4** illustrates the effect of the active perfusion in thick and densely populated construct with a 3D complex vasculature. The presented construct had controlled mechanical properties (e.g., liver), and HepG2 cells encapsulated on it. It is, therefore, demonstrated that the control of the ECM environment and the active perfusion could sustain a high concentration encapsulated cells, inducing them to proliferate and to aggregate forming spheroids with compact morphology.

In **Chapter 5** is introduced a hydrogel-based fluidic system fabricated to simulate physiological barriers. Two parallel channels (1.2 cm long) are separated by 370 μm of gelatin that acts as a relevant tissue barrier. The fluidic system integrates electrodes for measuring the trans-epithelial electrical resistance (TEER), a common-used parameter to assess biological membranes integrity.an electrical setup to perform impedance measurements in real-time. The system was electrically characterized showing the potential of the fabricated device.

Finally, the conclusions of this thesis and the considerations regarding the future perspectives of the presented research concerning the challenges in the field are described in **Chapter 6**.

References

[1]   E. Lavik, R. Langer, Tissue engineering :current state and perspectives, Appl Microbiol Biotechnol. 65 (2004) 1–8. doi:10.1007/s00253-004-1580-z.

[2]   R.M. Nerem, Tissue engineering: confronting the transplantation crisis., Proc. Inst. Mech. Eng. H. 214 (2000) 95–99. doi:10.1243/0954411001535273.

[3]   G. Orlando, P. Baptista, M. Birchall, P. De Coppi, A. Farney, N.K. Guimaraes-Souza, E. Opara, J. Rogers, D. Seliktar, K. Shapira-Schweitzer, R.J. Stratta, A. Atala, K.J. Wood, S. Soker, Regenerative medicine as applied to solid organ transplantation: Current status and future challenges, Transpl. Int. 24 (2011) 223–232. doi:10.1111/j.1432-2277.2010.01182.x.

[4]   M.E. Furth, A. Atala, Chapter 6 - Tissue Engineering: Future Perspectives, in: R. Lanza, R. Langer, J. Vacanti (Eds.), Princ. Tissue Eng. (Fourth Ed., Fourth Edi, Academic Press, Boston, 2014: pp. 83–123. doi:http://dx.doi.org/10.1016/B978-0-12-398358-9.00006-9.

[5]   J.P. Vacanti, C.A. Vacanti, Chapter 1 - The History and Scope of Tissue Engineering, in: R. Lanza, R. Langer, J. Vacanti (Eds.), Princ. Tissue Eng. (Fourth Ed., Fourth Edi, Academic Press, Boston, 2014: pp. 3–8. doi:http://dx.doi.org/10.1016/B978-0-12-398358-9.00001-X.

[6]   H. Bae, A.S. Puranik, R. Gauvin, F. Edalat, B. Carrillo-Conde, N.A. Peppas, A. Khademhosseini, Building Vascular Networks, Sci. Transl. Med. 4 (2012) 160ps23-160ps23. doi:10.1126/scitranslmed.3003688.

[7]   S. V Murphy, A. Atala, 3D bioprinting of tissues and organs., Nat. Biotechnol. 32 (2014) 773–785. doi:10.1038/nbt.2958.

[8]   A.G. Mikos, S.W. Herring, P. Ochareon, J. Elisseeff, H.H. Lu, R. Kandel, F.J. Schoen, M. Toner, D. Mooney, A. Atala, M.E. Van Dyke, D. Kaplan, G. Vunjak-Novakovic, Engineering complex tissues., Tissue Eng. 12 (2006) 3307–39. doi:10.1089/ten.2006.12.3307.

[9]   M. Lovett, K. Lee, A. Edwards, D.L. Kaplan, Vascularization Strategies for Tissue Engineering, Tissue Eng. Part B Rev. 15 (2009) 353–370. doi:10.1089/ten.TEB.2009.0085.

[10]   J. Rouwkema, A. Khademhosseini, Vascularization and Angiogenesis in Tissue Engineering: Beyond Creating Static Networks, Trends Biotechnol. 34 (2016) 733–745. doi:10.1016/j.tibtech.2016.03.002.

[11]   R.P. Visconti, V. Kasyanov, C. Gentile, J. Zhang, R.R. Markwald, V. Mironov, Towards organ printing: engineering an intra-organ branched vascular tree., Expert Opin. Biol. Ther. 10 (2010) 409–20. doi:10.1517/14712590903563352.

[12]   H. Ko, B. Milthorpe, C. McFarland, Engineering thick tissues - the vascularisation problem, Eur. Cells Mater. 14 (2007) 1–19. doi:10.22203/eCM.v014a01.

[13]   R.K. Jain, P. Au, J. Tam, D.G. Duda, D. Fukumura, Engineering vascularized tissue., Nat. Biotechnol. 23 (2005) 821–3. doi:10.1038/nbt0705-821.

[14]   M.C. Peters, P.J. Polverini, D.J. Mooney, Engineering vascular networks in porous polymer matrices, J. Biomed. Mater. Res. 60 (2002) 668–678. doi:10.1002/jbm.10134.

[15]   S. Levenberg, J. Rouwkema, M. Macdonald, E.S. Garfein, D.S. Kohane, D.C. Darland,

R. Marini, C.A. van Blitterswijk, R.C. Mulligan, P.A. D'Amore, R. Langer, Engineering vascularized skeletal muscle tissue, Nat Biotechnol. 23 (2005) 879–884. doi:10.1038/nbt1109.

[16] V. Marx, Tissue engineering: Organs from the lab, Nature. 522 (2015) 373–377. doi:10.1038/522373a.

[17] M. Nikkhah, N. Eshak, P. Zorlutuna, N. Annabi, M. Castello, K. Kim, A. Dolatshahi-Pirouz, F. Edalat, H. Bae, Y. Yang, A. Khademhosseini, Directed endothelial cell morphogenesis in micropatterned gelatin methacrylate hydrogels, Biomaterials. 33 (2012) 9009–9018. doi:10.1016/j.biomaterials.2012.08.068.

[18] J. Rouwkema, N.C. Rivron, C.A. van Blitterswijk, Vascularization in tissue engineering, Trends Biotechnol. 26 (2008) 434–441. doi:10.1016/j.tibtech.2008.04.009.

[19] K. Bilodeau, D. Mantovani, Bioreactors for tissue engineering: focus on mechanical constraints. A comparative review., Tissue Eng. 12 (2006) 2367–83. doi:10.1089/ten.2006.12.2367.

[20] L.E. Freed, F. Guilak, X.E. Guo, M.L. Gray, R. Tranquillo, J.W. Holmes, M. Radisic, M. V Sefton, D. Kaplan, G. Vunjak-Novakovic, Advanced tools for tissue engineering: scaffolds, bioreactors, and signaling., Tissue Eng. 12 (2006) 3285–305. doi:10.1089/ten.2006.12.3285.

[21] S. Dermenoudis, Y.F. Missirlis, Bioreactors in Tissue Engineering, Adv. Eng. Mater. 12 (2010) B592–B608. doi:10.1002/adem.201080018.

[22] R. Sodian, T. Lemke, C. Fritsche, S.P. Hoerstrup, P. Fu, E. V Potapov, H. Hausmann, R. Hetzer, Tissue-engineering bioreactors: a new combined cell-seeding and perfusion system for vascular tissue engineering., Tissue Eng. 8 (2002) 863–70. doi:10.1089/10763270260424222.

[23] H.E. Abaci, R. Devendra, Q. Smith, S. Gerecht, G. Drazer, Design and development of microbioreactors for long-term cell culture in controlled oxygen microenvironments., Biomed. Microdevices. 14 (2012) 145–52. doi:10.1007/s10544-011-9592-9.

[24] B.J. Lawrence, M. Devarapalli, S. V Madihally, Flow dynamics in bioreactors containing tissue engineering scaffolds., Biotechnol. Bioeng. 102 (2009) 935–47. doi:10.1002/bit.22106.

[25] K.L. Moffat, R.A. Neal, L.E. Freed, F. Guilak, Chapter 13 - Engineering Functional Tissues: In Vitro Culture Parameters, in: R. Lanza, R. Langer, J. Vacanti (Eds.), Princ. Tissue Eng. (Fourth Ed., Fourth Edi, Academic Press, Boston, 2014: pp. 237–259. doi:http://dx.doi.org/10.1016/B978-0-12-398358-9.00013-6.

[26] S. Bhumiratana, J. Bernhard, E. Cimetta, G. Vunjak-Novakovic, Chapter 14 - Principles of Bioreactor Design for Tissue Engineering, in: R. Lanza, R. Langer, J. Vacanti (Eds.), Princ. Tissue Eng. (Fourth Ed., Fourth Edi, Academic Press, Boston, 2014: pp. 261–278. doi:http://dx.doi.org/10.1016/B978-0-12-398358-9.00014-8.

[27] L.G. Griffith, M. a Swartz, Capturing complex 3D tissue physiology in vitro., Nat. Rev. Mol. Cell Biol. 7 (2006) 211–24. doi:10.1038/nrm1858.

[28] Y.S. Zhang, A. Arneri, S. Bersini, S.R. Shin, K. Zhu, Z. Goli-Malekabadi, J. Aleman, C. Colosi, F. Busignani, V. Dell'Erba, C. Bishop, T. Shupe, D. Demarchi, M. Moretti, M. Rasponi, M.R. Dokmeci, A. Atala, A. Khademhosseini, Bioprinting 3D microfibrous scaffolds for engineering endothelialized myocardium and heart-on-a-chip,

Biomaterials. 110 (2016) 45–59. doi:10.1016/j.biomaterials.2016.09.003.

[29]   A. Schepers, C. Li, A. Chhabra, B.T. Seney, S. Bhatia, Engineering a perfusable 3D human liver platform from iPS cells., Lab Chip. 16 (2016) 2644–53. doi:10.1039/c6lc00598e.

[30]   S.N. Bhatia, G.H. Underhill, K.S. Zaret, I.J. Fox, Cell and tissue engineering for liver disease., Sci. Transl. Med. 6 (2014) 245sr2. doi:10.1126/scitranslmed.3005975.

[31]   J.W. Allen, S.N. Bhatia, Formation of steady-state oxygen gradients in vitro: application to liver zonation., Biotechnol. Bioeng. 82 (2003) 253–62. doi:10.1002/bit.10569.

[32]   S.N. Bhatia, D.E. Ingber, Microfluidic organs-on-chips, Nat. Biotechnol. 32 (2014) 760–772. doi:10.1038/nbt.2989.

[33]   H. Jiankang, L. Dichen, L. Yaxiong, Y. Bo, Z. Hanxiang, L. Qin, L. Bingheng, L. Yi, Preparation of chitosan-gelatin hybrid scaffolds with well-organized microstructures for hepatic tissue engineering., Acta Biomater. 5 (2009) 453–61. doi:10.1016/j.actbio.2008.07.002.

[34]   S.J. Hollister, Porous scaffold design for tissue engineering., Nat. Mater. 4 (2005) 518–24. doi:10.1038/nmat1421.

[35]   D.W. Hutmacher, Scaffolds in tissue engineering bone and cartilage., Biomaterials. 21 (2000) 2529–43. http://www.ncbi.nlm.nih.gov/pubmed/11071603.

[36]   D. Donato, I. Napoli, G. Catapano, Model-Based Optimization of Scaffold Geometry and Operating Conditions of Radial Flow Packed-Bed Bioreactors for Therapeutic Applications, Processes. 2 (2014) 34–57. doi:10.3390/pr2010034.

[37]   J. He, D. Li, Y. Liu, H. Gong, B. Lu, Indirect fabrication of microstructured chitosan-gelatin scaffolds using rapid prototyping, Virtual Phys. Prototyp. 3 (2008) 159–166. doi:10.1080/17452750802315033.

[38]   M. Devarapalli, B.J. Lawrence, S. V Madihally, Modeling nutrient consumptions in large flow-through bioreactors for tissue engineering., Biotechnol. Bioeng. 103 (2009) 1003–15. doi:10.1002/bit.22333.

[39]   I. Zein, D.W. Hutmacher, K.C. Tan, S.H. Teoh, Fused deposition modeling of novel scaffold architectures for tissue engineering applications, Biomaterials. 23 (2002) 1169–1185. doi:10.1016/S0142-9612(01)00232-0.

[40]   C.Y. Lin, N. Kikuchi, S.J. Hollister, A novel method for biomaterial scaffold internal architecture design to match bone elastic properties with desired porosity., J. Biomech. 37 (2004) 623–36. doi:10.1016/j.jbiomech.2003.09.029.

[41]   G. Mattei, S. Giusti, A. Ahluwalia, Design Criteria for Generating Physiologically Relevant In Vitro Models in Bioreactors, Processes. 2 (2014) 548–569. doi:10.3390/pr2030548.

[42]   C.A. Chung, C.W. Chen, C.P. Chen, C.S. Tseng, Enhancement of cell growth in tissue-engineering constructs under direct perfusion: Modeling and simulation., Biotechnol. Bioeng. 97 (2007) 1603–16. doi:10.1002/bit.21378.

[43]   E.C. Novosel, C. Kleinhans, P.J. Kluger, Vascularization is the key challenge in tissue engineering., Adv. Drug Deliv. Rev. 63 (2011) 300–11. doi:10.1016/j.addr.2011.03.004.

[44] Y. Naito, T. Shinoka, D. Duncan, N. Hibino, D. Solomon, M. Cleary, A. Rathore, C. Fein, S. Church, C. Breuer, Vascular tissue engineering: Towards the next generation vascular grafts, Adv. Drug Deliv. Rev. 63 (2011) 312–323. doi:10.1016/j.addr.2011.03.001.

[45] V. van Duinen, S.J. Trietsch, J. Joore, P. Vulto, T. Hankemeier, Microfluidic 3D cell culture: From tools to tissue models, Curr. Opin. Biotechnol. 35 (2015) 118–126. doi:10.1016/j.copbio.2015.05.002.

[46] E.L.S. Fong, D.A. Harrington, M.C. Farach-Carson, H. Yu, Heralding a new paradigm in 3D tumor modeling, Biomaterials. 108 (2016) 197–213. doi:10.1016/j.biomaterials.2016.08.052.

[47] F. Pampaloni, E.G. Reynaud, E.H.K. Stelzer, The third dimension bridges the gap between cell culture and live tissue., Nat. Rev. Mol. Cell Biol. 8 (2007) 839–845. doi:10.1038/nrm2236.

[48] R. Devolder, H.J. Kong, Hydrogels for in vivo-like three-dimensional cellular studies, Wiley Interdiscip. Rev. Syst. Biol. Med. 4 (2012) 351–365. doi:10.1002/wsbm.1174.

[49] A.W. Lund, B. Yener, J.P. Stegemann, G.E. Plopper, The natural and engineered 3D microenvironment as a regulatory cue during stem cell fate determination., Tissue Eng. Part B. Rev. 15 (2009) 371–80. doi:10.1089/ten.TEB.2009.0270.

[50] L. Gasperini, J.F. Mano, R.L. Reis, Natural polymers for the microencapsulation of cells., J. R. Soc. Interface. 11 (2014). doi:10.1098/rsif.2014.0817.

[51] E. Santos, R.M. Hernández, J.L. Pedraz, G. Orive, Novel advances in the design of three-dimensional bio-scaffolds to control cell fate: translation from 2D to 3D., Trends Biotechnol. 30 (2012) 331–41. doi:10.1016/j.tibtech.2012.03.005.

[52] J. Malda, T.J. Klein, Z. Upton, The roles of hypoxia in the in vitro engineering of tissues., Tissue Eng. 13 (2007) 2153–2162. doi:10.1089/ten.2006.0417.

[53] C.K. Griffith, S.C. George, The effect of hypoxia on in vitro prevascularization of a thick soft tissue., Tissue Eng. Part A. 15 (2009) 2423–2434. doi:10.1089/ten.tea.2008.0267.

[54] M.P. Cuchiara, D.J. Gould, M.K. McHale, M.E. Dickinson, J.L. West, Integration of self-assembled microvascular networks with microfabricated PEG-based hydrogels, Adv. Funct. Mater. 22 (2012) 4511–4518. doi:10.1002/adfm.201200976.

[55] F.P.W. Melchels, M.A.N. Domingos, T.J. Klein, J. Malda, P.J. Bartolo, D.W. Hutmacher, Additive manufacturing of tissues and organs, Prog. Polym. Sci. 37 (2012) 1079–1104. doi:10.1016/j.progpolymsci.2011.11.007.

[56] S.J. Paulsen, J.S. Miller, Tissue vascularization through 3D printing: Will technology bring us flow?, Dev. Dyn. 244 (2015) 629–640. doi:10.1002/dvdy.24254.

[57] S.J. Hollister, Scaffold design and manufacturing: from concept to clinic., Adv. Mater. 21 (2009) 3330–42. doi:10.1002/adma.200802977.

[58] C.M. Magin, D.L. Alge, K.S. Anseth, Bio-inspired 3D microenvironments: a new dimension in tissue engineering., Biomed. Mater. 11 (2016) 22001. doi:10.1088/1748-6041/11/2/022001.

[59] J.D. Ahlstrom, Chapter 8 - Molecular Organization of Cells, in: R. Lanza, R. Langer, J. Vacanti (Eds.), Princ. Tissue Eng. (Fourth Ed., Fourth Edi, Academic Press, Boston, 2014: pp. 147–160. doi:http://dx.doi.org/10.1016/B978-0-12-398358-9.00008-2.

[60]   A. Atala, F.K. Kasper, A.G. Mikos, Engineering complex tissues., Sci. Transl. Med. 4 (2012) 160rv12. doi:10.1126/scitranslmed.3004890.

[61]   M. Petreaca, M. Martins-Green, Chapter 9 - The Dynamics of Cell-ECM Interactions, with Implications for Tissue Engineering, in: R. Lanza, R. Langer, J. Vacanti (Eds.), Princ. Tissue Eng. (Fourth Ed., Fourth Edi, Academic Press, Boston, 2014: pp. 161–187. doi:http://dx.doi.org/10.1016/B978-0-12-398358-9.00009-4.

[62]   D. Anton, H. Burckel, E. Josset, G. Noel, Three-dimensional cell culture: A breakthrough in vivo, Int. J. Mol. Sci. 16 (2015) 5517–5527. doi:10.3390/ijms16035517.

[63]   M.W. Tibbitt, K.S. Anseth, Dynamic microenvironments: the fourth dimension., Sci. Transl. Med. 4 (2012) 160ps24. doi:10.1126/scitranslmed.3004804.

[64]   M.P. Lutolf, J. a Hubbell, Synthetic biomaterials as instructive extracellular microenvironments for morphogenesis in tissue engineering., Nat. Biotechnol. 23 (2005) 47–55. doi:10.1038/nbt1055.

[65]   C.V.C. Bouten, P.Y.W. Dankers, a. Driessen-Mol, S. Pedron, a. M. a. Brizard, F.P.T. Baaijens, Substrates for cardiovascular tissue engineering, Adv. Drug Deliv. Rev. 63 (2011) 221–241. doi:10.1016/j.addr.2011.01.007.

[66]   N. Wang, I.M. Tolić-Nørrelykke, J. Chen, S.M. Mijailovich, J.P. Butler, J.J. Fredberg, D. Stamenović, Cell prestress. I. Stiffness and prestress are closely associated in adherent contractile cells., Am. J. Physiol. Cell Physiol. 282 (2002) C606-16. doi:10.1152/ajpcell.00269.2001.

[67]   T. Chen, M.J. Hilton, E.B. Brown, M.J. Zuscik, H.A. Awad, Engineering superficial zone features in tissue engineered cartilage, Biotechnol. Bioeng. 110 (2013) 1476–1486. doi:10.1002/bit.24799.

[68]   J. Sanchez-Adams, K.A. Athanasiou, Dermis isolated adult stem cells for cartilage tissue engineering, Biomaterials. 33 (2012) 109–119. doi:10.1016/j.biomaterials.2011.09.038.

[69]   G. Feil, L. Daum, B. Amend, S. Maurer, M. Renninger, M. Vaegler, J. Seibold, A. Stenzl, K.-D. Sievert, From tissue engineering to regenerative medicine in urology--the potential and the pitfalls., Adv. Drug Deliv. Rev. 63 (2011) 375–8. doi:10.1016/j.addr.2010.12.003.

[70]   A. Atala, Tissue engineering of human bladder, Br. Med. Bull. 97 (2011) 81–104. doi:10.1093/bmb/ldr003.

[71]   N.F. Davis, R. Mooney, A. V Piterina, A. Callanan, B.B. McGuire, H.D. Flood, T.M. McGloughlin, Construction and Evaluation of Urinary Bladder Bioreactor for Urologic Tissue-engineering Purposes, Urology. 78 (2011) 954–960. doi:10.1016/j.urology.2011.06.036.

[72]   I. Stanasel, M. Mirzazadeh, J.J. Smith, Bladder Tissue Engineering, Urol. Clin. North Am. 37 (2010). doi:10.1016/j.ucl.2010.06.008.

[73]   L.S. Gardel, L.A. Serra, R.L. Reis, M.E. Gomes, Use of Perfusion Bioreactors and Large Animal Models for Long Bone Tissue Engineering., Tissue Eng. Part B. Rev. 0 (2013). doi:10.1089/ten.TEB.2013.0010.

[74]   A.J. Salgado, O.P. Coutinho, R.L. Reis, Bone tissue engineering: State of the art and future trends, Macromol. Biosci. 4 (2004) 743–765. doi:10.1002/mabi.200400026.

[75]   J.M. Holzwarth, P.X. Ma, Biomimetic nanofibrous scaffolds for bone tissue engineering, Biomaterials. 32 (2011) 9622–9629. doi:10.1016/j.biomaterials.2011.09.009.

[76]   T. Cordonnier, J. Sohier, P. Rosset, P. Layrolle, Biomimetic Materials for Bone Tissue Engineering - State of the Art and Future Trends, Adv. Eng. Mater. 13 (2011) B135–B150. doi:10.1002/adem.201080098.

[77]   L. Cai, Q. Wang, C. Gu, J. Wu, J. Wang, N. Kang, J. Hu, F. Xie, L. Yan, X. Liu, Y. Cao, R. Xiao, Vascular and micro-environmental influences on MSC-coral hydroxyapatite construct-based bone tissue engineering, Biomaterials. 32 (2011) 8497–8505. doi:10.1016/j.biomaterials.2011.07.087.

[78]   F. Groeber, M. Holeiter, M. Hampel, S. Hinderer, K. Schenke-Layland, Skin tissue engineering — In vivo and in vitro applications, Adv. Drug Deliv. Rev. 63 (2011) 352–366. doi:10.1016/j.addr.2011.01.005.

[79]   C. Velasquillo, Skin 3D Bioprinting. Applications in Cosmetology, J. Cosmet. Dermatological Sci. Appl. 3 (2013) 85–89. doi:10.4236/jcdsa.2013.31A012.

[80]   J. Goldstein, V. Horsley, Home sweet home: skin stem cell niches., Cell. Mol. Life Sci. 69 (2012) 2573–82. doi:10.1007/s00018-012-0943-3.

[81]   L. Ma, C.Y. Gao, Z.W. Mao, J. Zhou, J.C. Shen, X.Q. Hu, C.M. Han, Collagen/chitosan porous scaffolds with improved biostability for skin tissue engineering, Biomaterials. 24 (2003) 4833–4841. doi:10.1016/S0142-9612(03)00374-0.

[82]   J.T. Butcher, G.J. Mahler, L. a. Hockaday, Aortic valve disease and treatment: The need for naturally engineered solutions, Adv. Drug Deliv. Rev. 63 (2011) 242–268. doi:10.1016/j.addr.2011.01.008.

[83]   M. Radisic, L. Yang, J. Boublik, R.J. Cohen, R. Langer, L.E. Freed, G. Vunjak-Novakovic, Medium perfusion enables engineering of compact and contractile cardiac tissue., Am. J. Physiol. Heart Circ. Physiol. 286 (2004) H507-16. doi:10.1152/ajpheart.00171.2003.

[84]   B. Duan, L. a Hockaday, K.H. Kang, J.T. Butcher, 3D bioprinting of heterogeneous aortic valve conduits with alginate/gelatin hydrogels., J. Biomed. Mater. Res. A. 101 (2013) 1255–64. doi:10.1002/jbm.a.34420.

[85]   S. Pagliari, A. Tirella, A. Ahluwalia, S. Duim, M.-J. Goumans, T. Aoyagi, G. Forte, A multistep procedure to prepare pre-vascularized cardiac tissue constructs using adult stem sells, dynamic cell cultures, and porous scaffolds., Front. Physiol. 5 (2014) 210. doi:10.3389/fphys.2014.00210.

[86]   L. Perin, S. Da Sacco, R.E. De Filippo, Regenerative medicine of the kidney, Adv. Drug Deliv. Rev. 63 (2011) 379–387. doi:10.1016/j.addr.2010.12.001.

[87]   K.A. Homan, D.B. Kolesky, M.A. Skylar-Scott, J. Herrmann, H. Obuobi, A. Moisan, J.A. Lewis, Bioprinting of 3D Convoluted Renal Proximal Tubules on Perfusable Chips, Sci. Rep. 6 (2016) 34845. doi:10.1038/srep34845.

[88]   W.W. Minuth, L. Denk, The Interstitial Interface within the Renal Stem/Progenitor Cell Niche Exhibits an Unique Microheterogeneous Composition., Int. J. Mol. Sci. 14 (2013) 13657–69. doi:10.3390/ijms140713657.

[89]   J.C. Gerlach, K. Zeilinger, J.F. Patzer Ii, Bioartificial liver systems: why, what,

whither?, Regen. Med. 3 (2008) 575–95. doi:10.2217/17460751.3.4.575.

[90] I. Jasmund, A. Bader, Bioreactor developments for tissue engineering applications by the example of the bioartificial liver., Adv. Biochem. Eng. Biotechnol. 74 (2002) 99–109. http://www.ncbi.nlm.nih.gov/pubmed/11991185.

[91] K. Choi, W.P. Pfund, M.E. Andersen, R.S. Thomas, H.J. Clewell, E.L. Lecluyse, Development of 3D Dynamic Flow Model of Human Liver and Its Application to Prediction of Metabolic Clearance of 7-Ethoxycoumarin., Tissue Eng. Part C. Methods. 20 (2014) 1–11. doi:10.1089/ten.TEC.2013.0562.

[92] M. Baker, Tissue models: A living system on a chip, Nature. 471 (2011) 661–665. doi:10.1038/471661a.

[93] J.F. Patzer, Oxygen consumption in a hollow fiber bioartificial liver--revisited., Artif. Organs. 28 (2004) 83–98. http://www.ncbi.nlm.nih.gov/pubmed/14720293.

[94] E. Schmelzer, F. Triolo, M.E. Turner, R.L. Thompson, K. Zeilinger, L.M. Reid, B. Gridelli, J.C. Gerlach, Three-dimensional perfusion bioreactor culture supports differentiation of human fetal liver cells., Tissue Eng. Part A. 16 (2010) 2007–16. doi:10.1089/ten.TEA.2009.0569.

[95] J.W. Haycock, 3D cell culture: a review of current approaches and techniques., 2011. doi:10.1007/978-1-60761-984-0_1.

[96] A. Rodriguez, Y.L. Cao, C. Ibarra, S. Pap, M. Vacanti, R.D. Eavey, C.A. Vacanti, Characteristics of Cartilage Engineered from Human Pediatric Auricular Cartilage, Plast. Reconstr. Surg. 103 (1999) 1111–1119. doi:10.1097/00006534-199904040-00001.

[97] M.P. Van De Kerkhove, E. Di Florio, V. Scuderi, A. Mancini, A. Belli, A. Bracco, M. Dauri, G. Tisone, G. Di Nicuolo, P. Amoroso, A. Spadari, G. Lombardi, R. Hoekstra, F. Calise, R.A.F.M. Chamuleau, Phase I clinical trial with the AMC-bioartificial liver, Int. J. Artif. Organs. 25 (2002) 950–959. doi:0391-3988/950-10.

[98] E. Fuchs, T. Chen, A matter of life and death: self-renewal in stem cells., EMBO Rep. 14 (2013) 39–48. doi:10.1038/embor.2012.197.

[99] X. Huang, S. Cho, G.J. Spangrude, Hematopoietic stem cells: generation and self-renewal., Cell Death Differ. 14 (2007) 1851–9. doi:10.1038/sj.cdd.4402225.

[100] I. Klimanskaya, E.A. Kimbrel, R. Lanza, Chapter 29 - Embryonic Stem Cells BT - Principles of Tissue Engineering (Fourth Edition), in: Academic Press, Boston, 2014: pp. 565–579. doi:http://dx.doi.org/10.1016/B978-0-12-398358-9.00029-X.

[101] J. Yu, J.A. Thomson, Chapter 30 - Induced Pluripotent Stem Cells A2 - Lanza, Robert, in: R. Langer, J.B.T.-P. of T.E. (Fourth E. Vacanti (Eds.), Academic Press, Boston, 2014: pp. 581–594. doi:http://dx.doi.org/10.1016/B978-0-12-398358-9.00030-6.

[102] H. Obokata, C.A. Vacanti, Chapter 31 - Stem Cells in Tissue Engineering BT - Principles of Tissue Engineering (Fourth Edition), in: Academic Press, Boston, 2014: pp. 595–608. doi:http://dx.doi.org/10.1016/B978-0-12-398358-9.00031-8.

[103] A. Khademhosseini, J.M. Karp, S. Gerecht-Nir, L. Ferreira, N. Annabi, D. Sirabella, G. Vunjak-Novakovic, R. Langer, Chapter 32 - Embryonic Stem Cells as a Cell Source for Tissue Engineering BT - Principles of Tissue Engineering (Fourth Edition), in: Academic Press, Boston, 2014: pp. 609–638. doi:http://dx.doi.org/10.1016/B978-0-

12-398358-9.00032-X.

[104] P.G. Robey, P. Bianco, Chapter 33 - Postnatal Stem Cells in Tissue Engineering A2 - Lanza, Robert, in: R. Langer, J.B.T.-P. of T.E. (Fourth E. Vacanti (Eds.), Academic Press, Boston, 2014: pp. 639–653. doi:http://dx.doi.org/10.1016/B978-0-12-398358-9.00033-1.

[105] Correction: Derivation of Pluripotent Stem Cells from Cultured Human Primordial Germ Cells, Proc. Natl. Acad. Sci. U. S. A. 96 (1999). doi:10.2307/46964, 10.2307/46964.

[106] K. Takahashi, K. Tanabe, M. Ohnuki, M. Narita, T. Ichisaka, K. Tomoda, S. Yamanaka, Induction of Pluripotent Stem Cells from Adult Human Fibroblasts by Defined Factors, Cell. 131 (2007) 861–872. doi:10.1016/j.cell.2007.11.019.

[107] A. Pessina, L. Gribaldo, The key role of adult stem cells: therapeutic perspectives, Curr. Med. Res. Opin. 22 (2006) 2287–2300. doi:10.1185/030079906X148517.

[108] G. Lin, X. Zhang, J. Ren, Z. Pang, C. Wang, N. Xu, R. Xi, Integrin signaling is required for maintenance and proliferation of intestinal stem cells in Drosophila., Dev. Biol. 377 (2013) 177–87. doi:10.1016/j.ydbio.2013.01.032.

[109] F.D. Miller, A. Gauthier-Fisher, C.S. Cell, Home at last: neural stem cell niches defined., Cell Stem Cell. 4 (2009) 507–10. doi:10.1016/j.stem.2009.05.008.

[110] A.J. Engler, S. Sen, H.L. Sweeney, D.E. Discher, Matrix elasticity directs stem cell lineage specification., Cell. 126 (2006) 677–89. doi:10.1016/j.cell.2006.06.044.

[111] D. Mazzei, M. a Guzzardi, S. Giusti, a Ahluwalia, A low shear stress modular bioreactor for connected cell culture under high flow rates., Biotechnol. Bioeng. 106 (2010) 127–37. doi:10.1002/bit.22671.

[112] Y. Wang, T. Susando, X. Lei, C. Anene-Nzelu, H. Zhou, L.H. Liang, H. Yu, Current development of bioreactors for extracorporeal bioartificial liver (Review)., Biointerphases. 5 (2010) FA116-31. doi:10.1116/1.3521520.

[113] N. Tandon, E. Cimetta, S. Bhumiratana, A. Godier-Furnemont, R. Maidhof, G. Vunjak-Novakovic, Bioreactors for Tissue Engineering, in: Biomater. Sci., Third Edit, Elsevier, 2013: pp. 1178–1194. doi:10.1016/B978-0-08-087780-8.00112-1.

[114] I. Martin, D. Wendt, M. Heberer, The role of bioreactors in tissue engineering, Trends Biotechnol. 22 (2004) 80–86. doi:10.1016/j.tibtech.2003.12.001.

[115] Y. Martin, P. Vermette, Bioreactors for tissue mass culture: Design, characterization, and recent advances, Biomaterials. 26 (2005) 7481–7503. doi:10.1016/j.biomaterials.2005.05.057.

[116] J.J. Zhong, Recent advances in bioreactor engineering, Korean J. Chem. Eng. 27 (2010) 1035–1041. doi:10.1007/s11814-010-0277-5.

[117] N. Pallua, C. V. Suschek, Tissue engineering: From lab to clinic, 2011. doi:10.1007/978-3-642-02824-3.

[118] G. Vunjak-Novakovic, L.E. Freed, R.J. Biron, R. Langer, Effects of mixing on the composition and morphology of tissue-engineered cartilage, Aiche J. 42 (1996) 850–860. doi:10.1002/aic.690420323, 10.1002/(ISSN)1547-5905.

[119] H.-C. Chen, Y.-C. Hu, Bioreactors for tissue engineering, Biotechnol. Lett. 28 (2006) 1415–1423. doi:10.1007/s10529-006-9111-x.

[120] A.J. Strain, J.M. Neuberger, A bioartificial liver--state of the art., Science. 295 (2002) 1005–9. doi:10.1126/science.1068660.

[121] E. Figallo, C. Cannizzaro, S. Gerecht, J. a Burdick, R. Langer, N. Elvassore, G. Vunjak-Novakovic, Micro-bioreactor array for controlling cellular microenvironments., Lab Chip. 7 (2007) 710–9. doi:10.1039/b700063d.

[122] E. Cimetta, E. Figallo, C. Cannizzaro, N. Elvassore, G. Vunjak-Novakovic, Micro-bioreactor arrays for controlling cellular environments: design principles for human embryonic stem cell applications., Methods. 47 (2009) 81–9. doi:10.1016/j.ymeth.2008.10.015.

[123] F.J. O'Brien, B. a Harley, I. V Yannas, L.J. Gibson, The effect of pore size on cell adhesion in collagen-GAG scaffolds., Biomaterials. 26 (2005) 433–41. doi:10.1016/j.biomaterials.2004.02.052.

[124] T.S. Karande, J.L. Ong, C.M. Agrawal, Diffusion in musculoskeletal tissue engineering scaffolds: design issues related to porosity, permeability, architecture, and nutrient mixing., Ann. Biomed. Eng. 32 (2004) 1728–43. http://www.ncbi.nlm.nih.gov/pubmed/15675684.

[125] M.N. Collins, C. Birkinshaw, Hyaluronic acid based scaffolds for tissue engineering--a review., Carbohydr. Polym. 92 (2013) 1262–79. doi:10.1016/j.carbpol.2012.10.028.

[126] C.W. Yung, L.Q. Wu, J.A. Tullman, G.F. Payne, W.E. Bentley, T.A. Barbari, Transglutaminase crosslinked gelatin as a tissue engineering scaffold., J. Biomed. Mater. Res. A. 83 (2007) 1039–46. doi:10.1002/jbm.a.31431.

[127] D.E. Discher, D.J. Mooney, P.W. Zandstra, Growth factors, matrices, and forces combine and control stem cells., Science. 324 (2009) 1673–7. doi:10.1126/science.1171643.

[128] M.M. Nava, M.T. Raimondi, R. Pietrabissa, Controlling self-renewal and differentiation of stem cells via mechanical cues., J. Biomed. Biotechnol. 2012 (2012) 797410. doi:10.1155/2012/797410.

[129] M.L. Kutys, C.S. Chen, Forces and mechanotransduction in 3D vascular biology, Curr. Opin. Cell Biol. 42 (2016) 73–79. doi:10.1016/j.ceb.2016.04.011.

[130] P.C. Georges, P. a Janmey, Cell type-specific response to growth on soft materials., J. Appl. Physiol. 98 (2005) 1547–53. doi:10.1152/japplphysiol.01121.2004.

[131] M.A. Schwartz, Integrins and extracellular matrix in mechanotransduction., Cold Spring Harb. Perspect. Biol. 2 (2010) a005066. doi:10.1101/cshperspect.a005066.

[132] F. Spill, D.S. Reynolds, R.D. Kamm, M.H. Zaman, Impact of the physical microenvironment on tumor progression and metastasis, Curr. Opin. Biotechnol. 40 (2016) 41–48. doi:10.1016/j.copbio.2016.02.007.

[133] E. Hadjipanayi, V. Mudera, R. a Brown, Guiding cell migration in 3D: a collagen matrix with graded directional stiffness., Cell Motil. Cytoskeleton. 66 (2009) 121–8. doi:10.1002/cm.20331.

[134] C.-C. Lin, K.S. Anseth, Cell–cell communication mimicry with poly(ethylene glycol) hydrogels for enhancing β-cell function, Proc Natl Acad Sci. 108 (2011) 6380–6385.

[135] S. Eshghi, D. V Schaffer, C. Engineering, Engineering microenvironments to control stem cell fate and function, StemBook. (2008) 1–12. doi:10.3824/stembook.1.5.1.

[136] D.E. Discher, P. Janmey, Y.-L. Wang, Tissue cells feel and respond to the stiffness of their substrate., Science. 310 (2005) 1139–43. doi:10.1126/science.1116995.

[137] M.E. Dolega, M. Delarue, F. Ingremeau, J. Prost, A. Delon, G. Cappello, Cell-like pressure sensors reveal increase of mechanical stress towards the core of multicellular spheroids under compression, Nat. Commun. 8 (2017) 14056. doi:10.1038/ncomms14056.

[138] D.S.W. Benoit, M.P. Schwartz, A.R. Durney, K.S. Anseth, Small functional groups for controlled differentiation of hydrogel-encapsulated human mesenchymal stem cells, Nat. Mater. 7 (2008) 816–823. doi:10.1038/nmat2269.

[139] E. Carletti, A. Motta, C. Migliaresi, Scaffolds for tissue engineering and 3D cell culture, Methods Mol. Biol. 695 (2011) 17–39. doi:10.1007/978-1-60761-984-0_2.

[140] J.L. Drury, D.J. Mooney, Hydrogels for tissue engineering: scaffold design variables and applications, Biomaterials. 24 (2003) 4337–4351. doi:10.1016/S0142-9612(03)00340-5.

[141] M.M. Stevens, J.H. George, Exploring and engineering the cell surface interface., Science. 310 (2005) 1135–1138. doi:10.1126/science.1106587.

[142] Y. Luo, G. Engelmayr, D.T. Auguste, L. da Silva Ferreira, J.M. Karp, R. Saigal, R. Langer, Chapter 24 - 3D Scaffolds, in: Academic Press, Boston, 2014: pp. 475–494. doi:http://dx.doi.org/10.1016/B978-0-12-398358-9.00024-0.

[143] Z. Zhang, O. Ortiz, R. Goyal, J. Kohn, Chapter 23 - Biodegradable Polymers, in: R. Langer, J.B.T.-P. of T.E. (Fourth E. Vacanti (Eds.), Academic Press, Boston, 2014: pp. 441–473. doi:http://dx.doi.org/10.1016/B978-0-12-398358-9.00023-9.

[144] B.J. Klotz, D. Gawlitta, A.J.W.P. Rosenberg, J. Malda, F.P.W. Melchels, Gelatin-Methacryloyl Hydrogels: Towards Biofabrication-Based Tissue Repair, Trends Biotechnol. 34 (2016) 394–407. doi:10.1016/j.tibtech.2016.01.002.

[145] S. Gorgieva, V. Kokol, Collagen- vs. Gelatine-Based Biomaterials and Their Biocompatibility: Review and Perspectives, in: Biomater. Appl. Nanomedicine, InTech, 2011. doi:10.5772/24118.

[146] J.M. Pachence, Collagen-based devices for soft tissue repair, J. Biomed. Mater. Res. 33 (1996) 35–40. doi:10.1002/(SICI)1097-4636(199621)33:1<35::AID-JBM6>3.0.CO;2-N.

[147] M. van der Rest, B. Dublet, M.F. Champliaud, Fibril-associated collagens., Biomaterials. 11 (1990) 28–31. http://www.ncbi.nlm.nih.gov/pubmed/2204435.

[148] S. Ber, G.T. Kose, V. Hasirci, Bone tissue engineering on patterned collagen films: an in vitro study, Biomaterials. 26 (2005) 1977–1986. doi:10.1016/j.biomaterials.2004.07.007.

[149] D.A.D. Parry, The molecular fibrillar structure of collagen and its relationship to the mechanical properties of connective tissue, Biophys. Chem. 29 (1988) 195–209. doi:10.1016/0301-4622(88)87039-X.

[150] M. van der Rest, R. Garrone, Collagen family of proteins., FASEB J. Off. Publ. Fed. Am. Soc. Exp. Biol. 5 (1991) 2814–23. http://www.ncbi.nlm.nih.gov/pubmed/10171194.

[151] K. Anselme, C. Bacques, G. Charriere, D.J. Hartmann, D. Herbage, R. Garrone, Tissue reaction to subcutaneous implantation of a collagen sponge. A histological,

ultrastructural, and immunological study, J. Biomed. Mater. Res. 24 (1990) 689–703. doi:10.1002/jbm.820240605, 10.1002/(ISSN)1097-4636.

[152] K.S. Weadock, E.J. Miller, E.L. Keuffel, M.G. Dunn, Effect of physical crosslinking methods on collagen-fiber durability in proteolytic solutions, J. Biomed. Mater. Res. 32 (1996) 221–226. doi:10.1002/(SICI)1097-4636(199610)32:2<221::AID-JBM11>3.0.CO;2-M.

[153] N.F. Huang, S. Li, Regulation of the matrix microenvironment for stem cell engineering and regenerative medicine., Ann. Biomed. Eng. 39 (2011) 1201–14. doi:10.1007/s10439-011-0297-2.

[154] B.C. Toolan, S.R. Frenkel, J.M. Pachence, L. Yalowitz, H. Alexander, Effects of growth-factor-enhanced culture on a chondrocyte-collagen implant for cartilage repair, J. Biomed. Mater. Res. 31 (1996) 273–280. doi:10.1002/(SICI)1097-4636(199606)31:2<273::AID-JBM15>3.0.CO;2-M.

[155] C.H. Lee, A. Singla, Y. Lee, Biomedical applications of collagen, Int. J. Pharm. 221 (2001) 1–22. doi:10.1016/S0378-5173(01)00691-3.

[156] S. Nehrer, H.A. Breinan, A. Ramappa, H.-P. Hsu, T. Minas, S. Shortkroff, C.B. Sledge, I. V Yannas, M. Spector, Chondrocyte-seeded collagen matrices implanted in a chondral defect in a canine model, Biomaterials. 19 (1998) 2313–2328. doi:http://dx.doi.org/10.1016/S0142-9612(98)00143-4.

[157] A.J. Kuijpers, G.H.M. Engbers, J. Feijen, S.C. De Smedt, T.K.L. Meyvis, J. Demeester, J. Krijgsveld, S.A.J. Zaat, J. Dankert, Characterization of the network structure of carbodiimide cross-linked gelatin gels, Macromolecules. 32 (1999) 3325–3333. doi:10.1021/ma981929v.

[158] S. Young, M. Wong, Y. Tabata, A.G. Mikos, Gelatin as a delivery vehicle for the controlled release of bioactive molecules., J. Control. Release. 109 (2005) 256–74. doi:10.1016/j.jconrel.2005.09.023.

[159] P.E. Van den Steen, B. Dubois, I. Nelissen, P.M. Rudd, R.A. Dwek, G. Opdenakker, Biochemistry and molecular biology of gelatinase B or matrix metalloproteinase-9 (MMP-9), Crit. Rev. Biochem. Mol. Biol. 37 (2002) 375–536. doi:10.1080/10409230290771546.

[160] J.W. Nichol, S.T. Koshy, H. Bae, C.M. Hwang, S. Yamanlar, A. Khademhosseini, Cell-laden microengineered gelatin methacrylate hydrogels, Biomaterials. 31 (2010) 5536–5544. doi:10.1016/j.biomaterials.2010.03.064.

[161] J. Heino, M. Huhtala, J. Kapyla, M.S. Johnson, Evolution of collagen-based adhesion systems, Int. J. Biochem. Cell Biol. 41 (2009) 341–348. doi:10.1016/j.biocel.2008.08.021.

[162] A. Talebian, S. Kordestani, A. Rashidi, The Effect of Glutaraldehyde on the Properties of Gelatin Films, Kem. U Ind. Časopis Kemičara I Kem. Inženjera Hrvat. 56 (2007) 537–541.

[163] P. Davis, B.E. Tabor, Kinetic study of the crosslinking of gelatin by formaldehyde and glyoxal, J. Polym. Sci. Part A Gen. Pap. 1 (1963) 799–815. doi:10.1002/pol.1963.100010217.

[164] H.C. Liang, W.H. Chang, H.F. Liang, M.H. Lee, H.W. Sung, Crosslinking structures of gelatin hydrogels crosslinked with genipin or a water-soluble carbodiimide, J. Appl. Polym. Sci. 91 (2004) 4017–4026. doi:10.1002/app.13563.

[165] A. Ito, A. Mase, Y. Takizawa, M. Shinkai, H. Honda, K.-I. Hata, M. Ueda, T. Kobayashi, Transglutaminase-mediated gelatin matrices incorporating cell adhesion factors as a biomaterial for tissue engineering, J. Biosci. Bioeng. 95 (2003) 196–199. doi:10.1016/S1389-1723(03)80129-9.

[166] N. Reddy, R. Reddy, Q. Jiang, Crosslinking biopolymers for biomedical applications, Trends Biotechnol. 33 (2015) 362–369. doi:10.1016/j.tibtech.2015.03.008.

[167] H.-W. Sung, D.-M. Huang, W.-H. Chang, R.-N. Huang, J.-C. Hsu, Evaluation of gelatin hydrogel crosslinked with various crosslinking agents as bioadhesives:In vitro study, J. Biomed. Mater. Res. 46 (1999) 520–530. doi:10.1002/(SICI)1097-4636(19990915)46:4<520::AID-JBM10>3.0.CO;2-9.

[168] M. Mariani, F. Rosatini, G. Vozzi, A. Previti, A. Ahluwalia, Characterization of Tissue-Engineered Scaffolds Microfabricated with PAM, Tissue Eng. 12 (2006) 547–558. doi:10.1089/ten.2006.12.547.

[169] B.D. Ratner, A.S. Hoffman, F.J. Schoen, J.E. Lemons, Biomaterials science: an introduction to materials in medicine, Academic press, 2004.

[170] M. Ajioka, K. Enomoto, S. K., The basic properties of poly lactic acid produced by the direct condensation polymerisation of lactic acid, J. Environ. Polym. Degrad. 3 (1995) 225–234. doi:10.1007/BF02068677.

[171] R.A. Casper, R.L. Dunn, D.R. Cowsar, Biodegradable Fracture Fixation Plates for Use in Maxillofacial Surgery, in: Corros. Degrad. Implant Mater. Second Symp., 1985: pp. 340–348. doi:10.1520/STP33262S, 10.1520/STP33262S.

[172] J.W. Leenslag, A.J. Pennings, R.R.M. Bos, F.R. Rozema, G. Boering, Resorbable materials of poly(l-lactide). VI. Plates and screws for internal fracture fixation, Biomaterials. 8 (1987) 70–73. doi:http://dx.doi.org/10.1016/0142-9612(87)90034-2.

[173] D.W. Grijpma, A.J. Nijenhuis, P.G.T. van Wijk, A.J. Pennings, High impact strength as-polymerized PLLA, Polym. Bull. 29 (1992) 571–578. doi:10.1007/BF00296720.

[174] L. Fambri, A. Pegoretti, R. Fenner, S.D. Incardona, C. Migliaresi, Biodegradable fibres of poly(L-lactic acid) produced by melt spinning, Polymer (Guildf). 38 (1997) 79–85. doi:10.1016/S0032-3861(96)00486-7.

[175] H. Tsuji, Y. Ikada, Stereocomplex formation between enantiomeric poly(lactic acid)s. XI. Mechanical properties and morphology of solution-cast films, Polymer (Guildf). 40 (1999) 6699–6708. doi:http://dx.doi.org/10.1016/S0032-3861(99)00004-X.

[176] C.C. Chu, Degradation phenomena of two linear aliphatic polyester fibres used in medicine and surgery, Polymer (Guildf). 26 (1985) 591–594. doi:10.1016/0032-3861(85)90160-0.

[177] L.E. Freed, G. Vunjak-Novakovic, R.J. Biron, D.B. Eagles, D.C. Lesnoy, S.K. Barlow, R. Langer, Biodegradable Polymer Scaffolds for Tissue Engineering, Bio/Technology. 12 (1994) 689–693. doi:10.1038/nbt0794-689.

[178] E. Eisenbarth, Biomaterials for Tissue Engineering, Adv. Eng. Mater. 9 (2007) 1051–1060. doi:10.1002/adem.200700287.

[179] M.I. Baker, S.P. Walsh, Z. Schwartz, B.D. Boyan, A review of polyvinyl alcohol and its uses in cartilage and orthopedic applications, J. Biomed. Mater. Res. - Part B Appl. Biomater. 100 B (2012) 1451–1457. doi:10.1002/jbm.b.32694.

[180] C.A. Finch, Polyvinyl alcohol; properties and applications, John Wiley & Sons, 1973.

[181] K. Leja, G. Lewandowicz, Polymer biodegradation and biodegradable polymers - A review, Polish J. Environ. Stud. 19 (2010) 255–266.

[182] B.L. Lopez, A.I. Mejia, L. Sierra, Biodegradability of Poly(Vinyl Alcohol), Polym. Eng. Sci. 39 (1999).

[183] T.S. Gaaz, A.B. Sulong, M.N. Akhtar, A.A.H. Kadhum, A.B. Mohamad, A.A. Al-Amiery, D.J. McPhee, Properties and applications of polyvinyl alcohol, halloysite nanotubes and their nanocomposites, Molecules. 20 (2015) 22833–22847. doi:10.3390/molecules201219884.

[184] L. Nie, D. Chen, J. Suo, P. Zou, S. Feng, Q. Yang, S. Yang, S. Ye, Physicochemical characterization and biocompatibility in vitro of biphasic calcium phosphate/polyvinyl alcohol scaffolds prepared by freeze-drying method for bone tissue engineering applications, Colloids Surfaces B Biointerfaces. 100 (2012) 169–176. doi:10.1016/j.colsurfb.2012.04.046.

[185] M.H. Alves, B.E.B. Jensen, A.A.A. Smith, A.N. Zelikin, Poly(vinyl alcohol) physical hydrogels: New vista on a long serving biomaterial, Macromol. Biosci. 11 (2011) 1293–1313. doi:10.1002/mabi.201100145.

[186] M. Kita, Y. Ogura, Y. Honda, Suong-Hyu Hyon, Evaluation of polyvinyl alcohol hydrogel as a soft contact lens material, Graefe´s Arch Clin Exp Ophtalmol. 228 (1990) 533–537. doi:10.1007/BF00918486.

[187] T.H. Young, N.K. Yao, R.F. Chang, L.W. Chen, Evaluation of asymmetric poly(vinyl alcohol) membranes for use in artificial islets, Biomaterials. 17 (1996) 2139–2145. doi:10.1016/0142-9612(96)00043-9.

[188] K. Burczak, E. Gamian, A. Kochman, Long-term in vivo performance and biocompatibility of poly(vinyl alcohol) hydrogel macrocapsules for hybrid-type artificial pancreas, Biomaterials. 17 (1996) 2351–2356. doi:10.1016/S0142-9612(96)00076-2.

[189] W. Paul, C.P. Sharma, Acetylsalicylic acid loaded poly(vinyl alcohol) hemodialysis membranes: effect of drug release on blood compatibility and permeability, J. Biomater. Sci. Polym. Ed. 8 (1997) 755–764. doi:10.1163/156856297X00290.

[190] S. Maruoka, T. Matsuura, K. Kawasaki, M. Okamoto, H. Yoshiaki, M. Kodama, M. Sugiyama, M. Annaka, Biocompatibility of polyvinylalcohol gel as a vitreous substitute, Curr. Eye Res. 31 (2006) 599–606. doi:10.1080/02713680600813854.

[191] M. Oka, Biomechanics and repair of articular cartilage, J. Orthop. Sci. 6 (2001).

[192] J.A. Stammen, S. Williams, D.N. Ku, R.E. Guldberg, Mechanical properties of a novel PVA hydrogel in shear and unconfined compression, Biomaterials. 22 (2001) 799–806. doi:10.1016/S0142-9612(00)00242-8.

[193] W. Swieszkowski, D.N. Ku, H.E.N. Bersee, K.J. Kurzydlowski, An elastic material for cartilage replacement in an arthritic shoulder joint, Biomaterials. 27 (2006) 1534–1541. doi:10.1016/j.biomaterials.2005.08.032.

[194] M. Kobayashi, Y.S. Chang, M. Oka, A two year in vivo study of polyvinyl alcohol-hydrogel (PVA-H) artificial meniscus, Biomaterials. 26 (2005) 3243–3248. doi:10.1016/j.biomaterials.2004.08.028.

[195] M. Kobayashi, J. Toguchida, M. Oka, Preliminary study of polyvinyl alcohol-hydrogel (PVA-H) artificial meniscus, Biomaterials. 24 (2003) 639–647. doi:10.1016/S0142-

9612(02)00378-2.

[196] P. Bajaj, R.M. Schweller, A. Khademhosseini, J.L. West, R. Bashir, 3D Biofabrication Strategies for Tissue Engineering and Regenerative Medicine., Annu. Rev. Biomed. Eng. 16 (2014) 247–76. doi:10.1146/annurev-bioeng-071813-105155.

[197] F.J. O'Brien, B.A. Harley, I. V Yannas, L. Gibson, Influence of freezing rate on pore structure in freeze-dried collagen-GAG scaffolds, Biomaterials. 25 (2004) 1077–1086. doi:10.1016/S0142-9612(03)00630-6.

[198] M.G. Haugh, C.M. Murphy, F.J. O'Brien, Novel Freeze-Drying Methods to Produce a Range of Collagen-Glycosaminoglycan Scaffolds with Tailored Mean Pore Sizes, Tissue Eng. Part C-Methods. 16 (2010) 887–894. doi:10.1089/ten.tec.2009.0422.

[199] A. Szentivanyi, T. Chakradeo, H. Zernetsch, B. Glasmacher, Electrospun cellular microenvironments: Understanding controlled release and scaffold structure, Adv. Drug Deliv. Rev. 63 (2011) 209–220. doi:10.1016/j.addr.2010.12.002.

[200] H. Yoshimoto, Y.M. Shin, H. Terai, J.P. Vacanti, A biodegradable nanofiber scaffold by electrospinning and its potential for bone tissue engineering, Biomaterials. 24 (2003) 2077–2082. doi:10.1016/S0142-9612(02)00635-X.

[201] D. Sin, X. Miao, G. Liu, F. Wei, G. Chadwick, C. Yan, T. Friis, Polyurethane (PU) scaffolds prepared by solvent casting/particulate leaching (SCPL) combined with centrifugation, Mater. Sci. Eng. C-Materials Biol. Appl. 30 (2010) 78–85. doi:10.1016/j.msec.2009.09.002.

[202] S. Mohanty, K. Kuldeep, A. Heiskanen, J. Trifol Guzman, P. Szabo, M. Dufva, J. Emnéus, A. Wolff, Fabrication of scalable tissue engineering scaffolds with dual-pore microarchitecture by combining 3D printing and particle leaching, Mater. Sci. Eng. C Mater. Biol. Appl. 61 (2016) 180–189. doi:10.1016/j.msec.2015.12.032.

[203] F. Intranuovo, R. Gristina, F. Brun, S. Mohammadi, G. Ceccone, E. Sardella, F. Rossi, G. Tromba, P. Favia, Plasma Modification of PCL Porous Scaffolds Fabricated by Solvent-Casting/Particulate-Leaching for Tissue Engineering, Plasma Process. Polym. 11 (2014) 184–195. doi:10.1002/ppap.201300149.

[204] W. Gao, Y. Zhang, D. Ramanujan, K. Ramani, Y. Chen, C.B. Williams, C.C.L. Wang, Y.C. Shin, S. Zhang, P.D. Zavattieri, The status, challenges, and future of additive manufacturing in engineering, Comput. Des. 69 (2015) 65–89. doi:10.1016/j.cad.2015.04.001.

[205] M. Tarik Arafat, I. Gibson, X. Li, State of the art and future direction of additive manufactured scaffolds-based bone tissue engineering, Rapid Prototyp. J. 20 (2014) 13–26. doi:10.1108/RPJ-03-2012-0023.

[206] S.H. Masood, Advances in Fused Deposition Modeling, Elsevier, 2014. doi:10.1016/B978-0-08-096532-1.01002-5.

[207] J. Kundu, J. Shim, J. Jang, S. Kim, D. Cho, An additive manufacturing-based PCL-alginate-chondrocyte bioprinted scaffold for cartilage tissue engineering., J. Tissue Eng. Regen. Med. (2013). doi:10.1002/term.1682.

[208] S. Mohanty, L.B. Larsen, J. Trifol, P. Szabo, H.V.R. Burri, C. Canali, M. Dufva, J. Emnéus, A. Wolff, Fabrication of scalable and structured tissue engineering scaffolds using water dissolvable sacrificial 3D printed moulds, Mater. Sci. Eng. C. 55 (2015) 569–578. doi:10.1016/j.msec.2015.06.002.

[209] A. Skardal, A. Atala, Biomaterials for Integration with 3-D Bioprinting, Ann. Biomed. Eng. 43 (2015) 730–746. doi:10.1007/s10439-014-1207-1.

[210] B. Guillotin, A. Souquet, S. Catros, M. Duocastella, B. Pippenger, S. Bellance, R. Bareille, M. Rémy, L. Bordenave, J. Amédée, F. Guillemot, Laser assisted bioprinting of engineered tissue with high cell density and microscale organization, Biomaterials. 31 (2010) 7250–7256. doi:10.1016/j.biomaterials.2010.05.055.

[211] R. Gauvin, Y.C. Chen, J.W. Lee, P. Soman, P. Zorlutuna, J.W. Nichol, H. Bae, S. Chen, A. Khademhosseini, Microfabrication of complex porous tissue engineering scaffolds using 3D projection stereolithography, Biomaterials. 33 (2012) 3824–3834. doi:10.1016/j.biomaterials.2012.01.048.

[212] H. Lin, D. Zhang, P.G. Alexander, G. Yang, J. Tan, A.W.M. Cheng, R.S. Tuan, Application of visible light-based projection stereolithography for live cell-scaffold fabrication with designed architecture, Biomaterials. 34 (2013) 331–339. doi:10.1016/j.biomaterials.2012.09.048.

[213] M.W. Tibbitt, K.S. Anseth, Hydrogels as extracellular matrix mimics for 3D cell culture., Biotechnol. Bioeng. 103 (2009) 655–63. doi:10.1002/bit.22361.

[214] A. Mogilner, D. Odde, Modeling cellular processes in 3D, Trends Cell Biol. 21 (2011) 692–700. doi:10.1016/j.tcb.2011.09.007.

[215] K. Tanner, M.M. Gottesman, Beyond 3D culture models of cancer, Sci. Transl. Med. 7 (2015) 7–10. doi:10.1126/scitranslmed.3009367.

[216] C. Wang, X. Tong, F. Yang, Bioengineered 3D brain tumor model to elucidate the effects of matrix stiffness on glioblastoma cell behavior using PEG-based hydrogels., Mol. Pharm. 11 (2014) 2115–25. doi:10.1021/mp5000828.

[217] W.J. Polacheck, A.E. German, A. Mammoto, D.E. Ingber, R.D. Kamm, Mechanotransduction of fluid stresses governs 3D cell migration., Proc. Natl. Acad. Sci. U. S. A. 111 (2014) 2447–52. doi:10.1073/pnas.1316848111.

[218] W.J. Polacheck, J.L. Charest, R.D. Kamm, B. Shu Chien, Interstitial flow influences direction of tumor cell migration through competing mechanisms, Proc. Natl. Acad. Sci. 108 (2011) 11115–11120. doi:10.1073/pnas.1103581108.

[219] U. Haessler, J.C.M. Teo, D. Foretay, P. Renaud, M. a. Swartz, Migration dynamics of breast cancer cells in a tunable 3D interstitial flow chamber, Integr. Biol. 4 (2012) 401. doi:10.1039/c1ib00128k.

[220] K.R. Leventhal, H. Yu, L. Kass, J.N. Lakins, M. Egeblad, J.T. Erler, S.F.T. Fong, K. Csiszar, A. Giaccia, W. Weninger, M. Yamauchi, D.L. Gasser, V.M. Weaver, Matrix Crosslinking Forces Tumor Progression by Enhancing Integrin Signaling, Cell. 139 (2009) 891–906. doi:10.1016/j.cell.2009.10.027.

[221] N.R. Lang, K. Skodzek, S. Hurst, A. Mainka, J. Steinwachs, J. Schneider, K.E. Aifantis, B. Fabry, Biphasic response of cell invasion to matrix stiffness in three-dimensional biopolymer networks, Acta Biomater. 13 (2015) 61–67. doi:10.1016/j.actbio.2014.11.003.

[222] D. Huh, G. a. Hamilton, D.E. Ingber, From 3D cell culture to organs-on-chips, Trends Cell Biol. 21 (2011) 745–754. doi:10.1016/j.tcb.2011.09.005.

[223] B. Derby, Printing and prototyping of tissues and scaffolds., Science. 338 (2012) 921–6. doi:10.1126/science.1226340.

[224] T. Billiet, M. Vandenhaute, J. Schelfhout, S. Van Vlierberghe, P. Dubruel, A review of trends and limitations in hydrogel-rapid prototyping for tissue engineering, Biomaterials. 33 (2012) 6020–6041. doi:10.1016/j.biomaterials.2012.04.050.

[225] C. Mandrycky, Z. Wang, K. Kim, D.H. Kim, 3D bioprinting for engineering complex tissues, Biotechnol. Adv. 34 (2016) 422–434. doi:10.1016/j.biotechadv.2015.12.011.

[226] M. Kesti, C. Eberhardt, G. Pagliccia, D. Kenkel, D. Grande, A. Boss, M. Zenobi-Wong, Bioprinting Complex Cartilaginous Structures with Clinically Compliant Biomaterials, Adv. Funct. Mater. (2015) 7406–7417. doi:10.1002/adfm.201503423.

[227] E.T. Pashuck, M. Stevens, From clinical imaging to implantation of 3D printed tissues, Nat. Biotechnol. 34 (2016) 295–296. doi:10.1038/nbt.3503.

[228] T. Kaully, K. Kaufman-Francis, A. Lesman, S. Levenberg, Vascularization: the conduit to viable engineered tissues., Tissue Eng. Part B. Rev. 15 (2009) 159–169. doi:10.1089/ten.teb.2008.0193.

[229] Y. Zheng, J. Chen, M. Craven, N.W. Choi, S. Totorica, A. Diaz-Santana, P. Kermani, B. Hempstead, C. Fischbach-Teschl, J.A. López, A.D. Stroock, In vitro microvessels for the study of angiogenesis and thrombosis., Proc. Natl. Acad. Sci. U. S. A. 109 (2012) 9342–7. doi:10.1073/pnas.1201240109.

[230] M.P. Cuchiara, A.C.B. Allen, T.M. Chen, J.S. Miller, J.L. West, Multilayer microfluidic PEGDA hydrogels, Biomaterials. 31 (2010) 5491–5497. doi:10.1016/j.biomaterials.2010.03.031.

[231] L.L.Y. Chiu, M. Montgomery, Y. Liang, H. Liu, M. Radisic, Perfusable branching microvessel bed for vascularization of engineered tissues., Proc. Natl. Acad. Sci. U. S. A. 109 (2012) E3414-23. doi:10.1073/pnas.1210580109.

[232] M.P. Lee, G.J.T. Cooper, T. Hinkley, G.M. Gibson, M.J. Padgett, L. Cronin, Development of a 3D printer using scanning projection stereolithography., Sci. Rep. 5 (2015) 9875. doi:10.1038/srep09875.

[233] B. Dhariwala, E. Hunt, T. Boland, Rapid prototyping of tissue-engineering constructs, using photopolymerizable hydrogels and stereolithography, Tissue Eng. 10 (2004) 1316–1322. doi:10.1089/ten.2004.10.1316.

[234] Y. Lu, G. Mapili, G. Suhali, S.C. Chen, K. Roy, A digital micro-mirror device-based system for the microfabrication of complex, spatially patterned tissue engineering scaffolds, J. Biomed. Mater. Res. Part a. 77A (2006) 396–405. doi:10.1002/jbm.a.30601.

[235] V.K. Popov, E.N. Antonov, V.N. Bagratashvili, A. V Evseev, V.Y. Panchenko, J.J.A. Barry, S.M. Howdle, Laser rapid prototyping for tissue engineering and regeneration, Proc. Spie--the Int. Soc. Opt. Eng. 6606 (2007). doi:10.1117/12.729514.

[236] D. Yuan, A. Lasagni, P. Shao, S. Das, Rapid prototyping of microstructured hydrogels via laser direct-write and laser interference photopolymerisation, Virtual Phys. Prototyp. 3 (2008) 221–229. doi:10.1080/17452750802615713.

[237] R. Schade, T. Weiss, A. Berg, M. Schnabelrauch, K. Liefeith, Two-photon techniques in tissue engineering, Int. J. Artif. Organs. 33 (2010) 219–227.

[238] A. Ovsianikov, M. Gruene, M. Pflaum, L. Koch, F. Maiorana, M. Wilhelmi, A. Haverich, B. Chichkov, Laser printing of cells into 3D scaffolds, Biofabrication. 2 (2010). doi:10.1088/1758-5082/2/1/014104.

[239] D. Therriault, S.R. White, J. a Lewis, Chaotic mixing in three-dimensional microvascular networks fabricated by direct-write assembly., Nat. Mater. 2 (2003) 265–71. doi:10.1038/nmat863.

[240] J.S. Miller, K.R. Stevens, M.T. Yang, B.M. Baker, D.-H.T. Nguyen, D.M. Cohen, E. Toro, A. a Chen, P. a Galie, X. Yu, R. Chaturvedi, S.N. Bhatia, C.S. Chen, Rapid casting of patterned vascular networks for perfusable engineered three-dimensional tissues., Nat. Mater. 11 (2012) 768–74. doi:10.1038/nmat3357.

[241] L.E. Bertassoni, M. Cecconi, V. Manoharan, M. Nikkhah, J. Hjortnaes, A.L. Cristino, G. Barabaschi, D. Demarchi, M.R. Dokmeci, Y. Yang, A. Khademhosseini, Hydrogel bioprinted microchannel networks for vascularization of tissue engineering constructs, Lab Chip. 14 (2014) 2202–2211. doi:10.1039/C4LC00030G.

[242] A. Tocchio, M. Tamplenizza, F. Martello, I. Gerges, E. Rossi, S. Argentiere, S. Rodighiero, W. Zhao, P. Milani, C. Lenardi, Versatile fabrication of vascularizable scaffolds for large tissue engineering in bioreactor, Biomaterials. 45 (2015) 124–131. doi:10.1016/j.biomaterials.2014.12.031.

[243] X.-Y. Wang, Z.-H. Jin, B.-W. Gan, S.-W. Lv, M. Xie, W.-H. Huang, Engineering interconnected 3D vascular networks in hydrogels using molded sodium alginate lattice as the sacrificial template., Lab Chip. (2014). doi:10.1039/c4lc00069b.

[244] A.W. Justin, R.A. Brooks, A.E. Markaki, Multi-casting approach for vascular networks in cellularized hydrogels, J. R. Soc. Interface. 13 (2016) 20160768. doi:10.1098/rsif.2016.0768.

[245] S. Li, Y.-Y. Liu, L.-J. Liu, Q.-X. Hu, A Versatile Method for Fabricating Tissue Engineering Scaffolds with a Three-Dimensional Channel for Prevasculature Networks., ACS Appl. Mater. Interfaces. 8 (2016) 25096–103. doi:10.1021/acsami.6b07725.

[246] H.N. Chan, Q. Tian, Y. Shu, H. Wu, Replicating 3D printed structures into hydrogels, Mater. Horizons. 3 (2015) 132–134. doi:10.1039/C6MH00058D.

[247] T.Y. Kang, J.M. Hong, J.W. Jung, H.W. Kang, D.W. Cho, Construction of large-volume tissue mimics with 3D functional vascular networks, PLoS One. 11 (2016) 1–16. doi:10.1371/journal.pone.0156529.

[248] I.T. Ozbolat, Bioprinting scale-up tissue and organ constructs for transplantation, Trends Biotechnol. 33 (2015) 395–400. doi:10.1016/j.tibtech.2015.04.005.

[249] D. Richards, J. Jia, M. Yost, R. Markwald, Y. Mei, 3D Bioprinting for Vascularized Tissue Fabrication, Ann. Biomed. Eng. 45 (2016) 1–16. doi:10.1007/s10439-016-1653-z.

[250] Q. Gao, Y. He, J. zhong Fu, A. Liu, L. Ma, Coaxial nozzle-assisted 3D bioprinting with built-in microchannels for nutrients delivery, Biomaterials. 61 (2015) 203–215. doi:10.1016/j.biomaterials.2015.05.031.

[251] C. Colosi, S.R. Shin, V. Manoharan, S. Massa, M. Costantini, A. Barbetta, M.R. Dokmeci, M. Dentini, A. Khademhosseini, Microfluidic Bioprinting of Heterogeneous 3D Tissue Constructs Using Low-Viscosity Bioink, Adv. Mater. 28 (2016) 677–684a. doi:10.1002/adma.201503310.

[252] W. Jia, P.S. Gungor-Ozkerim, Y.S. Zhang, K. Yue, K. Zhu, W. Liu, Q. Pi, B. Byambaa, M.R. Dokmeci, S.R. Shin, A. Khademhosseini, Direct 3D bioprinting of perfusable vascular constructs using a blend bioink, Biomaterials. 106 (2016) 58–68.

doi:10.1016/j.biomaterials.2016.07.038.

[253] W. Zhu, X. Qu, J. Zhu, X. Ma, S. Patel, J. Liu, P. Wang, C.S.E. Lai, M. Gou, Y. Xu, K. Zhang, S. Chen, Direct 3D bioprinting of prevascularized tissue constructs with complex microarchitecture, Biomaterials. 124 (2017) 106–115. doi:10.1016/j.biomaterials.2017.01.042.

[254] T.J. Hinton, Q. Jallerat, R.N. Palchesko, J.H. Park, M.S. Grodzicki, H. Shue, M.H. Ramadan, A.R. Hudson, A.W. Feinberg, Three-dimensional printing of complex biological structures by freeform reversible embedding of suspended hydrogels, Sci. Adv. 1 (2015) 1–10. doi:10.1126/sciadv.1500758.

[255] D.B. Kolesky, R.L. Truby, a S. Gladman, T. a Busbee, K. a Homan, J. a Lewis, 3D Bioprinting of Vascularized, Heterogeneous Cell-Laden Tissue Constructs., Adv. Mater. (2014) 1–7. doi:10.1002/adma.201305506.

[256] D.B. Kolesky, K.A. Homan, M.A. Skylar-Scott, J.A. Lewis, Three-dimensional bioprinting of thick vascularized tissues., Proc. Natl. Acad. Sci. U. S. A. 113 (2016) 3179–84. doi:10.1073/pnas.1521342113.

[257] H.-W. Kang, S.J. Lee, I.K. Ko, C. Kengla, J.J. Yoo, A. Atala, A 3D bioprinting system to produce human-scale tissue constructs with structural integrity, Nat. Biotechnol. 34 (2016) 312–319. doi:10.1038/nbt.3413.

[258] V.K. Lee, D.Y. Kim, H. Ngo, Y. Lee, L. Seo, S.S. Yoo, P.A. Vincent, G. Dai, Creating perfused functional vascular channels using 3D bio-printing technology, Biomaterials. 35 (2014) 8092–8102. doi:10.1016/j.biomaterials.2014.05.083.

[259] V.K. Lee, A.M. Lanzi, H. Ngo, S.S. Yoo, P.A. Vincent, G. Dai, Generation of multi-scale vascular network system within 3D hydrogel using 3D bio-printing technology, Cell. Mol. Bioeng. 7 (2014) 460–472. doi:10.1007/s12195-014-0340-0.

[260] E. Lippens, I. Swennen, J. Girones, H. Declercq, G. Vertenten, L. Vlaminck, F. Gasthuys, E. Schacht, R. Cornelissen, Cell survival and proliferation after encapsulation in a chemically modified Pluronic((R)) F127 hydrogel, J. Biomater. Appl. 27 (2013) 828–839. doi:10.1177/0885328211427774.

CHAPTER 2

DIFFERENTIATION OF HUMAN INDUCED PLURIPOTENT STEM CELL UNDER FLOW CONDITIONS TO MATURE HEPATOCYTES FOR LIVER TISSUE ENGINEERING

Differentiation of Human Induced Pluripotent Stem Cell under Flow Conditions to Mature Hepatocytes for Liver Tissue Engineering

Viktoriia Starokozhko[2*], Mette Hemmingsen[1*], Layla Larsen[1], Soumyaranjan Mohanty[1], Marjolijn Merema[2], Rodrigo Pimentel C.[1], Anders Wolff[1], Jenny Emnéus[1], Anders Aspegren[3], Geny Groothuis[2#], and Martin Dufva[1#]

[1] *Department of Micro- and Nanotechnology, Technical University of Denmark, Denmark*

[2] *Department of Pharmacy, University of Groningen, The Netherlands*

[3] *Cellartis, Takara Bio Europe AB, Sweden*

[*] *Shared first author*

[#] *Shared last author*

Corresponding author:

Martin Dufva

Associate Professor

Technical University of Denmark

Mobile +45 51333753

martin.dufva@nanotech.dtu.dk

Abstract

Hepatic differentiation of hiPSCs under flow conditions in a 3D scaffold is expected to be a major step forward for construction of bioartificial livers. The aims of this study were to induce hepatic differentiation of hiPSCs under perfusion conditions and to perform functional comparisons with fresh human precision cut liver slices (hPCLS), an excellent benchmark for the human liver *in vivo*. The majority of the mRNA expression of CYP isoenzymes and transporters and the tested CYP activities, phase II metabolism, and albumin, urea and bile acid synthesis in the hiPSC derived cells reached values that overlap those of hPCLS, which indicates a higher degree of hepatic differentiation than observed until now. Flow based compared to static differentiation had a strong positive effect on phase II metabolism, suppressed AFP expression but resulted in slightly lower activity of some of the phase I metabolism enzymes. Gene expression data indicates that hiPSCs differentiated into both hepatic and biliary directions. In conclusion, the hiPSC differentiated under flow conditions towards hepatocytes express a wide spectrum of liver functions at levels comparable to hPCLS indicating excellent future perspectives for the development of a bioartificial liver system for toxicity testing or as liver support device for patients.

Keywords: hepatic differentiation, bioartificial liver, stem cells

Introduction

Even though fully matured primary human hepatocytes (PHH) exhibit all the specific liver functions, their limited availability and loss of liver specific functions during culturing *in vitro* are still the major limitations for their application in a bioartificial liver (BAL) [1, 2]. Therefore, porcine primary hepatocytes and carcinoma cell lines (HepG2, HepG2/C3A and HepaRG) have been widely employed in liver engineering [3-5]. The drawbacks of these cells are however the risk of zoonotic diseases, immunological responses, tumor formation or poor liver specific functions compared to PHH [3, 4].

Stem cells, especially human induced pluripotent stem cells (hiPSCs), have therefore received great attention during the past years for liver tissue engineering [1, 3]. hiPSCs represent a potentially unlimited cell source for a large-scale production of hepatocytes required for BAL development. Furthermore, the use of the patients' own hiPSCs may allow for personalized treatment and thereby avoiding immunological reactions. Although hiPSC-derived hepatocyte-like cells have been shown to have certain liver-specific phenotypic characteristics and exhibit many of the liver specific functions [6-9], most of these functions are expressed at levels several magnitudes lower than in fresh liver tissue or freshly isolated human hepatocytes [10] suggesting that improvements in the differentiation protocols are still warranted.

In most of these studies the induced pluripotent stem cell derived hepatocyte-like cells were obtained by maturation in 2D cultures, and the cells are loaded in a bioreactor only after maturation. Hepatic differentiation and maturation directly in the 3D bioreactor may offer great advantages such as overcoming the need to harvest the total amount of cells needed for the BAL from the 2D culture and loading in a 3D bioreactor. However, relatively few studies have investigated the hepatic differentiation of stem cells directly in a 3D perfusion bioreactor or BAL using embryonic stem cells [11-16], and only two of them used hiPSCs [17, 18]. Flow of the medium was shown to have beneficial effects on hepatic differentiation of ESC and fetal liver cells and to improve liver functions of ESC-derived hepatocytes [13, 15, 19, 20]. Even simple recirculation of medium in a rotating bioreactor improved the function of the differentiated hepatocyte-like cells [14, 16]. The flow may not only physically influence the cells by creating flow forces, but it also may improve mass as well as gas transfer between the cells and the medium, and promote the removal of waste products [15, 20]. However, in another study perfu-

sion inhibited adipogenic differentiation of adipose derived stem cells possibly by washing away auto- or paracrine factors [21].

A limitation of many studies is the absence of a proper benchmark to evaluate whether the cells are fully differentiated with respect to the expression levels of liver specific markers and liver functions of the generated hepatocytes. For example, many studies have not used a benchmark at all while others have used PHH cultured *in vitro* for 2 days or more [6, 22, 23]. However, it is known that PHH cultured beyond 24-48 hours rapidly lose their phenotype and liver-specific functions, and using these cells as a benchmark results therefore in an overestimation of the maturation level of the stem cell derived hepatocytes [10]. By contrast, fresh human precision-cut liver slices (hPCLS) contain hepatocytes in their natural 3D tissue-matrix configuration, in contact to the other liver cell types, and retain expression as well as activity of phase I and phase II metabolic enzymes at levels comparable to the *in vivo* situation [24, 25]. Therefore, hPCLS can be considered the gold standard for assessing the maturation of stem-cell derived hepatocytes into fully differentiated hepatocytes.

Here, we differentiate hiPSC-derived definitive endoderm (DE) cells into hepatocytes *in situ* in a perfusion bioreactor system. Hepatic differentiation and functionality of hiPSC-derived hepatocytes were assessed using fresh hPCLS as benchmark for *ex vivo* liver, and 2D static cultures were used to compare differentiation efficacy in 2D static and 3D flow systems.

Results

Differentiation of definitive endoderm cells into hepatocyte-like cells under 3D flow condition.

Differentiation of hiPSC-derived DE cells into hepatocytes was performed in perfused 3D bioreactors with highly porous 3D PDMS scaffolds and for comparison in conventional 2D cultures in polystyrene (PS) wells or PDMS coated wells. Frozen DE cells were seeded at a density of 2.5 x 10^6 cells per scaffold and differentiated into hepatocytes as illustrated in Figure 1A. Differentiation under flow on 2D surface showed very good morphology of differentiated cells (Figure 1B), provided that the amount of differentiation factors was reduced by 50%, since 100% differentiation factor concentration results in poor cell adhesion during flow (Supplementary Figure S2 left panels). Cells differentiated on PS and PDMS respectively under static conditions showed similar morphology (Figure 1C, Supplementary Figure S3). It

was not possible to obtain bright field images of the cells in the 3D scaffold due to the poor optical characteristics of the scaffold.

The cells adhered typically in clusters in the scaffolds (Figure 1F) at a relatively low overall final cell density (200.000-300.000 cells/scaffold) as determined by visual inspection (Supplementary Figure S4) and measurement of protein content (Supplementary Figure S5) in the scaffold. As DE cells and differentiated hepatocytes adhere well to PDMS (Supplementary Figure S4), the relatively low number of adhering cells to the scaffold is likely due to difficulties to seed the cells in the scaffolds although seeding was performed by rotating the scaffolds in six different directions with 30 min incubation in each direction. Calculations indicate that a scaffold has a surface area of approximately 10 cm^2 (Supplementary Figure S6) and thus the cells in the 3D scaffold had an effective cell density of 20.000-30.000 cells/cm^2, which is lower than the corresponding 2D static cultures (usually 80.000-100.000 stem cell derived hepatocytes/cm^2, data not shown). However, as determined by visual inspection, the cells adhered typically in clusters, and therefore, the local cell densities were probably higher.

Differentiation of hiPSC-derived DE cells loaded in the scaffolds was performed at a flow rate of 1 μl/min (exchange rate every 50 minutes) and 5 μL/min (exchange rate every 10 minutes). It was calculated that in both flow regimens, shear forces were very low (1.1e-4 dyn/cm^2, or less, Supplementary Figure S7 and S8). Furthermore, the exchange rate of once per 10 minutes was shown to be compatible with differentiation into hepatocytes in 2D flow cultures (Supplementary Figure S2) and has previously shown to support differentiation of adipose derived stem cells into adipocytes using conditioned medium [21].
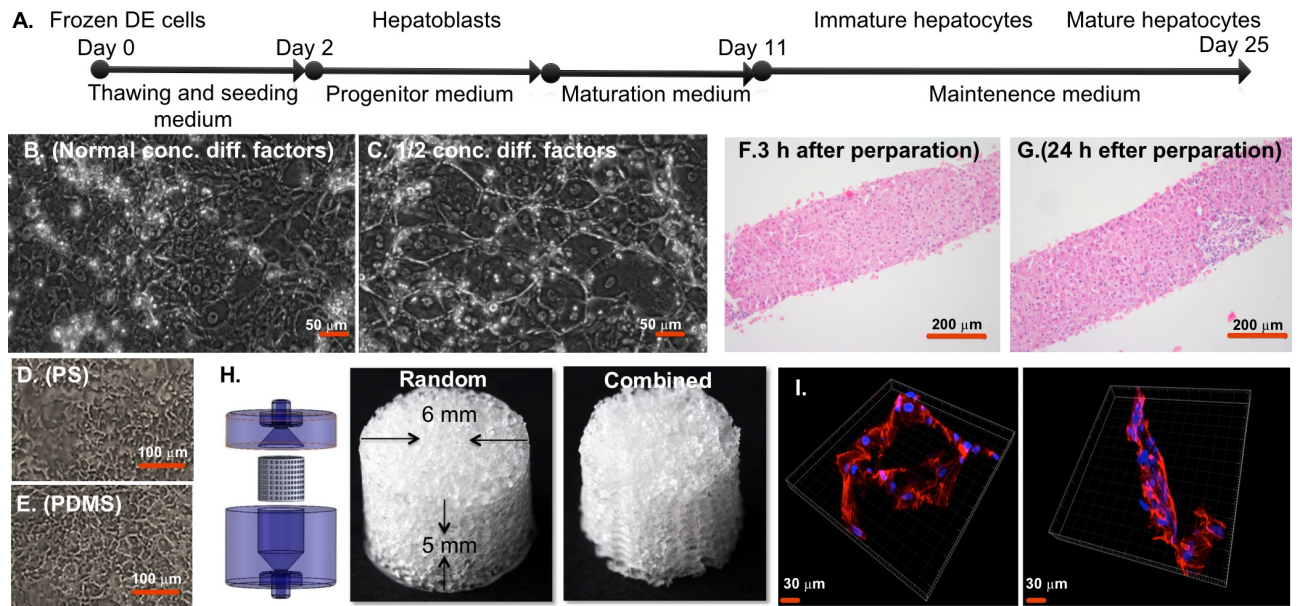
Figure 1. A: Schematic overview of the experimental process of differentiation of DE cells to mature hepatocytes. B: Differentiation of iPSC under flow regime (500 nL/min) on flat surface for 25 day using normal concentration of differentiation factors or ½ concentration of differentiation factors. C: Differentiation of iPSC for 19 days on polystyrene and on PDMS. D: hPCLS at 0h and 24h of incubation (Haematoxylin & eosin staining). E: Scaffolds and house (left panel) used for perfusion. F: Confocal microscopy images of iPSCS derived hepatocyte like cells. Blue is nucleus (DAPI) and red is actin staining.

Comparison of gene expression of hepatocyte markers of human iPSC-derived hepatocytes and hPCLS

We investigated the hepatic differentiation of hiPSC-derived DE cells in the 3D scaffold at two different flow rates, 1 µL/min and 5 µL/min, and in two different scaffold designs (Figure 1E), and compared the results with cells differentiated under static 2D conditions in standard polystyrene (PS) well plates or in well plates coated with a PDMS layer. hPCLS were used as a benchmark for cells differentiated in the scaffold under perfusion. hPCLS were prepared from 10 individual livers of human donors, aged 20-73 year (60% female) as described [26]. Due to the limited amount of liver material, not every test was performed on all donor livers. The morphological appearance and ATP content of the hPCLS after a preincubation of 1 hour to restore ATP levels (0h) and after 24h of incubation, indicated that the slices were viable. ATP levels were 9.7±1.3 pmol/µg protein and 8.24±0.76 pmol/µg protein at 0h and 24h respectively (mean±SEM). Morphology showed intact liver tissue at 0h and after 24 h of incubation (Figure 1D).

The gene expression of the liver-specific genes of the cells differentiated under the conditions outlined above and the hPCLS is depicted in Figure 2. A summary based on classification of gene expression into broader groups is presented in Figure 3. When comparing the differentiated cells in static cultures on PS with hPCLS, most of the CYP genes, the expression of the epithelial biliary cell markers (CK7, BGP) and the drug transporter ABCB1 (multidrug resistance protein, P-gp) in the cells was in the range of that seen in hPCLS. Large differences in gene expression were observed for the genes CAR, ALB and BSEP, which were clearly under expressed in differentiated cells compared to hPCLS. These three genes were, however, higher expressed in differentiated cells than in the DE cells (Figure 2 and 3). Furthermore, the differentiated cells showed higher expression of AFP and HNF4a than the hPCLS. The differentiated cells on PS therefore had a mixed phenotype, where some genes suggest a partly to fully maturated phenotype (HNF4a, CYP3A4, 3A5, 3A7 and 2B6 and P-gp), while others suggest a less mature phenotype (ALB, AFP, CAR, BSEP). In addition, maturation of a part of the cells into biliary epithelial cells is suggested by expression of CK7 and BGP.
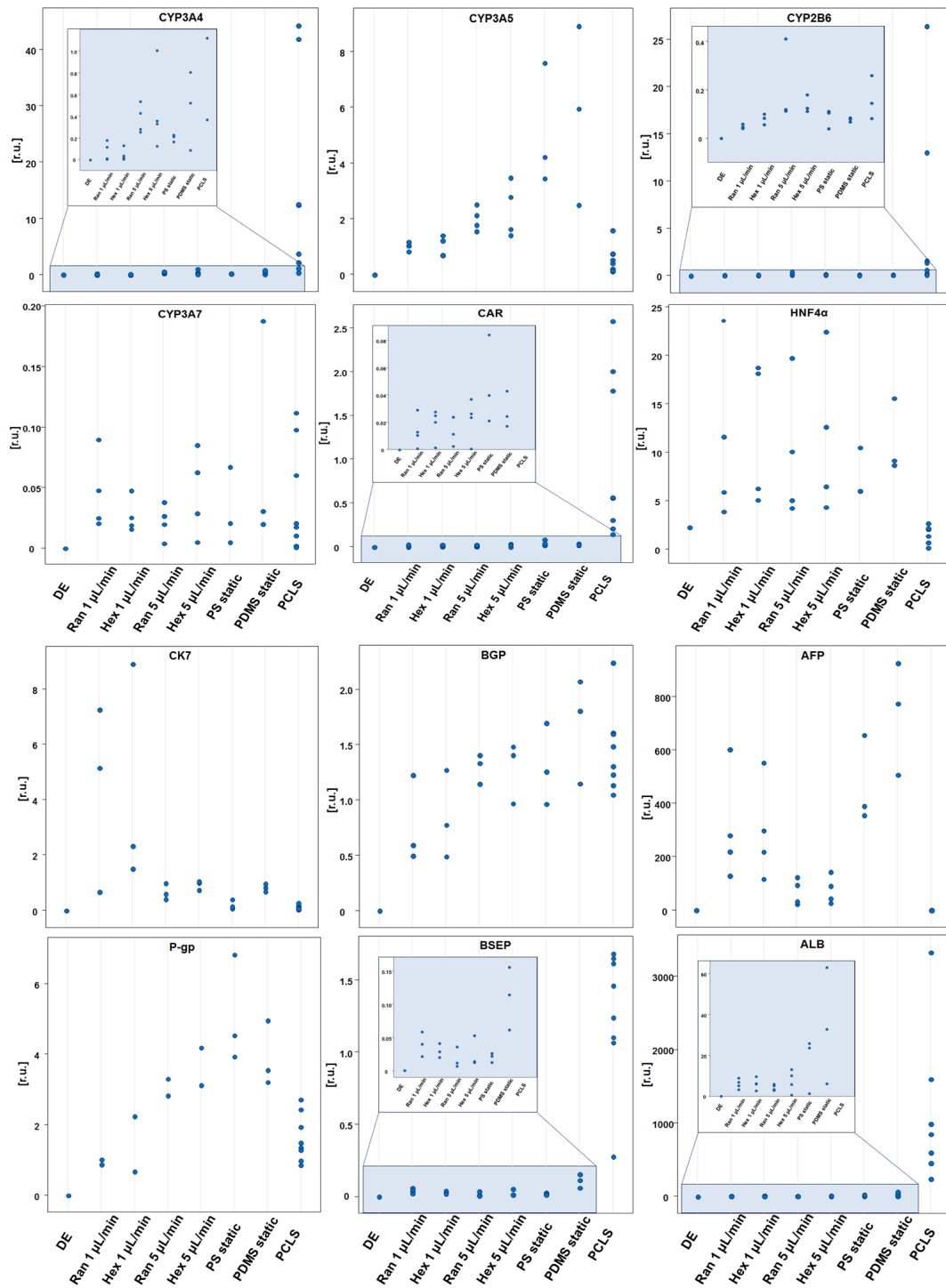
Figure 2. Expression of different hepatic genes by DE cells cultured and differentiated under different conditions. Data are given for each individual sample to appreciate the variation within each condition and the overlap between the different conditions. Data are presented as Ct values of the respective genes normalized to Ct values of the housekeeping gene CREBBP. Results are from four independent differentiation experiments and seven donors. Due to poor RNA yield, some genes where only analyzed in two (P-gp) or three (CK7, BSEP, BGP) of the cultures.

Differentiation on the scaffold material PDMS in static cultures had only a minor impact on the gene expression compared to cells on PS; all genes showed overlapping expression in cells on PDMS and PS respectively (Figure 2 and 3).

Flow modulated the gene expression of differentiated cells only to a small extent, with 5 µl/min performing slightly better than 1 µl/min for CYP 3A4 and 2B6. Flow also modulated the ALB and AFP expression; the ALB expression was suppressed by flow compared to the corresponding static cultures. The AFP expression was lowest in cells exposed to the 5 µl/min perfusion compared to static and perfusion with 1 µl/min, but did not result in the very low levels observed in hPCLS (Figure 2 and 3).

	1µL/min		5µL/min		Static		Fresh
	Ran	Hex	Ran	Hex	PS	PDMS	hPCLS
CYP3A4							
CYP3A5							
CYP2B6							
CYP3A7							
CAR							
HNF4α							
AFP							
ALB							
CK7							
BGP							
P-gp							
BSEP							

Figure 3. Summary of the comparison of the gene expression levels between the differentiated cells and the hPSLC as benchmark from Fig 3. The different grades of color in the chart represent the gene expression levels in the hiPSC-derived hepatocytes relative to the gene expression levels in hPCLS as follows: Black: all individual data of the cells are higher than those in hPCLS. Dark grey: the individual data of the cells are higher than or in the higher range of those of hPCLS. Middle grey: all data of the cells are in the same range as those of hPCLS. Light grey: the individual data of the cells are lower than or in the lower range of those of hPCLS. White: all individual data of the cells are lower than those of the hPCLS.

Liver functions

Phase I and Phase II metabolic activity, albumin, urea and total bile acid (TBA) production was analyzed in hPCLS and the hiPSC-derived hepatocytes for each of the different conditions described above.

Phase I metabolism

Differentiated hiPSC-derived DE cells as well as hPCLS were exposed to the substrates under both static and flow conditions to account for possible effects of flow on metabolism. The metabolic activities in the hPCLS showed large inter-donor variations as expected, as inter-individual differences in drug metabolism are well described.

Overall the hPCLS showed similar metabolic activity when cultured under flow or in static conditions, although a lower metabolic activity was found for CYP3A and CYP2B6 activity under flow (Figure 4). These differences may be explained by binding of the lipophilic substrates midazolam and bupropion to the PDMS of the biochip [27], although it cannot be excluded that the perfusion conditions may have influenced the metabolic activity.

The hiPSC-derived hepatocytes differentiated under flow conditions as well as under static conditions showed overlapping activities of CYP3A, CYP1A, CYP2C9, CYP2D6 and CYP2C19 with the hPCLS (Figure 4). However, at a flow of 1 μl/min somewhat lower activities of CYP2C9 and CYP2C19 were found compared to a flow of 5 μl/min. CYP2B6 showed very low activities in cells compared to hPCLS irrespective of perfusion or static culture conditions. The overlap in activities of most of the CYP isoforms, with exception of CYP2B6, in the differentiated cells with those of hPCLS under flow, indicate a high degree of hepatocyte drug metabolic function in the differentiated cells.
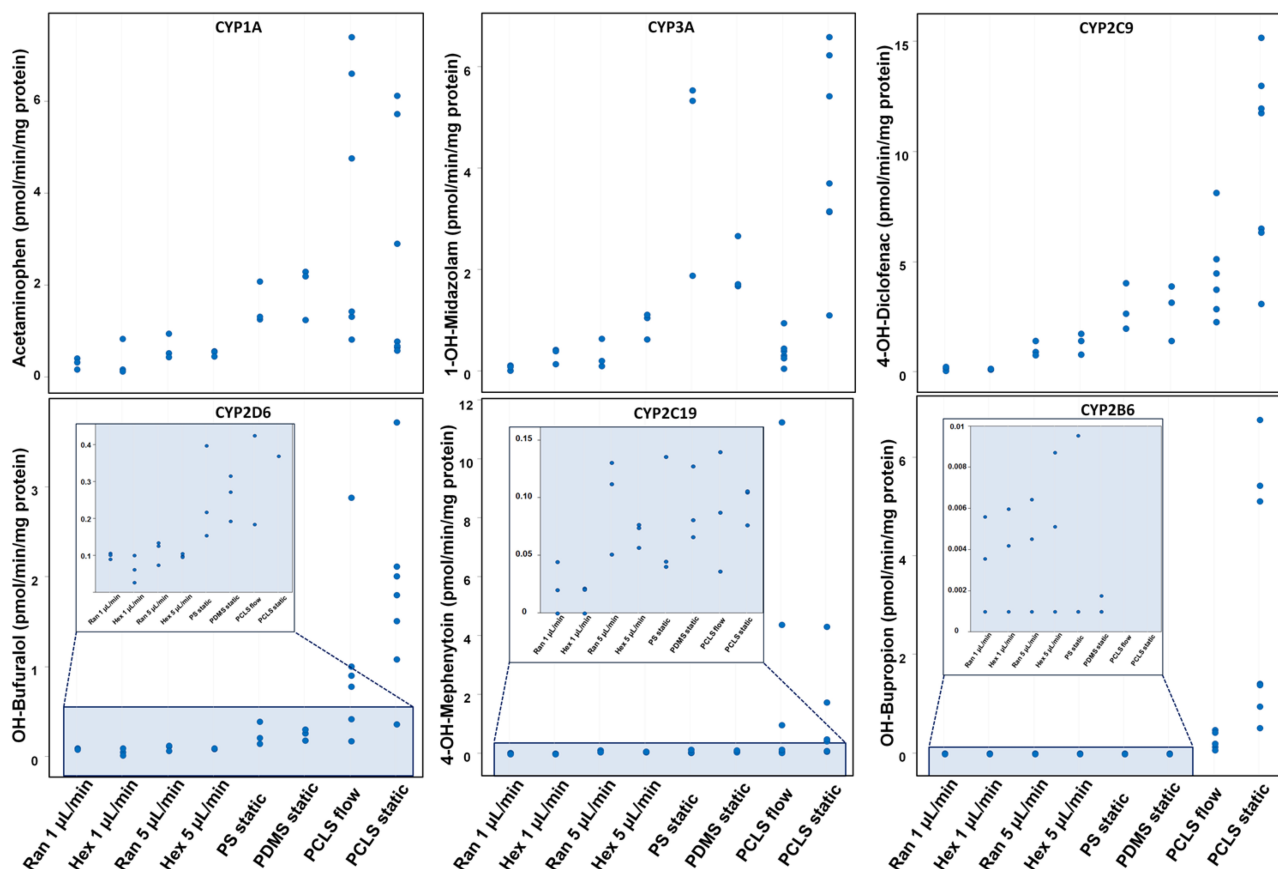
Figure 4. Phase I metabolite production of midazolam, phenacetin, diclofenac, bufuralol, bupropion and me-phenytoin by hiPSC-derived hepatocytes and hPCLS cultured in static or under flow conditions. The individual values are expressed as pmol/min/mg protein. Results are from three independent differentiation experiments and seven donors.

Phase II metabolism.

Differentiated cells exhibited high uridine UDP-glucuronyltransferase (UGT) and sulfotrans-ferase (SULT) activities when exposed to 7-hydroxycoumarin (7-HC) (Figure 5). Both phase II activities were higher in hiPSC-derived hepatocytes at a flow of 5 μl/min than at 1 μl/min. While the activities in cells cultured under static conditions were similar to those in hPCLS static cultures, the 7-HC-glucuronide (HC-G) production by cells cultured at 5μl/min flow in both hexagonal and random scaffolds was on average two-fold higher than in liver slices at flow conditions. In addition, the sulfation rate of 7-HC resulting in 7-hydroxycoumarin sulfate (HC-S) was 30-40 fold higher in cells differentiated under flow condition compared to differ-entiation under static condition and the hPCLS.
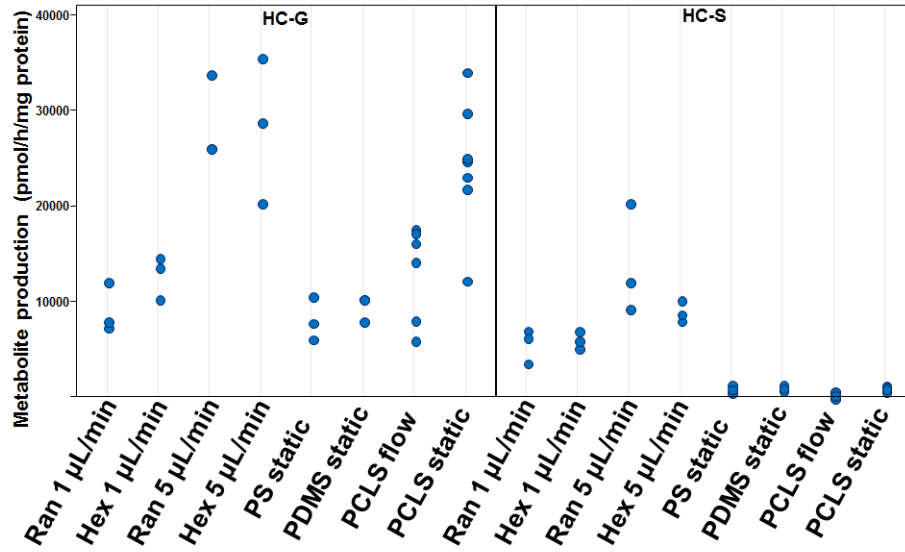
Figure 5. Production of 7-hydroxycoumarin glucuronide (HC-G) (left panel) and 7-hydrocycoumarine sulfate (HC-S) (right panel) from 7-hydroxycoumarin by hiPSC-derived hepatocytes and hPCLS cultured in static or under flow conditions. The individual values are expressed as pmol/h/mg protein. Results are from three independent differentiation experiments and seven donors).

Albumin production

Albumin production by the hiPSC-derived hepatocytes was in the lower range of that of hPCLS (Figure 6). No difference was observed between the two types of scaffolds at both flow rates or between static and perfusion cultures.
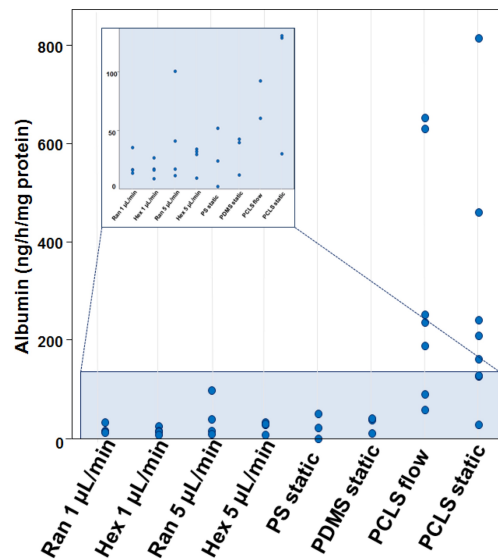
Figure 6. Albumin production by hiPSC-derived hepatocytes and hPCLS cultured in static or under flow conditions. The individual data values are expressed as ng/h/mg protein. Results are from three independent of differentiation experiments and seven donors.

Bile acid secretion and urea synthesis.

Bile acid secretion by the hiPSC-derived hepatocytes was at the same level of 25-30 pmol/h/mg protein in cells differentiated under static conditions for 22 days or 24 days as in hPCLS (Supplementary Figure S9). We could not detect bile acids in the samples of the outflow medium obtained of the scaffolds, due to the high dilution of the excreted compounds, which is a consequence of the perfusion flow rate. The observed total bile acid secretion of 25-30 pmol/h/mg protein by differentiated cells or hPCLS would result in a concentration of about 20-100 pmol/ml at a flow rate of 1 and 5µl/min respectively, which is below the detection limit.

On average, the urea production by hiPSC-derived hepatocytes was below or in the lower range of that of hPCLS (0.06-7.6 µg/h/mg protein for hiPSC-derived hepatocytes and 1.6-11.9 µg/h/mg protein for hPCLS) (Supplementary Figure S10). Cells differentiated at 5µl/min flow and under static conditions tended to show higher urea synthesis (0.3-7.6 µg/h/mg protein) than those differentiated under 1µl/min flow (0.06-0.55 µg/h/mg protein).

Discussion

We have obtained highly differentiated hepatocytes from hiPSCs. To assess their differentiation status, we compared the expression and function of the cells in this BAL model with fresh human liver slices that have *in vivo* like activities [25-27] and found as yet unprecedented liver functions in the differentiated cells. Moreover, we found that DE cells can be successfully differentiated into hepatocyte-like cells in a 3D scaffold in a bioreactor under flow conditions, to a similar or only slightly better differentiation grade than under static 2D conditions, especially with respect to phase II sulfation activity and a lower AFP expression, which can make the production of a BAL easier and more effective in the future.

hiPSC derived cells differentiated under flow in a 3D bioreactor resulted in a BAL model with overlapping phase I metabolism (except for CYP2B6) and similar or higher phase II metabolism, compared to fresh human liver slices. Urea production was present in the hiPSC but was below or in the lower range of the hPCLS. However, the capacity of urea production in

the BAL from ammonia from extrahepatic sources was not assessed since no ammonia was added to the medium and, further studies with exposure to extracellular ammonia are needed to show the ability of the cells to detoxify ammonia, which is important for patients with liver diseases where high concentrations of neurotoxic ammonia are detected. Bile acid production by hiPSC-derived hepatocytes was on the same level as in fresh tissue slices. The gene expression of P-gp in hiPSC-derived hepatocytes was shown to be higher than in hPCLS, which is remarkable as a 10-20 fold lower expression in differentiated hiPSC compared to human hepatocytes was found by *Lu et al.* [19]. However, the gene expression of BSEP in the differentiated cells was lower than in the hPCLS. Similar to hPCLS, the hiPSC derived cells expressed both CK-7 and BGP indicating that the hiPSC derived cells are a mixture of both hepatocytes and biliary epithelial cells (BEC). This bipotent differentiation potential of iPSC-derived hepatic progenitor cells was also found previously [28]. The albumin secretion of stem cell-derived hepatocytes achieved here is similar to hiPSC-derived hepatocytes [8] or 10-100 fold higher than in human ESC-derived hepatocytes [12] and 3-40 fold higher than mouse iPSC-derived hepatocytes [22], but lower than in fresh tissue slices. Although the mRNA expression was high for HNF4a indicating hepatic differentiation and low for CYP3A7, which is a fetal enzyme with low expression in the adult liver, the relatively high expression of the fetal protein AFP indicates that maturation of the cells is not fully complete. This has also been observed by others [7, 8, 22, 29], and it needs to be addressed how relevant this is for the functioning of the BAL in patients who need liver support or for toxicity testing. Taken together, these results show overall that hiPSC differentiated under static conditions as well as under flow in a scaffold have liver functions close to those in fresh human liver tissue. The significant improvements with respect to liver functions of the differentiated cells presented here compared to other studies could be due to better differentiation protocols, resulting in a favorable balance of paracrine or autocrine factors affecting differentiation, whereas the difference between the cells differentiated under 2D static and 3D perfusion conditions could be ascribed to better nutrient delivery and waste removal.

Most studies have used PHH cultured *in vitro* for 1-3 days as benchmark for hepatic activity [8, 10, 19, 23]. Because PHH functions decrease rapidly and drastically (10-1000 fold after 48h culture) during *in vitro* culture [10], using these PHH as standard tends to overestimate the metabolic function of hiPSC-derived hepatocytes. Therefore, the comparison of those data with our study is difficult. Moreover, comparison of the metabolic activity data between different stud-

ies is further hampered by the fact that the substrate concentrations and experimental conditions used are largely different. Fresh human PCLS, on the other hand, show similar metabolic activity as the fresh PHH and give a good representation of liver functions *in vivo* [44]. Even though nowadays it is possible to culture PHH for several days with preservation of their metabolic capacities in certain culture conditions, none of the above mentioned studies have described or showed that the appropriate measures have been taken to maintain PHH functions. The only published study which used fresh hepatocytes as a control is the study of *Ulvestad et al.* [10]. Comparison of the results of that study with our data shows that the CYP3A, CYP2C9 and CYP1A activities of hiPSC-derived hepatocytes in our study were ten to several hundred folds higher than those of the iPSC-derived hepatocytes in the study of *Ulvestad et al*. We were the first to measure phase II metabolism in hiPSC and found that glucuronidation was comparable to PCLS but sulfation was remarkably higher after differentiation under flow, which requires further studies.

The gene expression of CYP-enzymes and their activity varied notably between donor livers, which is very well known in the human population, which is among others a result of polymorphisms and induction by environmental and physiological factors. For example, CYP1A2, CYP2D6, CYP2C9, CYP2C19, CYP2B6 and CYP3A4 are known to be important polymorphic and highly inducible enzymes in human [30]. With this in mind it is noteworthy that the gene expression and enzyme activities in hiPSC derived cells overlapped in most cases with a few discrepancies noted below. For example, the CYP3A5 gene was higher expressed in hiPSC-derived hepatocytes compared to hPCLS, whereas CYP3A4 gene expression only reached up to the lower range of human livers (Figure 2). However, as CYP3A4 and 3A5 have strongly overlapping specificities [31], it may explain why the total CYP3A metabolism of midazolam was similar in hiPSC-derived hepatocytes and hPCLS (Figure 4). Although, the gene expression of CYP2B6 in the differentiated cells was in the lower range of hPCLS possibly due to low CAR expression, the activity of this enzyme was at least 10 times lower in hiPSC-derived hepatocytes than in hPCLS indicating a post transcriptional regulation. Future research will be focused to improve also the as yet under expressed CAR mediated pathway.

We found a limited influence of the flow rate on the hepatic differentiation of hiPSC in the BAL, as 5μL/min flow resulted in a somewhat better hepatocyte differentiation and maturation than the 1μL/min flow. This might be explained by the better nutrient and oxygen supply

and removal of waste metabolites at the higher flow rate. Also the type of scaffold had no obvious impact on the differentiation.

In conclusion, most of the drug metabolism enzyme activities of the developed hiPSC-based BAL were in the same order of magnitude as in the fresh human tissue, which is an important achievement in liver tissue engineering and for future applications in drug metabolism and toxicity testing. A limitation of the present study is that besides hepatocytes and biliary epithelial cells, which were present in the developed BAL according to gene expression profiling, no non-parenchymal cells are present yet. Although no toxicity studies have been done yet, for future toxicity tests it is necessary to also add these other liver cell types to better represent the liver functions by the BAL. Moreover, future experiments with more donor individuals for both iPSC and PCLS will help to better estimate the variation in the population as well as the robustness of the differentiation protocol. Finally, future studies should show the BAL's detoxification capacities for human serum.

Materials and Methods

Differentiation of hiPSC-DE cells into hepatocytes under static conditions and flow conditions.

Human iPS-derived definitive endoderm (DE) cells (Cellartis Definitive Endoderm ChiPSC18, Cat. No. Y10040, derived from human dermal fibroblasts, authenticated using STR and mycoplasma free according to qPCR (see further information about this cell line on http://www.clontech.com) were cultured and differentiated into hepatocytes for 25 days according to the suppliers' recommendations in the Cellartis Hepatocyte Differentiation Kit (Cat. No. Y30050), see Figure 1A. Briefly, the cell culture surface (cell culture plates or scaffold) was coated with Hepatocyte Coating (from Cellartis Hepatocyte Differentiation Kit, Cat. No. Y30050) at 37°C for 1-2 days and subsequently washed with Phosphate buffered saline solution (PBS, 10 mM Na phosphate in 0.9% NaCl, pH 7.4). DE cells were thawed and seeded in Hepatocyte Thawing and Seeding Medium at an initial density of 2.5×10^6 cells/scaffold and for the static references 1.5×10^5 cells/cm^2 in 24 well plate format (using polystyrene well plates or corresponding PDMS coated well plates, see below) in 1 ml of medium. The DE cells were differentiated in Hepatocyte Thawing and Seeding Medium for 2 days at 37°C,

before changing to Hepatocyte Progenitor Medium for another 5 days of differentiation to hepatoblasts. The cells were then differentiated further in Hepatocyte Maturation Medium for 4 days to immature hepatocytes and finally matured in Hepatocyte Maintenance Medium for another 14 days of culture to mature hepatocytes. In the static cultures, the medium was exchanged every 2-3 days. The derivation of DE cells from iPSC cells as well as the robustness of the hepatic differentiation protocol has already been shown before in 2D conditions on hiPSC cell lines from different donors [44].

Scaffolds fabrication and p**erfusion cell differentiation culture**

Polydimethylsiloxane (PDMS) was chosen instead of hydrogels as scaffold material to due to its biocompatibility and structural stability enabling production of liter-sized scaffolds [32, 33]. Random porous scaffolds (Figure 1E) were fabricated from PDMS by using salt leaching techniques similar to that described previously [34]. Hexagonal combined structured/porous scaffolds (Figure 1E) were made using a sacrificial mold with hexagonal pattern fabricated by 3D printing using commercially available water dissolvable polyvinyl alcohol (PVA) (MakerBot, USA) and packed with salt crystals as described in [32]. The scaffolds were treated with oxygen plasma (125 W, 13.5 MHz, 50 sccm, and 40 millitorr) to render their surfaces hydrophilic and sterilized by autoclaving. They were coated with Hepatocyte coating (from Cellartis Hepatocyte Differentiation Kit, Cat. No. Y30050) by centrifugation at 300 x g for 5 minutes and then left overnight at 37 °C. The scaffolds were subsequently washed with PBS centrifugation at 300 x g for 5 minutes and then left in a media at 37 °C for 2h prior to being used to experiments.

A self-sustained perfusion system with 16 parallel reactors was constructed (Supplementary Figure S1) holding PDMS scaffolds. The scaffold bioreactor array, glass vials, caps and PTFE tubing were sterilized by autoclaving before assembling in a laminar flow bench. 0.5 M NaOH was flushed throughout the system to ensure a sterile fluidic path. The system was subsequently flushed with sterile water and then with culture medium. Coated scaffolds were placed in cylindrical holes in a custom built tray. 2.5×10^6 freshly thawed DE cells in 30 μL of Hepatocyte Thawing and Seeding Medium was pipetted into each scaffold and cells were allowed to adhere for 3h at 37 °C under 95% air/5% CO_2. The seeding tray was inverted as well as placed vertically in four different positions to allow the cells to distribute throughout the scaffolds during the 3h. The scaffolds were then placed in the 4×4 bioreactor array of the

fluidic platform, and media was perfused through the scaffolds at flow rates of either 1 μL/ min or 5 μL/ min. The entire system was incubated at 37 °C under 95%air/5% CO_2. Cells were cultured and differentiated for 25 days.

Human liver tissue

Human liver material was obtained from liver tissue of 10 individual patients, remaining as surgical waste after reduced liver transplantation patients, from liver tissue donated after cardiac death but not suitable for transplantation due to the age or from patients undergoing hepatectomy for the removal of carcinoma. This study was approved by the Medical Ethical Committee of the University Medical Centre Groningen, according to Dutch legislation and the Code of Conduct for dealing responsibly with human tissue in the context of health research (http://www.federa.org), refraining the need of written consent for ''further use'' of coded-anonymous human tissue. The procedures were carried out in accordance with the experimental protocols approved by the Medical Ethical Committee of the University Medical Centre Groningen.

hPCLS were prepared as described previously by de Graaf et al. [26]. The hPCLS were made about 200μm thick and had 5 mg wet weight. In order to remove cell debris and to restore function, hPCLS were pre-incubated in the incubator (Panasonic, USA) for 1 hour at 37ºC in a 12-well plate filled with 1.3 ml of Williams' Medium E (Gibco, USA) saturated with $80\%O_2/5\%CO_2$ while gently shaking 90 cycles per minute.

Static hPCLS culture. After pre-incubation, slices were transferred individually to a 12-well plate filled with 1.3 ml of Hepatocyte Maintenance Medium (from Cellartis Hepatocyte Diff Kit (Cat. No. Y30050) saturated with $80\%O_2/5CO_2$ and supplemented with 50 µg/ml gentamycin (Invitrogen). Plates were gently shaking 90 cycles per minute in the incubator at 37ºC.

hPCLS culture under flow condition. After pre-incubation, slices were transferred individually into small micro-chambers of PDMS biochips. The fabrication process of the biochip, as well as a schematic view of the biochip set-up was extensively described before [35]. Slices were embedded in Matrigel[TM] (BD Biosciences, Bedford, MA, USA) as described previously and the biochips were perfused with 2 times diluted Hepatocyte Maintenance Medium from Cellartis Hepatocyte Diff Kit supplemented with 50 mg/ml gentamycin at 10µl/min flow in a

humidified incubation chamber saturated with a mixture of 95%O_2/5%CO_2 as described in detail before [36]. Viability of hPCLS was assessed by analysis of ATP content and morphological examination after 0h and 24 h. More details are provided in Supplementary materials.

Imaging and confocal microscopy

Phase contrast images of 2D flow cultures and fluorescence based imaging of the scaffolds were acquired by a Zeiss Axio Observer as described in details in Supplementary materials. Confocal acquisitions of the scaffolds were performed using a Zeiss LSM 700 module in the Axio Imager M2 upright microscope using a 40x/1.20 W Korr C-Apo objective. More details are provided in Supplementary materials.

Functional characterization of hiPSC-derived hepatocytes and hPCLS

Phase I metabolism. To test the activities of several different CYP isoenzymes, hPCLS and cells in perfused and static systems were exposed for 1-3 hours to a drug cocktail containing 10µM phenacetin (CYP1A), 10µM bupropion (CYP2B6), 50µM mephenytoin (CYP2C19), 10µM diclofenac (CYP2C9), 10µM bufuralol (CYP2D6) and 5µM midazolam (CYP3A) in Hepatocyte Maintenance Medium without phenol red and supplemented with 2mM L-glutamine and antibiotics (50 mg/ml gentamycin for hPCLS and 0.1% penicillin and streptavidin for cells. Medium was collected and stored at -80°C until further analysis. Metabolite concentrations were measured at Pharmacelsus (Germany) by LC/MS according to in house protocols. The metabolite production was normalized per milligram protein and per hour.

Phase II metabolism. For Phase II metabolism studies, hPCLS and cells in perfused systems or in static condition were exposed to 100µM of 7-hydroxycoumarin (7-HC) (Sigma-Aldrich, St.Louis, MO, USA) for 1-3 hours. Medium was collected at outlet tubes or from the incubation medium and stored at -20°C until further analysis, using 7-HC, 7-HC-G and 7-HC-S as standards. The metabolite production was normalized per milligram protein and per hour.

Gene expression

Total cellular RNA from cells or PCLS was purified by using the RNeasy Micro kit (Qiagen, 74004) or using Maxwell 16 LEV simplyRNA Tissue Kit (Promega, USA) respectively. The RNA was converted to cDNA using the High Capacity cDNA Reverse Transcription Kit (Applied Biosystems, 4374966) and quantitative real time PCR was conducted using the TaqMan

Gene Expression Assays (Applied Biosystems 4331182). More details are provided in Supplementary Materials.

Statistical analysis

Four independent experiments were performed with 4 batches of DE cells from one donor, and hPCLS from 7 different human donors. Since the number of donor livers for slices and number of donors for stem cells are limited, and inter-individual variations are large in the human population, we conclude on the differentiation of the cells by comparing the range of expression or activity rather than the mean or median values.

Additional Methods can be found in Supplementary materials.

References

1. Ordovás, L., Park, Y. & Verfaillie, C. M. Stem cells and liver engineering. *Biotechnol. Adv.* **31**, 1094-1107 (2013).

2. Mizumoto, H. *et al*. Evaluation of a Hybrid Artificial Liver Module Based on a Spheroid Culture System of Embryonic Stem Cell-Derived Hepatic Cells. *Cell Transplant.* **21**, 421-428 (2012).

3. Nibourg, G. A. A., Chamuleau, R. A. F. M., van Gulik, T.,M. & Hoekstra, R. Proliferative human cell sources applied as biocomponent in bioartificial livers: a review. *Expert Opin. Biol. Ther.* **12**, 905-921 (2012).

4. Palakkan AA, Hay, D. C., Anil Kumar, P. R., Kumary, T. V. & Ross, J. A. Liver tissue engineering and cell sources: issues and challenges. *Liver International* **33**, 666-76 (2013).

5. Schwartz RE, Fleming, H. E., Khetani, S. R. & Bhatia, S. N. Pluripotent stem cell-derived hepatocyte-like cells. *Biotechnol. Adv.* **32**, 504-513 (2014).

6. Song ZH *et al*. Efficient generation of hepatocyte-like cells from human induced pluripotent stem cells. *Cell Res.* **19**, 1233-1242 (2009).

7. Chen YF *et al*. Rapid generation of mature hepatocyte-like cells from human induced pluripotent stem cells by an efficient three-step protocol. *Hepatology* **55**, 1193-203 (2012).

8. Gieseck, R. L. *et al*. Maturation of induced pluripotent stem cell derived hepatocytes by 3D-culture. *PLoS ONE* **9** (2014).

9. Si-Tayeb K *et al*. Highly efficient generation of human hepatocyte-like cells from induced pluripotent stem cells. *Hepatology* **51**, 297-305 (2010).

10. Ulvestad M *et al*. Drug metabolizing enzyme and transporter protein profiles of hepatocytes derived from human embryonic and induced pluripotent stem cells. *Biochem. Pharmacol.* **86**, 691-702 (2013).

11. Sivertsson L, Synnergren, J., Jensen, J., Bjorquist, P. & Ingelman-Sundberg, M. Hepatic Differentiation and Maturation of Human Embryonic Stem Cells Cultured in a Perfused Three-Dimensional Bioreactor. *Stem Cells and Development* **22**, 581-594 (2013).

12. Miki, T., Ring, A., Gerlach, J. Hepatic differentiation of human embryonic stem cells is promoted by three-dimensional dynamic perfusion culture conditions. *Tissue Engineering, Part C: Methods* **17**, 557-68 (2011).

13. Schmelzer E *et al*. Three-Dimensional Perfusion Bioreactor Culture Supports Differentiation of Human Fetal Liver Cells. *Tissue Engineering Part A* **16**, 2007-2016 (2010).

14. Fonsato V *et al*. Use of a Rotary Bioartificial Liver in the Differentiation of Human Liver Stem Cells. *Tissue Engineering, Part C: Methods* **16**, 123-132 (2010).

15. Pekor, C., Gerlach, J. C., Nettleship, I., Schmelzer, E. Induction of Hepatic and Endothelial Differentiation by Perfusion in a Three-Dimensional Cell Culture Model of Human Fetal Liver. *Tissue Engineering, Part C: Methods* (2015).

16. Wang YJ *et al*. Rotating Microgravity-Bioreactor Cultivation Enhances the Hepatic Differentiation of Mouse Embryonic Stem Cells on Biodegradable Polymer Scaffolds. *Tissue Engineering Part A* **18**, 2376-2385 (2012).

17. Luni, C. *et al.* High-efficiency cellular reprogramming with microfluidics. *Nature Methods* **13**, 446-52 (2016).

18. Giobbe GG *et al*. Functional differentiation of human pluripotent stem cells on a chip. *Nature Methods* **12**, 637-40 (2015).

19. Lu J *et al*. Morphological and Functional Characterization and Assessment of iPSC-Derived Hepatocytes for In Vitro Toxicity Testing. *Toxicol. Sci.* **147**, 39-54 (2015).

20. Yu, C. *et al*. Evaluation of a novel choanoid fluidized bed bioreactor for future bioartificial livers. *World Journal of Gastroenterology : WJG* **20**, 6869-6877 (2014).

21. Hemmingsen M *et al*. The role of paracrine and autocrine signaling in the early phase of adipogenic differentiation of adipose-derived stem cells. *PLoS ONE* **8**, 63638 (2013).

22. Iwamuro M *et al*. A preliminary study for constructing a bioartificial liver device with induced pluripotent stem cell-derived hepatocytes. *BioMedical Engineering OnLine* **11**, 93 (2012).

23. Takayama K *et al*. Efficient generation of functional hepatocytes from human embryonic stem cells and induced pluripotent stem cells by HNF4a transduction. *Molecular Therapy* **20**, 127-37 (2012).

24. Elferink, M. G. L. *et al*. Gene expression analysis of precision-cut human liver slices indicates stable expression of ADME-Tox related genes. *Toxicol. Appl. Pharmacol.* **253**, 57-69 (2011).

25. de Graaf, I. A. M., Groothuis, G. M. M. & Olinga, P. Precision-cut tissue slices as a tool to predict metabolism of novel drugs. *Expert Opin. Drug Metab. Toxicol.* **3**, 879-898 (2007).

26. de Graaf, I.,A.M. *et al*. Preparation and incubation of precision-cut liver and intestinal slices for application in drug metabolism and toxicity studies. *Nat. Protocols* **5**, 1540-1551 (2010).

27. van Midwoud PM, Merema, M. T., Verpoorte, E. & Groothuis, G. M. Microfluidics enables small-scale tissue-based drug metabolism studies with scarce human tissue. *Journal of Laboratory Automation* **16**, 468-76 (2011).

28. Yanagida A, Ito, K., Chikada, H., Nakauchi, H. & Kamiya, A. An in vitro expansion system for generation of human iPS cell-derived hepatic progenitor-like cells exhibiting a bipotent differentiation potential. *PLoS ONE* **8**, 67541 (2013).

29. Kim JH *et al*. Enhanced Metabolizing Activity of Human ES Cell-Derived Hepatocytes Using a 3D Culture System with Repeated Exposures to Xenobiotics. *Toxicol. Sci.* **147**, 190-206 (2015).

30. Zhou SF, Liu, J. P. & Chowbay, B. Polymorphism of human cytochrome P450 enzymes and its clinical impact. *Drug Metab. Rev.* **41**, 89-295 (2009).

31. Emoto C & Iwasaki, K. Enzymatic characteristics of CYP3A5 and CYP3A4: a comparison of in vitro kinetic and drug-drug interaction patterns. *Xenobiotica* **36**, 219-33 (2006).

32. Mohanty S *et al*. Fabrication of scalable and structured tissue engineering scaffolds using water dissolvable sacrificial 3D printed moulds. *Materials Science and Engineering: C* **55**, 569-78 (2015).

33. Mohanty S *et al*. Fabrication of scalable tissue engineering scaffolds with dual-pore microarchitecture by combining 3D printing and particle leaching. *Materials Science and Engineering: C* **61**, 180-9 (2016).

34. Yuen PK, Su, H., Goral, V. N. & Fink, K. A. Three-dimensional interconnected microporous poly(dimethylsiloxane) microfluidic devices. *Lab on a Chip* **11**, 1541-1544 (2011).

35. van Midwoud, P. M., Groothuis, G. M., Merema, M.T., Verpoorte, E. Microfluidic biochip for the perifusion of precision-cut rat liver slices for metabolism and toxicology studies. *Biotechnol. Bioeng.* **105**, 184-94 (2010).

36. van Midwoud PM, Merema, M. T., Verweij, N., Groothuis, G. M. & Verpoorte, E. Hydrogel embedding of precision-cut liver slices in a microfluidic device improves drug metabolic activity. *Biotechnol. Bioeng.* **108**, 1404-12 (2011).

37. Skafte-Pedersen Peder, Sabourin, D., Dufva, M. & Snakenborg, D. Multi-channel peristaltic pump for microfluidic applications featuring monolithic PDMS inlay. *Lab on a Chip* **9**, 3003-3006 (2009).

38. Sabourin D *et al*. The MainSTREAM component platform: a holistic approach to microfluidic system design. *Journal of Laboratory Automation* **18**, 212-28 (2013).

39. Okkels, F., Dufva, M. & Bruus, H. Optimal Homogenization of Perfusion Flows in Microfluidic Bio-Reactors: A Numerical Study. *PLoS ONE* **6**, e14574 (2010).

40. Patrachari, A. R., Podichetty, J. T., Madihally, S. V. Application of computational fluid dynamics in tissue engineering. *Journal of Bioscience and Bioengineering* **114**, 123-32 (2012).

41. Starokozhko V *et al*. Viability, function and morphological integrity of precision-cut liver slices during prolonged incubation: Effects of culture medium. *Toxicology in Vitro* **30**, 288-99 (2015).

42. Synnergren J *et al*. Differentiating human embryonic stem cells express a unique housekeeping gene signature. *Stem Cells* **25**, 473-80 (2007).

43. Canali C *et al*. Impedance Spectroscopic Characterisation of Porosity in 3D Cell Culture Scaffolds with Different Channel Networks Electroanalysis Volume 27, Issue 1. *Electroanalysis* **27**, 193-199 (2015).

44. Asplund A *et al*. One Standardized Differentiation Procedure Robustly Generates Homogenous Hepatocyte Cultures Displaying Metabolic Diversity from a Large Panel of Human Pluripotent Stem Cells. *Stem Cell Reviews and Reports* **27**, 90-104 (2016).

Author contribution

V.S. has designed the experiments, performed the experiments with PCLS, analyzed and interpreted the data, made graphs and wrote the manuscript. M.H. has designed the experiments, performed experiments with hiPSC, analyzed and interpreted the data and contributed to writing the manuscript. L.L. has designed the cell culture perfused platform, performed experiments and analyzed the data. S.M. has designed the PDMS scaffolds used in this study to culture cells. M.M. helped with the experiments with tissue slices and the analysis. R.P. did the imaging of the cell cultures and calculations on the shear stress, contributed to writing the paper. A.W. and J.E. designed the experiments and contributed with materials/tools. A.A. has provided the hiPSCs and protocols for the hepatic differentiation and designed experiments. G.G. and M.D. have designed the experiments, interpreted the results and wrote the manuscript.

Competing Financial Interest Statement

Anders Aspegren is an employee of Takara Bio Europe.

Acknowledgements

Differentiation of Human Induced Pluripotent Stem Cell under Flow Conditions to Mature Hepatocytes for Liver Tissue Engineering

Viktoriia Starokozhko[2*], Mette Hemmingsen[1*], Layla Larsen[1], Soumyaranjan Mohanty[1], Marjolijn Merema[2], Rodrigo Pimentel C.[1], Anders Wolff[1], Jenny Emnéus[1], Anders Aspegren[3], Geny Groothuis[2#], and Martin Dufva[1#]

Supplementary Information

Description of perfusion system

A schematic view of the perfusion culture system and fluidic/air circuit is illustrated in Supplementary Figure S1. The main components of the system include an array of 4×4 bioreactors for culture of cells, vials and vial trays for storage of culture media and waste and peristaltic pumps and motors for perfusion of media. All parts are secured onto a single platform. Four 8-channel micropumps (previously described [37, 38]) that generate pulsatile flow are included in the system, controlled by motors and controllers from the Lego Mindstorm (Lego, Billund, Denmark) kit. This allows culturing of cells at four different flow rates in a single experiment. The pumps allow flow rates of sub-μl/min to approximately 90 μl/min [38]. The fluidic circuit is formed by the pumps, bioreactor array and media storage vials that are connected using polytetrafluoroethylene (PTFE) tubing (inner diameter of 0.8 mm) (BOLA 1818-10, Bohlender GmbH, Germany). Inlet and outlet vials are coupled with PTFE tubing and supplied with air supplemented with 5% CO_2 through a sterile filter. To avoid the formation of gas bubbles in the microfluidic network, an overpressure of 30 kPa is put on the flow system during its operation. All components are mounted onto a base platform for portability and user-friendly handling. The entire system can be placed in an incubator for cell culture experiments.

Design of the bioreactor array

The bioreactor array (Supplementary Figure S1) allows culture of 16 cylindrical 3D constructs having thicknesses of 5 mm and diameters of 6 mm (Figure 1E). The bioreactors are designed with conical inlets and outlets for uniform delivery of media through the pores of a scaffold in the cylindrical cavity [39, 40]. Additionally, the conical inlet geometry gives rise to lower shear stress in the areas of the scaffold close to the inlet as assessed from a finite ele-

ment study of the flow profile within two bioreactor designs as discussed in following sections. Silicone tubes (having inner diameter of 1.8 mm and 1 cm in height) are press fit to the ports of the bioreactor (inner diameter of 1 mm and outer diameter of 2 mm) and serve as connectors between the bioreactor and the rest of the perfusion network.

The 4×4 bioreactor array was implemented in an easily exchangeable single device, as shown in Figure S1. The upper plate of the device (having dimensions of 100 x 100 x 5 mm^3) incorporates the outlet ports for waste removal from each bioreactor. The lower plate (with dimensions of 100 x 100 x 10 mm^3) incorporates 4×4 cylindrical chambers (each with a diameter of 6 mm and height of 5 mm) for housing scaffolds and inlet ports for perfusion of media into the chambers. The two parts of the array are secured together using screws with a custom designed polydimethylsiloxane (PDMS) gasket (having a thickness of 1 mm) placed between them in order to ensure a tight seal and form a leak proof system. The gasket was designed such that it incorporated a raised lip (0.5 mm high) around each bioreactor array.

Fabrication

The two parts of the bioreactor array were fabricated by micromilling the required features into polycarbonate substrates. The gasket was fabricated by moulding of PDMS in a custom milled polycarbonate mould. Vial trays capable of housing 32 vials (16 for holding cell culture media and 16 for storage of the waste media), were fabricated in 5 mm sheets of polymethylmethacrylate (PMMA) using a CO2 laser cutter (Epilog Mini 18 Laser, CO 80403, USA).

Viability determination of hPCLS

ATP content of hPCLS was assessed according to the manufacturer's protocol of the ATP Bioluminescence Assay Kit CLS II (Roche, Mannheim, Germany) in a black 96-well plate in the Lucyl luminometer (Anthos, Durham, NC) using a standard ATP calibration curve. The ATP content was normalized for protein content of the hPCLS as described below. Morphology was assessed on 4 μm sections of formaldehyde fixated, paraffin-embedded slices, stained with hematoxylin and eosin according to the described protocol [26].

Protein Content of hPCLS and IPSC-derived hepatocytes in the scaffold

The pellet left from homogenized ATP samples was used to determine the protein content of hPCLS according to Lowry by using the Bio-Rad DC Protein Assay (Bio-Rad, Munich, Germany) as described before using bovine serum albumin for the standard curve [41]. Protein content of cells in the scaffold was measured according to the manufacturer instructions of Pierce BCA Protein Assay Kit (cat. no. 23227) after protein extraction by an over-night incubation of the scaffold in 0.2 M NaOH. More information is found in Supplementary Figure S5.

Gene expression analysis

Total cellular RNA was purified by using the RNeasy Micro kit (Qiagen, 74004). Differentiated cells were lysed directly in the scaffold in the bioreactor using the lysis buffer provided in the Qiagen RNeasy Micro kit. The lysate was collected in microtubes and purified according to manufacturer's instructions (Qiagen, 12/2007). Total RNA from the hPCLS was isolated using Maxwell 16 LEV simplyRNA Tissue Kit (Promega, USA). The RNA was converted to cDNA using the High Capacity cDNA Reverse Transcription Kit (Applied Biosystems, 4374966) according to the manufacturer's instructions (06/2010). Quantitative real time PCR was conducted using the TaqMan Gene Expression Assays (Applied Biosystems 4331182), ALB (albumin) ID: Hs00910225_m1, AFP (alpha-fetoprotein) ID: Hs00173490_m1, CYP2B6 ID: Hs04183483_g1, CYP3A4 ID: Hs00604506_m1, CYP3A5 ID: Hs00241417_m1, CYP3A7 ID: Hs00426361_m1, HNF4A (hepatocyte nuclear factor-4-alpha) ID: Hs00230853_m1, NR1I3 (CAR, constitutive androstane receptor) ID: Hs00231959_m1, ABCB11 (BSEP, Bile Salt Export Pump) ID: Hs00184824_m1, ABCB1 (P-gp, permeability glycoprotein) ID: Hs00184500_m1, and KRT7 (cytokeratin-7) ID: Hs00559840_m1), TaqMan Gene Expression Master mix (Applied Biosystems, 4370048) and RNase-free water according to the manufacturer's instructions (Applied Biosystems 11/2010). The respective C_t values obtained after analysis in a Chroma4 real time PCR machine (MJ Research, the program run at 50 ºC for 2 minutes, 95 ºC for 10 minutes and 40 cycles of 15 sec at 95 ºC and 1 minute at 60 ºC) were normalized to the C_t value of CREBBP (CREB-binding protein) ID: Hs00231733_m1. CREBBP has been shown to be a good candidate to use for normalization since the gene expression does not change significantly during differentiation [42]. The gene expression is presented as individual data points using the formula: $2^{-\Delta Ct}$.

Imaging

Phase contrast images of 2D flow cultures were acquired by a Zeiss Axio Observer.Z1 microscope equipped with a 10x/0.3 Plan-Neofluar objective, and a Zeiss Axiocam MRm B/W camera. A scan of each cell culture chamber was recorded with an exposure time of 5 msec. All images were acquired with a z-stack of 5 image planes (6 μm between each image plane). The images were processed by applying the AxioVision Extended Focus module on the z-stacks to obtain the best focused image, stitching the individual images together and finally converting the stitched images to one image.

Fluorescence based imaging of a cross section of the scaffold was carried out at day 22 of the cell culture differentiation. Scaffolds were sectioned longitudinally (along the axis of flow). Each scaffold was stained with either Höechst for showing cell distribution or Calcein AM for live cell imaging. Non-fluorescent Calcein AM is converted to highly fluorescent Calcein by intracellular esterase activity and stains viable cells green. Cells were imaged using an inverted microscope (Zeiss Axio Observer) using the appropriate excitation lights and filters.

Confocal Microscopy

Scaffolds were sectioned longitudinally (along the axis of flow) on day 22 of the cell culture differentiation. Each sample was fixed in 3% paraformaldehyde (in PBS) for 10 minutes and permeabilized with Triton X-100 for 5 minutes. Subsequently, they were stained for 30 minutes with either Höechst 33342 (Invitrogen) for labeling the cell nuclei as well as Phalloidin (F432, Invitrogen) for labeling the F-actin. Confocal acquisitions were performed using a Zeiss LSM 700 module in the Axio Imager M2 upright microscope using a 40x/1.20 W Korr C-Apo objective. The confocal settings were as follows, section thickness 0.8 μm, pixel dwell 0.79 μs, pixel size 145 nm, optimal Z section number determined by the confocal software. To eliminate any possible cross-talk between channels, images were collected with a sequential scan, using the following laser lines and mirror settings: 488(30%) 495-560nm; 555(30%) 605-700nm.

Albumin synthesis

Albumin production was measured using the Human Albumin ELISA kit (Bethyl Laboratories, Mongomery, USA) according to the supplier's recommendations. In brief, medium was collected from the well plate (static conditions) after 24 hours of incubation or at the outlet tubes (perfused systems) for 24 hours from both differentiated cell and hPCLS cultures and

stored at -20°C until analysis. Samples were diluted if necessary and human albumin was used to prepare a calibration curve. The amount of albumin was calculated based on a standard curve generated as a parameter curve fit. Values are expressed as ng albumin produced per hour, per milligram total protein.
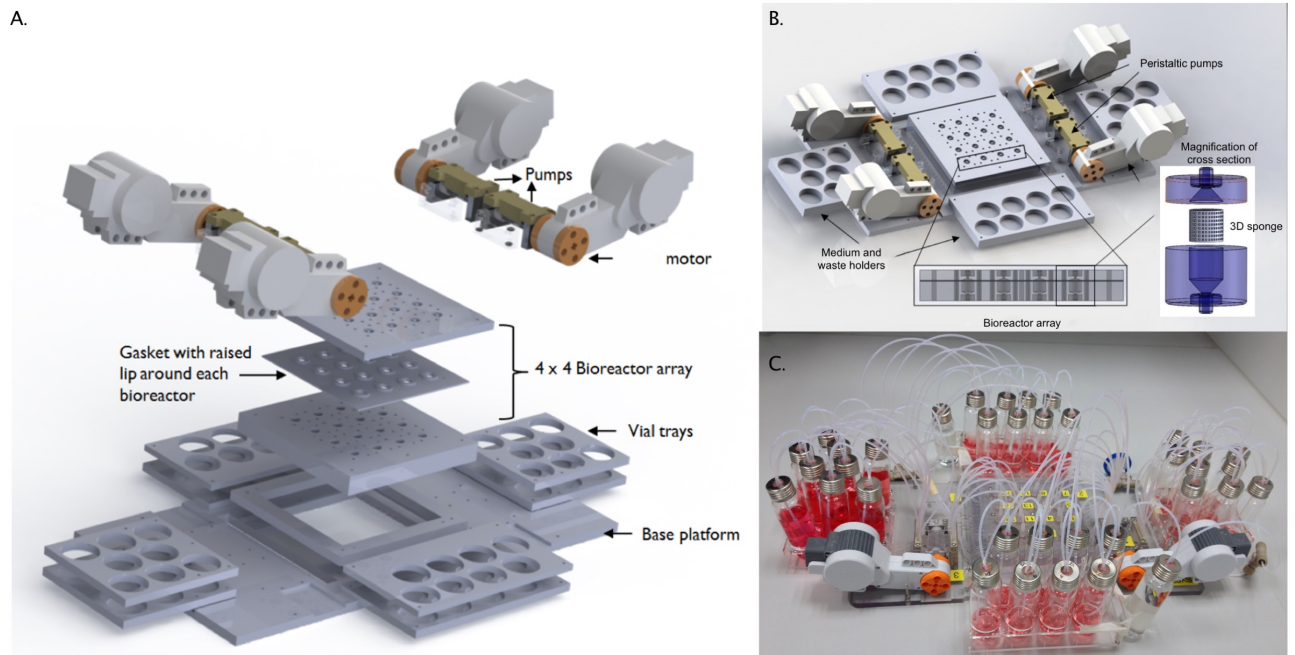
Supplementary Figure S1. System Description Figure 1. A: Parts of the 3D perfusion system. B: Render of assembled 3D perfusion system. C: Picture of a perfusion system with tubes and vials.
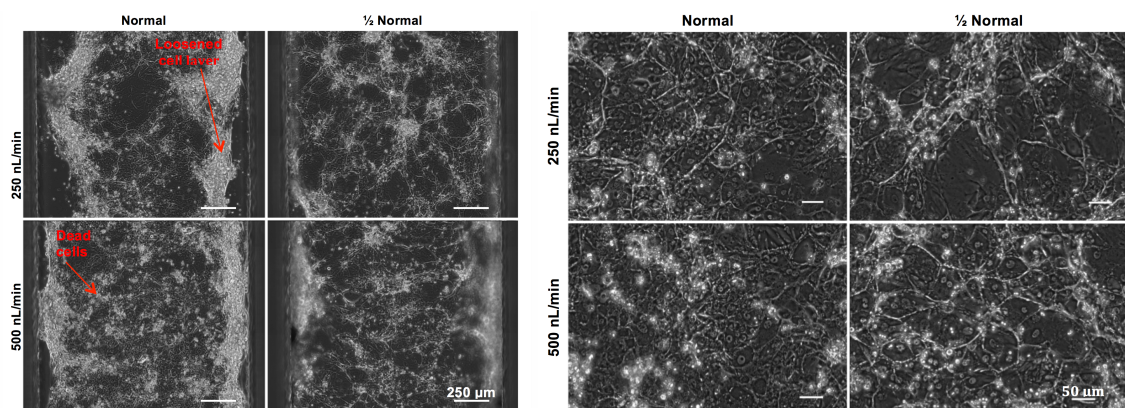
Supplementary Figure S2. Effect of concentration of signalling factors on cell morphology at flow conditions. Left panels: low magnifications, right panels high magnifications. DE cells were cultured and differentiated at 2D flow conditions in a chamber having dimensions of 1.5 mm (w) x 6 mm (l) x 0.5 mm (h). The concentration of signalling factors was either the normal used and optimized for static culture conditions or 1⁄2 the

normal concentration but otherwise a full base medium. The cells were perfused at two different flow rates, 250 nL/min or 500 nL/min, corresponding to an exchange of the medium in the entire chamber every 20 and 10 minutes. Phase contrast images acquired at day 25. The shown images are a representative area of one chamber out of 4 chambers for each condition. A better cell attachment and less dead/floating cells were observed at perfusion with medium supplemented with half of the normal concentration of signalling factors compared to perfusion with medium supplemented with the normal concentration of signalling factors.
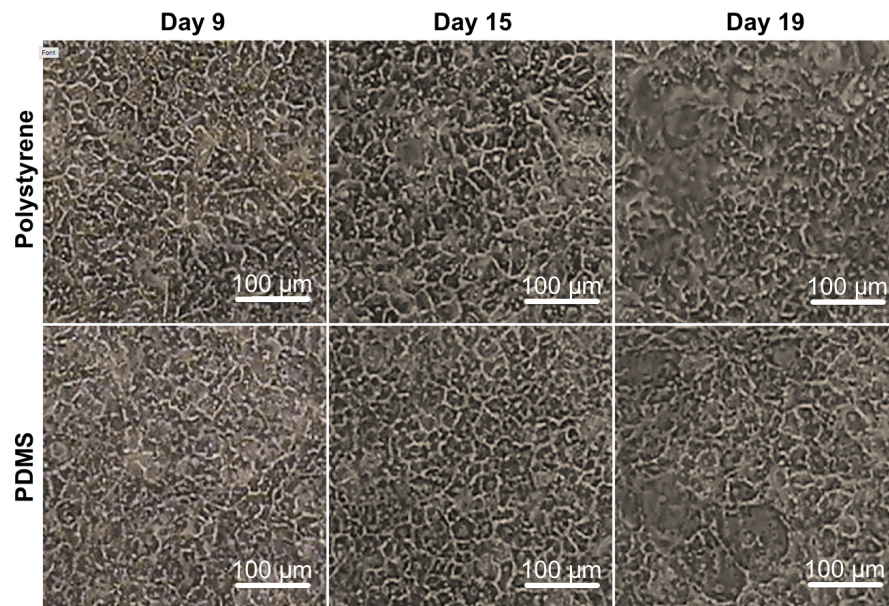
Supplementary Figure S3. Cell morphology of differentiating cells at static conditions. Phase contrast images were acquired at day 9, 15, and 19. The cell morphology was very similar between the PDMS scaffold material and the PS conventional surface substrate, although some larger cells were observed on PDMS)
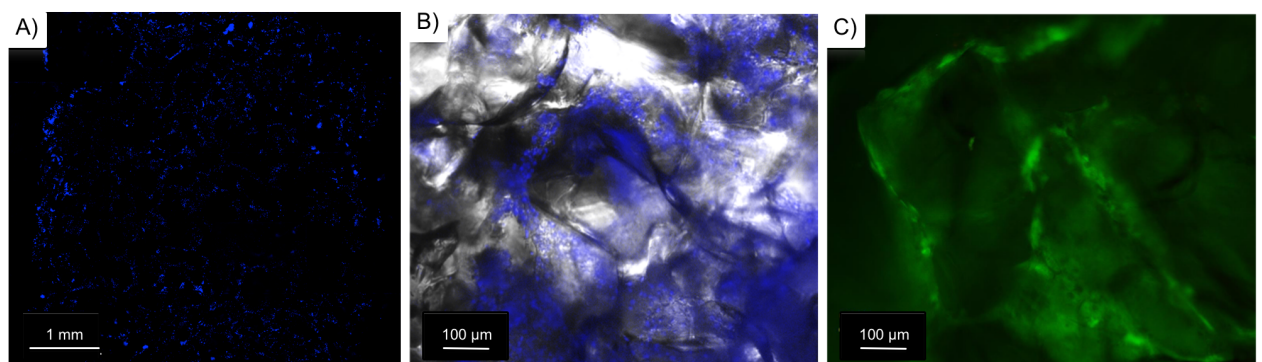
Supplementary Figure S4. Microscopy imaging of hiPSC-derived DE cells cultured and hepatic differentiated inside a porous scaffold at perfusion conditions: Image at day 22 after cell seeding of the middle of a cross-

sectioned scaffold. A) Scan of entire cross-sectioned scaffold showing cell distribution. Höechst stained cell nuclei in blue color. B) Close-up view of cell distribution with Höechst stained cell nuclei. The homogeneus blue fields in the image is likely not cells but reflections within the scaffold. The fluorescence image is merged with a phase contrast image of the scaffold. C) Calcein-AM live-stained cells in green.

Total protein [mg]
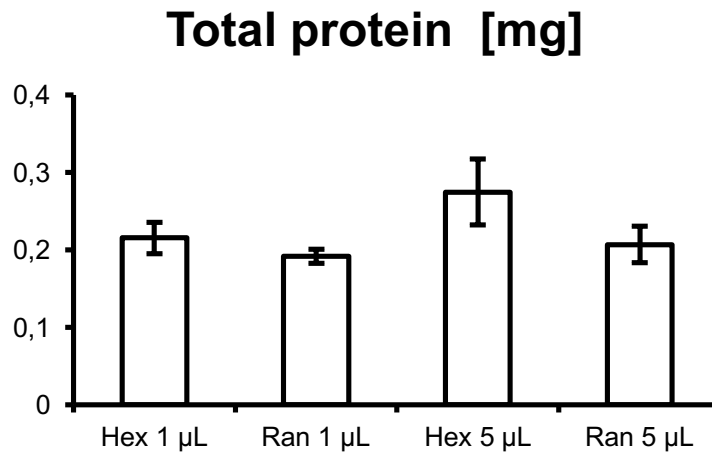
Supplementary Figure S5. Determination of protein content in the BAL. DE cells were loaded into the BAL as described in material and methods. Three replicates of the four investigated BALs (two different scaffold designs and two different flow conditions), where prepared and cultured for one week. Scaffolds with cells were perfused with Dulbecco's Phosphate Buffered Saline with $MgCl_2$ and $CaCl_2$ (Sigma D8662) for 30 min to re-move protein containing medium and then transferred to a 1.5 mL Eppendorf tube with 0.5 mL 0.2M NaOH. To enhance distribution of NaOH within the scaffold, the tubes were vortexed for 30 seconds three times with 10 minutes incubation between each vortex. The tubes were incubated over night at 4°C. To enhance the release of cell material from the scaffold into the NaOH, the tube was again vortexed for 3 X 30 seconds with 10 minutes incubation between each vortex, and then centrifuged at 500 x g for 5 minutes. The supernatant was diluted 1:1 with milliQ water to 0.1M NaOH. The protein content was measured using the Pierce® BCA Protein Assay Kit (cat. no. 23227) according to the supplier's microplate procedure. The absorbance was read at 570 nm and pro-tein calculated based on a standard curve for bovine serum albumin. The results showed that the variance be-tween the same type of scaffold was limited. If it is assumed that 0.1 mg protein corresponds to 100.000 cells (Anders Aspegren, personal observations), each BAL contains about 200.000-270.000 cells. This corresponds well with theoretical calculations that there can be a maximum of about 600,000-1,000,000 cells per BAL (see supplementary figure 6).
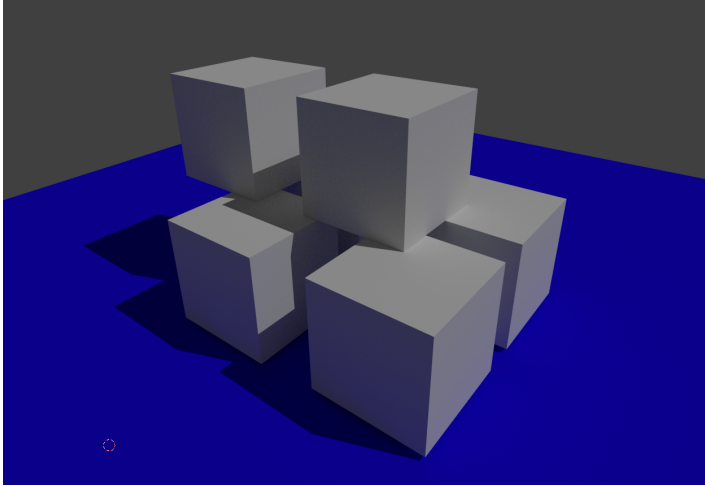
Supplementary Figure S6. Theoretical calculations of the surface area of a scaffold. Two estimates were made: **Estimate 1** was based on an idealized network of cubes that are connected and then surrounded by PDMS. The calculation involved trying to find out how many salt cubes that can fit into the volume of the scaffold and then calculate the surface area by taking the number of salt particles multiplied by the total surface of one salt particle. The side of a salt cube is approximately 0.35 mm as determined by scanning electron microscopy investigations 43. The distance to the next salt particle is estimated to be 0.1 mm (can also be larger) meaning that a salt crystal takes up about $0.45*0.45*0.45= 0.091125$ mm^3 including the surrounding PDMS. The cylinder volume (Figure 1C) is $r^2*pi*h=3*3*pi*5=141$mm3. $141/0.091125= 1556$ particles. The surface area of a salt particle is $0.35*0.35*6=0.735$ mm^2. $1556*0.735= 11.39$ cm^2. However, because the salt crystals need to touch each other in order to form a network, some of the area is lost. In the idealized situation, each cube loses about 1.5 sides in surface area as it shares that area with other salt crystals. Therefore, the area is estimated to be $11.39*9/12=8.5$ cm^2 In **Estimate 2** we used the measured porosity (determined to be 65%) 43 of a random scaffold as input parameter and calculated the number of salt molecules that could fit into pores with a total volume of 0.65 multiplied by the scaffold volume: $r^2*pi*h*0.65=3*3*pi*5*0.65=92$ mm^3. Volume of salt particle is $0.35*0.35*0.35$mm^3=0.042875mm^3. Number of salt particles in scaffold are $92/0.042875 = 2145$ particles. Number of particles multiplied by the surface of each salt cube ($6*0.35*0.35$mm^2=0.735mm^2) = total surface volume: 1577 mm^2=15.8 cm^2. However, just as in the case above, some of the sides of the cubes are shared between each sugar cube. Using the estimate above, it is suggested that the surface area is 15.8 cm^2*9/12= 11.85 cm^2. In this case, the surface area is estimated to be about 12 cm^2, which is close to **Estimate 1** of 11.39 cm^2. For simplicity, we estimate the surface of a scaffold to 10 cm^2 (1000 mm^2).

The number of cells fitting the scaffold is proportional to the surface of one side of the cuboidal cell. A 20 μm x 20 μm cell surface will result in a theoretical cell limit of $1000/(0.02*0.02)=2.5$ million cells per scaffold. This is given that the cell surface area is the same in the 3D scaffold as on the 2D batch culture. Typically, 80,000-100,000 iPSC-differentiated hepatocytes can be harvested per cm2 cell culture dish indicating that the maximal total cell number in the scaffold is between 800,000- 1,000,000 cells.
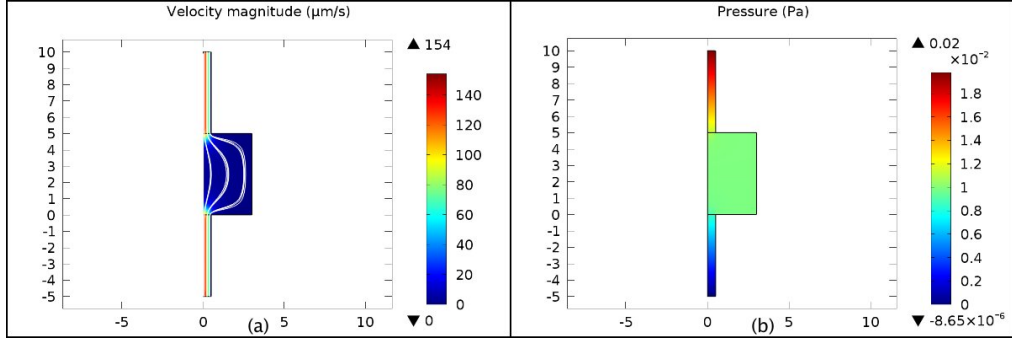
Supplementary Figure S7. Evaluation of shear stress acting on the 3D scaffold at the microscale

Velocity profile (a) and pressure gradient (b) within the bioreactor as well as in the 3D scaffold. Different COMSOL simulations were performed to calculate the shear stress that cells sense within the 3D scaffold. The first analysis was made at the macro scale, evaluating the velocity field and pressure gradient in the reactor as well as in the 3D porous scaffold.

The domain region outside the scaffold was modeled by using the incompressible Navier-Stokes equation, which describes how the velocity, pressure, temperature and density of a moving fluid are related and include the effects of viscosity on the flow.

$$\rho \frac{\partial u}{\partial t} - \eta \nabla^2 u + \rho(u \cdot \nabla)u + \nabla p = F \tag{1}$$

$$\nabla \cdot u = 0 \tag{2}$$

where, ρ is fluid density (kg·m^{-3}), u is the fluid velocity (m·s^{-1}), η is viscosity (Pa·s), p is the pressure (Pa), F the volume force (N), and ∇ the standard del (nabla) operator.

The region containing the porous scaffold was modeled by using the Darcy-Brinkman equation, assuming that the scaffold has uniform microarchitecture and cylindrical pores.

$$\mu \nabla^2 u_s - \frac{\mu}{\kappa} u_s = \nabla \tag{3}$$

$$\nabla u_s = 0 \tag{4}$$

where μ is the effective viscosity of the porous medium (Pa·s), u_s is the fluid velocity (m·s^{-1}), p is the fluid pressure (Pa) and κ is the permeability of the porous scaffold (m^2).

A flow rate of 3.3 μl/min was applied to the inlet, the boundary condition at the outlet was set at zero pressure, and the no slip boundary conditions were used along the walls of the model.

(a)

(b)
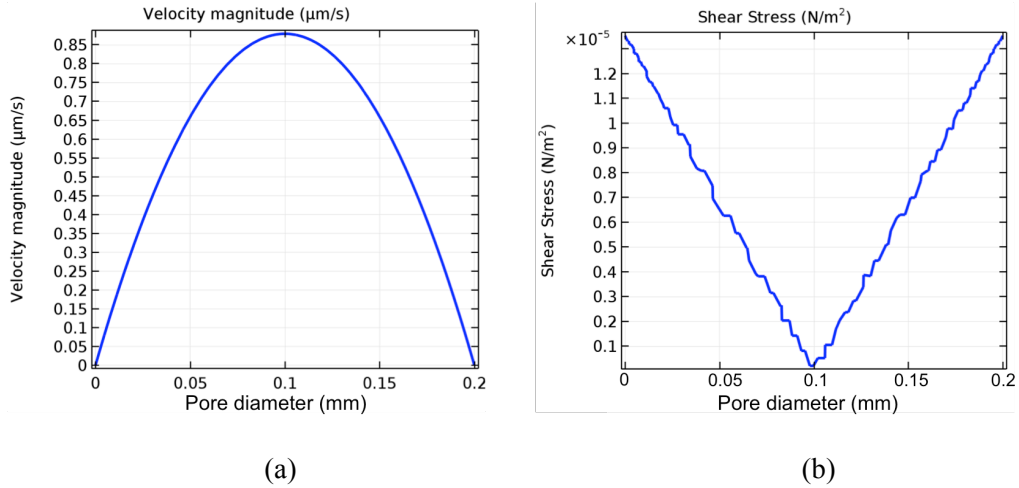
Supplementary Figure S8.

Velocity profile (a) and shear stress (b) profile inside of a single channel having a pore diameter of 200μm within the 3D porous scaffold. The model shows that with a pore diameter of 200μm the shear stress acting on the wall is $1.2 \cdot 10^{-5}$N·m^{-2}, which is beyond the shear stress limit that leads hepatocytes to death. To evaluate the magnitude of the shear stress acting on the walls of the porous channels within the 3D scaffold, an analysis at the micro-scale was assessed.

If we considered the scaffold as a cylindrical structure with interconnected channels with different pores diameters, the flow rate for a single channel is described by the Fanning equation:

$$Q_i = \frac{\pi D_i^4 \Delta P}{128 \mu L} \qquad (5)$$

where μ is the medium viscosity and L and D$_i$ are the channel length (that is the scaffold height), and the channel diameter respectively and ΔP is the total pressure drop. The total pressure drop was evaluated in the analysis at the macro-scale, and the mean pore diameter was evaluated experimentally and it was found to be 200μm [33]. The single channel was modeled with the equation (1) and (2), by using as input the flow rate calculated with the equation (5). For a channel having the diameter of 200μm, the shear stress acting on the walls, which correspond to the domain where the cells formed focal adhesions, is approximately $1.2 \cdot 10^{-5}$N·m^{-2}.
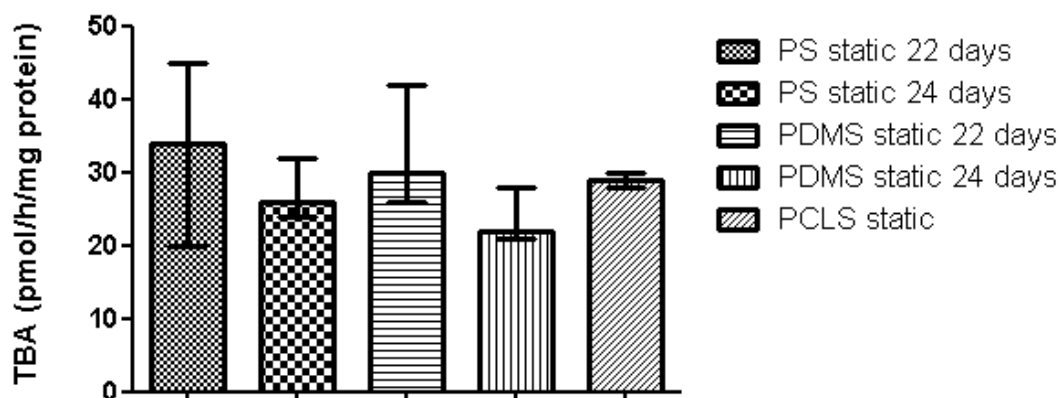
Supplementary Figure S9. Bile acid production by hiPSC-derived hepatocytes and human PCLS. Graph represents mean values ± SEM. Total bile acid (TBA) content was measured using the Total Bile Acid kit (Diazyme Laboratories, Poway, CA, USA) in medium after 24 h incubation (static cultures) or 24 h perfusion (perfused cells and slices). 1ml of medium was concentrated 10 times using the CentriVap Bench-top Vacuum Concentrator at 35°C (Labconco, Kansas City, MO, USA). TBA content was determined according to the manufacturer's protocol of the TBA kit with a few modifications. Conjugated cholic acid (50μM) was used as a calibrator. Measurement was performed at 37°C in a 96-well plate in the Synergy HT plate reader (BioTek, Winooski, VT, USA). The absorbance was read at 405nm at 5 and 30 min. The TBA production is expressed as median with interquartile range.
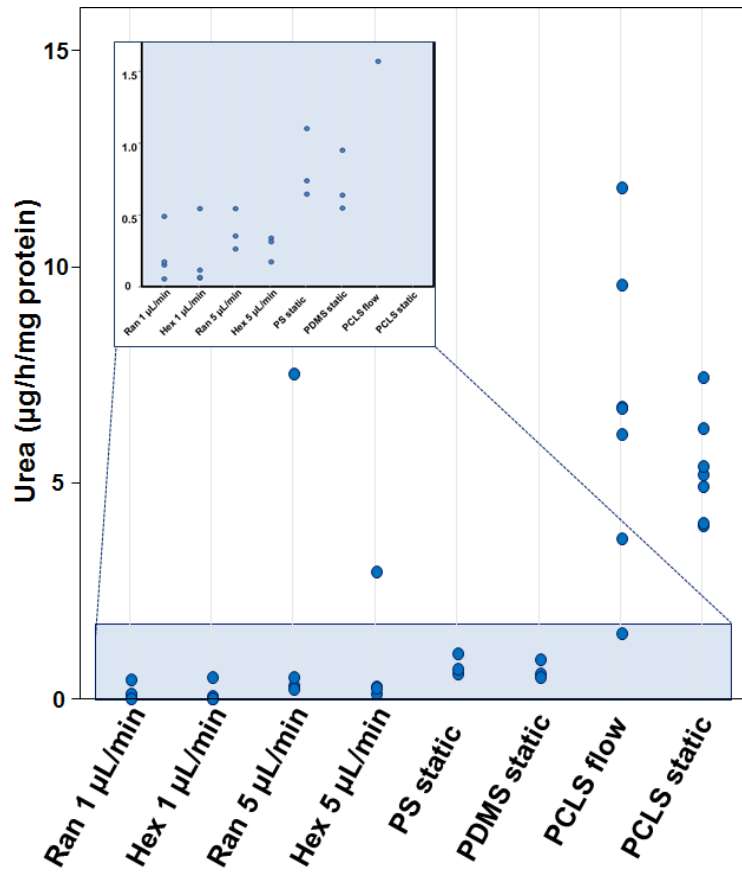
Supplementary Figure S10. Urea production. Urea concentrations in the medium were measured using the Urea Assay Kit (Abnova, Taiwan). Medium samples from differentiated cells and PCLS flow and static cultures were concentrated 10 times before measurement using the CentriVap Benchtop Vacuum Concentrator at 35°C. Urea content was determined according to the manufacturer's protocol of the Urea Assay kit with a few modifications. Accordingly, 25μL of samples were added to each well and incubated for 30 min at room temperature with a reagent mix. The absorbance was read at 430nm and urea levels calculated based on standard curve of urea standard provided with the kit and expressed as μg urea produced per h, per mg total protein. Data are expressed as individual values

CHAPTER 3

FABRICATION OF CELL LADEN SOFT HYDROGELS PERFORATED WITH A 3D

CHANNELS NETWORK INTERFACED TO A PERFUSION SYSTEM

Fabrication of cell laden soft hydrogels perforated with a 3D channels network interfaced to a perfusion system

Rodrigo Pimentel C.[1], Mette Hemmingsen[1], Anders Aspegren[2], Anders Wolff[1], Fridolin Okkels[1], Jenny Emnéus[1], and Martin Dufva[1]

[1] *Department of Micro- and Nanotechnology, Technical University of Denmark, Denmark*

[2] *Cellartis, Takara Bio Europe AB, Sweden*

Abstract

Vascularization is recognized to be the biggest challenge to the fabrication of tissues and finally, organs in vitro. Vascularization within hydrogels with mechanical properties in the range of soft tissues has not been achieved. Therefore, we developed a three-dimensional (3D) molding technique using 3D printed poly(vinyl alcohol) (PVA) to fabricate microchannel networks with two-dimensional (2D) and 3D architecture within large gelatin hydrogel constructs targeting the stiffness range of 1 - 10 kPa. A two-step gelation process was developed leading to well defined channels by sacrificial molding of PVA in gelatin. Perfusion of such soft construct is not trivial as the mechanical strength of these gels are very poor. A plasma treated PDMS case, "fluidic mold", was developed in which gelatin was cased around PVA sacrificial structures. The direct casting of gelatin in the fluidic mold ensured leakage free perfusion immediately after gelation. This was utilized to rapidly extract out the PVA sacrificial mold by perfusion. Stem cell derived hepatospheres were encapsulated into soft gelatin (3kPa) structures and perfused for seven days without any apparent signs of cell death indicating excellent biocompatibility and robustness of the complete system. The proposed method represents a powerful and simple way to engineer thick constructs with controlled mechanical properties and controlled vasculature that could pave the way towards a new range of relevant applications for tissue engineering.

Introduction

Vascularization is currently regarded as one of the main challenges that need to be solved to translate tissue engineering to clinical applications at a large scale [1–4]. When designing tissue engineer-constructs with relevant dimensions that are much larger than the diffusional limit for nutrients and oxygen, the absence of existing vasculature is still the missing key. Ideally, a cell must be located at a maximum distance of 200 μm from any vascular network to be metabolically active [5,6]. However, the presence of channel networks might be not sufficient to guarantee the necessary exchange of oxygen and nutrients that are needed in thick engineered constructs containing biologically relevant cell densities [7,8]. Therefore, it is important to create a strategy to induce perfusion through the channel network to guarantee the final success of the engineered construct [2].

Current vascularization methods relies either on cellular strategies or in the fabrication of a network of microchannels [8,9]. Cellular strategies involve the use of endothelial cells, often in combination of other cell types such as pericytes and stem cells, to induce the formation of stable capillaries embedded within constructs [10–15]. Cellular strategies, however, require time as being heavily dependent on complex biological mechanisms, and mostly remains restricted to relatively thin constructs [14,16]. By contrast, there has been an extensive use of different fabrication techniques to create organized vascular networks [17,18]. In particular, direct printing technology [19–25], 3D sacrificial molding technique [26–28] or a combination by both techniques [29–44] have gained a dominant role for the fabrication of vascularized constructs. So far, many reports have described vascularized constructs fabricated via several layer-by-layer techniques such as bioprinting [21,29], stereo lithography [41,44], and fused deposition modeling (FDM) [31]. Recently, direct printing of three different inks has been used with FDM to fabricate constructs with controlled architecture in a process denoted integrated tissue-organ printer [21]. The first two inks were composed by different cell-hydrogel mixture and were used for the patterning of cells. The third ink, Pluronic F127, was used as a sacrificial material for the 3D printing of a lattice of microchannels. To ensure mechanical stability to the final construct a thermoplastic biopolymer (poly(ε-caprolactone)) was printed at the same time with the other three inks. By contrast, stereolitography has been employed in combination with a sequential 3D molding approach to create sacrificial templates [44]. A photocrosslinked resin was used to 3D print the negative mold for the subsequent fab-

rication of the sacrificial templates. Then, the sacrificial templates were embedded in an agarose hydrogel for the formation of the vascular channels. Finally, FDM in combination with the 3D molding technique has been used to 3D print carbohydrate glass structures serving as the sacrificial template [31]. Then, a poly(ethylene glycol) based hydrogel with cells encapsulated was cast around the sacrificial template. The sacrificial template was dissolved and removed leaving behind an open microchannel network within the PEG hydrogel. Although all these approaches are innovative and promising, most of them rely on complicated and expensive modified machines [21] and require several fabrication steps [44]. The majority of the proposed engineered constructs relies on vascular structures composed by single microchannels or by square lattices [23,33–35], and this is due to the inability of the 3D printing technology to achieve a real 3D freedom that the technology has to offer without the presence of a support material [45]. By contrast, when a complex vascular network was achieved, the final construct did not have the expected cellular viability since the focus was not the ECMs employed. Furthermore, the freedom of tuning the construct stiffness has not been explored in detail [2–4,6,7,46–49]. From a mechanical point of view, the demonstrated methods resulted in constructs that where either very stiff or soft [2–4,6,7,46–49]. For the tissue constructs fabricated with direct bioprinting process, the hydrogels employed needed to work in a narrow viscosity window to provide suitable viscoelastic properties to be used as ink [21,24,25,29,30]. By contrast, in the 3D molding technique, the majority of employed hydrogels are photo-cross-linked, making it difficult to decrease the mechanical properties below 10 kPa [23,26,31]. Finally, it is still unclear how these constructs can be effectively perfused to guarantee the cells to stay metabolically active in thick and densely populated constructs.

In this paper, we describe a method for the creation of 3D constructs with engineered vascular networks and with stiffness in the range of soft tissues. Planar and non-planar PVA sacrificial structures with a well-defined and controlled architecture were 3D printed. Such structures were used to create embedded channel networks within a gelatin hydrogel crosslinked with microbial transglutaminase (TG) having stiffness in the range of 1-10 kPa. To demonstrate the flexibility of our fabricated constructs, a fluidic mold and a fluidic platform were developed to allows the fabricated engineer constructs to be actively perfused for long term periods. The fluidic platform was entirely 3D printed and integrated all components required for the direct perfusion of the constructs (e.g. peristaltic pumps along with electronics, reservoirs, etc.). Finally, hepatospheres were encapsulated within gelatin/TG hydrogel and kept alive by perfu-

sion for seven days proving that our platform could be beneficial for the design of more complex and more bio-inspired constructs for tissue engineering and regenerative medicine.

Materials and Methods

Characterization of the PVA dissolution in water

Water dissolvable poly(vinyl alcohol) (PVA, Makerbot Industries, Brooklyn, NY, USA) filament was cut in cylindrical shapes (figure S1A). Each cylindrical PVA filament part was weighted and its radius and thickness were measured (figure S1A). The cylindrical PVA part was submerged (time = 0) in 1L of distilled water in a beaker. The liquid was stirred at a maximum and constant speed to ensure the Nernst model validity, and therefore a sink condition. At defined time intervals, the cylindrical PVA was taken out of the solution, dried, weighted, and its radius and thickness were measured. The temperature of the solution was kept constant at 25 °C for the entire duration of the experiment.

Hydrogel preparation

Gelatin cross-linked with TG was used in this study. A total of 7.5% (w/v) gelatin (48723 Fluka) was mixed with serum-free cell culture medium (Cellartis Medium) and stirred at 60 °C until fully dissolved. The degree of cross-linking of the resultant gelatin/TG hydrogel was controlled by varying the amount of TG in respect to the mass of the gelatin. The TG (Activa-TI, Ajinomoto, Inc., activity of approximately 100 $U \cdot g^{-1}$ of TG according to the manufacturer) was dissolved in 15 mL of PBS (Sigma Aldrich) using the appropriate mass of TG to give concentrations of 2.5, 5, 10, and 20 Units of TG per g of gelatin. The final concentrations of the gelatin/TG hydrogel used were 5% (w/v) gelatin, with 2.5, 5, 10, and 20 Units of TG per g of gelatin.

Mechanical properties

A total of 1mL of the 5% (w/v) gelatin/TG pre-polymer solutions with varying concentrations of TG (2.5, 5, 10 and 20 Units of TG per g of gelatin) were poured in a cylindrical mold of 10 mm in diameter (n = 6). The cylindrical samples were incubated at 37°C for 24 hours and then, they were compressed to 10% of the initial length using 0.1% strain rate using a Solid Analyzer instrument (RSA II, Rheometrics, Inc.). The compressive elastic modulus of each

sample was evaluated within the first linear zone from the strain stress curve (i.e. within 2% strain).

Design and 3D Printing

All the sacrificial structures and molds used in this study were designed and converted into STL files using CAD software (computer aided design, Dassault Systemes SolidWorks Corporation, US). All STL files were processed by KISSlicer (www.kisslicer.com/) software and sliced into 100-µm-thick layers to generate G-code instructions for the 3D printer. G-code instruction sets were sent to the printer using Repetier-host (https://www.repetier.com), an open-source 3D printer host program. Then commercially available PVA and poly(lactice acid) (PLA) filaments (Makerbot Industries, Brooklyn, NY, USA) were printed using the Felix 3 (Felix Printers, IJsselstein, Netherlands) printer with a nozzle diameter of 250 µm.

3D Printing of planar and 3D sacrificial templates

All 2D sacrificial templates were printed using PVA as material. The printing settings were as follows: nozzle temperature 200 °C for the PVA, bed temperature 55 °C. The 3D sacrificial templates were printed using a dual material strategy where PVA and PLA were used as main and support material respectively. The 3D printing settings were as follows: nozzle temperature 190 °C for PLA and 200 °C for the PVA, bed temperature 55 °C.

Dissolution of support material in the 3D sacrificial structures

Chloroform was used as solvent to remove the PLA support from the PVA sacrificial template for the non-planar structures. The 3D printed structures were immersed in 200 mL of chloroform under continues stirring until all the solid PLA support was dissolved. After the total dissolution of the PLA, the 3D sacrificial structures were immersed in 20 mL of clean chloroform for a day to get rid of the residual PLA.

Fluidic mold fabrication

The fluidic mold was fabricated from a flexible clear polydimethylsiloxane (PDMS, Sylgard 184, Dow Corning Corporation) polymer by using a molding technique. The designed mold consisted on three main parts responsible to define the external surface of the fluidic mold, one part responsible to define the internal chamber (14 mm (L) x 11.5 mm (W) x 10 mm (H)),

and two hub-free stainless steel blunt needles (18G; Kimble Chase, Vineland, NJ) used to define the fluidic connections. The mold was fabricated by 3D printing the internal chamber in PVA and all the remaining parts in PLA. The 3D printing settings were as follows: nozzle temperature 190 °C for PLA and 195 °C for the PVA, bed temperature 55 °C. The mold 3D printed parts were assembled and secured together using screws. PDMS pre-polymer (10:1 w/w ratio of PDMS to curing agent) was casted in the assembled 3D printed mold. The mold was degassed in a vacuum chamber to ensure the removal of the entrapped bubbles. The mold with the polymer was placed in an oven overnight at 60°C to ensure the polymer to be completely cured. After curing, the mold was disassembled and the resultant PDMS fluidic mold was immersed into water to dissolve the PVA printed part responsible to define the internal chamber of the fluidic mold. The fluidic molds were treated with oxygen plasma (125 W, 13.5 MHz, 50 sccm, and 40 millitorr) to render their surface hydrophilic and sterilised by autoclaving.

Fluidic Platform: hardware

Figure 1(A) shows the schematic of the designed fluidic platform. The fluidic platform was fabricated from PLA polymer by using a 3D printer. The designed fluidic platform consisted on one modular platform that integrates an array for 3 fluidic molds, vial trays for storage of culture medium, a one 4-channel micro peristaltic pump (previously described in [50,51]), a stepper motor, and the electronics controlling the pumps. The whole platform, except for the array and the lid for the electronics, was 3D printed in a single part, and the 3D printing settings were as follows: nozzle temperature 190 °C for PLA, bed temperature 55 °C. The device is simple, compact, light and can be easily positioned in a sterile hood as well as inside the sterile incubator for long-term experiments. Two electronics boards are integrated in the fluidic platform. An arduino micro (Arduino, Italy) and an easydriver stepper motor driver (Brian Schmalz, Creative Commons Attribution 3.0 United States License) were used to control and to power supply the stepper motor respectively. Using the dedicated software (see below), the flow rate, and the direction of the flow rate can be set and controlled in the range of 1-120 μL·min^{-1}. The 3D CAD assembly designed using SolidWorks, as well as Gcodes generated for every part can be downloaded at https://3dprint.nih.gov.

Fluidic Platform: software

Figure 1(B) shows the dedicated software designed to control the peristaltic pumps integrated in the fluidic platform utilized in the present study. The fluidic platform control software (PumP Interface) was developed in Microsoft Visual Studio 2014. The libraries to control the hardware components were compiled with C# .NET, while the graphical user interface (GUI) was designed using windows forms application. In the case of the stepper motor low-level control, the microcontroller was programmed in the Arduino IDE environment. To enable easy installation, a single executable file was compiled including all the .NET libraries, and can be used standalone on any windows computer. The GUI helps the user to control the volumetric flow rate by: (i) enabling the stepper motor, (ii) setting the system in stand-by mode, (iii) setting the direction of pumping, and (iv) setting the desired volumetric flow rate.
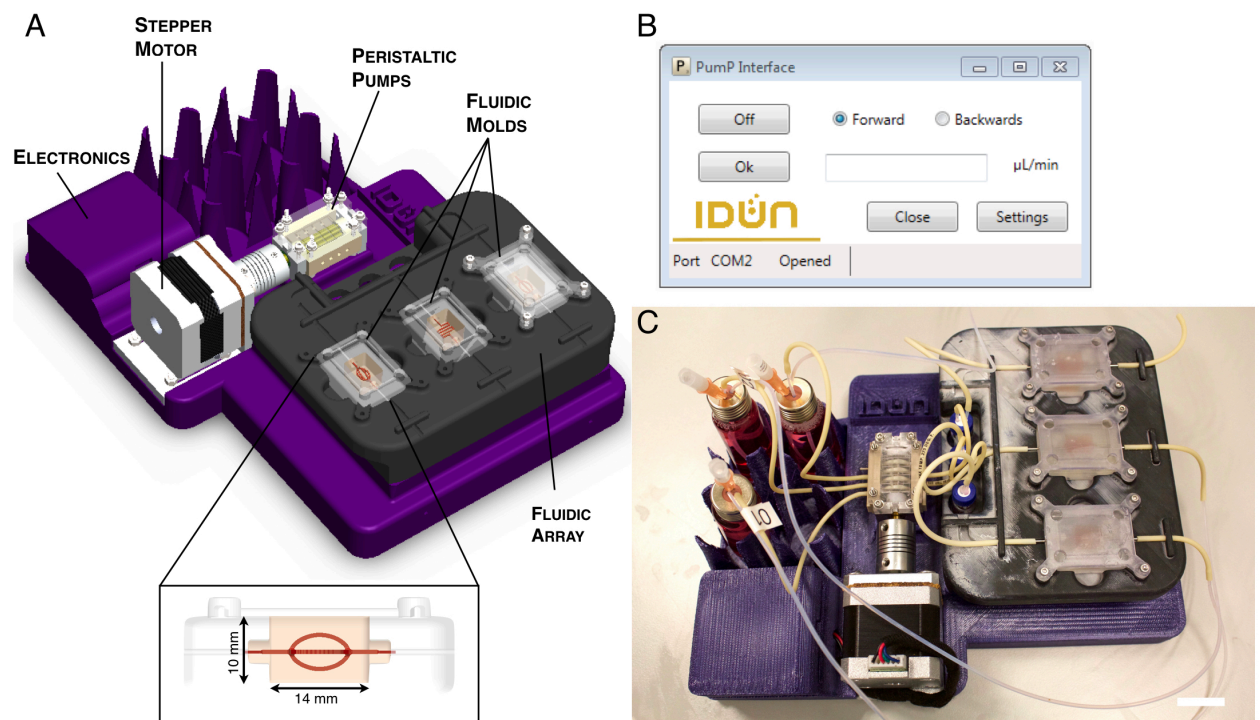
Figure 1. (A) Designed fluidic platform. (B) GUI used to control the peristaltic pumps. (C) Photograph of the assembled fluidic platform with the three fabricated tissue constructs. (Scale bars: 6 mm) printing branch. Lines of green indicate the dispensing paths of PLA whereas lines of blue indicate the dispensing paths of PVA. (Scale bars: 6 mm)

Encapsulation of hepatospheres and active perfusion of the 3D tissue constructs

The fluidic platform, glass vials, caps and polytetrafluoroethylene (PTFE) tubing (inner diameter of 0.8 mm) (BOLA 1818-10, Bohlender GmbH, Germany) were sterilized by autoclaving before assembling in a laminar flow bench. 0.5 M NaOH was flushed throughout the system

to ensure a sterile fluidic path. The system was subsequently flushed with sterile water and then with culture medium. The fluidic molds were treated with oxygen plasma (125 W, 13.5 MHz, 50 sccm, and 40 millitorr) to render their surface hydrophilic and sterilized by leaving them in ethanol overnight.

Gelatin 5% (w/v) was partly cross-linked with 5 Units of TG per g^{-1} of gelatin was prepared and incubated for 45 minutes at 37°C. A total of 0.5% (v/v) of chloroform was added to sterilize the solution. Then, the 3D sacrificial structure was inserted inside the fluidic molds. Subsequently, stem cell derived hepatospheres were mixed with 1.5 mL of the gelatin/TG hydrogel and then casted into the fluidic molds. After the casting, the samples were incubated at 4°C for 30 minutes to convert the liquid gelatin into a solid state. The construct was subsequently incubated for 1h at ambient temperature to ensure the chemical cross-linking of the gelatin ensuring mechanical stability at higher temperatures. The final dimensions of the tissue constructs were 14 mm (L) x 11.5 mm (W) x 10 mm (H) with a resultant volume of $\approx$ 1.5 cm^3. The fluidic molds were then placed in the fluidic platform and media was perfused through at $5\mu L \cdot min^{-1}$ for 30 minutes to ensure the total removal of the sacrificial template from the 3D constructs. After the total removal of the sacrificial structures from all the samples, the flow rate was increased to 10 $\mu L \cdot min^{-1}$. The entire system was incubated at 37 °C under 95% air 5% CO_2. The hepatospheres were cultured for 7 days. A fully assembled fluidic platform along with the vascularized tissue constructs is shown in figure 1(C). As a control, hepatospheres encapsulated in the same gelatin/TG hydrogel were cast around the sacrificial template in the fluidic mold and after sacrificial template removal, the part was submerged in a petri dish with fresh medium. The controls were then incubated at 37 °C under 95% air /5% CO2 for one week exchanging the media every second day.

Fluorescent staining

The cell viability of the engineered 3D tissue constructs was assessed using a LIVE/DEAD assay (Thermo Fisher Scientific). The constructs were removed from the fluidic mold, and sectioned along the cross-sectional direction. The constructs were removed from the mold, and sectioned along the cross-sectional direction. Since the gel was soft, it was impossible to get a clear cut, thus the surface was not entirely flat making it difficult to perform the microscopy analysis. The samples were then washed with Hank's balanced salt solution (HBSS) and incubated for 30 minutes with 1.5 mL of HBSS containing 5 µL of SYTO 10 and DEAD read.

Then, samples were washed again with HBSS and imaged on a Zeiss LSM confocal microscope.

Imaging and analysis

Confocal acquisitions were performed using a Zeiss LSM 700 module in the Axio Imager M2 upright microscope using an epiplan-neofluar 5X/0.13 HD, an epiplan-neofluar 10X/0.25 HD, an epiplan-neofluar 20X/0.5 HD. To eliminate any possible crosstalk between channels, images were collected with a sequential scan, using the following laser lines and mirror settings: 488(30%) 495-560nm; 555(30%) 605-700nm. Photographs and videos of tissue fabrication were acquired using a DSLR camera (Canon EOS, 5D Mark II; Canon). Fluorescent dyes were used to improve visualization of gelatin construct (Fluorescein). ImageJ was used to visualize composite images by combining fluorescent channels. The diameter of the channels was measured by ImageJ software using at least 4 images from different areas of 2 constructs for each condition.

Results and discussion

Fluidic mold design

The fluidic mold used for casting the hydrogel and subsequent perfusion was manufactured using a molding technique, where PDMS was cast in a 3D printed mold (figure 2(A)). The 3D printed mold consisted of three main parts responsible for defining the external surface of the fluidic chip and one part responsible for defining the internal chamber. The mold was designed to simplify insertion of the 3D printed template within the internal chamber and to simplify insertion of fluidic connections (figure 2(A)). Attention was given to the internal chamber (figure 2(B)-(C)). The internal chamber was inverse fabricated from a PVA printed mold. The mold responsible for defining the internal chamber was designed to have a volume of 1.5 cm^3 and to include protrusion in correspondence of the inlet and outlet respectively (figure 2(C)). The protrusions were responsible for defining the cavities within the PDMS mold (figure 2(A)). These cavities were required to avoid delamination in the internal channel between the hydrogel and the PDMS during the dissolution and removal of the PVA. Furthermore, the cavities helped to avoid undesired leaking from the constructs during the perfusion (data not shown). Due to the complexity of the inner chamber, the part defining the negative of the internal channel was 3D printed in PVA. The PVA material was needed since it

was not possible otherwise to de-mold the part defining the inner chamber from the fluidic mold without breaking the PDMS or to use multiple layers of PDMS. In this way, the PVA printed part enclosed in the fluidic mold was dissolved in water revealing the desired inner chamber in the fluidic mold (figure 2(D)).
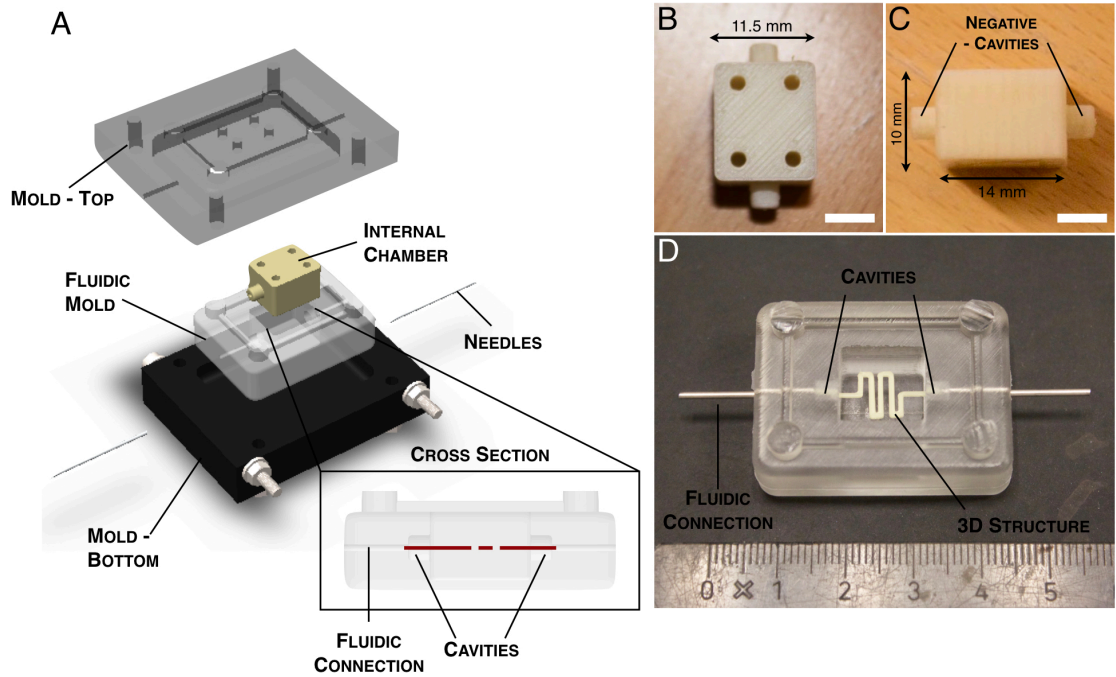
Figure 2. (A) Designed mold used to the fabrication of the fluidic mold. The mold consisted in three external parts responsible for defining the external surface of the fluidic mold while the internal chamber was designed and 3D printed in PVA to include the final cavities. (B-C) Photograph of the PVA printed mold used to the define the inner chamber of the fluidic mold. (Scale bars: 4 mm) (D) Photograph of the fabricated fluidic mold after the demold process and dissolution of the PVA printed part, which was responsible for defining the internal chamber.

3D printing of planar and non-planar sacrificial structures

One of the most employed method for the fabrication of micro- and milli-channels within hydrogels is the 3D sacrificial molding technique [29–44]. In this study, PVA was used as sacrificial material, and it was 3D printed in planar and non-planar structures to demonstrate the versatility of the method proposed. Figure 3(A)-(D) shows the designed CAD and the 3D printed template for a "ring" and "zig-zag" structure respectively. Both structures were planar and were designed to have width dimensions of 500 μm (W) x 500 μm (H). The final printed structures had width dimensions of 550 ± 50 μm (W) and x 500 μm layer thickness (H). To

demonstrate the simplicity of the method, planar and quasi 3D structures were printed with the same printing parameters of the previous one (figure S1(B)-(C)). Like the 3D printing of most materials, the resolution of the 3D printed structures was strictly dependent on machine settings that required optimization. In particular, PVA is a hygroscopic [52,53] material and has very close melting and degradation temperatures [54]. As consequence, it can be difficult to maintain stable PVA during the cycles of increase and decrease of temperature within the printing process [54,55]. This often leads to the failure of the printing process. When printing simple and regular geometries such as square lattices, cubic forms that doesn't require the presence of support structure it is easier to control the PVA because the temperature is constant during the fabrication process. However, when printing structures that can be freely designed into the 3D space and needs support structure underneath, the failure of the printing process is more pronounced because the 3D printer will need to switch material every layer, and the risk of oozing and clogging increases dramatically.

Since one of the key points of this study was to create freeform 3D structures, a 3D branch was designed and 3D printed (figure 3(E)-(F)). The 3D branch was printed using a dual printing strategy, where the primary structure was printed using PVA, and the support material was printed using PLA. The support structure was selectively removed with chloroform. Attention was given to the generation of the support structure. At first, Kisslicer was used to generate multiple support structures by tuning different parameters, such as the support density, support inflation, and distance between the support and the designed part (first two samples from the left, figure 3(G)). However, none of the support structures generated could achieve successful printing of the designed branch and to ensure the total removal of the PLA support material without disrupting the printed PVA structure (first sample from the left, figure S1(D)). Moreover, the very few 3D branch obtained after the successful dissolution of the PLA were characterized by poor quality (last sample from the left, figure S1(D)). Therefore, the support structure was designed directly on the 3D branch using the CAD tool (last two sample from the left, figure 3(G)). The support structure was designed with the aim of minimizing the amount of support material to be dissolved, but at the same time, use enough support material to give a mechanically stable support during the printing process. The new support structures covered the entire 3D branch maintaining however a distance of 100 μm from it to avoid any cross contamination of materials during the printing phase. However, none of the printed structures were capable of being dissolved without disrupting the PVA printed part

in the branch point (figure S1(E). Finally, a new version was designed. The main difference from the previous one was the almost absence of support material within the four channels of the branch but at the same time enough material to ensure mechanical stability during the printing phase (figure 3(H)). The new part was sliced with Kisslicer, using the same machine parameters used for the PVA part and 3D printed (figure 3(I)). The design and the Gcode parameters for the 3D branch, and all the other designed sacrificial templates can be downloaded from https://3dprint.nih.gov that can be printed on any two headed RepRap or MakerBot 3D printer. The resulting dimension of the 3D branch was ≈ 700μm for line width and layer thickness respectively (for a CAD design of 600μm) after the dissolution of the PLA support. The final resolution and quality of the 3D printed branch was a clear indication of how crucial was the design of the support structure to ensure mechanical stability of the PVA sacrificial template during the printing and PLA dissolution phase. Although there have been other strategies to design PVA sacrificial structures, going from simple square lattices [39,40], to quasi 3D structures [26,32], they still lack the versatility to be geometrically free in the 3D space which is enabled using the PLA support as described here. In contrast to other who rely on modified FDM printers [32] or modified materials [31], we achieve total geometric freedom of sacrificial molds using standard FDM printers as well as bio filaments.
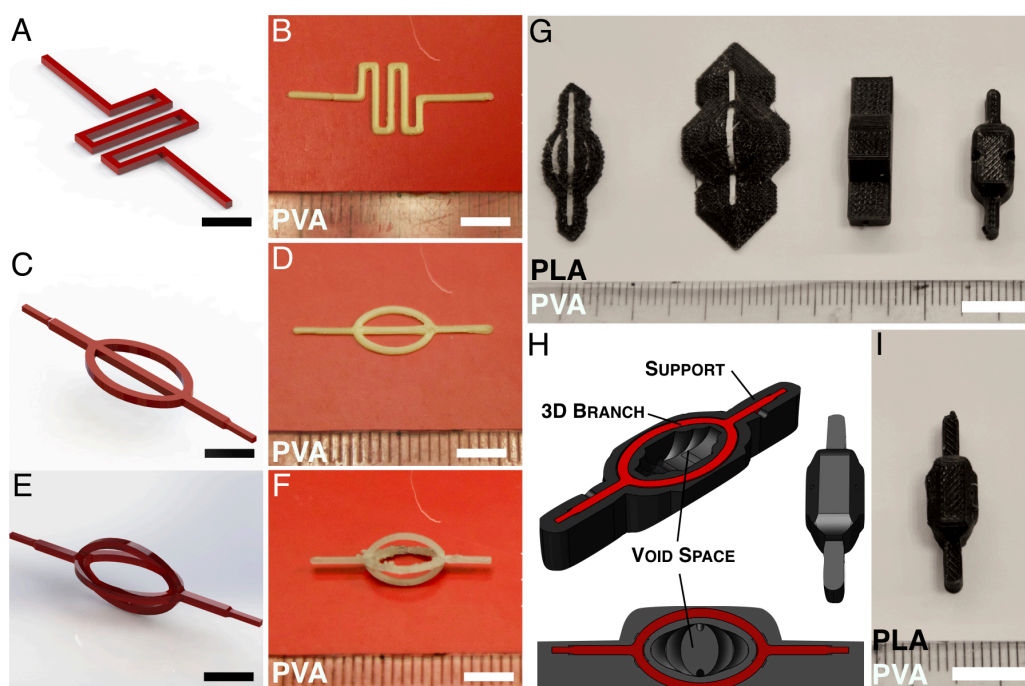

Figure 3. (A-B) Designed model and photograph of the 3D Printed "zig-zag" structure using PVA as sacrificial material. (Scale bars: 3 mm, 6 mm) (C-D) Designed model and photograph of the 3D Printed "ring"

structure using PVA as sacrificial material (Scale bars: 3 mm, 6 mm) (E-F) Designed model and photograph of the 3D Printed "branch" structure using PVA as sacrificial material and PLA as support material. (Scale bars: 3 mm, 6 mm) (G) Photograph of the 3D Printed branch with four curved arms using PVA as sacrificial template and different support structures generated. (Scale bar: 8 mm) (H) CAD model of the designed 3D Branch and the customized support structure. The quantity of support material in the center was the minimal quantity necessary to ensure the mechanical stability of the 3D Branch. (I) Photograph of the 3D Printed branch with four curved arms using PVA as sacrificial template and PLA as support material used. (Scale bar: 8 mm)

PVA dissolution in water and soft hydrogels

To estimate the kinetics of the dissolution in water of the PVA, the radius and length of the PVA filament were followed over time, and data was analyzed by the Noyes-Whitney equation (SI methods) [56,57]. Figure 4(A) shows the linear variation over time of the PVA filament mass in respect of a function f(t), which is the integral of a polynomial function F(t). F(t) represents a polynomial function used to fit the variation over time of the radius and length of the PVA filament dissolved in water (figure S1(F)). The calculated slope on figure 4(A) represents the rate constant of the dissolution, and it was found to be 1.9 $\mu m \cdot s^{-1}$. The rate of dissolution shows that in water the PVA filament would lose approximately 100 μm of PVA every minute. A fast rate of dissolution means that when in contact with water, a fabricated PVA structure will rapidly lose material leading towards the loss of mechanical and structural stability. However, if the bulk is changed from water to a hydrogel material the model used to evaluate the rate of dissolution of PVA in water is not valid anymore because the sink condition is lost and this would likely result in slower degradation. It is important to realize that cross linking of the hydrogel and the dissolution of the PVA needs to be timed so the hydrogel is formed before the PVA is completely dissolved. Ideally the PVA will essentially appear to be as defined after the dissolution as the initial 3D printed structures.

The dissolution of the PVA and hydrogel formation was studied by varying the concentration of gelatin, the added cross linker TG and the temperature (figure 4(B)-(C)). The PVA structure was not at all defined after 25 minutes in PBS leaving the PBS as a milky dispersion. Considering the rapid dissolution of PVA (figure 4(A)), this was expected but also emphasized that the crosslinking of hydrogels need to happen fast. PVA structures in 7.5% (w/v) gelatin at ambient temperature resulted in a well-defined PVA essentially confined to the space of the initial PVA structure (Figure 4B). By contrast, a PVA structure in 5% (w/v) gelatin resulted no such confinement. The difference between was that PBS and 5% (w/v) gelatin at ambient temperature was not a gel while 7.5% (w/v) gelatin was (Supplementary figure

S1(G)). To chemically crosslink the gelatin, various additions of TG were investigated. The results showed that increasing the TG concentration and thus the cross linking of 5% (w/v) gelatin gave more confined PVA after 25 min incubation at ambient temperature (figure 4(C)). Despite this, PVA was not as confined in 5% (w/v) gelatin with highest tested amount of TG as in 7.5% (w/v) gelatin indicating that the kinetics of chemical cross linking is still too slow for the lower percentage gels. Crosslinking of hydrogels was investigated by tilting the mold 90 degrees and observed if the gel was intact (S1(H)). All concentration of TG tested could crosslink 5% (w/v) gelatin in 25 min at ambient temperature. Since gelatin can be phys-ically crosslinked via thermal cooling [58,59], 5% (w/v) gelatin hydrogel crosslinked with various concentration of TG were used to encapsulate a PVA structure at 4 °C for 25 minutes. The PVA structures were better confined but not compared to 7.5% (w/v) gelatin at ambient temperature (Figure 5(D)). To increase the rate of gelation, gelatin was partly crosslinked before casting. Partly crosslinking was evident by an increase in viscosity. The partly cross-linked 5% (w/v) gelatin/TG solution was casted around PVA and cooled to 4 °C to rapidly induce thermal gelation by the reduced temperature. The TG could then create chemical crosslinks of the gelatin while still being in a gel state by the low temperature. This resulted in PVA being well contained in the gelatin during the dissolution phase (see for instance figure 5(A)) resulting in well-defined channels (figure 5(B)) and this method was subsequently used throughout the study. It was possible to make well defined structures using 2.5 Units of TG·g^{-1} of gelatin using this method. The partial cross linking was dependent on the concentration of TG for a given concentration of gelatin (data not shown). As varying the TG concentration resulted in hydrogels with varying stiffness (figure 4(E)), the time for partly crosslinking must be considered in each case. Here we use 2.5 or 5 Units of TG·g^{-1} gelatin and for that we incu-bate 3.5h and 1h, respectively, at 37 °C before casting. Higher concentration such as 50 U TG·g^{-1} of gelatin requires only a 10-minute incubation before casting. To our knowledge, partly crosslinking of gelatin before casting to improved PVA sacrificial molding has not been reported in the literature. Partly chemical crosslinking and the physical gelation enabled us using 5% (w/v) gelatin. Such low gelatin concentration has not been possible to use in PVA sacrificial molding before.
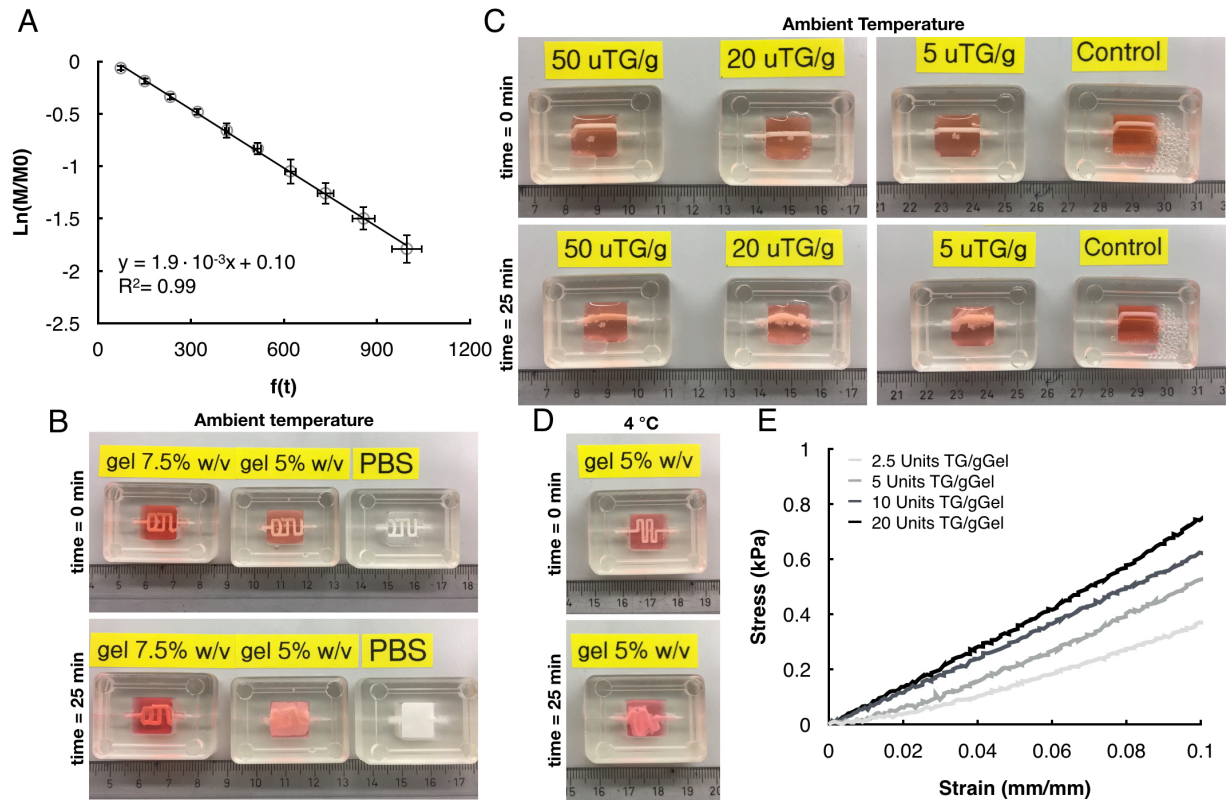
Figure 4. (A) Linear variation over time of the PVA mass in respect of a function f(t), which is the integral of a polynomial function F(t). F(t) represents a polynomial function used to fit the variation over time of the radius and length of the PVA filament dissolved in water (SI methods). (B) PVA dissolution of a molded structure within a 7.5% (w/v) gelatin, 5% (w/v) gelatin and PBS at ambient temperature right after the casting and after 25 minutes. (C) PVA dissolution of a molded structure within a 5% (w/v) gelatin hydrogel chemically crosslinked with 50, 20, and 5 Units of TG per g of gelatin, and within a 7.5 % (w/v) gelatin (control) at ambient temperature immediately after the casting and after 25 minutes. (D) PVA dissolution of a molded structure within a 5% (w/v) gelatin at 4 °C temperature right after the casting and after 25 minutes. (E) Stress and strain response of gelatin 5% (w/v) cross-linked with different degrees of TG under compressive loading.

Fabrication of vascular engineered constructs

The method to structure soft gels was tested on planar and non-planar PVA structures inserted into the fluidic mold (figure 5(A)-(C)). The sacrificial template was dissolved and removed from all the construct leaving a well-defined and open channel networks (figure 5(D)-(F)). It was possible to create engineered constructs with planar channel networks (figure S1(J)-(K)), with 3D lattice channel networks (figure S1(L)-(M)), and with 3D channel networks. Moreover, the creation of different channel networks was obtained either for hydrogels with low and high compressive modulus (e.g. 2 kPa, 6.5 kPa). The final vascular construct had dimensions of 14 mm (L) x 11.5 mm (W) x 10 mm (H) with a resultant volume of ≈ 1.5 cm^3, and although the tissue construct was extremely soft, the channels didn't collapse (figure 5(G)). The

final diameter of the channels within the construct was 1 mm for 2D constructs (figure 5(I)) while 3D structure had a final diameter of 1.3 mm (figure 5(I)). The structural stability of the fabricated constructs along with its different vascular networks was tested by perfusing them with 100 $\mu L \cdot min^{-1}$ for 24 hours at 37 °C. It was found that the construct along with its built-in channel network were mechanically stable without any structural deformation in response to the increased volumetric flow rate or increase in temperature. Crucial to the final morphology of the embedded channel networks within the construct was the structural stability of the PVA structures. It was found that the planar printed PVA structures with dimensions smaller than 500 μm (W) x 500 μm (H) were unable to maintain their mechanical stability when in contact with the hydrogels used in this study. By contrast, for the non-planar, the limit was higher, and it was found to be 700 μm. This limitation is more important when dealing with non-planar structures where their structural stability is crucial to the creation of complex perfusable networks. Moreover, when increasing the diameter of the printed PVA structures, the quantity of the material to be dissolved and removed increased significantly. This lead likely to an increase in the intra pressure within the hydrogel and the result was an increase of the final diameter of the vascular channel. To control the internal overpressure generated during the PVA dissolution inside the channels embedded within the construct the dissolved PVA was continuously extracted. The extraction of the dissolved PVA from the embedded channels was obtained by perfusing the fabricated constructs with a volumetric flow rate of 5 $\mu L \cdot min^{-1}$ for 30 minutes (figure 5(H)). The flow rate was sufficient to slowly dissolve the PVA structures and to ensure a continuous extraction of the dissolved PVA from the channel networks without damaging extensively the surrounding ECM (Supplementary Movie S1). The interface between the fluidic mold fabricated in PDMS and the gelatin hydrogel is critical for the active perfusion of the constructs. At first, poly(methyl methacrylate) (PMMA) was used as the material for the fabrication of the fluidic mold. However, during the dissolution of the PVA and the perfusion of cell culture medium, the hydrogel was fully delaminated from the PMMA mold (Supplementary Movie S2). PLA was subsequently chosen as the main material for the fabrication of the fluidic mold. Despite this, the delamination was still apparent during the dissolution of the PVA leading again to the leaking (Supplementary Movie S3). Considering that both PLA and PMMA are highly hydrophobic materials [60,61] and that gelatin is mainly water-based, the leaking was an indication that the surface of the molds needed to be functionalized. Therefore, both PMMA and PLA molds were plasma treated thus

making their surface hydrophilic. The plasma treatment of the molds fabricated in PMMA resulted in gelatin gels adherent to PMMA during the dissolution of the PVA and perfusion of constructs without any visible leaking (Supplementary Movie S4). By contrast, the plasma treatment did not work for the fluidic mold fabricated in PLA (data not shown). Although PMMA material was a viable candidate for the fabrication of the fluidic molds, the manufacturing process required for manufacture the designed fluidic molds were complicated and labor consuming. Instead, the fluidic mold was fabricated in PDMS using a molding technique where the inner chamber contained features that suppress leakage (as previously described in figure 2). Plasma treated PDMS was hydrophilic [62] resulted in a fluidic mold to which gelatin bound making the construct completely leak proof for long term perfusion experiments (Supplementary Movie S5).
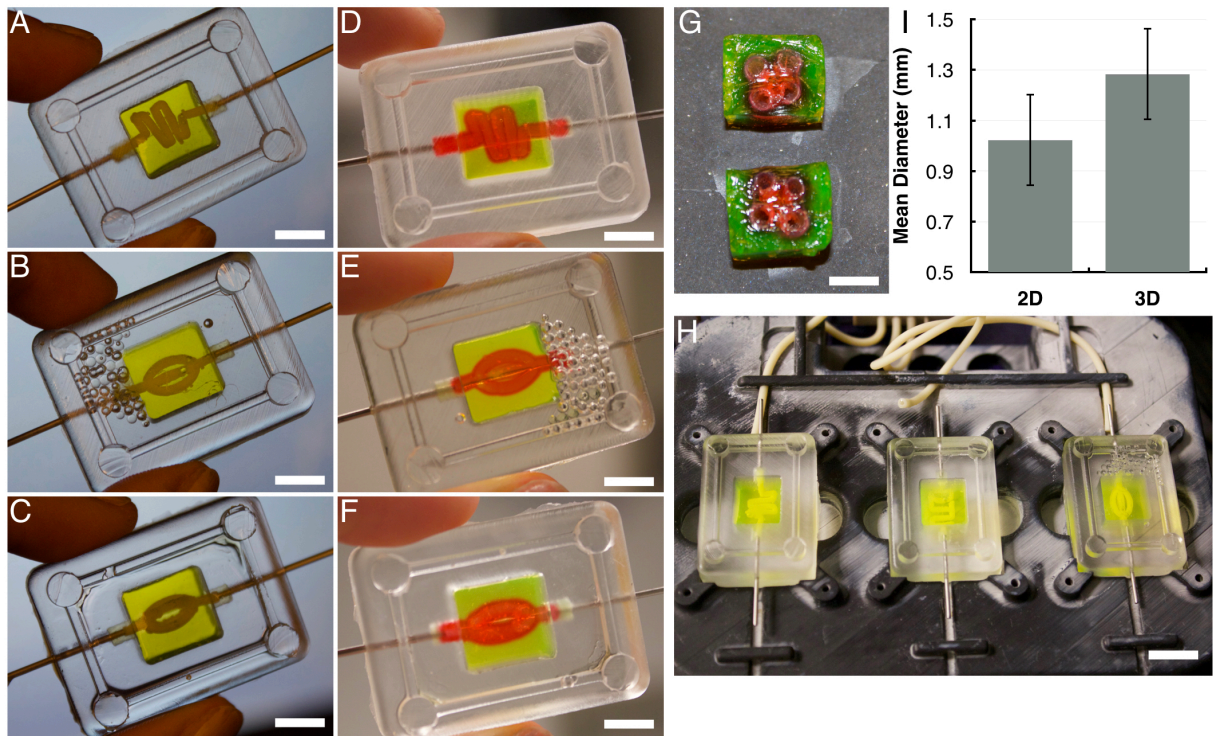
Figure 5. (A-C) Photograph of the planar and non-planar 3D printed sacrificial templates embedded in a gelatin hydrogel construct before the dissolution and removal of PVA. (Scale bars: 9 mm) (D-F) Photograph of the resulting vascularized 3D construct with different networks. (Scale bars: 8 cm) (G) Photograph of the cross section of the vascularized 3D construct showing the volumetric distribution and structural stability of the channels. (Scale bar: 6 mm) (H) Photograph of fluidic platform and the three engineered constructs allocated for the smart dissolution/removal of the PVA under fluid flow. (Scale bar: 12 mm) (I) Quantification of the diameter of the embedded channels for the engineered constructs actively perfused comparing planar and non-planar networks.

Encapsulation of hepatospheres and active perfusion in soft constructs

To demonstrate the ability of our platform to induce active perfusion throughout the engineered construct with embedded channel networks, hepatospheres were encapsulated in 1.5 mL of a gelatin/TG solution, with a stiffness of 3.3 kPa (stiffness of a liver [63–65]). To that end, the hepatospheres were mixed with gelatin/TG solution that was previously incubated for 1h, and cast in the fluidic mold (see material and methods for details), around the "zig-zag" sacrificial template. The PVA template was removed and the constructs were perfused with a volumetric flow rate of $10\mu L \cdot min^{-1}$ for 7 days (figure 6(A)-(B)). Fluorescence micrographs of the constructs sagittal plane were taken on multiple time points (days 1, 7) (figure 6(C)-(D)) to investigate the cellular viability, the effect of dissolution and removal of PVA, and the effect of the perfusion over time. Confocal microscopy images of live/dead stained hepatospheres were taken at the inlet and at the center of the constructs (figure 6(D)-day 1, inlet-center). The hepatospheres had similar viability after 7 days perfusion as after one day perfusion. Furthermore, the hepatospheres maintained similar morphology during the seven days of perfusion (figure 6(E)-(H)) thus indicating that the system and processes used to encapsulate the hepatospheres and structure the gel is biocompatible. The hepatospheres were homogeneously distributed in the gel. It is likely that the partial cross linking, which resulted in a gel with high viscosity, suppressed sedimentation of the relatively heavy hepatospheres during the casting and crosslinking process. In principle, this method could be translated for the encapsulation of a single or a multiple cell population into the same hydrogel creating a more complex construct. This together with the ability of engineer several perfusable networks suggests the possibility for the engineering of complex and thick tissue constructs with controlled micro- and milli- environment.
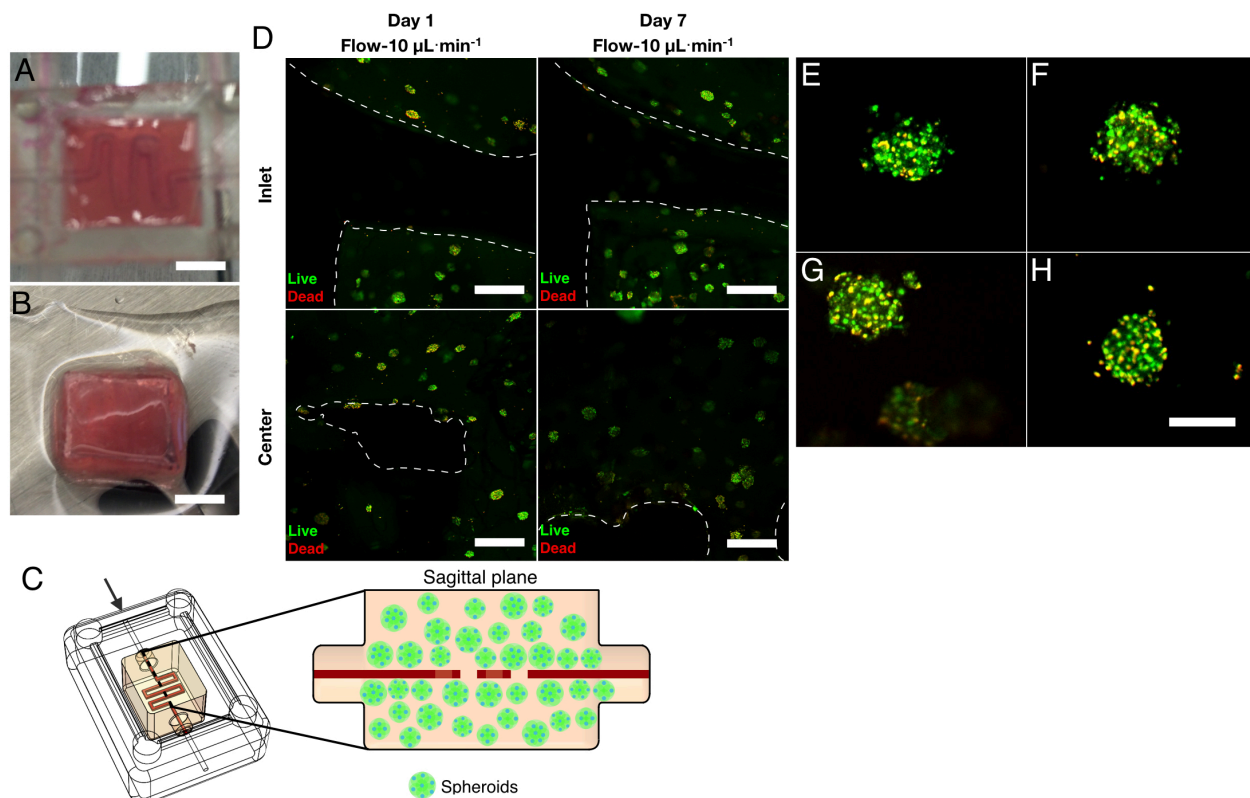
Figure 6. (A-B) Photograph of vascularized 3D tissue construct with encapsulated hepatospheres after 7 days of active perfusion using a flow rate of 10 µL min^{-1} (A) inside the fluidic mold (Scale bars: 2mm), and (B) removed from the fluidic mold. (Scale bar: 2mm) (C) Schematic of the cross section through the sagittal plane of the 3D tissue construct on depicting the distribution of hepatospheres in respect to the channel networks. The arrow indicates the inlet of the active perfusion. (D) Live/dead confocal microscopy through the cross section of the sagittal plane in the constructs with embedded channels in correspondece of the inlet of the perfusion and the center of the construct. The hepatospheres were encapsulated in a hydrogel with stiffness of 3 kPa and perfused for 7 days. The stripped lines represents the embedded channel networks within the constructs. (Scale bar: 500 µm) (E-H) Live/dead confocal microscopy of encapsulated hepatospheres after 7 days of active perfusion showing the morphology within the tissue constructs. (Scale bar: 50 µm)

Conclusions

Here we show a method to fabricate thick, soft, cell laden hydrogels perforated with fluidic channel. We also demonstrate a method to interface such constructs to a fluidic system for long term perfusion. The approach to achieve well defined channels in soft gelatin gels using PVA sacrificial layer depended on a partial crosslinking of gelatin by TG before casting and a physical gelation immediately after casting. Leak free perfusion of such hydrogels depended on the design of the case ("fluidic mold"), plasma treatment of the case and molding of gelatin directly in the case. The case material was PDMS which could be structured by sacrificial

molding which was necessary to introduce features suppressing leakage. The encapsulated hepatospheres were homogeneously distributed with gelatin/TG having stiffness of 3kPa. The fabricated construct with the encapsulated hepatospheres was perfused for 7 days indicating that all steps were biocompatible. The proposed method coupled with the presented fluidic platform would allow the fabrication of engineered constructs able to recapitulate the complex 3D micro- and milli-environment and with perfusable vasculature, which could enable advances in designing tissue engineered constructs with translational potential and for the modeling of tumors.

Acknowledgements

References

[1] Bae H, Puranik A S, Gauvin R, Edalat F, Carrillo-Conde B, Peppas N A and Khademhosseini A 2012 Building Vascular Networks *Sci. Transl. Med.* **4** 160ps23-160ps23

[2] Paulsen S J and Miller J S 2015 Tissue vascularization through 3D printing: Will technology bring us flow? *Dev. Dyn.* **244** 629–40

[3] Novosel E C, Kleinhans C and Kluger P J 2011 Vascularization is the key challenge in tissue engineering. *Adv. Drug Deliv. Rev.* **63** 300–11

[4] Levenberg S, Rouwkema J, Macdonald M, Garfein E S, Kohane D S, Darland D C, Marini R, Blitterswijk C A van, Mulligan R C, D'Amore P A and Langer R 2005 Engineering vascularized skeletal muscle tissue *Nat Biotechnol* **23** 879–84

[5] Griffith L G and Swartz M a 2006 Capturing complex 3D tissue physiology in vitro. *Nat. Rev. Mol. Cell Biol.* **7** 211–24

[6] Jain R K, Au P, Tam J, Duda D G and Fukumura D 2005 Engineering vascularized tissue. *Nat. Biotechnol.* **23** 821–3

[7] Pashuck E T and Stevens M 2016 From clinical imaging to implantation of 3D printed tissues *Nat. Biotechnol.* **34** 295–6

[8] Lovett M, Lee K, Edwards A and Kaplan D L 2009 Vascularization Strategies for Tissue Engineering *Tissue Eng. Part B Rev.* **15** 353–70

[9] Annabi N, Tamayol A, Uquillas J A, Akbari M, Bertassoni L E, Cha C, Camci-Unal G, Dokmeci M R, Peppas N A and Khademhosseini A 2014 25th anniversary article: Rational design and applications of hydrogels in regenerative medicine *Adv. Mater.* **26** 85–124

[10] Nikkhah M, Eshak N, Zorlutuna P, Annabi N, Castello M, Kim K, Dolatshahi-Pirouz A, Edalat F, Bae H, Yang Y and Khademhosseini A 2012 Directed endothelial cell morphogenesis in micropatterned gelatin methacrylate hydrogels *Biomaterials* **33** 9009–18

[11] Chen Y C, Lin R Z, Qi H, Yang Y, Bae H, Melero-Martin J M and Khademhosseini A 2012 Functional human vascular network generated in photocrosslinkable gelatin methacrylate hydrogels *Adv. Funct. Mater.* **22** 2027–39

[12]   Leslie-Barbick J E, Saik J E, Gould D J, Dickinson M E and West J L 2011 The promotion of microvasculature formation in poly(ethylene glycol) diacrylate hydrogels by an immobilized VEGF-mimetic peptide *Biomaterials* **32** 5782–9

[13]   Elbjeirami W M and West J L 2006 Angiogenesis-like Activity of Endothelial Cells Co-cultured with VEGF-producing Smooth Muscle Cells *Tissue Eng.* **12** 60421084845001

[14]   Chiu L L Y, Montgomery M, Liang Y, Liu H and Radisic M 2012 Perfusable branching microvessel bed for vascularization of engineered tissues. *Proc. Natl. Acad. Sci. U. S. A.* **109** E3414-23

[15]   Peters M C, Polverini P J and Mooney D J 2002 Engineering vascular networks in porous polymer matrices *J. Biomed. Mater. Res.* **60** 668–78

[16]   Cuchiara M P, Gould D J, McHale M K, Dickinson M E and West J L 2012 Integration of self-assembled microvascular networks with microfabricated PEG-based hydrogels *Adv. Funct. Mater.* **22** 4511–8

[17]   Bajaj P, Schweller R M, Khademhosseini A, West J L and Bashir R 2014 3D Biofabrication Strategies for Tissue Engineering and Regenerative Medicine. *Annu. Rev. Biomed. Eng.* **16** 247–76

[18]   Mandrycky C, Wang Z, Kim K and Kim D H 2016 3D bioprinting for engineering complex tissues *Biotechnol. Adv.* **34** 422–34

[19]   Homan K A, Kolesky D B, Skylar-Scott M A, Herrmann J, Obuobi H, Moisan A and Lewis J A 2016 Bioprinting of 3D Convoluted Renal Proximal Tubules on Perfusable Chips *Sci. Rep.* **6** 34845

[20]   Murphy S V and Atala A 2014 3D bioprinting of tissues and organs. *Nat. Biotechnol.* **32** 773–85

[21]   Kang H-W, Lee S J, Ko I K, Kengla C, Yoo J J and Atala A 2016 A 3D bioprinting system to produce human-scale tissue constructs with structural integrity *Nat. Biotechnol.* **34** 312–9

[22]   Jang J, Park H J, Kim S W, Kim H, Park J Y, Na S J, Kim H J, Park M N, Choi S H, Park S H, Kim S W, Kwon S M, Kim P J and Cho D W 2017 3D printed complex tissue construct using stem cell-laden decellularized extracellular matrix bioinks for cardiac repair *Biomaterials* **112** 264–74

[23]   Bertassoni L E, Cecconi M, Manoharan V, Nikkhah M, Hjortnaes J, Cristino A L, Barabaschi G, Demarchi D, Dokmeci M R, Yang Y and Khademhosseini A 2014 Hydrogel bioprinted microchannel networks for vascularization of tissue engineering constructs *Lab Chip* **14** 2202–11

[24]   Colosi C, Shin S R, Manoharan V, Massa S, Costantini M, Barbetta A, Dokmeci M R, Dentini M and Khademhosseini A 2016 Microfluidic Bioprinting of Heterogeneous 3D Tissue Constructs Using Low-Viscosity Bioink *Adv. Mater.* **28**677–684a

[25]   Jia W, Gungor-Ozkerim P S, Zhang Y S, Yue K, Zhu K, Liu W, Pi Q, Byambaa B, Dokmeci M R, Shin S R and Khademhosseini A 2016 Direct 3D bioprinting of perfusable vascular constructs using a blend bioink *Biomaterials* **106** 58–68

[26]   Tocchio A, Tamplenizza M, Martello F, Gerges I, Rossi E, Argentiere S, Rodighiero S, Zhao W, Milani P and Lenardi C 2015 Versatile fabrication of vascularizable scaffolds for large tissue engineering in bioreactor *Biomaterials* **45** 124–31

[27]   Wang X-Y, Jin Z-H, Gan B-W, Lv S-W, Xie M and Huang W-H 2014 Engineering interconnected 3D vascular networks in hydrogels using molded sodium alginate lattice as the sacrificial template. *Lab Chip*

[28]   Lee J B, Wang X, Faley S, Baer B, Balikov D A, Sung H J and Bellan L M 2016 Development of 3D Microvascular Networks Within Gelatin Hydrogels Using Thermoresponsive Sacrificial Microfibers *Adv. Healthc. Mater.* **5** 781–5

[29]   Kolesky D B, Homan K A, Skylar-Scott M A and Lewis J A 2016 Three-dimensional bioprinting of thick vascularized tissues. *Proc. Natl. Acad. Sci. U. S. A.* **113** 3179–84

[30]   Zhang Y S, Arneri A, Bersini S, Shin S R, Zhu K, Goli-Malekabadi Z, Aleman J, Colosi C, Busignani F, Dell'Erba V, Bishop C, Shupe T, Demarchi D, Moretti M, Rasponi M, Dokmeci M R, Atala A and Khademhosseini A 2016 Bioprinting 3D microfibrous scaffolds for engineering endothelialized myocardium and heart-on-a-chip *Biomaterials* **110** 45–59

[31]   Miller J S, Stevens K R, Yang M T, Baker B M, Nguyen D-H T, Cohen D M, Toro E, Chen A a, Galie P a, Yu X, Chaturvedi R, Bhatia S N and Chen C S 2012 Rapid casting of patterned vascular networks for perfusable engineered three-dimensional tissues. *Nat. Mater.* **11** 768–74

[32]   Li S, Liu Y-Y, Liu L-J and Hu Q-X 2016 A Versatile Method for Fabricating Tissue Engineering Scaffolds with a Three-Dimensional Channel for Prevasculature Networks. *ACS Appl. Mater. Interfaces* **8** 25096–103

[33]   Kolesky D B, Truby R L, Gladman a S, Busbee T a, Homan K a and Lewis J a 2014 3D Bioprinting of Vascularized, Heterogeneous Cell-Laden Tissue Constructs. *Adv. Mater.* 1–7

[34]   Lee V K, Kim D Y, Ngo H, Lee Y, Seo L, Yoo S S, Vincent P A and Dai G 2014 Creating perfused functional vascular channels using 3D bio-printing technology *Biomaterials* **35** 8092–102

[35]   Lee V K, Lanzi A M, Ngo H, Yoo S S, Vincent P A and Dai G 2014 Generation of multi-scale vascular network system within 3D hydrogel using 3D bio-printing technology *Cell. Mol. Bioeng.* **7** 460–72

[36]   Yeong W-Y, Chua C-K, Leong K-F, Chandrasekaran M and Lee M-W 2006 Indirect fabrication of collagen scaffold based on inkjet printing technique *Rapid Prototyp. J.* **12** 229–37

[37]   He J, Li D, Liu Y, Gong H and Lu B 2008 Indirect fabrication of microstructured chitosan-gelatin scaffolds using rapid prototyping *Virtual Phys. Prototyp.* **3** 159–66

[38]   Tan J Y, Chua C K and Leong K F 2010 Indirect fabrication of gelatin scaffolds using rapid prototyping technology *Virtual Phys. Prototyp.* **5** 45–53

[39]   Mohanty S, Larsen L B, Trifol J, Szabo P, Burri H V R, Canali C, Dufva M, Emnéus J and Wolff A 2015 Fabrication of scalable and structured tissue engineering scaffolds using water dissolvable sacrificial 3D printed moulds *Mater. Sci. Eng. C* **55** 569–78

[40]   Mohanty S, Kuldeep K, Heiskanen A, Trifol Guzman J, Szabo P, Dufva M, Emnéus J and Wolff A 2016 Fabrication of scalable tissue engineering scaffolds with dual-pore microarchitecture by combining 3D printing and particle leaching *Mater. Sci. Eng. C Mater. Biol. Appl.* **61** 180–9

[41]   Kang T Y, Hong J M, Jung J W, Kang H W and Cho D W 2016 Construction of large-volume tissue mimics with 3D functional vascular networks *PLoS One* **11** 1–16

[42]   Singh S P, Schwartz M P, Lee J Y, Fairbanks B D and Anseth K S 2014 A peptide functionalized poly(ethylene glycol) (PEG) hydrogel for investigating the influence of biochemical and biophysical matrix properties on tumor cell migration *Biomater. Sci.* **2** 1024–34

[43]   Justin A W, Brooks R A and Markaki A E 2016 Multi-casting approach for vascular networks in

cellularized hydrogels *J. R. Soc. Interface* **13** 20160768

[44]   Chan H N, Tian Q, Shu Y and Wu H 2015 Replicating 3D printed structures into hydrogels *Mater. Horizons* **3** 132–4

[45]   Hinton T J, Jallerat Q, Palchesko R N, Park J H, Grodzicki M S, Shue H, Ramadan M H, Hudson A R and Feinberg A W 2015 Three-dimensional printing of complex biological structures by freeform reversible embedding of suspended hydrogels *Sci. Adv.* **1** 1–10

[46]   Ko H C H, Milthorpe B K and McFarland C D 2007 Engineering thick tissues--the vascularisation problem. *Eur. Cell. Mater.* **14** 1-18-9

[47]   Rouwkema J and Khademhosseini A 2016 Vascularization and Angiogenesis in Tissue Engineering: Beyond Creating Static Networks *Trends Biotechnol.* **34** 733–45

[48]   Schepers A, Li C, Chhabra A, Seney B T and Bhatia S 2016 Engineering a perfusable 3D human liver platform from iPS cells. *Lab Chip* **16** 2644–53

[49]   Ling Y, Rubin J, Deng Y, Huang C, Demirci U, Karp J M and Khademhosseini A 2007 A cell-laden microfluidic hydrogel. *Lab Chip* **7** 756–62

[50]   Skafte-Pedersen P, Sabourin D, Dufva M and Snakenborg D 2009 Multi-channel peristaltic pump for microfluidic applications featuring monolithic PDMS inlay. *Lab Chip* **9** 3003–6

[51]   Nunes P S, Kjaerulff S, Dufva M and Mogensen K B 2015 Real-time direct cell concentration and viability determination using a fully automated microfluidic platform for standalone process monitoring *Analyst* **140** 4007–20

[52]   Müller-Plathe F 1998 Diffusion of water in swollen poly(vinyl alcohol) membranes studied by molecular dynamics simulation *J. Memb. Sci.* **141** 147–54

[53]   Müller-Plathe F and van Gunsteren W F 1997 Solvation of poly(vinyl alcohol) in water, ethanol and an equimolar water-ethanol mixture: structure and dynamics studied by molecular dynamics simulation *Polymer (Guildf).* **38** 2259–68

[54]   Lin C-A, Tsai H-C and Ku T-H 2007 Manufacturing Process and Application of Pseudo-thermoplastic Polyvinyl Alcohol *Polym. Technol. Eng.* **46** 689–93

[55]   Goyanes A, Buanz A B M, Basit A W and Gaisford S 2014 Fused-filament 3D printing (3DP) for

fabrication of tablets *Int. J. Pharm.* **476** 88–92

[56]   Hixson A W and Crowell J H 1931 Dependence of Reaction Velocity upon surface and Agitation *Ind. Eng. Chem.* **23** 923–31

[57]   Costa P and Sousa Lobo J M 2001 Modeling and comparison of dissolution profiles. *Eur. J. Pharm. Sci.* **13** 123–33

[58]   Fuchsbauer H 1996 Influence of gelatin matrices cross-linked with transglutaminase on the properties of an enclosed bioactive material using β-galactosidase as model system *Biomaterials* **17** 1481–8

[59]   Bigi A, Cojazzi G, Panzavolta S, Rubini K and Roveri N 2001 Mechanical and thermal properties of gelatin films at different degrees of glutaraldehyde crosslinking *Biomaterials* **22** 763–8

[60]   Vesel A and Mozetic M 2012 Surface modification and ageing of PMMA polymer by oxygen plasma treatment *Vacuum* **86** 634–7

[61]   Xiao L, Wang B, Yang G and Gauthier M 2006 Poly(Lactic Acid)-Based Biomaterials : Synthesis , Modification and Applications *Biomed. Sci. Eng. Technol.* 247–82

[62]   Bodas D and Khan-Malek C 2007 Hydrophilization and hydrophobic recovery of PDMS by oxygen plasma and chemical treatment-An SEM investigation *Sensors Actuators, B Chem.* **123** 368–73

[63]   Yoneda M, Yoneda M, Yoneda M, Fujita K, Fujita K, Inamori M, Inamori M, Tamano M, Tamano M, Hiriishi H, Hiraishi H, Nakajima A and Nakajima A 2007 Transient elastography in patients with non-alcoholic fatty liver disease (NAFLD). *Gut* **56** 1330–1

[64]   Liang Y, Jeong J, DeVolder R J, Cha C, Wang F, Tong Y W and Kong H 2011 A cell-instructive hydrogel to regulate malignancy of 3D tumor spheroids with matrix rigidity *Biomaterials* **32** 9308–15

[65]   Georges P C, Hui J-J, Gombos Z, McCormick M E, Wang A Y, Uemura M, Mick R, Janmey P a, Furth E E and Wells R G 2007 Increased stiffness of the rat liver precedes matrix deposition: implications for fibrosis. *Am. J. Physiol. Gastrointest. Liver Physiol.* **293** G1147-54

Author contribution

R.P.C. has designed and performed the experiments, analyzed and interpreted the data, made graphs and wrote the manuscript. Also, R.P.C has designed the hydrogel formulation, fabricated all the hardware parts (3D printing characterization, CAD modelling, electronic part) and wrote the software for controlling the pumps. M.H. and R.P.C. have performed experiments with hepatospheres and R.P.C. did the confocal imaging of the cell constructs.

F.O. has designed the experiments, A.A. has provided the hepatospheres and protocols, A.W. and J.E. contributed with materials/tools. M.D. have designed the experiments, interpreted the results and wrote the manuscript.

Competing Financial Interest Statement

Anders Aspegren is an employee of Takara Bio Europe.

Fabrication of cell laden soft hydrogels perforated with a 3D channels network interfaced to a perfusion system

Rodrigo Pimentel C.[1], Mette Hemmingsen[1], Fridolin Okkels[1], Anders Aspegren[2], Anders Wolff[1], Jenny Emnéus[1], and Martin Dufva[1]

Supplementary information

Methods

Noyes-Whitney equation

The dissolution phenomena of a solid particle in a excess of water follows the Noyes–Whitney Equation:

$$-\frac{dm}{dt} = \frac{DS}{h_N}(c_s - c_t)$$

(S1)

where m is the solid mass at time t , D is the solute diffusion in the water, S is the solid surface, h is the width of the diffusion layer, c_s is the solid concentration at saturation, and c_t is the concentration of the solution at time t. The equation can be re-written as:

$$-\frac{dm}{dt} = K(c_s - c_t)$$

(S2)

where K represents the rate constant of dissolution. When the solute is highly soluble in water and the water in excess as well as stirring at a constant and rapid velocity (to ensure the Nernst model validity) $c_s \gg c_t$ and the equation S2 can be written as:

$$-\frac{dm}{dt} = Kc_s$$

(S3)

For a cylindrical shape, the surface is described as:

$$S = 2\pi r^2 + 2\pi r l$$

(S4)

And the mass is described by:

$$m = \rho\pi r^2 l \qquad (S5)$$

If the equation S4 and S5 are substituted in the equation S3, the equation S6 can be written as:

$$-\frac{dm}{dt} = \frac{2Dc_s}{h\rho}\left(\frac{1}{r} + \frac{1}{l}\right)m \qquad (S6)$$

It is difficult to evaluate how the mass m vary with the time since both r and l are time dependent. Therefore, r and l where experimentally measured over time and the sum $[(1/r)+(1/l)]$ was fitted to a polynomial function $F(t)$ using the least-squares method. The integration of the equation S6 leads to:

$$\ln\left(\frac{m}{m_0}\right) = -2\frac{Dc_s}{h\rho}f(t) \qquad (S7)$$

where m_0 and m are the masses at time 0 and t respectively, and $f(t)$ is the integral of the polynomial function $F(t)$. We can therefore define a new constant k' that can be written as:

$$k' = 2k\frac{c_s}{\rho} = 2\frac{Dc_s}{h\rho} \qquad (S8)$$

From calculating the slope in the equation S7 it is possible to evaluate the rate costant k' that describes the dissolution process of the PVA in water.
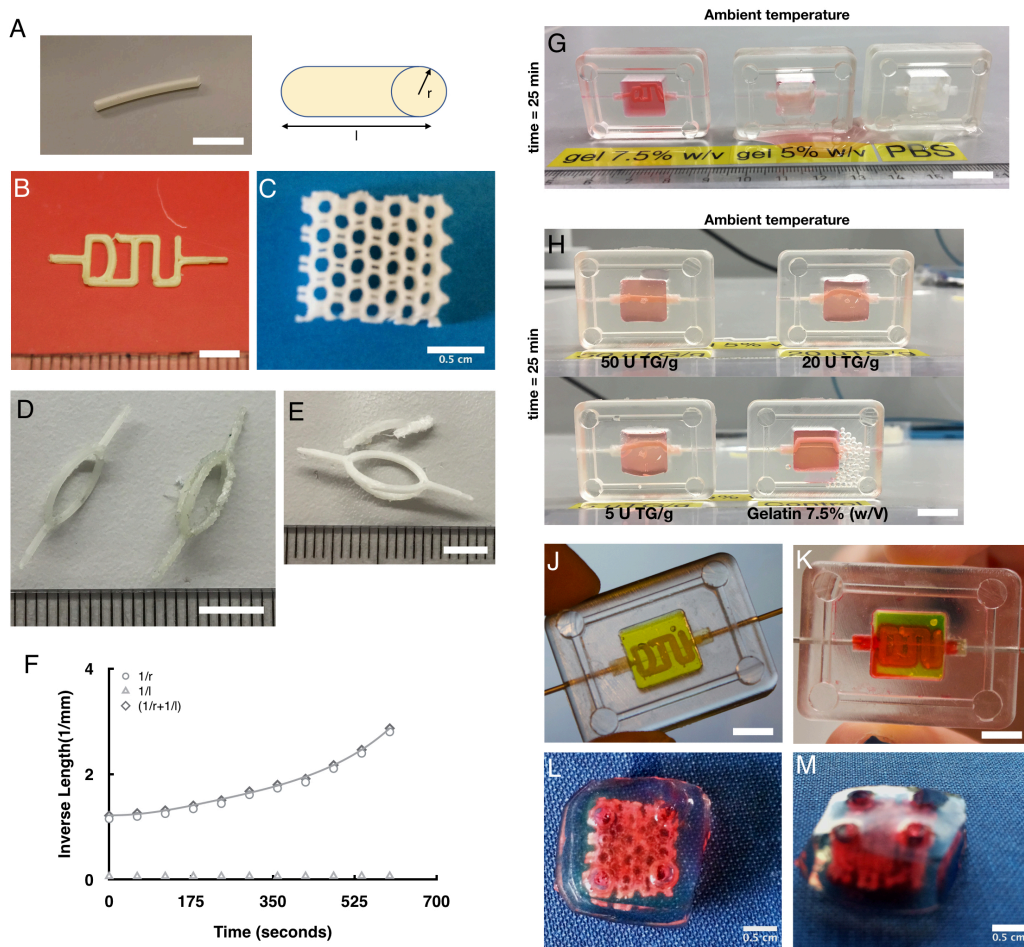
Figure S1. (A) Photograph of a cylindrical PVA filament, with radius r and height l, used to study the dissolution in water. (Scale bar: 5 mm) **(B)** photograph of a PVA Printed part with a planar structure. **(C)** photograph of a PVA Printed part with a square lattice structure. **(D)** Printed PVA branch obtained after the dissolution of PLA fabricated using the support structure generated from Kisslicer. (Scale bar: 5 mm) **(E)** Printed PVA branch obtained after the dissolution of PLA fabricated using the support structure custom designed. (Scale bar: 5 mm) **(F)** Variation in time of the inverse of the radius r, the inverse of the length l, the sum, and the fitted polynomial function F(t) for the PVA filament dissolved in water. **(G)** PVA dissolution of a molded structure within a 7.5% (w/v) gelatin, 5% (w/v) gelatin and PBS at ambient temperature after 25 minutes. (Scale bar: 10 mm). **(H)** PVA dissolution of a molded structure within 5% (w/v) gelatin chemically crosslinked with 50, 20, 5 Units of TG per g of gelatin in respect to gelatin 7.5 % (w/v) (control) at ambient temperature immediately after the casting and after 25 minutes. (Scale bars: 10 mm) **(J)** Photograph of a planar 3D printed sacrificial templates embedded in a gelatin hydrogel construct before the dissolution and removal of PVA. (Scale bar: 9 mm) **(K)** Photograph of the resulting vascularized 3D construct with an embedded planar channel network. (Scale bar: 8 mm) **(L-M)** Photograph of the resulting vascularized 3D construct with an embedded square lattice channel networks. (Scale bars: 5 mm)

CHAPTER 4

THREE-DIMENSIONAL FABRICATION OF THICK AND DENSELY POPULATED SOFT

CONSTRUCTS WITH COMPLEX AND ACTIVELY PERFUSED CHANNEL NETWORK

Three-dimensional fabrication of thick and densely populated soft constructs with complex and actively perfused channel network

Rodrigo Pimentel C.[1], Suk Kyu Ko[1], Claudia Caviglia[1], Jenny Emnéus[1], Stephan Sylvest Keller[1] and Martin Dufva[1]

[1] *Department of Micro- and Nanotechnology, Technical University of Denmark, Denmark*

Abstract

One of the fundamental steps needed to design functional tissues and, ultimately organs is the ability to fabricate thick and densely populated tissue constructs with controlled vasculature and microenvironment. To date, bioprinting methods have been employed to manufacture tissue constructs with open vasculature in a square-lattice geometry that lacks the ability to be directly perfused. Moreover, it appears to be difficult to fabricate vascular tissue constructs targeting the stiffness soft tissues such as the liver. Here we present a method for the fabrication of thick (e.g. 1 cm) and densely populated (e.g. 10 million cells·mL^{-1}) tissue constructs with a three-dimensional (3D) four arm branch network and stiffness in the range of soft tissues (1-10 kPa), which can be directly perfused on a fluidic platform for long time periods (> 14 days). Specifically, we co-print a 3D four-arm branch using water-soluble Poly(vinyl alcohol) (PVA) as main material and Poly(lactic acid) (PLA) as the support structure. The PLA support structure was selectively removed, and the water soluble PVA structure was used for creating a 3D vascular network within a customized extracellular matrix (ECM) targeting the stiffness of the liver and with encapsulated hepatocellular carcinoma (HepG2) cells. These constructs were directly perfused with medium inducing the proliferation of HepG2 cells and the formation of spheroids. The highest spheroid density was obtained with perfusion, but overall the tissue construct displayed two distinct zones, one of rapid proliferation and one with almost no cell division and high cell death. The created model, therefore, simulate gradients in tissues of necrotic regions in tumors. This versatile method could represent a fundamental step in the fabrication of large functional and complex tissues and finally organs.

Introduction

In the last decade, significant effort has been made to fabricate functional three-dimensional (3D) Tissue Engineering constructs to simulate a portion of a human tissue [1–6]. Such constructs could open up for a new world of applications in drug delivery [7,8], 3D cell culture [9–11], disease model platforms [12] and tissue regeneration [13–16].

The current challenge in fabricating functional 3D constructs relies on the difficulties in creating relevant perfusable vasculatures, necessary to overcome the regarded diffusion limit of oxygen and nutrients (i.e., 200 μm) [17], within an ECM simulating soft tissue stiffness (e.g. liver) [18,19]. This is mainly due to the fact that it is hard to maintain the physical integrity of the ECM and the channels within [20]. In addition, to keep densely populated tissue constructs alive (cell density in the range of $10 - 500$ million $cells \cdot mL^{-1}$ [21]), an open vasculature without active perfusion would probably not be sufficient [22]. Therefore, to guarantee the final success of the fabricated construct it is necessary to developed a strategy to actively perfuse these tissues constructs [23]. Direct 3D printing has gained an important role in the fabrication of thick, vascularized, and complex 3D constructs [14,15,18,22,24–32], since it allows layer-by-layer printing of a variety of complex shapes. The drawback is that it is not possible to print structures with 3D degree of freedom, without having a support structure underneath. This has mainly led to the fabrication of simple self-sustained square lattices which do not represent the complexity of real tissues [15,21,25,27,30,33]. Kolesky et al [33] reported a technique where they printed two different inks at the same time followed by casting an ECM into the printed structure. The first ink used was Pluronic F127, which was the sacrificial material responsible for defining the vascular channels. The second ink was a mixture of cells and suitable ECM that was made by a blend of gelatin and fibrinogen, which was direct printed in the positions along the vascular channels. Then, another mixture of gelatin and fibrinogen cross-linked by a dual-enzymatic strategy by using thrombin and transglutaminase (TG) was cast around the direct printed structure. The thrombin was used to rapidly polymerize fibrinogen, and TG, which is a slow-acting Ca2+-dependent enzymatic cross-linker, acted on the gelatin to give mechanical stability on the final printed construct.

Another strategy that has been employed to fabricate 3D constructs is the 3D sacrificial molding technique [21,28,33–45]. Bio-printers have been used to print gelatin [44,45], agarose [46], Pluronic F127 [43] as sacrificial material to create vascular networks. Miller *et al.* [21]

reported a method for fabricating 3D vascular constructs, in which a modified Fused Deposition Modelling (FDM) printer has been used to 3D print carbohydrate glass structures serving as sacrificial template. Then, a poly(ethylene glycol) (PEG) based hydrogel with cells encapsulated was cast around the sacrificial template. Subsequently, the sacrificial material was removed from the PEG hydrogel leaving behind a network of open microchannels. FDM has been also used to print sacrificial templates in PVA [39,40,42]. However, in some cases the 3D printed structures were used to create porous elastomeric scaffolds [39,40] for 2D cell culture. In another case, although custom modified machines allowed the realization of more complex PVA structures, the ECM used was extremely stiff with no cells encapsulated in it [42]. Finally, molds have been used to create sacrificial templates using sodium alginate [37] and PVA [38]. Although direct printing and 3D molding strategies have shown advantages in fabricating tissue engineered constructs with perfusable vasculature there are some aspects that needs to be addressed. The majority of the proposed vascular networks were composed by single [44,46] or multiple microchannels in a single plane [21,28,37,38,42,43,47], or in a square lattices-like structure [15,26,27,30,33,48]. It appears to be difficult to manufacture thick tissue constructs able to integrates (1) soft tissues stiffness (2) relevant cell density (3) complex vascular networks and (4) perfusion. We believe these four points are critical for the final success of an engineered construct and this is what are addressing in this paper.

Here, we describe a method for the fabrication of a thick and densely populate tissue construct with full 3D perfusable network and stiffness in the range of soft tissues. The obtained 3D tissue constructs are relatively thick (1 cm^3) allowing a connection with a custom fluidic platform and being perfused for extended time periods (> 14 days). Long term cell culture demonstrated strong dependence of nutrient and oxygen feed for cell growth.

Materials and Methods

Hydrogel preparation

Gelatin cross-linked with transglutaminase (Activa-TI, Ajinomoto North America Inc., Illinois, US, (TG)) was used in this study. Briefly, 7.5% (w/v) gelatin (48723 Fluka) was mixed with cell culture medium (Roswell Park Memorial Institute, RPMI 1640) supplemented with 10% fetal bovine serum (FBS; Gibco Labs), and penicillin/streptomycin at 60 °C and stirred until fully solubilized. The degree of cross-linking of the resulting gelatin/TG hydrogel was

controlled by varying the amount of TG in respect to the mass of the gelatin. The appropriate mass of TG (Activa-TI, Ajinomoto, Inc., activity of approximately 100 U·g^{-1} of TG according to the manufacturer) was dissolved in 15 mL of PBS (Sigma Aldrich) to give concentrations of 2.5, 5, 10, and 20 units of TG per g of gelatin. The final concentrations of the gelatin/TG hydrogel used in this study were 5% (w/v) gelatin, with 2.5, 5, 10, and 20 units of TG per g of gelatin.

Mechanical properties

Mechanical tests were performed on cylindrical shaped samples (n= 6). Briefly, 1mL of the 5% (w/v) gelatin/TG pre-polymer solutions (ratio of TG (2.5, 5, 10 and 20 units of TG per g of gelatin) was cast in a cylindrical PMMA mold (10 mm in diameter, 10 mm in thickness). Samples were incubated at 37°C for 24 hours allowing gelatin cross-linking. The cylindrical samples were tested at 37°C, and compressed to 10% of the initial length using 0.1% strain rate using the Solid Analyzer instrument (0.1 µN force resolution, 0.5 mN minimum force, 1 nm displacement resolution) (RSA II, Rheometrics, Inc.). The compressive elastic modulus of each sample was calculated from the stress-strain curve (first linear zone, 2% strain).

Design and 3D Printing of the 3D sacrificial structures

The 3D sacrificial structures were designed and converted into STL files using Solid Works CAD software (computer aided design, Dassault Systemes SolidWorks Corporation, US). All STL files were processed by KISSlicer (www.kisslicer.com) software and sliced into 100-µm-thick layers to generate G-code instructions for the 3D printer. G-code instruction sets were sent to the printer using Repetier-host (https://www.repetier.com), an open-source 3D printer host program. Then commercially available PVA and PLA filaments (Makerbot Industries, Brooklyn, NY, USA) were printed using the Felix 3 (Felix Printers, IJsselstein, Netherlands) printer with a nozzle of 250 µm.

Dissolution of support material in the 3D sacrificial structures

The 3D sacrificial structures were printed with PLA as support material. Then, the structures were immersed in 200 mL of chloroform (Sigma Aldrich) under continuous stirring until all the solid PLA support was dissolved. After the total dissolution of the PLA, the 3D sacrificial

structures were immersed in 10 mL of clean chloroform for an additional day to reduce the layer of PLA around the 3D printed PVA.

HepG2 encapsulation and active perfusion of the 3D tissue constructs

All reagents were purchased from Sigma Aldrich unless otherwise specified. The liver hepatocellular carcinoma (HepG2) cells (American Type Culture Collection, Rockville, MD, USA) were cultured in RPMI 1640 supplemented with 10% (v/v) fetal bovine serum, and 1% (v/v) penicillin/streptomycin.

The fluidic platform was sterilized using ethanol. Glass vials, caps and polytetrafluoroethylene (PTFE) tubing (inner diameter of 0.8 mm) (BOLA 1818-10, Bohlender GmbH, Germany) were sterilized by autoclaving before assembling in a laminar flow bench. A total of 0.5 M NaOH was flushed throughout the system to ensure a sterile fluidic path. The system was subsequently flushed with 10 mL of sterile water and then with 10 mL of culture medium. The fluidic molds were fabricated using polydimethylsiloxane (fabrication not showed, PDMS) and were sterilized by washing the fluidic molds in ethanol.

Gelatin 5% (w/v) cross-linked with 5 units of TG per g of gelatin was prepared and incubated for 45 minutes at 37°C. A total of 0.5% (v/v) of chloroform was added to sterilize the solution. Then, the sacrificial template (Fig. 1B) was placed inside the fluidic molds (Fig. 2A). Subsequently, HepG2 cells were mixed with 1.5 mL of the gelatin/TG hydrogel and then cast into the fluidic molds, to have a final density of 1×10^7 cells·mL^{-1} of gelatin/TG hydrogel. After the casting, the samples were incubated at 4°C for 30 minutes to convert the liquid gelatin into solid state. The construct was subsequently incubated for 1h at ambient temperature to allow chemical cross-linking of the gelatin, ensuring mechanical stability at higher temperatures. The final dimensions of the tissue constructs were 14 mm (L) x 11.5 mm (W) x 10 mm (H) with a resultant volume of ≈ 1.5 cm^3. The fluidic molds were placed in a fluidic platform able to hold 3 samples at a time, and media was perfused through at 5μL·min^{-1} for 30 minutes to ensure the total removal of the 3D sacrificial structure from the 3D constructs. After complete removal of the 3D sacrificial structures from all the samples, the flow rate was increased to 100 μL·min^{-1}. The entire system was incubated at 37 °C under 95%air/5% CO$_2$, and the medium was exchanged every second day. Cells were cultured for up to 14 days. To investigate the importance of direct perfusion within the 3D constructs, control experiments with the

same cellular densities were prepared and conducted under passive media exchange. A total of 1.5 mL of encapsulated HepG2 cells were cast in the fluidic mold, in one case without the 3D sacrificial structure, and in another with the 3D sacrificial structure placed inside the fluidic mold, following subsequent removal, as described above. The tissue constructs (with and without perfusion channels) were placed in a petri dish with fresh medium to provide a passive exchange of medium. The controls were then incubated at 37 °C under 95%air/5% CO_2 for one week, exchanging the media every second day.

Fluorescence staining

The cell viability of the engineered 3D tissue constructs was assessed using a LIVE/DEAD assay (Thermo Fisher Scientific). The constructs were removed from the mold, and sectioned along the cross-sectional direction. Due to the softness of the gel, it was impossible to get a clear cut, and therefore the surface was not entirely flat making it difficult to perform the microscopy analysis. The samples were then washed with Hank's balanced salt solution (HBSS) and incubated for 30 minutes with 1.5 mL of HBSS containing 5 μL of SYTO 10 and DEAD read. After incubation, the samples were washed again with HBSS and then imaged with the Zeiss LSM confocal microscope. Engineered 3D tissue constructs were also stained for the nuclei, cellular membrane and F-actin. Briefly, samples were fixed in 4.5% (v/v) paraformaldehyde in phosphate buffered solution (PBS) for 20 minutes and permeabilized with 0.1% (v/v) Triton X-100 in PBS for 10 minutes followed by a PBS washing in between. Subsequently, they were stained for 1 hour with Höechst 33342 (Invitrogen) for labeling the cell nuclei, Phalloidin (F432, Invitrogen) for labeling the F-actins, and with Cell mask (C37068, Invitrogen) for labeling the cellular membrane according to manufacturer's instruction.

Imaging and analysis

Confocal acquisitions were performed using a Zeiss LSM 700 module in the Axio Imager M2 upright microscope using: an epiplan-neofluar 5X/0.13 HD, 10X/0.25 HD, 20X/0.5 HD, and a 40x/1.20 W Korr C-Apo objective. To eliminate any possible crosstalk between channels, images were collected with a sequential scan, using the following laser lines and mirror settings: 405 (30%) 420-480nm; 488(30%) 495-560nm; 555(30%) 605-700nm. Photographs and videos of tissue fabrication were acquired using a DSLR camera (Canon EOS, 5D Mark II; Canon). Fluorescein dye was used to improve visualization of gelatin construct. ImageJ was

used to visualize composite images by combining fluorescent channels. Three-dimensional rendering and visualization of confocal stacks were performed in Imaris 7.6.4, Bitplane Scientific Software. The diameter of vascular channels and spheroids was measured using ImageJ software using at least 4 images from different areas of 2 constructs for each condition.

Results and discussion

3D printing of sacrificial structures and support dissolution

One of the main challenges in engineering functional dense 3D tissue constructs or organs is the lack of a perfusable vasculature [1,15,17,23,49,50]. Considering that the vascular system within tissues and organs is not distributed in a single plane but is branched [23,51–53], we designed a 3D vascular branch with four curved arms distributed in the 3D space to ensure a volumetric distribution of flow throughout the tissue construct (Fig. 1A-D). When designing non-planar geometries, the main limitation on using any standard layer-by-layer 3D printer is the difficulties to deposit material in the 3D space without the presence of support material underneath. Therefore, the 3D bifurcated branch was printed using a dual printing strategy, where the primary structure was printed using PVA, and the support material was printed using PLA (Fig. 1A). The support structures were designed using the CAD tool (Fig. 1D) with the aim of minimizing the amount of support material to be dissolved, but at the same time using enough material to guarantee the mechanical stability of the part during the printing process. The support structure was then selectively removed with chloroform after completed printing (Fig. 1B). Like the 3D printing of most materials, the resolution and morphology of the 3D bifurcated branch was dependent on several machine settings and required optimization for the two materials used. The design for the 3D bifurcated branch can be downloaded as an STL file together with the generated Gcode from https://3dprint.nih.gov and can be printed on any two-headed RepRap or MakerBot 3D printer. After the dissolution of the PLA support of the 3D bifurcated branch, the resulting line width and layer thickness of the PVA structure was approximately 700 µm (for a CAD design of 600 µm). The final resolution and quality of the 3D printed branch showed that the created support structure was fundamental to ensure mechanical stability of the PVA structure during the printing phase. Also, the created

support structure was important because the amount of PLA used was minimized to induce the dissolution of the PLA without damaging or breaking the fragile 3D branch.

There have been several strategies to design sacrificial PVA structures, going from simple square lattices [39,40] to quasi 3D structures [38,42]. However, these attempts still lack the ability to create a branched vasculature with curvatures and points of junction in the 3D space that are characteristic for the human vasculature. The key advantage of our fabrication method is that it is not relying on modified FDM printers [42] or modified materials [21]. Instead, we focused on the design of the desired structure, and we used the built-in ability of the FDM printer to print complex structures by printing two materials at the same time, and by using biomaterials that are commercially available (e.g. PVA, PLA).
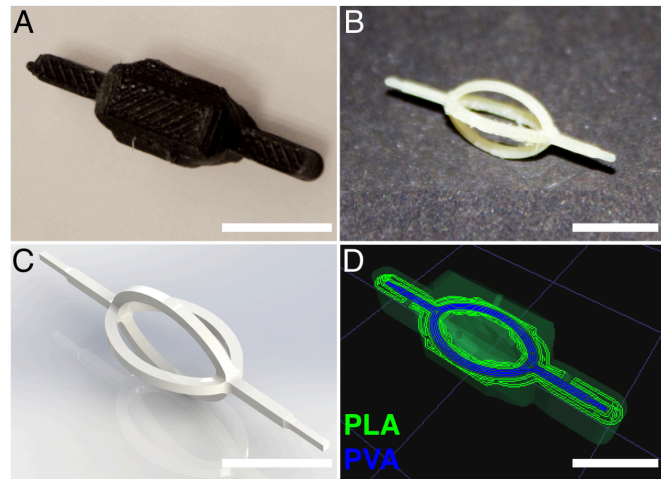
Fig. 1. (A) Photograph of the 3D printed branch with four curved arms using PVA as sacrificial template and PLA as support material. (B) Photograph of the 3D Printed branch with four curved arms after the dissolution of the PLA support material. (Scale bar: 3 mm) (C) CAD model of the designed 3D vascular branch. (D) Visualized motion program for 3D printing branch. Lines of green indicate the dispensing paths of PLA whereas lines of blue indicate the dispensing paths of PVA. (Scale bars: 6 mm)

3D vascular branch formation

The fabrication of the constructs with a built-in vasculature was achieved using the 3D molding technique (Fig. 2A). Since we wanted to create constructs in the range of soft tissues (i.e. $1.5 - 12$kPa [54–58]) with cells encapsulated in it, we used 5% (w/v) gelatin. To ensure thermal stability, and to control the mechanical properties of the gelatin hydrogel, TG, a slow-acting Ca^{2+}-dependent enzymatic cross-linker, was used [59–61]. To demonstrate that the

131

amount of gelatin and TG, respectively, resulted in constructs with stiffness in the range of the soft tissues, we performed uniaxial compressive tests after 24h at 37°C. The resultant compressive modulus (Fig. 2B) was found to be 2kPa for the samples with 2.5 units of TG per g of gelatin while for the samples with 20 units of TG per g of gelatin was 6.5kPa. To demonstrate the ability to create 3D vasculature within the gelatin/TG hydrogel, we cast 1.5 mL of 5% gelatin with the lowest ratio of TG per g of gelatin around the 3D branch printed with PVA (Fig. 2C). The sacrificial template was then dissolved and removed by perfusion leaving a well-defined and open 3D vasculature (Fig. 2D-E). To ensure a continuous removal of the dissolved PVA from the vasculature the constructs were perfused with a volumetric flow rate of 5 μL·min^{-1} for 30 minutes. This was sufficient to slowly dissolve and remove the PVA without damaging the surrounding ECM extensively. The perfusion of the constructs was achieved using a custom-made fluidic platform. The fluidic platform was 3D printed using PLA and integrates a peristaltic pump able to perfuse three samples at the same time and all the electronics needed to control the pumps (Fig. 2F). After the total removal of the PVA it was possible to create a 3D branch network within a hydrogel with stiffness of 2 kPa having dimensions of 14 mm (L) x 11.5 mm (W) x 10 mm (H) (Fig. 2D). The branch point was stable and capable of supporting the four rounded arms within the gelatin/TG construct; although the construct was extremely soft the channel network did not collapse (Fig. 2E). We then evaluated the diameter of the newly formed vasculature. It was found that the final diameter of the vasculature was 1.3 mm. To verify the structural stability of the fabricated constructs along with its vascular branch, constructs were perfused for 24 hours at 37 °C. It was found that both the construct and vascular branch were mechanically stable without any structural deformation in response of the increased volumetric flow rate or increase in temperature (Fig. 2G).
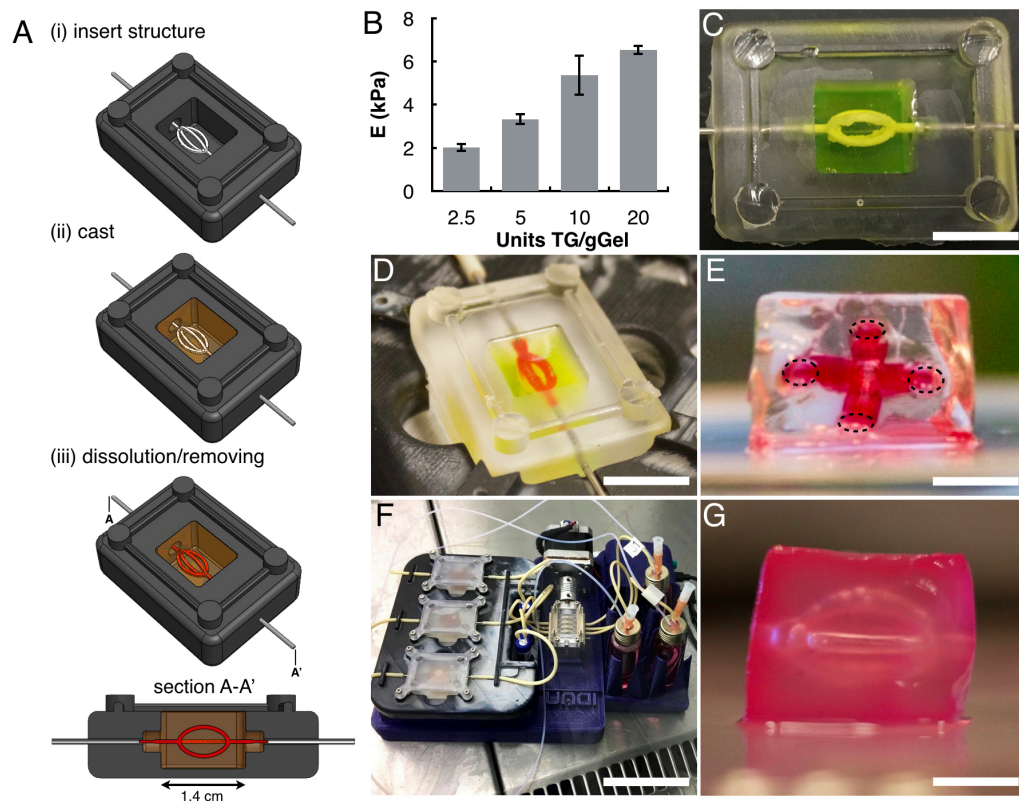
Fig. 2. (A) Schematic illustration of the fabrication of the 3D construct: **(i)** the PVA printed structure used as sacrificial template is inserted in the fluidic mold, **(ii)** ECM material is casted over the 3D printed template, and **(iii)** the PVA sacrificial template is then dissolved, removed and perfused by a peristaltic pump. **(B)** Elastic modulus of gelatin 5% (w/v) cross-linked with different amounts of TG. **(C)** Photograph of the 3D printed branch embedded in a gelatin hydrogel construct before the dissolution and removal of PVA. **(D)** Photograph of the resulting vascularized 3D construct (Scale bars: 1.4 cm). **(E)** Photograph of the cross section of the vascularized 3D construct, showing the volumetric distribution and structural stability of the channels (Scale bar: 5 mm). **(F)** Photograph of the custom made fluidic platform and the three tissue constructs allocated on it used for the long-term studies (Scale bar: 5 cm). **(G)** Photograph of vascularized 3D construct having stiffness of 2 kPa after 24h of direct perfusion using a flow rate of $100\mu L$ min^{-1} (Scale bar: 4.5 mm).

The sacrificial templates fabricated in this study were printed using PLA as support material and then the PLA support was dissolved in chloroform. The dissolution of the PLA was obtained by immersing one 3D printed structure in 200 mL of clean chloroform with constant stirring of 400 rpm until the PLA fully dissolved and went in solution revealing the PVA structure. However, it was observed the formation of a coating of PLA surrounding the sacrificial templates printed with PVA (black coating of PLA surrounding the otherwise white PVA, Fig. S1A). When these 3D printed structures were used as sacrificial template to fabricate hydrogel constructs with open and well-defined vasculature it was observed that the coating of PLA remained adherent within the walls of the hydrogel vasculature (Fig. S1B). It has been demonstrated that a coating layer of biopolymer material surrounding the sacrificial

template could be beneficial for the fabrication of tissue constructs with embedded vasculature [21,42]. However, if not carefully tuned, the coating of adherent PLA within the walls of the hydrogel vasculature could potentially inhibit the ability of the network to support convective and diffusive transport into the bulk gel. Therefore, the sacrificial templates were treated again in 10 mL of clean chloroform for one day without any stirring. The second treatment was sufficient to tune the formation of a layer of PLA thin enough to be removed from the hydrogel during the dissolution of PVA (Fig. S1C). This led to the formation of gelatin/TG constructs with open and well-defined 3D vasculature with no PLA residues within the vasculature of the hydrogel construct (Fig. S1D).

Another critical point concerned the use of the 3D molding technique is the final dissolusion of the fabricated vasculature within the hydrogel construct. It has been shown that the diameter of the vasculature is not only dependent on the diameter of the sacrificial templates, but it also depends on the hydrogel cross-linking strategy [38,42]. In fact, when using gelatin 7.5% (w/v) with 20 units of TG per g of gelatin in combination with a sacrificial template having dimensions of 500 μm (i.e., line width and layer thickness) it was possible to fabricate gelatin/TG constructs with an open and well defined built-in vasculature having diameter of 500 μm (Fig. S2A). By contrast, it was not possible to fabricate constructs with well-defined vasculature when using gelatin 5% (w/v) crosslinked with the same amount of TG and with a sacrificial template having dimensions of 500 μm. This was because the sacrificial templates printed with PVA lost their mechanical stability as consequence of the slow crosslinking reaction of the gelatin/TG hydrogel (Fig. S2B). The same occurred for structures having dimensions up to 700 μm. However, when increasing further the dimensions of the printed PVA structures, the quantity of material to be dissolved and removed increased significantly. For structures having 700 μm dimensions, the absence of an active removal of the dissolved PVA led to the formation of a vasculature with channel diameter of 2 mm (Fig. S2C). The increase in channel diameter was probably caused by an increase of the intra-pressure within the vasculature while dissolving the PVA during the slow cross-linking reaction. By contrast, when the PVA was dissolved and removed via perfusion, it was possible to control the intra pressure since the final diameter of the channel networks was 1.3 mm.
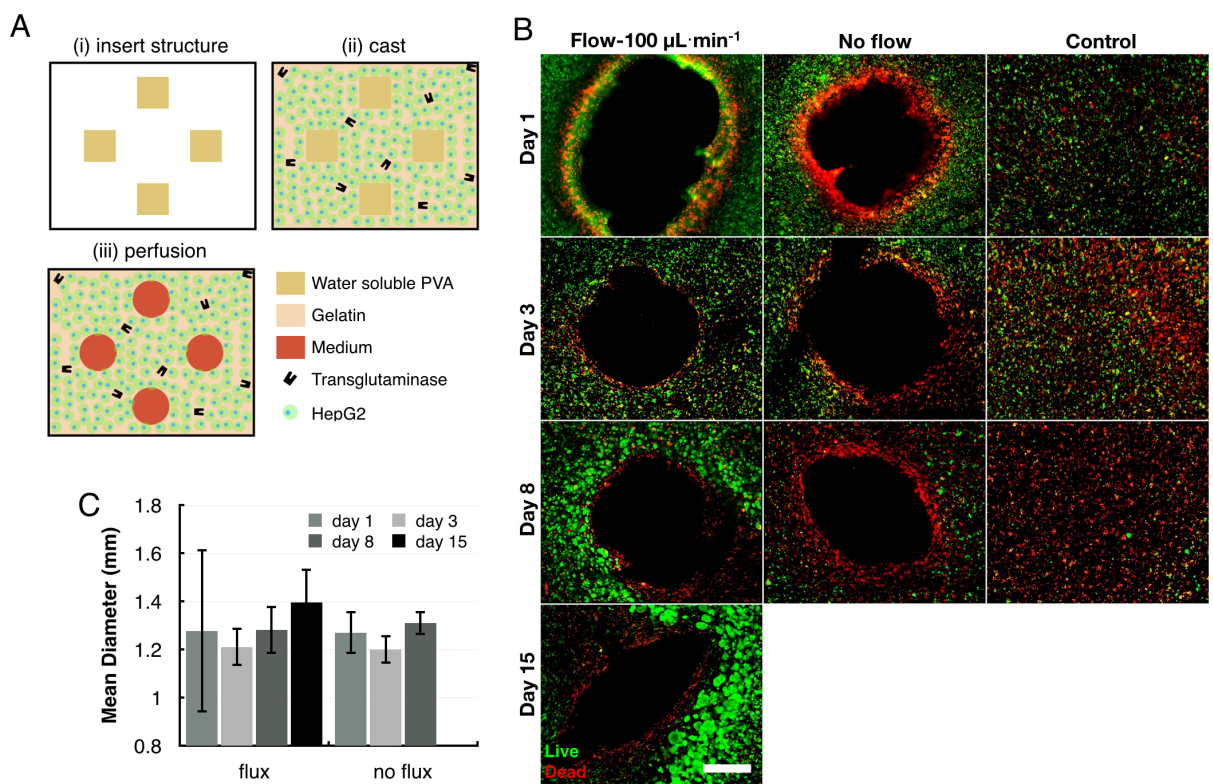
Fig. 3. (A) Schematic illustration of the fabrication of the 3D tissue construct: **(i)** the PVA printed structure used as sacrificial template is inserted in the fluidic mold, **(ii)** ECM material, which contains gelatin, cells, and TG, is cast over the 3D printed template. After casting, TG slowly cross-links the gelatin, and **(iii)** the PVA sacrificial template is dissolved, removed and perfused by a peristaltic pump with a flow rate of 100µL min⁻¹. **(B)** Viability of HepG2 cells encapsulated in 5% gelatin hydrogels with stiffness of 3 kPa, comparing constructs with embedded vasculature, with and without direct perfusion, versus control of blocks without vasculature for 15 days (Scale bar: 500 µm). **(C)** Quantification of the diameter of the embedded vasculature comparing tissue constructs directly perfused versus tissue constructs not perfused for several days.

HepG2 encapsulation and direct perfusion in soft constructs

To demonstrate the importance of direct perfusion within a densely populated thick tissue construct, we casted $1.5 \cdot 10^7$ HepG2 cells in 1.5 mL of a gelatin/TG pre-polymer solution into the fluidic mold, with a resultant stiffness of 3.3 kPa (stiffness of a liver [57,58,62]). PVA was dissolved and removed by the start of the perfusion (Fig. 3A). The constructs were perfused with a volumetric flow rate of 100µL·min⁻¹ for 15 days.

To investigate the cellular viability, the effect of dissolution and removal of PVA, and the effect of the direct perfusion over time fluorescence micrographs of the constructs, in closed proximity of one of the channels, were taken on multiple time points (days 1, 3, 7, and 15) (Fig. 3B). At day 1 we observed a ring of dead cells surrounding the channels (Fig. 3B-day1).

This ring of dead cells was also observed for both perfused and unperfused constructs at day 3, 7, and 15. The presence of the ring of dead cells in the unperfused constructs at day 1 indicates that cell death happened during the process of dissolution and removal of the PVA. It is possible that the over pressure created within the vasculature during the dissolution and removal of the PVA from the soft ECM could lead to a radial expansion of the vascular channels (see video S5). This could potentially disrupt all the cells in close proximity of the vasculature [42,63]. In addition, there was no substantial difference in the diameter for both perfused and unperfused constructs within the 15 days (Fig 3C). Our results show that the layer of dead cells is induced by the over pressure created during the dissolution and removal of the PVA and not by the shear stress coming from the fluid flow. Our observations are in agreement with previous studies that shows that for cells encapsulated on different ECMs the force due to a pressure drop across the encapsulated cell dominates the integrated shear force coming from the fluid flow [64–67].

To investigate the effect of perfusion on the cellular viability, we compared perfused and not perfused tissue constructs, versus a control with a confined block without vascular network (Fig. 3B). On day 1, all the encapsulated HepG2 were homogeneously distributed within the perfused and unperfused constructs and the control. At day 3, the cell viability dropped dramatically in the control, and at day 8, most the encapsulated HepG2 were dead. By contrast, the cellular viability was considerably higher for both the perfused and the unperfused constructs. At day 3, the cellular viability was considerably higher for the unperfused construct in respect to the control. However, at day 8, the cellular viability dropped significantly in the unperfused construct. Although the cellular viability was considerably higher in the unperfused construct in respect to the control, the directly perfused construct showed a better performance in terms of cellular viability. These findings are in accordance with previous studies [21,46] that have shown the importance of the vasculature to maintain a higher cellular viability for constructs with encapsulated cells. At day 8, perfused construct had high viability and showed signs of cell proliferation as indicated by spheroid formations (Fig. 3B). The HepG2 residing within the surrounding matrix exhibit cell spreading and proliferative phenotypes localized to regions in proximity of the vascular channels, allowing them to cluster into more organized structures. The HepG2 cells had high cell viability on day 15 (Fig 3B). The layer of spheroids increased in size from 300 μm to 600 μm between day 8 and day 15. The findings suggest that direct perfusion is crucial, which is in accordance with others [22]. 3D finite-

element simulation also showed that the vasculature was not sufficient to avoid the cell death for densely populated constructs (Fig. S3A). The perfusion was critical to ensure the amount of oxygen and nutrients required for the cells to stay metabolically functional (Fig. S3B).

Fig. 4. (A) Schematic of the cross section of the 3D tissue construct on day 15, depicting the formation and the distribution of spheroids in respect to the vasculature: (i) in the frontal plane, corresponding to a single channel in the inlet, (ii) in the frontal plane, corresponding to the center, and (iii) in the sagittal plane. (B-C) Live/dead confocal microscopy of the frontal-cross section in the inlet of the perfusion (B) and the center with the four channels (C) of a 1cm thick vascularized tissue construct on day 15, showing spheroid viability and distribution (Scale bar: 2 mm). (D) Live/dead confocal microscopy through the sagittal-cross section of the branching point in the vascularized tissue construct on day 15 showing spheroid viability and distribution (Scale bar: 1 mm).

The formation of spheroids was only observed in some specific regions within the tissue constructs (Fig. 4A). The analysis of the fluorescence micrographs of the cross section through the frontal plane, in correspondence to the single inlet channel within the construct, revealed a layer of viable spheroids surrounding the vasculature as well as in proximity to the walls of the fluidic mold (Fig. 4B). This pattern is likely because the oxygen concentration is considerably higher in the proximity of the channels, because of the media perfusion (Fig. S3B), and because the PDMS surrounding the construct in the fluidic mold is extremely permeable to oxygen [68] (Fig. S3). By contrast, the cells in the center of the construct, between the four vascular channels, showed signs of cell death and living cells showed no sign of cell proliferation (Fig. 4C). In addition, spheroids were found only in the outer proximity of the four channels (Fig. 4C). To further confirm the absence of the spheroids within the inner region of the tissue construct, fluorescence micrographs of the sagittal (longitudinal cross-section) plane were acquired (Fig. 4D). The fluorescence micrographs confirmed that the spheroids only populate regions in the vasculature towards the external surface of the constructs whereas only single cells populate the central core between the two vascular channels surfaces. This might be an indication of hypoxia in the core region, a hypothesis that was confirmed by a 3D finite-element model analyzing the transport of oxygen in the tissue construct (Fig. S3B). In agreement with previous studies [21,69], the direct perfusion allowed the HepG2 to proliferate in regions of the tissue construct where the concentration of oxygen was high. However, it is not clear why there were no spheroids surrounding the vasculature towards the core regions of the tissue construct. There has been reported some evidence that when cells are encapsulated in a 3D matrix, not only the biochemical cues are responsible for proliferation, but also several properties of the matrix and environment such as, composition [70], stiffness [71,72], compliance [24], and interstitial flow [65,67] play a decisive role [73]. Since the results showed the presence of spheroids only in some specific regions within the vascularized tissue construct, it might be possible that in some areas the matrix would react in a different way in response to e.g. the pressure caused by the flow. Therefore, a 3D finite-element model was developed to assess the displacement and stresses of the vascular walls embedded in the tissue construct that might occur while being directly perfused (Fig. S4). The model showed that the perfusion generated a pressure gradient within the walls of the vasculature that induced an expansion of the vasculature. The expansion of the vasculature caused by the pressure gradient generated by the flow created a pressure force that compressed the matrix in the outer sur-

face of the vasculature within the construct. Interestingly, the volumes where the hydrogel is predicted to be compressed can be correlated with the volumes where poor cell proliferation was observed.

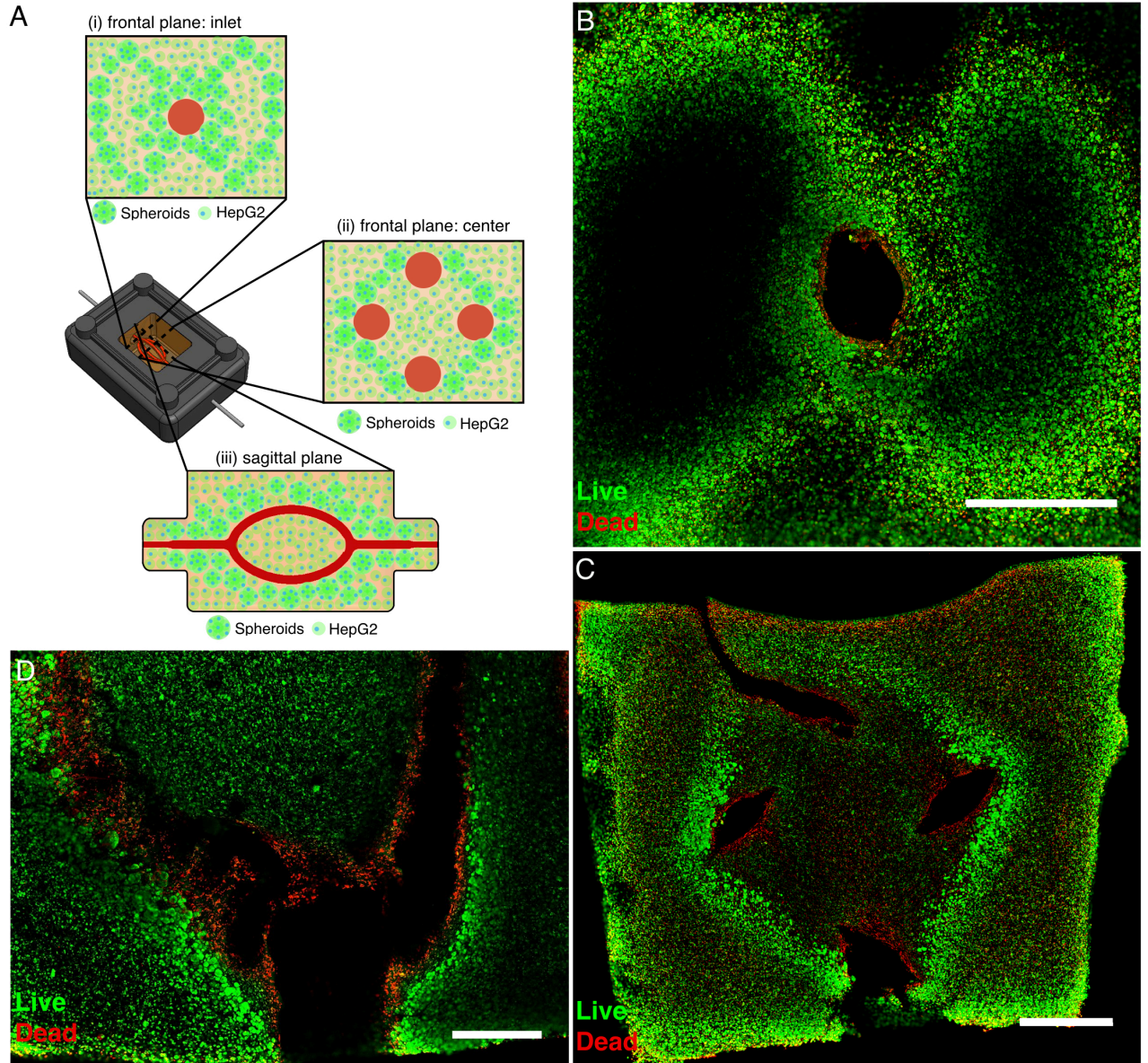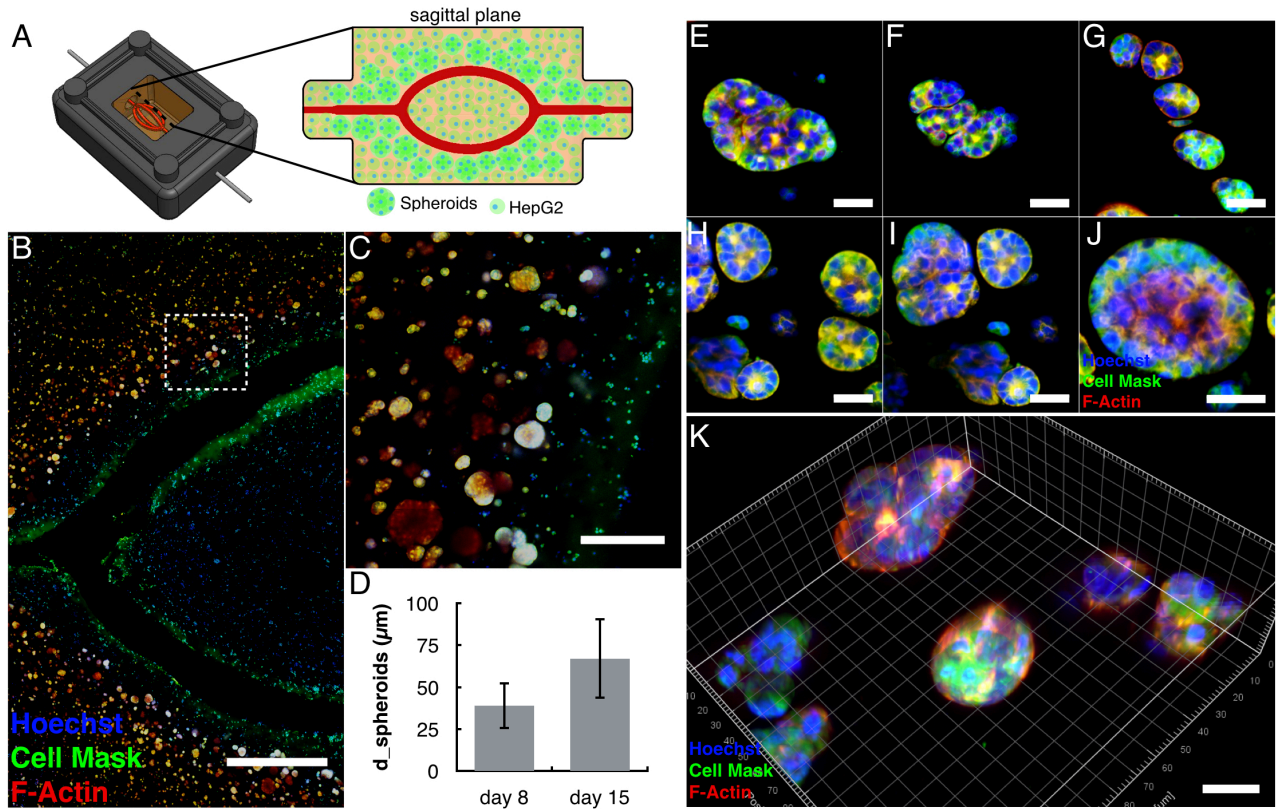Fig. 2. (A) Schematic of the cross section through the median plane of the 3D tissue construct on day 15, depicting the formation and the distribution of spheroids in respect to the vasculature. (B) Confocal microscopy images of nuclei (blu), cellular membrane (green) and F-actin (red) on day 15 of the 3D tissue construct cross-section, corresponding to the inlet of the perfusion, and the center, showing the spheroids morphology and distribution (Scale bar: 2 mm). (C) High resolution imaging of nuclei (blue), cellular membrane (green) and F-actin (red) on day 15, showing the morphology and the different dimensions of the spheroids in respect to the vasculature (Scale bar: 1 mm). (E-J) High resolution imaging of spheroids formed after 15 days by encapsulated HepG2 cells, showing different spheroid morphologies within the tissue construct. (K) 3D reconstruction of spheroids formed by HepG2 cells after 15 days within a vascularized 3D tissue construct possessing a stiffness of 3 kPa (Scale bars: 30 μm).

Spheroids Characterization

Since it has been demonstrated that the encapsulation of HepG2 in hydrogels with different stiffness could induce the formation of spheroids with various morphologies and liver specific functions [8,58,69,74], we evaluated the spheroid morphology within the directly perfused construct (Fig. 5). As expected, the fluorescence micrographs in the median plane of the tissue constructs (Fig. 5A) after 15 days of direct perfusion further confirmed that spheroids are located only on one side of the vasculature (Fig. 5B). Moreover, the dimensions of the sphe-

roids vary with the distance from the channnel, likely because of the oxygen and nutrients gradients (Fig. 5C). Spheroids with larger dimensions were in the regions close to the vasculature whereas those with small dimensions were located at a larger distance. It is recognized that the proliferation time for cells encapsulated within an ECM matrix is slower than for those cultured on 2D surfaces [73,74]. Nevertheless, after one week of direct perfusion, the diameter of the spheroids within the tissue construct increased from 40μm to 70μm (Fig 5D), showing extensive proliferation and self-aggregation activity within the tissue construct as these spheres likely were derived from single cells. Two distinct spheroid morphologies were encountered: a rounded-shape structure [75,76] characterized by robust cell-cell adhesion and organized nuclei distribution and a mass-shape structure [75,76] characterized by robust cell-cell adhesion and disorganized nuclei distribution (Fig. 5E-K). The rounded shape spheroids mostly resembled hepatoids, which are cluster of hepatocytes usually seen in in 3D matrices (Fig. 5E-K) [58]. Interestingly, our results are in agreement with a previous study [58], showing that HepG2 encapsulated within a collagen matrix with stiffness in the range of the physiological liver were able to induce the formation of spheroids with similar dimensions and morphologies as the ones presented in this study.

Conclusions

We introduce a novel strategy to fabricate and perfuse thick and densely populated engineered constructs with 3D vascular network and controlled mechanical properties, using the 3D molding approach. It was demonstrated that it is possible to fabricate 3D sacrificial templates with branches using commercially available FDM technology. The fabricated network, created in very soft gels, maintained their integrity and survived perfusion for more than two weeks. The proposed method allows the fabrication of tissue constructs, with cellular densities of native tissues (approximately 10–500 million cells ml^{-1}), able to sustain cellular survival, proliferation, and to promote more complex biological phenomena, as demonstrated by observations of in situ spheroid development. In addition, the engineered constructs could recapitulate the complex 3D microenvironment in terms of cellular adhesion, matrix elasticity and transport of molecules, which could enable advances in designing tissue engineered constructs for tumor modeling and for regenerative medicine.

Acknowledgements

References

[1]   L.G. Griffith, M. a Swartz, Capturing complex 3D tissue physiology in vitro., Nat. Rev. Mol. Cell Biol. 7 (2006) 211–24. doi:10.1038/nrm1858.

[2]   D. Huh, G. a. Hamilton, D.E. Ingber, From 3D cell culture to organs-on-chips, Trends Cell Biol. 21 (2011) 745–754. doi:10.1016/j.tcb.2011.09.005.

[3]   A. Schepers, C. Li, A. Chhabra, B.T. Seney, S. Bhatia, Engineering a perfusable 3D human liver platform from iPS cells., Lab Chip. 16 (2016) 2644–53. doi:10.1039/c6lc00598e.

[4]   S.N. Bhatia, D.E. Ingber, Microfluidic organs-on-chips, Nat. Biotechnol. 32 (2014) 760–772. doi:10.1038/nbt.2989.

[5]   V. Marx, Tissue engineering: Organs from the lab, Nature. 522 (2015) 373–377. doi:10.1038/522373a.

[6]   A. Atala, F.K. Kasper, A.G. Mikos, Engineering complex tissues., Sci. Transl. Med. 4 (2012) 160rv12. doi:10.1126/scitranslmed.3004890.

[7]   J. Yu, S. Peng, D. Luo, J.C. March, In vitro 3D human small intestinal villous model for drug permeability determination, Biotechnol. Bioeng. 109 (2012) 2173–2178. doi:10.1002/bit.24518.

[8]   S.C. Ramaiahgari, M.W. Den Braver, B. Herpers, V. Terpstra, J.N.M. Commandeur, B. Van De Water, L.S. Price, A 3D in vitro model of differentiated HepG2 cell spheroids with improved liver-like properties for repeated dose high-throughput toxicity studies, Arch. Toxicol. 88 (2014) 1083–1095. doi:10.1007/s00204-014-1215-9.

[9]   R. Alvania, The third dimension: cell biology comes alive, Trends Cell Biol. 21 (2011) 681. doi:10.1016/j.tcb.2011.09.009.

[10]   M.W. Tibbitt, K.S. Anseth, Dynamic microenvironments: the fourth dimension., Sci. Transl. Med. 4 (2012) 160ps24. doi:10.1126/scitranslmed.3004804.

[11]   F. Pampaloni, E.G. Reynaud, E.H.K. Stelzer, The third dimension bridges the gap between cell culture and live tissue., Nat. Rev. Mol. Cell Biol. 8 (2007) 839–845.

doi:10.1038/nrm2236.

[12]   S.N. Bhatia, G.H. Underhill, K.S. Zaret, I.J. Fox, Cell and tissue engineering for liver disease., Sci. Transl. Med. 6 (2014) 245sr2. doi:10.1126/scitranslmed.3005975.

[13]   R. Langer, J. Vacanti, Tissue engineering, Science (80-.). 260 (1993) 920–926. doi:10.1126/science.8493529.

[14]   S. V Murphy, A. Atala, 3D bioprinting of tissues and organs., Nat. Biotechnol. 32 (2014) 773–785. doi:10.1038/nbt.2958.

[15]   H.-W. Kang, S.J. Lee, I.K. Ko, C. Kengla, J.J. Yoo, A. Atala, A 3D bioprinting system to produce human-scale tissue constructs with structural integrity, Nat. Biotechnol. 34 (2016) 312–319. doi:10.1038/nbt.3413.

[16]   K. Schenke-Layland, R.M. Nerem, In vitro human tissue models — moving towards personalized regenerative medicine, Adv. Drug Deliv. Rev. 63 (2011) 195–196. doi:10.1016/j.addr.2011.05.001.

[17]   R.K. Jain, P. Au, J. Tam, D.G. Duda, D. Fukumura, Engineering vascularized tissue., Nat. Biotechnol. 23 (2005) 821–3. doi:10.1038/nbt0705-821.

[18]   T.J. Hinton, Q. Jallerat, R.N. Palchesko, J.H. Park, M.S. Grodzicki, H. Shue, M.H. Ramadan, A.R. Hudson, A.W. Feinberg, Three-dimensional printing of complex biological structures by freeform reversible embedding of suspended hydrogels, Sci. Adv. 1 (2015) 1–10. doi:10.1126/sciadv.1500758.

[19]   H. Bae, A.S. Puranik, R. Gauvin, F. Edalat, B. Carrillo-Conde, N.A. Peppas, A. Khademhosseini, Building Vascular Networks, Sci. Transl. Med. 4 (2012) 160ps23-160ps23. doi:10.1126/scitranslmed.3003688.

[20]   N. Annabi, A. Tamayol, J.A. Uquillas, M. Akbari, L.E. Bertassoni, C. Cha, G. Camci-Unal, M.R. Dokmeci, N.A. Peppas, A. Khademhosseini, 25th anniversary article: Rational design and applications of hydrogels in regenerative medicine, Adv. Mater. 26 (2014) 85–124. doi:10.1002/adma.201303233.

[21]   J.S. Miller, K.R. Stevens, M.T. Yang, B.M. Baker, D.-H.T. Nguyen, D.M. Cohen, E.

Toro, A. a Chen, P. a Galie, X. Yu, R. Chaturvedi, S.N. Bhatia, C.S. Chen, Rapid casting of patterned vascular networks for perfusable engineered three-dimensional tissues., Nat. Mater. 11 (2012) 768–74. doi:10.1038/nmat3357.

[22] E.T. Pashuck, M. Stevens, From clinical imaging to implantation of 3D printed tissues, Nat. Biotechnol. 34 (2016) 295–296. doi:10.1038/nbt.3503.

[23] S.J. Paulsen, J.S. Miller, Tissue vascularization through 3D printing: Will technology bring us flow?, Dev. Dyn. 244 (2015) 629–640. doi:10.1002/dvdy.24254.

[24] T. Billiet, M. Vandenhaute, J. Schelfhout, S. Van Vlierberghe, P. Dubruel, A review of trends and limitations in hydrogel-rapid prototyping for tissue engineering, Biomaterials. 33 (2012) 6020–6041. doi:10.1016/j.biomaterials.2012.04.050.

[25] F. Pati, J. Jang, D.-H. Ha, S. Won Kim, J.-W. Rhie, J.-H. Shim, D.-H. Kim, D.-W. Cho, Printing three-dimensional tissue analogues with decellularized extracellular matrix bioink, Nat. Commun. 5 (2014) 1–11. doi:10.1038/ncomms4935.

[26] W. Jia, P.S. Gungor-Ozkerim, Y.S. Zhang, K. Yue, K. Zhu, W. Liu, Q. Pi, B. Byambaa, M.R. Dokmeci, S.R. Shin, A. Khademhosseini, Direct 3D bioprinting of perfusable vascular constructs using a blend bioink, Biomaterials. 106 (2016) 58–68. doi:10.1016/j.biomaterials.2016.07.038.

[27] C. Colosi, S.R. Shin, V. Manoharan, S. Massa, M. Costantini, A. Barbetta, M.R. Dokmeci, M. Dentini, A. Khademhosseini, Microfluidic Bioprinting of Heterogeneous 3D Tissue Constructs Using Low-Viscosity Bioink, Adv. Mater. 28 (2016) 677–684a. doi:10.1002/adma.201503310.

[28] K.A. Homan, D.B. Kolesky, M.A. Skylar-Scott, J. Herrmann, H. Obuobi, A. Moisan, J.A. Lewis, Bioprinting of 3D Convoluted Renal Proximal Tubules on Perfusable Chips, Sci. Rep. 6 (2016) 34845. doi:10.1038/srep34845.

[29] C. Mandrycky, Z. Wang, K. Kim, D.H. Kim, 3D bioprinting for engineering complex tissues, Biotechnol. Adv. 34 (2016) 422–434. doi:10.1016/j.biotechadv.2015.12.011.

[30] Y.S. Zhang, A. Arneri, S. Bersini, S.R. Shin, K. Zhu, Z. Goli-Malekabadi, J. Aleman, C. Colosi, F. Busignani, V. Dell'Erba, C. Bishop, T. Shupe, D. Demarchi, M. Moretti,

M. Rasponi, M.R. Dokmeci, A. Atala, A. Khademhosseini, Bioprinting 3D microfibrous scaffolds for engineering endothelialized myocardium and heart-on-a-chip, Biomaterials. 110 (2016) 45–59. doi:10.1016/j.biomaterials.2016.09.003.

[31]   P. Bajaj, R.M. Schweller, A. Khademhosseini, J.L. West, R. Bashir, 3D Biofabrication Strategies for Tissue Engineering and Regenerative Medicine., Annu. Rev. Biomed. Eng. 16 (2014) 247–76. doi:10.1146/annurev-bioeng-071813-105155.

[32]   J. Jang, H.J. Park, S.W. Kim, H. Kim, J.Y. Park, S.J. Na, H.J. Kim, M.N. Park, S.H. Choi, S.H. Park, S.W. Kim, S.M. Kwon, P.J. Kim, D.W. Cho, 3D printed complex tissue construct using stem cell-laden decellularized extracellular matrix bioinks for cardiac repair, Biomaterials. 112 (2017) 264–274. doi:10.1016/j.biomaterials.2016.10.026.

[33]   D.B. Kolesky, K.A. Homan, M.A. Skylar-Scott, J.A. Lewis, Three-dimensional bioprinting of thick vascularized tissues., Proc. Natl. Acad. Sci. U. S. A. 113 (2016) 3179–84. doi:10.1073/pnas.1521342113.

[34]   W.-Y. Yeong, C.-K. Chua, K.-F. Leong, M. Chandrasekaran, M.-W. Lee, Indirect fabrication of collagen scaffold based on inkjet printing technique, Rapid Prototyp. J. 12 (2006) 229–237. doi:10.1108/13552540610682741.

[35]   J. He, D. Li, Y. Liu, H. Gong, B. Lu, Indirect fabrication of microstructured chitosan-gelatin scaffolds using rapid prototyping, Virtual Phys. Prototyp. 3 (2008) 159–166. doi:10.1080/17452750802315033.

[36]   J.Y. Tan, C.K. Chua, K.F. Leong, Indirect fabrication of gelatin scaffolds using rapid prototyping technology, Virtual Phys. Prototyp. 5 (2010) 45–53. doi:10.1080/17452751003759144.

[37]   X.-Y. Wang, Z.-H. Jin, B.-W. Gan, S.-W. Lv, M. Xie, W.-H. Huang, Engineering interconnected 3D vascular networks in hydrogels using molded sodium alginate lattice as the sacrificial template., Lab Chip. (2014). doi:10.1039/c4lc00069b.

[38]   A. Tocchio, M. Tamplenizza, F. Martello, I. Gerges, E. Rossi, S. Argentiere, S. Rodighiero, W. Zhao, P. Milani, C. Lenardi, Versatile fabrication of vascularizable

scaffolds for large tissue engineering in bioreactor, Biomaterials. 45 (2015) 124–131. doi:10.1016/j.biomaterials.2014.12.031.

[39]   S. Mohanty, L.B. Larsen, J. Trifol, P. Szabo, H.V.R. Burri, C. Canali, M. Dufva, J. Emnéus, A. Wolff, Fabrication of scalable and structured tissue engineering scaffolds using water dissolvable sacrificial 3D printed moulds, Mater. Sci. Eng. C. 55 (2015) 569–578. doi:10.1016/j.msec.2015.06.002.

[40]   S. Mohanty, K. Kuldeep, A. Heiskanen, J. Trifol Guzman, P. Szabo, M. Dufva, J. Emnéus, A. Wolff, Fabrication of scalable tissue engineering scaffolds with dual-pore microarchitecture by combining 3D printing and particle leaching, Mater. Sci. Eng. C Mater. Biol. Appl. 61 (2016) 180–189. doi:10.1016/j.msec.2015.12.032.

[41]   J.B. Lee, X. Wang, S. Faley, B. Baer, D.A. Balikov, H.J. Sung, L.M. Bellan, Development of 3D Microvascular Networks Within Gelatin Hydrogels Using Thermoresponsive Sacrificial Microfibers, Adv. Healthc. Mater. 5 (2016) 781–785. doi:10.1002/adhm.201500792.

[42]   S. Li, Y.-Y. Liu, L.-J. Liu, Q.-X. Hu, A Versatile Method for Fabricating Tissue Engineering Scaffolds with a Three-Dimensional Channel for Prevasculature Networks., ACS Appl. Mater. Interfaces. 8 (2016) 25096–103. doi:10.1021/acsami.6b07725.

[43]   D.B. Kolesky, R.L. Truby, a S. Gladman, T. a Busbee, K. a Homan, J. a Lewis, 3D Bioprinting of Vascularized, Heterogeneous Cell-Laden Tissue Constructs., Adv. Mater. (2014) 1–7. doi:10.1002/adma.201305506.

[44]   V.K. Lee, D.Y. Kim, H. Ngo, Y. Lee, L. Seo, S.S. Yoo, P.A. Vincent, G. Dai, Creating perfused functional vascular channels using 3D bio-printing technology, Biomaterials. 35 (2014) 8092–8102. doi:10.1016/j.biomaterials.2014.05.083.

[45]   V.K. Lee, A.M. Lanzi, H. Ngo, S.S. Yoo, P.A. Vincent, G. Dai, Generation of multi-scale vascular network system within 3D hydrogel using 3D bio-printing technology, Cell. Mol. Bioeng. 7 (2014) 460–472. doi:10.1007/s12195-014-0340-0.

[46]   L.E. Bertassoni, M. Cecconi, V. Manoharan, M. Nikkhah, J. Hjortnaes, A.L. Cristino,

G. Barabaschi, D. Demarchi, M.R. Dokmeci, Y. Yang, A. Khademhosseini, Hydrogel bioprinted microchannel networks for vascularization of tissue engineering constructs, Lab Chip. 14 (2014) 2202–2211. doi:10.1039/C4LC00030G.

[47] W. Zhu, X. Qu, J. Zhu, X. Ma, S. Patel, J. Liu, P. Wang, C.S.E. Lai, M. Gou, Y. Xu, K. Zhang, S. Chen, Direct 3D bioprinting of prevascularized tissue constructs with complex microarchitecture, Biomaterials. 124 (2017) 106–115. doi:10.1016/j.biomaterials.2017.01.042.

[48] Q. Gao, Y. He, J. zhong Fu, A. Liu, L. Ma, Coaxial nozzle-assisted 3D bioprinting with built-in microchannels for nutrients delivery, Biomaterials. 61 (2015) 203–215. doi:10.1016/j.biomaterials.2015.05.031.

[49] E.C. Novosel, C. Kleinhans, P.J. Kluger, Vascularization is the key challenge in tissue engineering., Adv. Drug Deliv. Rev. 63 (2011) 300–11. doi:10.1016/j.addr.2011.03.004.

[50] J. Rouwkema, A. Khademhosseini, Vascularization and Angiogenesis in Tissue Engineering: Beyond Creating Static Networks, Trends Biotechnol. 34 (2016) 733–745. doi:10.1016/j.tibtech.2016.03.002.

[51] A.G. Mikos, S.W. Herring, P. Ochareon, J. Elisseeff, H.H. Lu, R. Kandel, F.J. Schoen, M. Toner, D. Mooney, A. Atala, M.E. Van Dyke, D. Kaplan, G. Vunjak-Novakovic, Engineering complex tissues., Tissue Eng. 12 (2006) 3307–39. doi:10.1089/ten.2006.12.3307.

[52] A. Skardal, J. Zhang, L. McCoard, X. Xu, S. Oottamasathien, G.D. Prestwich, Photocrosslinkable hyaluronan-gelatin hydrogels for two-step bioprinting., Tissue Eng. Part A. 16 (2010) 2675–85. doi:10.1089/ten.TEA.2009.0798.

[53] Y. Xu, X. Wang, Fluid and cell behaviors along a 3D printed alginate/gelatin/fibrin channel, Biotechnol. Bioeng. 112 (2015) 1683–1695. doi:10.1002/bit.25579.

[54] A.J. Engler, S. Sen, H.L. Sweeney, D.E. Discher, Matrix elasticity directs stem cell lineage specification., Cell. 126 (2006) 677–89. doi:10.1016/j.cell.2006.06.044.

[55] P.M. Gilbert, K.L. Havenstrite, K.E.G. Magnusson, A. Sacco, N.A. Leonardi, P. Kraft,

N.K. Nguyen, S. Thrun, M.P. Lutolf, H.M. Blau, Substrate elasticity regulates skeletal muscle stem cell self-renewal in culture., Science. 329 (2010) 1078–81. doi:10.1126/science.1191035.

[56] P.N. Patel, C.K. Smith, C.W. Patrick, Rheological and recovery properties of poly(ethylene glycol) diacrylate hydrogels and human adipose tissue, J. Biomed. Mater. Res. - Part A. 73 (2005) 313–319. doi:10.1002/jbm.a.30291.

[57] M. Yoneda, M. Yoneda, M. Yoneda, K. Fujita, K. Fujita, M. Inamori, M. Inamori, M. Tamano, M. Tamano, H. Hiriishi, H. Hiraishi, A. Nakajima, A. Nakajima, Transient elastography in patients with non-alcoholic fatty liver disease (NAFLD)., Gut. 56 (2007) 1330–1. doi:10.1136/gut.2007.126417.

[58] Y. Liang, J. Jeong, R.J. DeVolder, C. Cha, F. Wang, Y.W. Tong, H. Kong, A cell-instructive hydrogel to regulate malignancy of 3D tumor spheroids with matrix rigidity, Biomaterials. 32 (2011) 9308–9315. doi:10.1016/j.biomaterials.2011.08.045.

[59] H. Fuchsbauer, Influence of gelatin matrices cross-linked with transglutaminase on the properties of an enclosed bioactive material using β-galactosidase as model system, Biomaterials. 17 (1996) 1481–1488. doi:10.1016/0142-9612(96)89772-9.

[60] D.Y.S. Chau, R.J. Collighan, E.A.M. Verderio, V.L. Addy, M. Griffin, The cellular response to transglutaminase-cross-linked collagen., Biomaterials. 26 (2005) 6518–29. doi:10.1016/j.biomaterials.2005.04.017.

[61] R.. de Carvalho, C.R.. Grosso, Characterization of gelatin based films modified with transglutaminase, glyoxal and formaldehyde, Food Hydrocoll. 18 (2004) 717–726. doi:10.1016/j.foodhyd.2003.10.005.

[62] P.C. Georges, J.-J. Hui, Z. Gombos, M.E. McCormick, A.Y. Wang, M. Uemura, R. Mick, P. a Janmey, E.E. Furth, R.G. Wells, Increased stiffness of the rat liver precedes matrix deposition: implications for fibrosis., Am. J. Physiol. Gastrointest. Liver Physiol. 293 (2007) G1147-54. doi:10.1152/ajpgi.00032.2007.

[63] F. Müller-Plathe, Diffusion of water in swollen poly(vinyl alcohol) membranes studied by molecular dynamics simulation, J. Memb. Sci. 141 (1998) 147–154.

doi:10.1016/S0376-7388(97)00289-5.

[64]   W.J. Polacheck, A.E. German, A. Mammoto, D.E. Ingber, R.D. Kamm,
        Mechanotransduction of fluid stresses governs 3D cell migration., Proc. Natl. Acad.
        Sci. U. S. A. 111 (2014) 2447–52. doi:10.1073/pnas.1316848111.

[65]   W.J. Polacheck, J.L. Charest, R.D. Kamm, B. Shu Chien, Interstitial flow influences
        direction of tumor cell migration through competing mechanisms, Proc. Natl. Acad.
        Sci. 108 (2011) 11115–11120. doi:10.1073/pnas.1103581108.

[66]   F. Spill, D.S. Reynolds, R.D. Kamm, M.H. Zaman, Impact of the physical
        microenvironment on tumor progression and metastasis, Curr. Opin. Biotechnol. 40
        (2016) 41–48. doi:10.1016/j.copbio.2016.02.007.

[67]   U. Haessler, J.C.M. Teo, D. Foretay, P. Renaud, M. a. Swartz, Migration dynamics of
        breast cancer cells in a tunable 3D interstitial flow chamber, Integr. Biol. 4 (2012) 401.
        doi:10.1039/c1ib00128k.

[68]   E. Leclerc, Y. Sakai, T. Fujii, Cell culture in 3-dimensional microfluidic structure of
        PDMS (polydimenthylsiloxane), Biomed. Microdevices. 5 (2003) 109–114.
        doi:10.1023/A:1024583026925.

[69]   A. Skardal, T. Shupe, A. Atala, Organoid-on-a-chip and body-on-a-chip systems for
        drug screening and disease modeling, Drug Discov. Today. 21 (2016) 1399–1411.
        doi:10.1016/j.drudis.2016.07.003.

[70]   E.L.S. Fong, D.A. Harrington, M.C. Farach-Carson, H. Yu, Heralding a new paradigm
        in 3D tumor modeling, Biomaterials. 108 (2016) 197–213.
        doi:10.1016/j.biomaterials.2016.08.052.

[71]   B.M. Baker, C.S. Chen, Deconstructing the third dimension - how 3D culture
        microenvironments alter cellular cues, J. Cell Sci. 125 (2012) 3015–3024.
        doi:10.1242/jcs.079509.

[72]   M.H. Zaman, L.M. Trapani, A.L. Sieminski, D. MacKellar, H. Gong, R.D. Kamm, A.
        Wells, D.A. Lauffenburger, P. Matsudaira, Migration of tumor cells in 3D matrices is
        governed by matrix stiffness along with cell-matrix adhesion and proteolysis, Proc.

Natl. Acad. Sci. 103 (2006) 10889–10894. doi:10.1073/pnas.0604460103.

[73]   M.E. Dolega, M. Delarue, F. Ingremeau, J. Prost, A. Delon, G. Cappello, Cell-like
        pressure sensors reveal increase of mechanical stress towards the core of multicellular
        spheroids under compression, Nat. Commun. 8 (2017) 14056.
        doi:10.1038/ncomms14056.

[74]   L. Meli, E.T. Jordan, D.S. Clark, R.J. Linhardt, J.S. Dordick, Influence of a three-
        dimensional, microarray environment on human Cell culture in drug screening systems,
        Biomaterials. 33 (2012) 9087–9096. doi:10.1016/j.biomaterials.2012.08.065.

[75]   P.A. Kenny, G.Y. Lee, C.A. Myers, R.M. Neve, J.R. Semeiks, P.T. Spellman, K.
        Lorenz, E.H. Lee, M.H. Barcellos-Hoff, O.W. Petersen, J.W. Gray, M.J. Bissell, The
        morphologies of breast cancer cell lines in three-dimensional assays correlate with their
        profiles of gene expression, Mol. Oncol. 1 (2007) 84–96.
        doi:10.1016/j.molonc.2007.02.004.

[76]   R. Edmondson, J.J. Broglie, A.F. Adcock, L. Yang, Three-dimensional cell culture
        systems and their applications in drug discovery and cell-based biosensors., Assay
        Drug Dev. Technol. 12 (2014) 207–18. doi:10.1089/adt.2014.573.

Author contribution

R.P.C. has designed and performed the experiments, analyzed and interpreted the data, made graphs and wrote the manuscript. Also, R.P.C has designed the hydrogel formulation and mechanically tested them, fabricated all the hardware parts (3D printing characterization, CAD modelling, electronic part), wrote the software for controlling the pumps, and made the theoretical analysis (i.e., FEM simulations). R.P.C. and S.K.K. have fabricated and characterized the 3D sacrificial structures printed in PVA. R.P.C. and C.C. have performed experiments with HepG2 cells and R.P.C. did the confocal imaging acquisitions of the cell constructs. J.E. and S.S.K. contributed with materials/tools. M.D. have designed the experiments, interpreted the results and wrote the manuscript.

Three-dimensional fabrication of thick and densely populated soft constructs with complex and actively perfused channel network

Rodrigo Pimentel C.[1], Suk Kyu Ko[1], Claudia Caviglia[1], Jenny Emnéus[1], Stephan Sylvest Keller[1] and Martin Dufva[1]
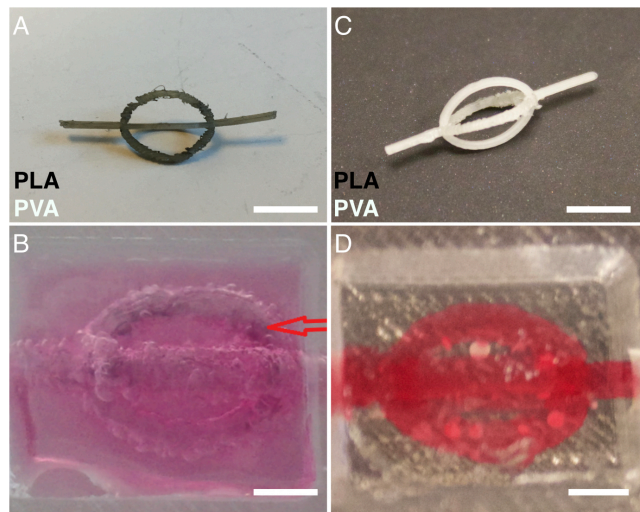
Supplementary information¨

Fig. S1. (A) Photograph of the 3D printed branch with four curved arms after the dissolution of the PLA material treated in 200 mL of chloroform and constant stirring (400 rpm). **(B)** Photograph of a 3D construct with the unremoved layer of PLA (arrow) fabricated using a 3D printed sacrificial template after the dissolution of the PLA material treated in 200 mL of chloroform and constant stirring (400 rpm) (Scale bar: 3 mm). **(C)** Photograph of the 3D printed branch with four curved arms. The sacrificial templates were treated as in **(A)** with the addition that the sacrificial templates were treated with 10 mL chloroform overnight (Scale bar: 5 mm). **(D)** Photograph of a 3D construct fabricated using a 3D printed sacrificial template with the extra treatment of PLA dissolution (Scale bar: 3 mm).
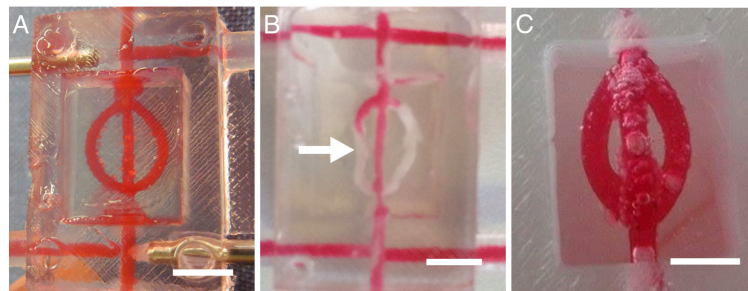
Fig. S2. (A) Photograph of a perfusable construct with 2D vasculature fabricated using gelatin 7.5% (w/v) cross-linked with 20 units of TG per g of gelatin, and a channel diameter smaller than 1mm. (B) Photograph of a perfusable 2D construct fabricated using gelatin 5% (w/v) cross-linked with 20 units of TG per g of gelatin with the undefined channel vasculature (arrow) (C) Photograph of a perfusable construct with 3D vasculature and channels diameter ~ 2mm fabricated using 3D sacrificial template, without actively removing the dissolved PVA. (Scale bars: 5mm).
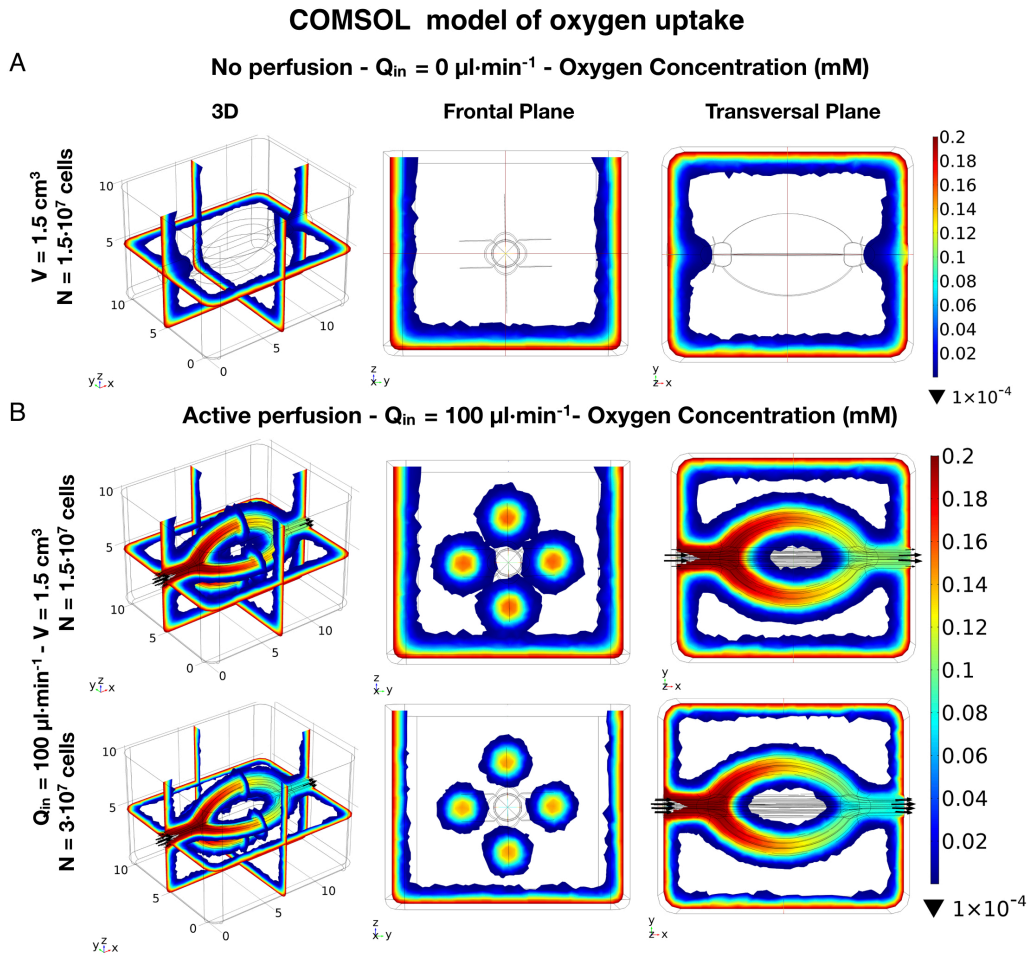

Fig. S3. Comsol model of oxygen uptake

Fig. S3. Comsol model of nutrient uptake (e.g. oxygen) of the vascularized 3D engineered tissue constructs with no active perfusion. The model shows that without the active perfusion, is theoretically not possible to maintain alive a thick and densely populated tissue construct. (B) Comsol model of nutrient uptake (e.g. oxygen) of the vascularized 3D engineered tissue constructs. Comparison of the consumption of oxygen between a tissue construct with $1.5 \cdot 10^7$ epG2 cells encapsulated into the interstitial space versus the second one with $3 \cdot 10^7$ HepG2 cells encapsulated cells encapsulated. In both cases the flow rate and the volume were the same (i.e., 100 µL·min^{-1} and 1.5 cm^3), matching the experimental one. The model shows that even by using a flow rate of 100 µL·min^{-1} theoretically is not possible to maintain alive all the cellular population within a thick and densely populated tissue construct.

Fig. S3

COMSOL Multiphysics (COMSOL Inc.) was used to estimate the oxygen and flow fields. Standard transport equations were used in the simulations. Navier-Stokes equations with no slip boundary was used for modelling of the flow. The concentration profile of dissolved oxy-

gen across the construct was simulated using a reaction-diffusion advection model. $1.5 \cdot 10^7$ and $3 \cdot 10^7$ non-growing HepG2 cells were assumed to be encapsulated evenly throughout a 1.5 cm^3 of hydrogel (modelled as water), and the inner vasculature was perfused with medium at the flow rate of 100 $\mu L \cdot min^{-1}$, and the oxygen concentration at the inlet was considered to be constant and uniform. At steady state, the mass transfer through the vasculature through the hydrogel construct can be described by Eq. 1 and 2:

$$\frac{\partial C_i}{\partial t} = D\nabla^2 C_i - \underline{v}\nabla C_i + R \tag{1}$$

$$\frac{\partial C_{Hyd}}{\partial t} = D_{eff}\nabla^2 C_{Hyd} + R \tag{2}$$

Here we assume that for the given cell concentration the rate of oxygen uptake can be described by Michaelis-Menten kinetics [1]:

$$R = -V_{max}\frac{C_{O_2}^{gel}}{K_M + C_{O_2}^{gel}} \cdot \delta(C_{O_2}^{gel} > C_{cr}^{gel}) \tag{3}$$

where V_{max} is the maximum oxygen uptake rate and K_M is the oxygen concentration at which uptake rate is half-maximal.

$$V_{max} = \frac{qN_{cells}}{V} \tag{4}$$

Although the cellular metabolic rate is recognized to be lower for the encapsulated cells within ECMs in comparison to the cells seeded in a 2D environment, the values used in this study were the ones obtained for the HepG2 cultured in a 2D environment [2]. In particular, q represents the oxygen consumption per cell; its value is $6.62 \cdot 10^{-17}$ $mol \cdot s^{-1}$ [3], N_{cells} is the number of cells, and V the volume of the hepatic construct in the bioreactor (1.5 mL). Moreover, a value of 6.3 μM [4] was considered for $K_{MM,O2}$, which represents the Michalis-Menten constant. A Heaviside function was implemented to account for the cellular necrosis and therefore to cut the oxygen consumption when the concentration falls below a critical value, $C_{Cr} = 1 \cdot 10^{-4}$ $mol \cdot m^3$ [5].

COMSOL model of fluid structure interaction in a vascular construct

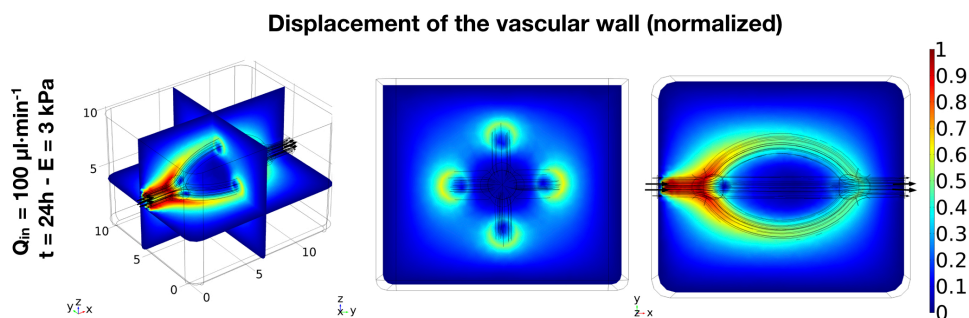**Displacement of the vascular wall (normalized)**

Fig. S4. Comsol model of the radial dilation of the vasculature walls within the hydrogel constructs in response to the pressure generated during the active perfusion. The dilation of the vascular walls leads to a compression of the hydrogel within the areas surrounding the vasculature

Fig. S4

COMSOL Multiphysics (COMSOL Inc.) was used to estimate the displacement and stresses of the vascular walls embedded in the hydrogel construct when subjected to the pressure generated by the fluid flow caused by the active perfusion of the construct. Standard mechanical equations were used in the simulations. Navier-Stokes equations with no-slip boundary was used for modeling of the flow. The displacement and stresses were modeled as one-way fluid interaction. The active perfusion and the fluid pressure is computed in the first step after 24h transient analysis. The forces exerted by the fluid on the walls of the vasculature are used as loads for the structural analysis of the surrounding hydrogel construct. Considering that the pressure generated during the active perfusion was small, it was sufficient to model the hydrogel as a linear elastic material. The compressive Young's modulus was evaluated experimentally from compressive mechanical tests. A compressive modulus of 3 kPa was used to simulate the construct. The structural analysis was calculated at 60-time points during 24 hours of active perfusion (every 24 minutes). A supplementary video was also created to illustrate the effect of the 24 hours perfusion within the tissue construct.

References

[1]   H.E. Abaci, R. Truitt, S. Tan, S. Gerecht, Unforeseen decreases in dissolved oxygen levels affect tube formation kinetics in collagen gels., Am. J. Physiol. Cell Physiol. 301 (2011) C431-40. doi:10.1152/ajpcell.00074.2011.

[2]   A. Ahluwalia, Allometric scaling in-vitro, Nat. Publ. Gr. (2016) 1–7. doi:10.1038/srep42113.

[3]   K. Mehta, G. Mehta, S. Takayama, J. Linderman, Quantitative inference of cellular parameters from microfluidic cell culture systems, Biotechnol. Bioeng. 103 (2009) 966–974. doi:10.1002/bit.22334.

[4]   N.S. Bhise, V. Manoharan, S. Massa, A. Tamayol, M. Ghaderi, M. Miscuglio, Q. Lang, Y. Shrike Zhang, S.R. Shin, G. Calzone, N. Annabi, T.D. Shupe, C.E. Bishop, A. Atala, M.R. Dokmeci, A. Khademhosseini, A liver-on-a-chip platform with bioprinted hepatic spheroids., Biofabrication. 8 (2016) 14101. doi:10.1088/1758-5090/8/1/014101.

[5]   P. Buchwald, FEM-based oxygen consumption and cell viability models for avascular pancreatic islets., Theor. Biol. Med. Model. 6 (2009) 5. doi:10.1186/1742-4682-6-5.

CHAPTER 5

FABRICATION OF A HYDROGEL-BASED FLUIDIC SYSTEM WITH INTEGRATED

SENSORS CAPABLE OF SIMULATING PHYSIOLOGICAL BARRIERS

Fabrication of a hydrogel-based fluidic system with integrated sensors capable of simulating physiological barriers

Rodrigo Pimentel C.[1], Claudia Caviglia[1], Maria Luisa Marini[1], Stephan Sylvest Keller[1] and Martin Dufva[1]

[1] *Department of Micro- and Nanotechnology, Technical University of Denmark, Denmark*

Keywords: Barrier models, TEER, 3D molding, perfusion, soft tissues

Abstract

Biological barriers are created in vitro on top of porous membranes which do not fully recapitulate the *in vivo* microenvironment. Here we present a gelatin hydrogel device composed by two parallel 1.2 cm long microfluidic channels separated by a gelatin membrane of 370 μm for simulation of physiological barriers such as intestine and blood-brain barriers. The hydrogel device has integrated electrodes suitable for measuring trans-epithelial electrical resistance (TEER), a common-used parameter to assess biological membranes integrity. The device is fabricated using polyvinyl alcohol sacrificial molding using guides to incorporate electrodes into channels having 1.7 mm diameter. The described device has electrodes to assess TEER of the "intestine" channel and the "blood" channel respectively. The electrical characterization of the sensor was performed by using buffers proving that different conductivities could be measured. Electrical signals varied very little (max ± 3.5 Ω) during 48h perfusion with medium, indicating that the device could support long term experiments. The presented model could represent a step forward for the fabrication of fluidic devices that could mimic more closely the physiological barrier microenvironment.

Introduction

In multicellular organisms, epithelial and endothelial cell layers form selectively permeable interfaces between several tissue compartments (blood-brain barrier (Obermeier et al., 2013), intestinal mucosal (Turner, 2009), lung alveolar-capillary interface (Whitsett and Alenghat, 2015)). Tight junctions (intercellular connections) connect adjacent cells, regulate diffusion and facilitate active transport processes along the paracellular and intracellular pathways, respectively, to maintain homeostasis (Zihni et al., 2016). An intact barrier is crucial for the physiological activities of the tissue. However, cellular barriers can be modulated to be open or close by exposure to specific external stimuli, thus allowing controlled passage of molecules (Zihni et al., 2016).

Several *in vitro* barrier models for drug permeability studies have been proposed (Moraes et al., 2012). Typically, these systems consist of cell culture monolayers grown on permeable porous membranes designed to define both apical and basolateral compartments (Bhatia and Ingber, 2014). However, such system lacks the presence of extracellular matrix representative of characteristic interstitial tissue confined within the two cellular layers (Thuenauer et al., 2014) that is critical to recapitulate the tissue-tissue interfaces (Huh et al., 2011).

Several techniques have been developed to assess barrier integrity *in vitro*. Among these quantitative measurements of the permeability of the barrier to paracellular hydrophilic compounds of various molecular weights like radioactively labeled markers (i.e., sucrose, inulin, mannitol, albumin), nonradioactive fluorescence-labeled marker proteins (i.e., fluorescein isothiocyanate (FITC)- labeled dextrans), or enzymatic markers (i.e., as horseradish peroxidase (HRP)) (Srinivasan et al., 2015). Aside from being labor intensive and resource consuming, most of these conventional assays require the use of chemicals and labeling steps that can interfere with the transport process and/or disrupt cellular functions and thus the barrier integrity. Moreover, many of these assays are based on single end-point measurements without providing real-time insight about the barrier quality during cell proliferation and growth. Trans-epithelial electrical resistance (TEER) assesses the electrical resistance across a cellular monolayer (Benson et al., 2013; Srinivasan et al., 2015). TEER measurements have become a well-established method to characterize epithelial and endothelial tissue barrier integrity, and represent a non-destructive, label-free method to quantitatively monitor the integrity and permeability of the barrier in real-time. TEER can be obtained according to Ohm's Law by ap-

plying either a DC or AC voltage (usually 12.5 Hz) across the barrier, and measuring the resulting current (Benson et al., 2013; Srinivasan et al., 2015). However, more information about the barrier electrical properties (e.g. TEER, capacitance) can be obtained if the electrical resistance is measured over a range of AC frequencies, which is known as impedance spectroscopy (Srinivasan et al., 2015; Stolwijk et al., 2015). Conventional devices consist either of two sets of chopstick-like electrodes (i.e., Ag/AgCl or Platinum) placed one on each side of the cell layer (Douville et al., 2010; Ferrell et al., 2010; Kim et al., 2012) or special chambers with patterned electrodes (Ag/AgCl, gold, or Platinum) that enable measurements in culture inserts (Booth and Kim, n.d.; Hediger et al., 2001; Sun et al., 2010). However, these technical approaches are strongly dependent on handling and positioning of the probing electrodes and thus prone to errors, artefacts and large variance (Benson et al., 2013; Srinivasan et al., 2015). Existing systems such as transwell plates, which are characterized by a thin porous membrane, are limited to batch culture environments. Thus, these simple and widely used devices has limited possibilities to mimic the characteristic dynamical flow experienced by the cells lining across the barrier. To address these issues, attempts have been made with microfluidic systems (Thuenauer et al., 2014) mimicking i) the small distance between the blood vessel and the endothelium (Genes et al., 2007; Kim et al., 2012; Kim and Ingber, 2013), ii) blood flow by channels having diameters representative of the resistance vessels *in vivo* (Genes et al., 2007) and iii) integration of technology for *in situ* detection of the integrity of the barrier (TEER, cell capacitance) (Kim et al., 2012; Vogel et al., 2011). Several strategies to perform on-chip TEER measurements of endothelial monolayers grown on a porous membrane separating two parallel fluidic channels. Most of the proposed systems are characterized by semi-permeable membranes fabricated in PDMS (Booth and Kim, n.d.; Douville et al., 2010; Ferrell et al., 2010; Griep et al., 2013; Hediger et al., 2001; Huh et al., 2011; Kim et al., 2012; Ramadan et al., 2013; Sun et al., 2010; Vogel et al., 2011). These PDMS membranes are unable of recapitulating the intricate *in vivo* environment of a native vascular barrier (i.e. cell-cell, cell-extracellular matrix (ECM) interactions) (Moraes et al., 2012). Moreover, these thin barriers do not allow the creation of the third comportment often presented within the barrier itself which consist on cells presented in the connective tissue (Moraes et al., 2012).

In this work, we present an *in vitro* model capable of simulating physiological barriers. The system consists of two 1.2 cm long parallel fluidic channels separated by a hydrogel barrier of 370 µm thickness. Such device has the capacity to for instance model an intestine barrier (the

first channel), tissue e.g., smooth muscles cells or immune cells embedded in the gel and blood vessels (the second channel). It was demonstrated that the fabricated system is capable of discriminate electrolytes with different conductivities and that the device was capable to perform under continuous perfusion over 48h. The proposed *in vitro* device could represent a step forward in the fabrication of a more biomimetic system capable of simulate more closely the barrier microenvironment that could be beneficial for drug permeability studies as well as disease models.

Materials and Methods

Hydrogel preparation

The sacrificial templates and molds were designed and converted into STL files using CAD software (computer aided design, Dassault Systemes SolidWorks Corporation, US). All STL files were processed by KISSlicer (www.kisslicer.com/) software and sliced into 100-μm-thick layers to generate G-code instructions for the 3D printer. G-code instruction sets were sent to the printer using Repetier-host (https://www.repetier.com), an open-source 3D printer host program. Commercially available poly(vinyl alcohol) (PVA) and poly(lactice acid) (PLA) filaments (Makerbot Industries, Brooklyn, NY, USA) were printed using the Felix 3 (Felix Printers, IJsselstein, The Netherlands) printer with a nozzle diameter of 250 μm. All the sacrificial templates were printed using PVA as material. The printing settings were as follows: nozzle temperature 200 °C for the PVA, bed temperature 55 °C.

Fluidic mold design and fabrication

The fluidic mold used for casting the hydrogel and subsequent perfusion was a modified version from the one presented in the Chapter 3. The new fluidic mold was manufactured using flexible clear polydimethylsiloxane (PDMS, Sylgard 184, Dow Corning Corporation) polymer within a 3D printed mold. The new mold consisted of three main parts responsible for defining the external surface of the fluidic mold and one part 3D printed in water soluble PVA was responsible for defining the internal chamber (18 mm (L) x 14 mm (W) x 9 mm (H)), four hub-free stainless steel blunt needles (18G; Kimble Chase, Vineland, NJ) were used to define the fluidic connections, and four solid stainless steel needle electrodes (active electrode) (Neuroline Monopolar (74325-36/40), Ambu) were used to create the electrode guides (Figure 1A). Central to the fabrication of the fluidic mold, was the integration of four stainless

steel electrodes having an external diameter of 350 μm. To avoid undesired movements that could cause changes in the recorder electrical measurements, the electrodes needed to be positioned at the same location every time. Therefore, the bottom as well as the top part of the mold was designed to precisely allocate the four electrodes (Figure 1B). Moreover, the printed PVA mold responsible for defining the internal chamber, presented two guiding holes on each side of the part allowing the electrodes to be inserted and located at the same position prior the casting of the PDMS (Figure 1C).

As opposed to a fluidic mold used in Chapter 3, the mold must harbor two pair inlets and outlets corresponding protrusions were used to define these inlets and outlets (Figure 1C). The parts responsible for defining the external surface of the fluidic molds were fabricated using the Form 2 SLA 3D printer (Formlabs, Somerville, Massachusetts, USA). The photocurable resin employed in this study were: GPCL02 clear resin and GPWH02 white resin (Formlabs, Somerville, Massachusetts, USA). By contrast, the part responsible to define the internal chamber was fabricated by 3D printing the internal chamber in PVA with the following settings: 195 °C for the PVA, bed temperature 55 °C. The 3D printed parts together with the stainless-steel needles and electrodes were assembled into a mold and secured together using screws (Figure 1D). PDMS prepolymer (10:1 w/w ratio of PDMS to curing agent) was casted in the assembled 3D printed mold. The mold was degassed in a vacuum chamber to ensure the removal of the bubbles entrapped. Then, the mold with the polymer was placed in an oven overnight at 60˚C to ensure the polymer to be completely cured. After curing, the mold was disassembled (Figure 2E) and the resultant PDMS fluidic mold was immersed into water. In this way, the PVA printed part enclosed in the fluidic mold was dissolved in water revealing the desired inner chamber and the insertion guides for the four electrodes in the fluidic mold (Figure 2F). The fluidic molds were treated with oxygen plasma (125 W, 13.5 MHz, 50 sccm, and 40 millitorr) to render their surface hydrophilic. The mold was subsequently sterilized by autoclaving.
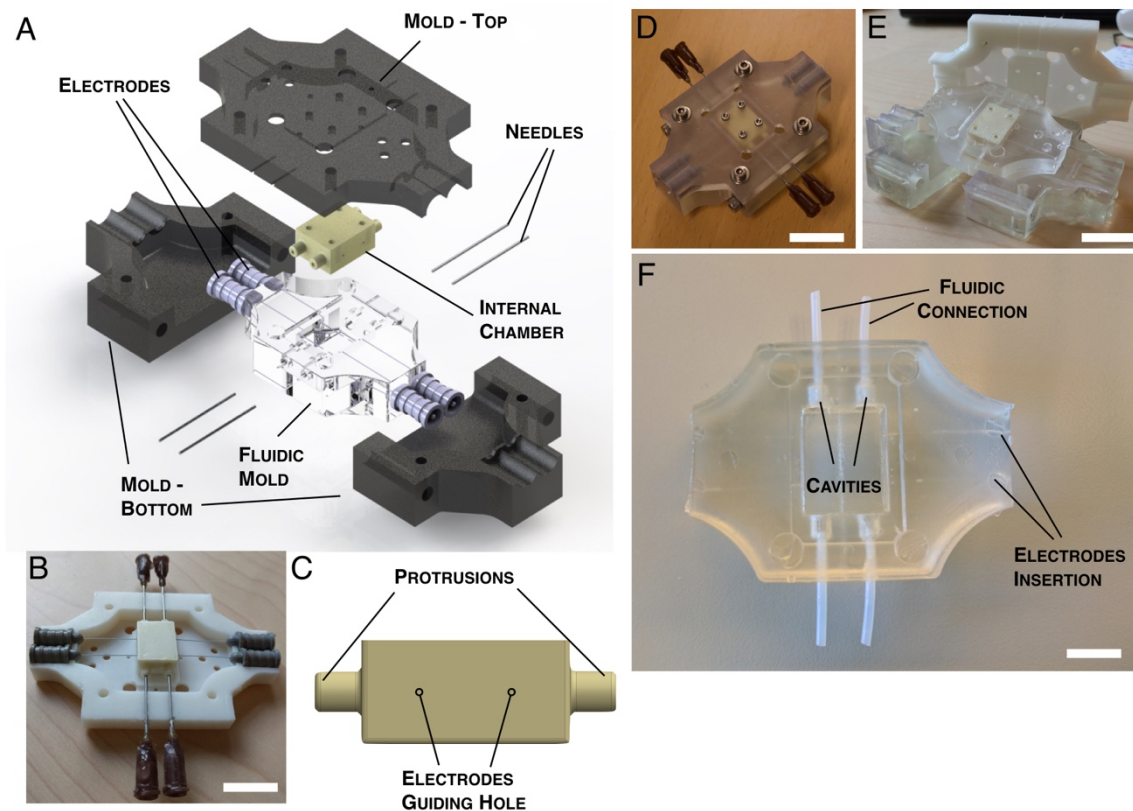
Figure 1. (A) Designed mold used for the fabrication of the fluidic mold. The mold consisted in three external parts responsible for defining the external surface of the fluidic mold while the internal chamber was designed and 3D printed in PVA to include the final cavities and the guides for the electrodes insertion. (B) Photograph of the mounted mold with screws and electrodes in place prior the casting of the PDMS used for the fabrication of the fluidic mold. (Scale bar: 3.5 cm) (C) Photograph of the de-molded mold revealing the fabricated fluidic mold before the dissolution of the 3D printed PVA structure responsible for defining the internal chamber. (Scale bar: 4 cm) (D) Photograph of the top part of the mold mounted with the PVA structure responsible for defining the internal chamber with the four electrodes in position and four needles responsible for defining the fluidic connections. (Scale bar: 2.5 cm) (E) CAD Designed of the part responsible for defining the internal chamber depicting the guides used to control the insertion and final position of the electrodes. (F) Photograph of the fabricated fluidic mold after the demold process and dissolution of the PVA printed part (Scale bar: 2.2 cm).

Fluidic Platform

Figure 2A shows the schematic of the fluidic platform utilized in the present study. The system has been described previously in chapter 3 of this thesis. Briefly, the fluidic platform was fabricated from PLA polymer by using a 3D printer. 3D printing settings were as follows: nozzle temperature 190 °C for PLA, bed temperature 55 °C. The device was modified to hold two fluidics devices with electrodes and cables by designing a new fluidic array. The fluidic array was fabricated using the Form 2 SLA 3D printer using the GPCL02 clear resin material. An arduino micro (Arduino, Italy) and an easydriver stepper motor driver (Brian Schmalz, Creative Commons Attribution 3.0 United States License) was mounted on the 3D printed

part to control and to power supply the stepper motor respectively. The 3D CAD assembly designed using SolidWorks, as well as Gcodes generated for every part can be downloaded at https://3dprint.nih.gov.
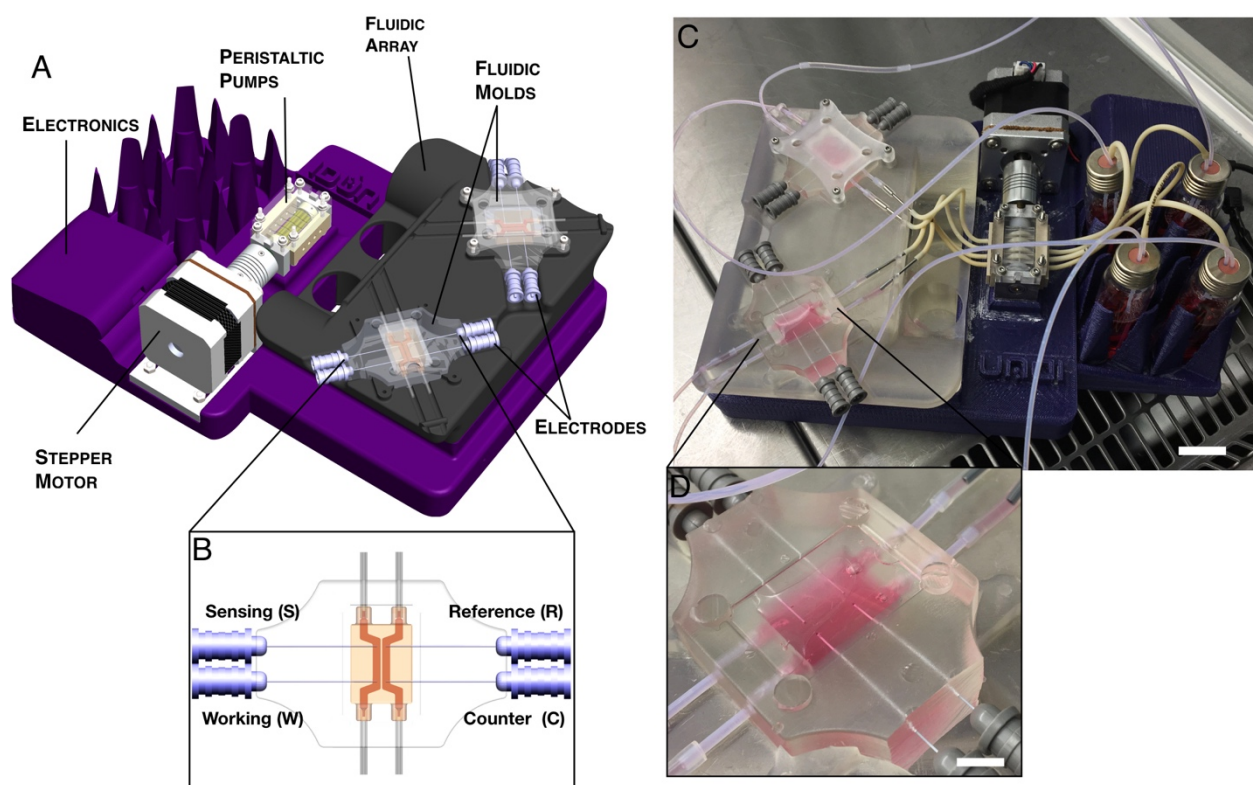

Figure 2. (A) Designed fluidic platform. (B) Designed hydrogel-based fluidic system with the schematic of the four-terminal sensing configuration used for impedance measurements. W and C form the source connections used to apply a defined current, while S and R form the sensing connections, used to record the resultant voltage. (C) Photograph of the assembled fluidic platform with the 2 fabricated hydrogel-based fluidic system. (Scale bars: 1.5 cm) (D) Photograph of the hydrogel-based fluidic system with integrated sensors for electrochemical impedance spectroscopy (EIS) measurements. (Scale bars: 1 cm)

Hydrogel based fluidic device fabrication and testing

The fluidic platform, glass vials, caps and polytetrafluoroethylene (PTFE) tubing (inner diameter of 0.8 mm) (BOLA 1818-10, Bohlender GmbH, Germany) were sterilized by autoclaving and then assembled in a laminar flow bench. 0.5 M NaOH was flushed throughout the system to ensure a sterile fluidic environment. The system was subsequently rinsed with sterile water and then perfused with culture medium. Sterile solid stainless steel needle electrodes were used. The needles were insulated except for the active electrode area determined by the exposed beveled tip. The 3D sacrificial templates were placed inside the fluidic molds. Subsequently, the four electrodes were inserted in the electrode guides until the needles went in

contact with the sacrificial templates. The electrodes were positioned across the barrier within the two channels and the configuration was as follows: working electrode facing the counter electrode (source connections) and sensing electrode facing the reference electrode (sensing connections) (Figure 2B). Gelatin 5% (w/v) cross-linked with 50 Units of TG per g of gelatin was prepared and incubated for 45 minutes at 37°C to partly crosslink the gelatin (it was still a solution although with high viscosity). A total of 0.5% (v/v) of chloroform was added to sterilize the solution. Once the electrodes and sacrificial templates were in position, 2.3 mL of gelatin/TG hydrogel was cast around the sacrificial templates and electrodes. After the casting, the samples were incubated at 4°C for 30 minutes to convert the liquid gelatin into a solid gel and to chemically cross link the gelatin. The fluidic device was subsequently incubated for 1h at ambient temperature to fully finalize the chemical cross-linking of the gelatin ensuring mechanical stability at higher temperatures. The fluidic molds were then placed in the fluidic platform and media was perfused through at $5\mu L\cdot min^{-1}$ for 30 minutes to ensure the total removal of the sacrificial template from the 3D constructs (Figure 2C-D). The final dimensions of the tissue constructs were 18 mm (L) x 14 mm (W) x 9 mm (H) with a resultant volume of $\approx 2.3\ cm^3$. Once the fluidic devices were ready, both channels were coated with 100 $\mu g\cdot mL^{-1}$ laminin in PBS for 20 minutes. Then, EIS measurements were performed for the fluidic devices in static and in perfusion conditions. A Four-terminal sensing method was used to perform the EIS measurements. In the perfusion conditions, the fluidic devices were placed in the fluidic platform, and both channels were continuously perfused with cell culture media at 65 $\mu L\cdot min^{-1}$ (fluid shear stress, 0.02 dyne·cm^{-2}) for 48h at 37 °C under 95% air 5% CO_2. In static conditions, the fluidic devices have both channels filled with cell culture media. EIS measurements were performed every 24h.

Electrical characterization

The electrical characterization was performed both on a gelatin hydrogel with and without the presence of fluidic channels. For the characterization of the hydrogel barrier, EIS measurements were acquired after filling the channels with solutions characterized by different conductivities. Air (σ = ~3-8 10^{-15} S·m^{-1}), 1:1, 1:2, 1:10 dilutions of phosphate buffered saline (PBS) in DI water (PBS σ = ~1.5 S·m^{-1}), and culture medium (DMEM Medium/1% Pen-Strep/20% fetal bovine serum (FBS)) (σ = ~0.25 S·m^{-1}) were employed as electrolytes. The influence of the position of the needle electrodes on the measured impedance was evaluated

by comparing spectra acquired at different distances (2, 3.5, 5.5 mm). The EIS analysis were performed using the galvanostic mode. For the recording of the EIS, a sinusoidal perturbation of 30 μA (RMS) with respect to the open circuit potential was applied in the frequency range between 1 kHz and 100 kHz, sampling at 10 points/decade. The measurements were performed using a PGSTAT128N potentiostat (Metronohm Autolab, The Netherlands), and MATLAB (Mathworks, Sweden) was used to analyze the acquired data. For every condition analyzed, three samples were used.

Cell seeding

Human intestinal epithelial Caco-2 cells (ATCC® HTB-37™) were grown in Dulbecco's Modified Eagle Medium (DMEM; Gibco) supplemented with 20% fetal bovine serum (FBS; Gibco), 1% penicillin/streptomycin (P/S; Gibco). Cells were maintained at 37°C in a humidified incubator under 5% CO_2 in air. Once the fluidic device was fabricated and both channels were coated with laminin for 15 minutes, Caco-2 cells were seeded into both channels at the cellular density of $1.5 \cdot 10^5$ cells·cm^{-2} and $8 \cdot 10^5$ cells·cm^{-2}. To avoid any aggregation or superposition of cells in the channels the device was flipped by 90° rotations every 30 minutes for 2 hours. Once the rotations were finished, one of the channels were gently flushed with fresh culture media and the other channel was not. After 24 hours, the hydrogel was removed from the fluidic mold, and was sectioned along the cross-sectional direction to evaluate the seeding quality.

Fluorescence staining

The seeding quality cell was assessed by staining the cells for the nuclei and F-actin within both the channels. Briefly, the samples were washed twice with PBS, fixed in 4.5% (v/v) paraformaldehyde in phosphate buffered solution (PBS) for 20 minutes, and permeabilized with 0.1% (v/v) Triton X-100 in PBS for 10 minutes followed by a PBS washing in between. Subsequently, they were stained for 45 minutes with Höechst 33342 (Invitrogen) for labeling the cell nuclei, and Phalloidin (F432, Invitrogen) for labeling the F-actins for labeling the cellular membrane according to manufacturer's instruction.

Imaging and analysis

Confocal acquisitions were performed using a Zeiss LSM 700 module in the Axio Imager M2 upright microscope using: an epiplan-neofluar 5X/0.13 HD, and 10X/0.25 HD. To eliminate any possible crosstalk between channels, images were collected with a sequential scan, using the following laser lines and mirror settings: 405 (30%) 420-480nm; 555(30%) 605-700nm. Photographs of the fabrication of the fluidic system were acquired using a DSLR camera (Canon EOS, 5D Mark II; Canon). ImageJ was used to visualize composite images by combining fluorescent channels, to visualize the dark-field mode images. The diameter of the channels was measured by ImageJ software using at least 4 images from different areas of 3 samples for each condition.

Results and discussion

3D printing and fabrication of the barrier fluidic device

3D printed PVA structures were used as the sacrificial template for creating two engineered channels separated by a barrier with a controlled thickness within hydrogels (fabrication described in chapter 3). Figure (3A-B) shows the designed CAD structure and the sacrificial templates 3D printed in PVA, respectively. The printed structure was planar and was designed to have dimensions of 1.2 mm (W) x 1.2 mm (H). The design of the printed PVA structure was chosen to give two independent channels separated by a hydrogel barrier with an intended thickness of 300 µm. The final printed structures had a width dimension of 1.33 ± 0.04 mm (W) and layer thickness of 1.21 ± 0.10 mm (H). The printed PVA templates and the four sensing electrodes were inserted into the fluidic mold. The position of the electrodes is controlled by the use to the guides for the electrodes integrated into the fluidic molds. The electrodes are inserted until the tip of the needle is in strong contact with the sacrificial templates printed in PVA (Figure 3C). Partially crosslinked gelatin/TG was cast around the printed PVA templates as well as the four electrodes (Figure 3D). The sacrificial templates were dissolved and removed from the gelatin/TG hydrogel leaving two well-defined and open channels separated by a thin barrier of hydrogel material (Figure 3E-F). The final gelatin/TG hydrogel fluidic device had dimensions of 18 mm (L) x 14 mm (W) x 9 mm (H) with a resultant volume of $\approx$ 2.3 cm^3. The width (W) and the height (H) of the two embedded channels within the hydrogel were then measured by microscopy. The final dimensions of the channels within the device were 1.78 ± 0.18 mm (W) and 1.76 ± 0.15 mm (H) (Figure 3G). The barrier thickness was

found to be 370 ± 75 µm (for a design of 300 µm). The structural stability of the fabricated device was tested by perfusing both channels with 65 µL·min⁻¹ for 48 hours at 37 °C. It was found that the device along with its built-in barrier was mechanically stable without any structural deformation in response to the volumetric flow rate or increase in temperature. The exposed area of the electrodes was in position inside the channels and stayed in place during perfusion (Figure 3H-G). Although it was possible to get barrier thickness smaller than 370 µm by changing the dimensions of the PVA sacrificial template, in most cases this resulted in merged channels. It was fundamental that the active area of the electrodes was precisely placed within both channels as well as without contacting the fluidic channels. Figure 3J shows that the exposed active electrode area is located within the fluidic channels. The presence of the electrodes insertion in the fluidic mold coupled with the crosslinked gelatin/TG hydrogel was sufficient to keep accurate the positioning of the electrodes. The electrodes neither influenced the final quality of the fabricated devices as well as the integrity of the barrier (Figure 3K).

As opposed to other proposed microfluidics devices (Bhatia and Ingber, 2014; Douville et al., 2010; Griep et al., 2013; Huh et al., 2013, 2011, 2010; Kim et al., 2012; Vogel et al., 2011),), the hydrogel-based fluidic system was fabricated using gelatin, a commonly used hydrogel material in tissue engineering applications (Drury and Mooney, 2003; Ito et al., 2003; Yung et al., 2007). This means that our system can present three distinct compartments (e.g., intestine, blood and connective/target tissue). This would allow the creation of different in vitro barrier models able to simulate different barrier environments (e.g., intestinal barrier, blood brain barrier) in more a physiological way by using the same device. The presence of the gelatin material would give the more characteristic cell-cell and cell-ECM interaction, which are so important for the cells correct functioning. The presence of two parallel channels of almost a cm in length would allow the formation of complex chemical gradients in both directions. The hydrogel barrier with thickness of 350 µm is at the same order of magnitude of the 200 µm distanced observed between capillaries (Thuenauer et al., 2014).
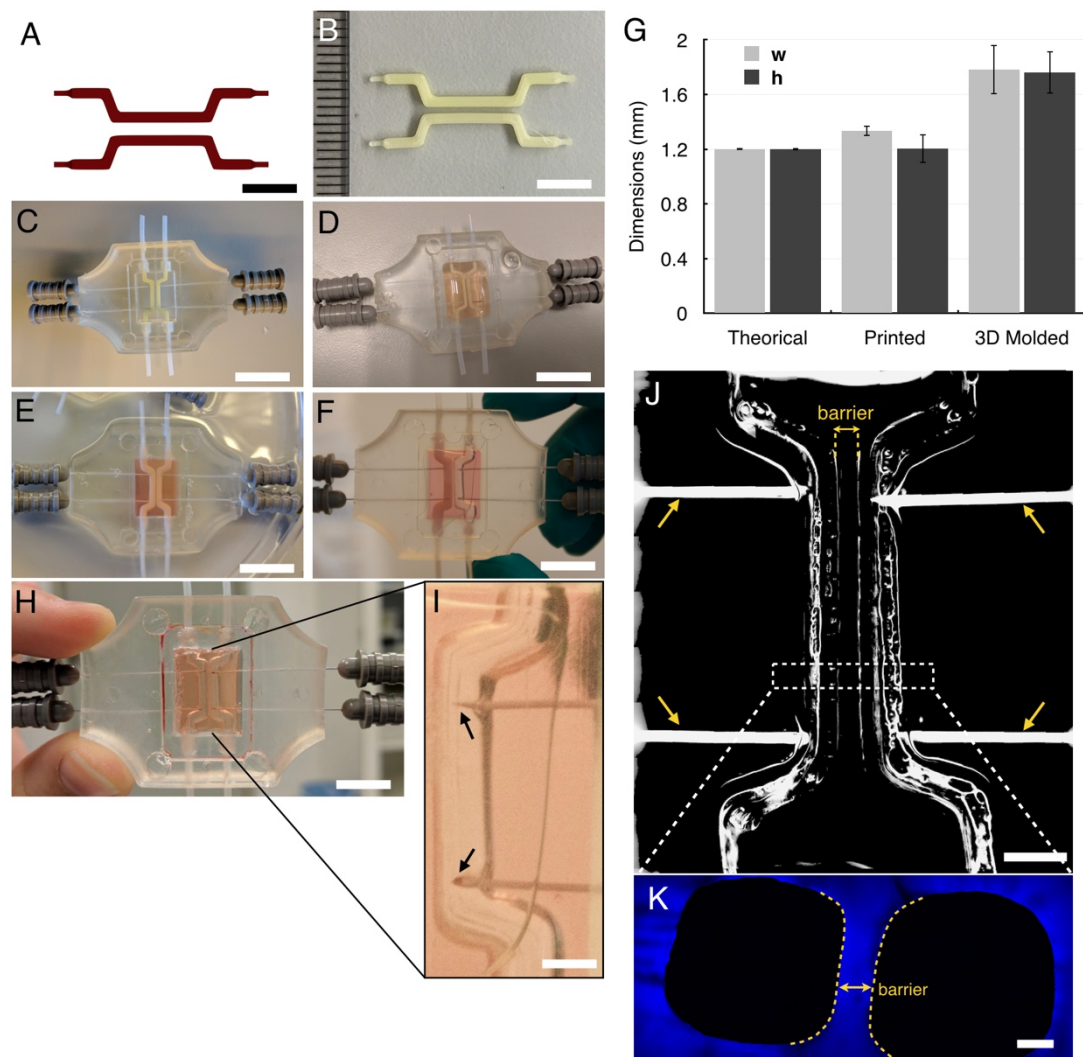
Figure 3. (A-B) Designed model and photograph of the two 3D printed structures using PVA as sacrificial material. (Scale bars: 6 mm) **(C)** Photograph of the inserted electrodes as well as the two PVA printed templates used for the creation of hydrogel-based fluidic device. (Scale bars: 2.5 cm) **(D)** Photograph of 3D printed sacrificial templates along with the electrodes embedded in a gelatin hydrogel construct before the dissolution and removal of PVA. (Scale bars: 2.2 cm) **(E-F)** Photograph of the **(E)** dissolved and **(F)** removed PVA from the right channel revealing the fluidic channel divided by the hydrogel barrier. (Scale bars: 2.2 cm, 1.8 cm) **(G)** Quantification of the dimensions of the designed channels, 3D printed templates, and embedded channels fabricated within the gelatin/TG hydrogel. **(H)** Hydrogel-based fluidic system continuously perfused on both channels at 65 µL·min⁻¹ after 48 h at 37°C. (Scale bar: 1.5 cm) **(I)** Magnification of the right channel depicted in G showing the active area of the electrodes inside the fluidic channels (indicated by the black arrows). (Scale bar: 1.5 cm) **(J)** Dark-field image of the hydrogel-base fluidic system integrating the needle electrodes: the two fluidic channels are separated by a hydrogel barrier with controlled thickness and the four electrodes (indicating by the yellow arrows) are inserted within the fluidic channels. (Scale bar: 2 mm) **(K)** Fluorescence micrograph of the cross-section of the fluidic device showing the two channels separated by the gelatin barrier (Scale bar: 500 µm)

Cell seeding optimization

Since the TEER represents the electrical resistance of a confluent monolayer of cells lining

within a channel, seeding tests were performed to form a confluent distribution of Caco2 cells

within the surface of the channels. When the seeding was performed using $1.5 \cdot 10^5$ cells·cm^{-2}, the Caco2 cells were lining on top of each other in one side of the channel after 24h incubation (Figure 4A). It is likely that the cells were aggregated on top of each as they had enough time to sediment. In contrast, we could observe a better cell distribution within the whole surface of the channels when rotating the fluidic device for 90° degrees every 45 minutes for a total of 3 hours (Figure 4B). To increase the coverage of the surface, $8 \cdot 10^5$ cells·cm^{-2} were seeded and the fluidic device was rotated as described above. After 45 minutes from the last rotation, one of the channels was flushed with fresh culture media, removing the excess of not adherent cells, while the other was not. After 24 hours, the cells were homogeneously distributed as well as covered the whole surface of the channels in both flushed and not flushed condition, respectively (Figure 4C-D). However, in the channel that was not flushed, a major aggregation and superposition of caco2 cells were observed after the last rotation (Figure 4C-D, left channel). This was not observed in the channel where the excess of non-adherent cells has been removed (Figure 4C-D, right channel).

Although in previous studies the caco2 density of $1.5 \cdot 10^5$ cells·cm^{-2} could create a confluent monolayer in a PDMS membrane (Kim et al., 2012; Kim and Ingber, 2013), the same did not happen for our gelatin fluidic device. One possible explanation is that since PDMS is a relatively stiff material and the surface occupied by the adherent cells is dependent on the stiffness of the substrate (Discher et al., 2009), it is possible to assume that the material could influence the number of cells needed for covering the whole surface. Considering that gelatin is softer compared to PDMS the overall morphology of the adherent caco2 cells most-likely would have been different. The results confirmed that it was necessary to increase five times the cell density necessary to form a confluent monolayer in a PDMS membrane to obtain the same confluent monolayer in our gelatin based fluidic device (Figure 4E).
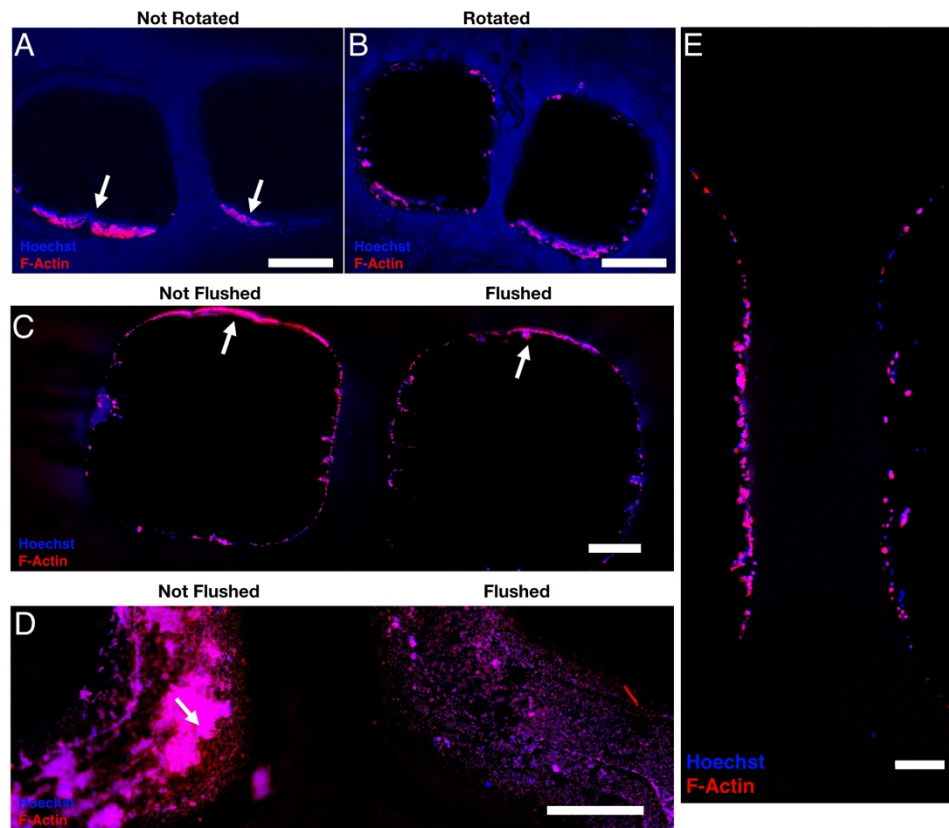
Figure 4. (A-B) Confocal microscopy images of nuclei (blue) and F-actin (red) of the hydrogel-based fluidic system cross-section at 24 hours after the seeding of $1.5 \cdot 10^5$ cells·cm^{-2} in both channels and without flushing; **(A)** when the fluidic device was not rotated the caco2 cells sediment on top of each other (as indicated by the white arrows) while **(B)** by rotating the fluidic device of 90° every 45 minutes, for a total of 3 hours, the cells started to be distributed within the surface of both channels. (Scale bars = 500 µm) **(C)** Confocal microscopy images of nuclei (blue) and F-actin (red) of the hydrogel-based fluidic system cross-section at 24 hours after the seeding of $8 \cdot 10^5$ cells·cm^{-2} in both channels and with rotation as described in B; when the fluidic device was not flushed (channel on the left) the caco2 cells sediment on top of each other in the last rotation position (as indicated by the white arrows) while when flushed (right channel) the amount of aggregate cells were smaller (as indicated by the white arrow) compared to the channel not flushed (Scale bar: 500 µm). **(D)** Confocal microscopy images of nuclei (blue) and F-actin (red) of the hydrogel-based fluidic system cross-section, parallel to both channels, at 24 hours after the seeding of $8 \cdot 10^5$ cells·cm^{-2} in both channels and with rotation as described in B confirming that when not flushed the cells will sediment on top of each other. (Scale bar: 1 mm) **(E)** Confocal microscopy images of nuclei (blue) and F-actin (red) of the hydrogel-based fluidic system cross-section, depicting the barrier and caco2 cells after 24 hours of the seeding of $8 \cdot 10^5$ cells·cm^{-2}. (Scale bar: 200 µm)

System characterization

A total of three different configurations were possible to use, allowing the sensing of three distinct areas in the barrier model (Figure 5A-C). When the couple S-R are inside of the 2 channels and characterized by a small distance, the measured TEER is an indication of the resistance of the barrier (Figure 5A). In this configuration, for a barrier model characterized by three compartments (e.g., intestinal channel, blood channels), the measured TEER repre-

sents the contribution of the sum of both compartments. When the R electrode is moved from inside the channel towards the hydrogel, it is possible to measure the TEER over a single compartment (Figure 5B). When the S electrode is moved away from inside the channel towards the hydrogel and the R electrode is moved back to the starting channel, it is possible to measure the TEER over the remaining compartment (Figure 5C). These three distinct configurations allow the independent measurement of each compartment at the time and, also, the contribution of both. The configuration with the couple S-R inside the channels was used throughout the rest of this study. To characterize the hydrogel barrier from an electrical point of view, impedance spectra were acquired in the configuration 1, both within a gelatin/TG hydrogel and across a gelatin/TG hydrogel barrier defined by two fluidic channels perfused with culture medium at 37 °C. Figure 5D shows that no significant differences could be observed between the recorded spectra for the hydrogel with channels filled with cell culture media and the hydrogel without channels. In both cases, the measured impedance magnitude was raging from 4Ω to 6Ω. The measured phase angle was ~0° throughout the whole frequency range (1-100 kHz), thus indicating that the bulk resistance (hydrogel) was measured (Figure 5E). The phase angle of 0° is characteristic from the impedance spectra acquired using the 4-point probe measurement setup as the electrode polarization does not occur in the sensing couple. On the contrary, the polarization of the system occurs at the source electrodes thus allowing the measuring system to be independent from the electrode polarization contribution (Grimnes and Martinsen, 2008). Since the gelatin/TG hydrogel was solubilized in the culture medium, and the channels were filled with the same medium, the conductivities of the two phases across the barrier (i.e., liquid and solid gel) were identical. This, together with the small width of the barrier (~370 μm) and the short distance between the needle electrodes (~1.2 mm) causes no relevant variations in the impedance magnitude. As the system needs to follow changes in conductivity, impedance measurements were conducted using air to model the insulating properties of a material having extremely lower conductivity. Figure 5D shows that when an insulating material, such as air, is present within the channels, the impedance magnitude increases from 6Ω to 10kΩ. To evaluate the system sensitivity, impedance spectra were acquired after injection of physiologically relevant solutions having different conductivity. As shown in Figure 5F, spectra were recorded using PBS (σ = ~1.5 S·m^{-1}), diluted PBS (1:2 and 1:10 in DI water) and culture medium (σ = ~0.25 S·m^{-1}). As expected, PBS had the lowest impedance magnitude value (~3 Ω) followed by medium (~4 Ω). By contrast, when

the conductivity of the solutions decreased (e.g., diluted PBS with DI water) the impedance magnitude increased (Figure 5F). However, due to the small volume of electrolyte within the fluidic channels (100 μl), the impedance magnitude variation did not scale up with overall conductivity changes. This was most-likely an indication of a fast diffusion of ions from the hydrogel bulk to the small volume of the measure electrolyte since the hydrogel was prepared by solubilizing gelatin material in cell culture media. Interesting to notice was that culture media in the channels resulted in a very stable impedance phase, with a resultant phase angle of 0 (Figure 5G). This proved that the system can discriminate between small variations in conductivity even though the volumes within the channels are small (~100 μL).
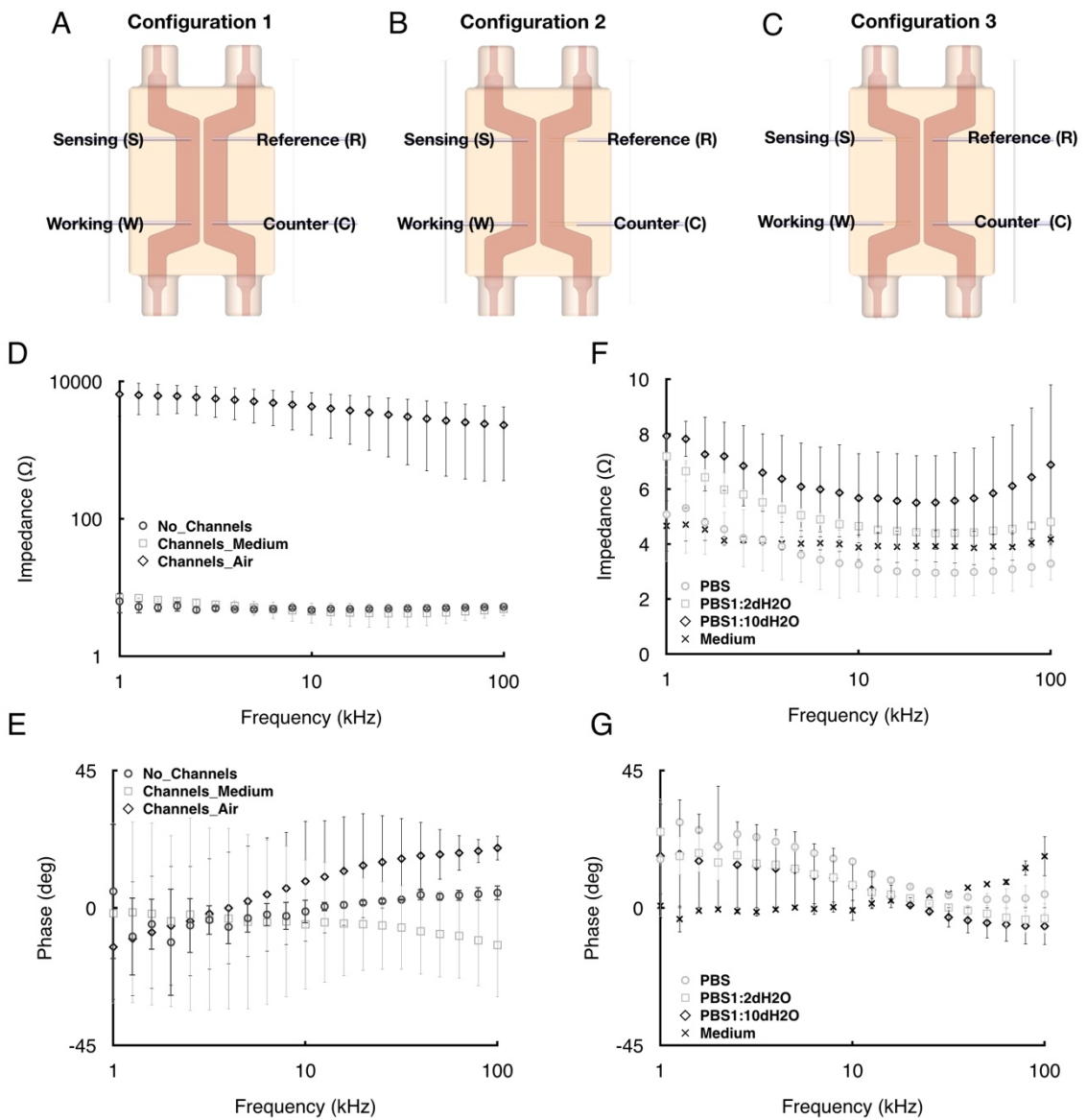
Figure 5. (A-C) Schematic of the four-terminal sensing with the 3 different configurations used for impedance measurements. W and C form the source connections used to apply a defined current, while S and R form the sensing connections, used to record the resultant voltage. (D-E) Bode plot ((D) magnitude and (E) phase angle) of the impedance spectra recorded at 37°C within a gelatin/TG hydrogel and across a gelatin/TG barrier defined by two fluidic channels perfused either with air or with culture medium. (F-G) Bode plot ((F) magnitude and (G) phase angle) of the impedance spectra acquired after injection of solutions having different conductivities: PBS (σ = ~1.5 S·m^{-1}), diluted PBS (1:2 and 1:10 in DI water) and culture medium (σ = ~0.25 S·m^{-1}). Data are presented as mean ± standard deviation (n = 3).

As reported in the literature, one of the main reasons for the significant variance of the reported TEER measurements is related to the electrode positioning across the barrier (Srinivasan et al., 2015). Therefore, we investigated the influence of the electrodes position on the recorded impedance. At first, we evaluated the effect of the needle electrodes being in contact with one of the walls inside the fluidic channel embedded in the hydrogel. To discriminate the contact effect of the needle, measurements were performed using air as an insulating material. Figure 6A shows impedance spectra recorded for electrodes well positioned within the fluidic channels and electrodes misplaced and in contact with the channel wall. The recorded values showed that the impedance significantly decreased (2 orders of magnitude) when the electrodes were not entirely insulated from the surrounding gelatin/TG hydrogel channels. This can be explained by the fact that the current flows throughout a path characterized by the higher conductance which in this case is the hydrogel rather than air. When the electrode is correctly inserted into the channels, the current is forced to flow throughout the air making the overall recorded impedance much higher. The needle contact effect has also an influence in the measured phase angle that widely deviates from the ideal behavior (phase angle = 0) with significant variations among the samples (Figure 6B). Next, the distance between the electrodes was varied by maintaining a pair of electrodes within one channel and moving the other pair of electrodes away from within the second channel until ending up in the hydrogel (Figure 6C). Impedance measurements were conducted for each distance (2, 3.5, 5.5 mm) with culture medium within the channels. As expected, by increasing the distance between the electrodes, the overall impedance magnitude increased (Figure 6D), and at the same time, the phase angle was almost zero (Figure 6E). However, when the electrodes were extremely close to each other, we could observe an increased phase shift probably due to an electrical coupling phenomenon.

As proof of concept, two fluidic samples integrating the measuring system were fabricated and the whole platform assembled. Then, a fluid flow of 65 µl·min^{-1} was applied (0.02 dyne·cm^{-2} shear stress) for 48h at 37 °C. In parallel, two other fluidic samples integrating the

measuring system were fabricated and were incubated at the same temperature for 48h as well. In all the cases cell culture media was used as the electrolyte. Figure 6F shows the impedance magnitude acquired every 24h for samples in static and flow conditions. It appears that for lower frequencies (1 kHz range) the impedance magnitude of samples under fluid flow is slightly higher than those not. By contrast, there is no significant difference between the static and the flow conditions for the mid-high frequencies range. The same behavior is seen in the phase as well (figure 6G). Samples in static conditions presented a phase angle close to the ideal behavior (phase angle = 0) whereas for samples in flow conditions there is a shift from the typical behavior for the low and for the high frequencies ($\sim$ -20° low frequencies, $\sim$ +40° high frequencies). The analysis of the equivalent circuit model of the impedance spectra can be used to quantify the electrical parameters which are characteristics of the barrier properties (i.e., TEER, cell capacitance) (Benson et al., 2013; Douville et al., 2010; Griep et al., 2013; Odijk et al., 2015; Srinivasan et al., 2015).
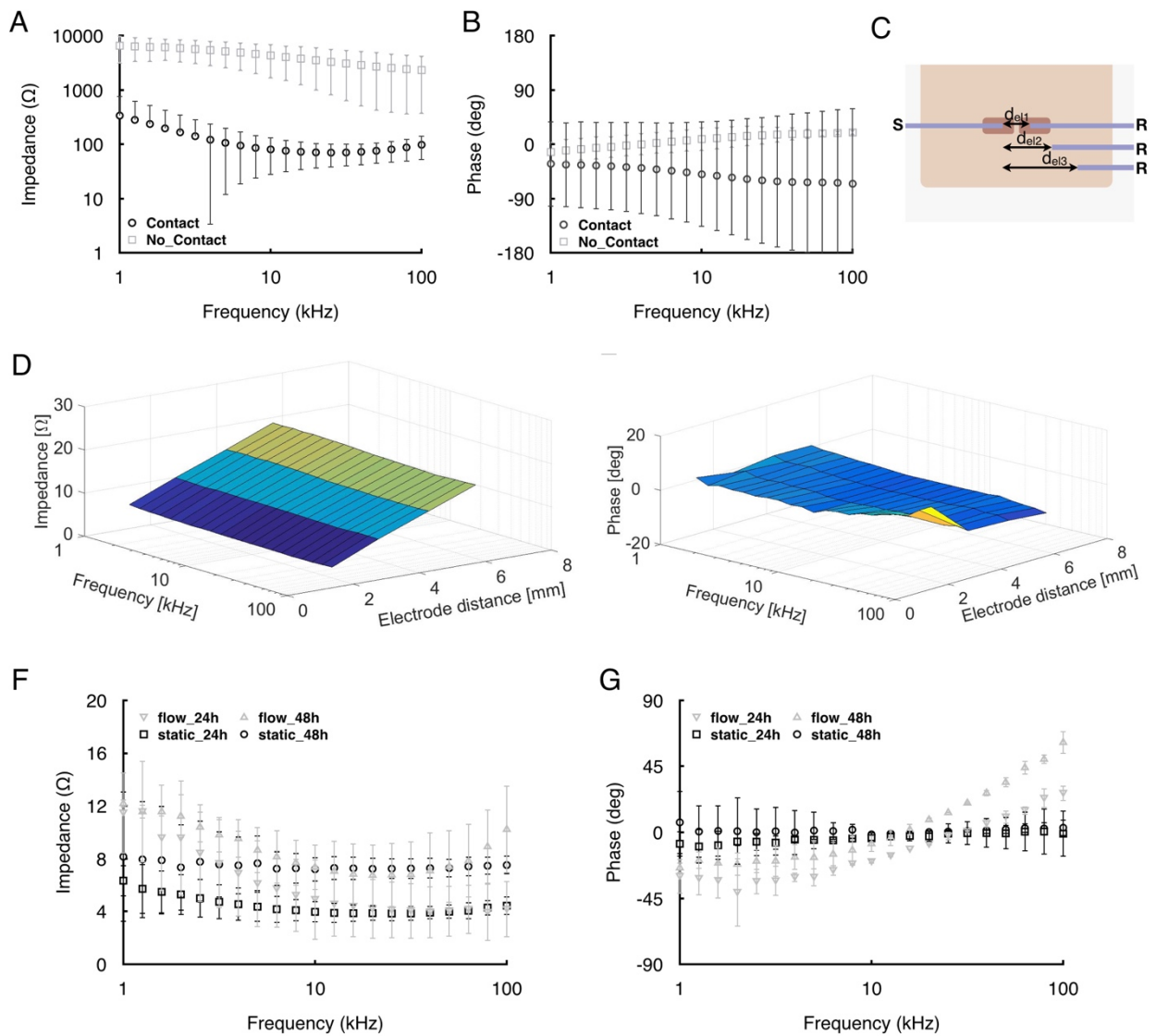
Figure 6. (A-B) Bode plot ((A) magnitude and (B) phase angle) of the impedance spectra acquired across a gelatin/TG barrier defined by two channels perfused with air. The plot shows the comparison of spectra acquired when the needle electrodes are correctly placed within the channel with spectra acquired when the electrodes are misplaced and in direct contact with the inner wall of the fluidic channels. **(C)** Schematic cross section of the hydrogel based fluidic system showing the needle electrodes positioning within the channels at different distances d_{ele} across the barrier. A pair of electrodes (S and W) was maintained within one channel while the other pair (R and C) was moved as depicted. **(D-E)** Representative 3D Bode plot ((D) magnitude and (E) phase angle), correlating the electrodes distance with the recorded impedance spectra. **(F-G)** Bode plot ((F) magnitude and (G) phase angle) of impedance measurements recorded across the barrier under static and flow condition at 37°C. Culture medium was used as electrolyte. Data are presented as mean ± standard deviation (n = 3).

Conclusions

Here we presented the fabrication of a hydrogel-based fluidic system with integrated needle electrodes capable of simulating physiological barriers. The system consisted of two inde-

pendent fluidic channels separated by a hydrogel membrane of 370 μm thickness. Four stainless steel electrodes with controlled position were integrated within the hydrogel construct. The system was fabricated using a gelatin/TG hydrogel and the electrodes were used for measuring impedance spectroscopy. It was shown that the sensor is capable to discriminate different materials with different conductivities maintaining a good sample to sample reproducibility. Finally, the fabricated fluidic devices were tested under continuous perfusion for 48h at 37 °C showing that the overall device is capable of perform real time and long term measurements. The proposed device could represent an ideal system to simulate different barrier models and could be beneficial for the fabrication of a more biomimetic device for drug permeability studies.

Acknowledgements

References

Benson, K., Cramer, S., Galla, H.-J., 2013. Impedance-based cell monitoring: barrier properties and beyond. Fluids Barriers CNS 10, 5. doi:10.1186/2045-8118-10-5

Bhatia, S.N., Ingber, D.E., 2014. Microfluidic organs-on-chips. Nat. Biotechnol. 32, 760–772. doi:10.1038/nbt.2989

Booth, R., Kim, H., n.d. Lab on a Chip Miniaturisation for che m istry , physics , biology , m aterials science and bioengineering. doi:10.1039/c2lc40094d

Discher, D.E., Mooney, D.J., Zandstra, P.W., 2009. Growth factors, matrices, and forces combine and control stem cells. Science 324, 1673–7. doi:10.1126/science.1171643

Douville, N.J., Tung, Y., Li, R., Wang, J.D., El-Sayed, M.E.H., Takayama, S., 2010. Fabrication of Two-Layered Channel System with Embedded Electrodes to Measure Resistance Across Epithelial and Endothelial Barriers. Anal. Chem. 82, 2505–2511. doi:10.1021/ac9029345

Drury, J.L., Mooney, D.J., 2003. Hydrogels for tissue engineering: scaffold design variables and applications. Biomaterials 24, 4337–4351. doi:10.1016/S0142-9612(03)00340-5

Ferrell, N., Desai, R.R., Fleischman, A.J., Roy, S., Humes, H.D., Fissell, W.H., 2010. A Microfluidic Bioreactor With Integrated Transepithelial Electrical Resistance (TEER) Measurement Electrodes for Evaluation of Renal Epithelial Cells. Biotechnol. Bioeng. 707–716. doi:10.1002/bit.22835

Genes, L.I., V Tolan, N., Hulvey, M.K., Martin, R.S., Spence, D.M., 2007. Addressing a vascular endothelium array with blood components using underlying microfluidic channels. Lab Chip 7, 1256–1259. doi:10.1039/b712619k

Griep, L.M., Wolbers, F., Wagenaar, B. De, Hall, W., 2013. BBB ON CHIP : microfluidic platform to mechanically and biochemically modulate blood-brain barrier function 15, 145–150. doi:10.1007/s10544-012-9699-7

Grimnes, S., Martinsen, Ø.G., 2008. Bioimpedance and Bioelectricity Basics, in: Bioimpedance and Bioelectricity Basics. Elsevier Ltd.

Hediger, S., Sayah, A., Horisberger, J.D., 2001. Modular microsystem for epithelial cell culture and electrical 16, 689–694.

Huh, D., Hamilton, G. a., Ingber, D.E., 2011. From 3D cell culture to organs-on-chips. Trends Cell Biol. 21, 745–754. doi:10.1016/j.tcb.2011.09.005

Huh, D., Kim, H.J., Fraser, J.P., Shea, D.E., Khan, M., Bahinski, A., Hamilton, G. a, Ingber, D.E., 2013. Microfabrication of human organs-on-chips. Nat. Protoc. 8, 2135–57. doi:10.1038/nprot.2013.137

Huh, D., Matthews, B.D., Mammoto, A., Hsin, H.Y., Ingber, D.E., 2010. Reconstituting Organ-Level

Lung Functions on a Chip. Science (80-.). 328, 1662–1668.

Ito, A., Mase, A., Takizawa, Y., Shinkai, M., Honda, H., Hata, K.-I., Ueda, M., Kobayashi, T., 2003. Transglutaminase-mediated gelatin matrices incorporating cell adhesion factors as a biomaterial for tissue engineering. J. Biosci. Bioeng. 95, 196–199. doi:10.1016/S1389-1723(03)80129-9

Kim, H.J., Huh, D., Hamilton, G., Ingber, D.E., 2012. Human gut-on-a-chip inhabited by microbial flora that experiences intestinal peristalsis-like motions and flow. Lab Chip 12, 2165. doi:10.1039/c2lc40074j

Kim, H.J., Ingber, D.E., 2013. Gut-on-a-Chip microenvironment induces human intestinal cells to undergo villus differentiation. Integr. Biol. 5, 1130. doi:10.1039/c3ib40126j

Moraes, C., Mehta, G., Lesher-Perez, S.C., Takayama, S., 2012. Organs-on-a-chip: a focus on compartmentalized microdevices. Ann. Biomed. Eng. 40, 1211–27. doi:10.1007/s10439-011-0455-6

Obermeier, B., Daneman, R., Ransohoff, R.M., 2013. Development , maintenance and disruption of the blood-brain barrier. Nat. Med. 19, 1584–1596. doi:10.1038/nm.3407

Odijk, M., van der Meer, A.D., Levner, D., Kim, H.J., van der Helm, M.W., Segerink, L.I., Frimat, J.-P., Hamilton, G.A., Ingber, D.E., van den Berg, A., 2015. Measuring direct current trans-epithelial electrical resistance in organ-on-a-chip microsystems. Lab Chip 15, 745–52. doi:10.1039/c4lc01219d

Ramadan, Q., Jafarpoorchekab, H., Huang, C., Silacci, P., Carrara, S., Koklü, G., Ghaye, J., Ramsden, J., Ruffert, C., Vergeres, G., Gijs, M.A.M., 2013. NutriChip: nutrition analysis meets microfluidics. Lab Chip 13, 196–203. doi:10.1039/C2LC40845G

Srinivasan, B., Kolli, A.R., Esch, M.B., Abaci, H.E., Shuler, M.L., Hickman, J.J., 2015. TEER Measurement Techniques for In Vitro Barrier Model Systems. J. Lab. Autom. 20, 107–126. doi:10.1177/2211068214561025

Stolwijk, J. a, Matrougui, K., Renken, C.W., Trebak, M., 2015. Impedance analysis of GPCR-mediated changes in endothelial barrier function: overview and fundamental considerations for stable and reproducible measurements. Pflügers Arch. - Eur. J. Physiol. 467, 2193–2218. doi:10.1007/s00424-014-1674-0

Sun, T., Swindle, E.J., Collins, J.E., Holloway, J.A., Davies, D.E., Morgan, H., 2010. On-chip epithelial barrier function assays using electrical impedance spectroscopy. Lab Chip 10, 1611. doi:10.1039/c000699h

Thuenauer, R., Rodriguez-Boulan, E., Römer, W., 2014. Microfluidic approaches for epithelial cell layer culture and characterisation. Analyst 139, 3206–3218. doi:10.1039/C4AN00056K

Turner, J.R., 2009. Intestinal mucosal barrier function in health and disease. Nat. Rev. Immunol. 9,

799–809. doi:10.1038/nri2653

Vogel, P.A., Halpin, S.T., Martin, R.S., Spence, D.M., 2011. Microfluidic transendothelial electrical resistance measurement device that enables blood flow and postgrowth experiments. Anal. Chem. 83, 4296–4301. doi:10.1021/ac2004746

Whitsett, J.A., Alenghat, T., 2015. Respiratory epithelial cells orchestrate pulmonary innate immunity. Nat. Publ. Gr. 16, 27–35. doi:10.1038/ni.3045

Yung, C.W., Wu, L.Q., Tullman, J.A., Payne, G.F., Bentley, W.E., Barbari, T.A., 2007. Transglutaminase crosslinked gelatin as a tissue engineering scaffold. J. Biomed. Mater. Res. A 83, 1039–46. doi:10.1002/jbm.a.31431

Zihni, C., Mills, C., Matter, K., Balda, M.S., 2016. Tight junctions : from simple barriers to multifunctional molecular gates. Nat. Publ. Gr. 17, 564–580. doi:10.1038/nrm.2016.80

CHAPTER 6
SUMMARY, CONCLUSIONS AND FUTURE WORK CONSIDERATIONS

6.1 Summary and Conclusions

This thesis presented two different approaches for the fabrication of *in vitro* systems for tissue engineered applications. In the first approach, scaffold, cells and bioreactors were used as building blocks (TE paradigm) to fabricate tissue constructs with relevant sizes. In the second approach, a sacrificial template is molded in hydrogels with controlled properties (e.g., chemical, mechanical) mixed with cells for fabricating constructs with integrated channel networks. The proposed approach offered several advantages, including that is easy to encapsulate the cells, it is perfusable, scalable, versatile and doesn't need any post fabrication procedures. Also, we showed an elegant solution to suppress leakage of these soft constructs while directly perfused for several days. The whole platform presented at this thesis would allow the design of modular TE constructs capable of simulating different compartments at the same time.

In **Chapter 2**, a modular in vitro system is presented for the differentiation under perfusion of hiPSCs. Porous elastomeric scaffolds with 3D architectures were fabricated using an inverse fabrication technique [1]. Such porous scaffolds were fabricated aiming to enhance the mass transport of oxygen and nutrients and the removal of waste within the construct. HiPSCs were seeded in the scaffolds and cultured in a perfusion bioreactor for 25 days. It was showed that controlling the flow rate, it was possible to control both the mass transport and the shear stress presented to the hiPSCs. It was demonstrated that the control of the culture parameters (e.g., induction factors and fluid flow) was critical for the maturation and differentiation of the hiPSCs towards hepatocytes. The differentiated hepatocytes under perfusion had several important overlapping markers with fresh human precision cut liver slices thus indicating a high degree of hepatic differentiation. These results indicate the importance of controlling the cellular microenvironment to guide the hiPSCs differentiation towards the desired phenotype. Such control is mediated by the synergies created between the scaffold, bioreactor and induction factors, as previously discussed in chapter one. Although the presented in vitro system was capable of differentiating hiPSCs into hepatocytes with a high degree of hepatic differentiation, there are some issues that need to be addressed. The proposed PDMS porous scaffold does not present mechanical properties comparable with the one presented by the liver, which is

critical in guiding differentiation, as previously described by Engler et al*. [2]. In addition, the porous architecture of the scaffold does not allow cell-cell and cell-ECM interactions in the 3D space. This is because the mean diameter of the pores is ~ 150 µm. Stevens et al. showed how the scaffold architecture affects the cell binding and spreading [3]. For scaffolds with microscale architecture, the cellular adhesion is comparable to the one found in flat surfaces (i.e., 2D cultures) (Figure 6.1(A-C)), which is comparable with the cell-ECM adhesion of the hiPSCs cultured in the porous scaffold after 21 days (Figure 6.1D).
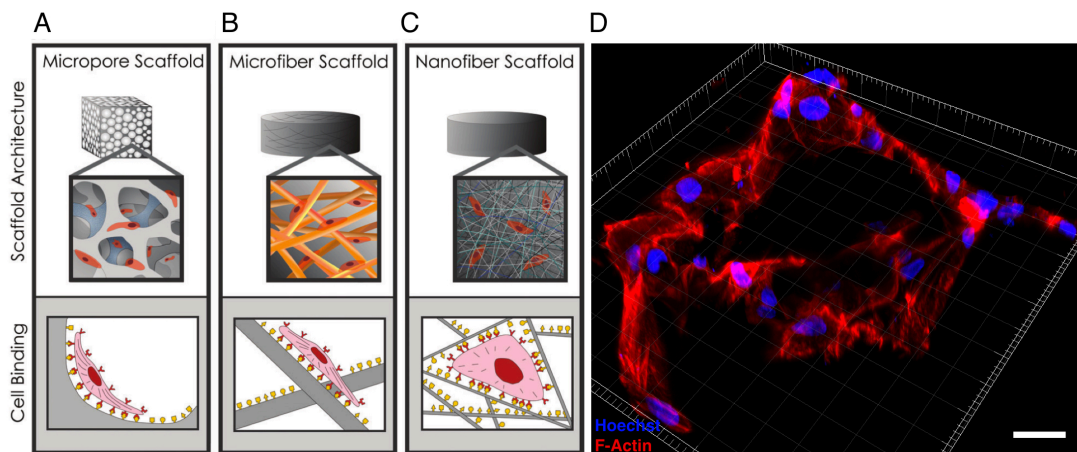

Figure 6.1. Scaffolds with microscale architecture: (A) Microporous scaffold and (B) microfiber scaffold. (C) Nanofiber scaffold with nanoscale architecture. The image is reprinted from [3]. (D) 3D reconstruction of differentiate hiPSCs cells after 25 days of dynamic culture within a porous elastomeric scaffold with pore diameter of 150 µm. (Scale bar: 30 µm).

These considerations led to the design of tissue engineered constructs (1) with targeted mechanical properties, (2) capable of inducing 3D interactions, and (3) able to integrate an efficient media exchanger. Therefore, in **Chapter 3** is presented a fabrication technique capable of creating thick (~ 1 cm) engineered hydrogel constructs with integrated channel networks. Gelatin hydrogel, was crosslinked with transglutaminase thus tuning the mechanical properties of the final construct in the range of soft tissues (i.e., 1 – 12 kPa). Using the 3D molding technique, it was created a network of perfusable microchannels in the construct allowin the transport of oxygen and nutrients needed to maintain viable the encapsulated cells in the hydrogel. A fluidic mold was then developed to allow the engineered construct to be directly perfused, which was connected to a home-made fluidic platform integrating a peristaltic pump. To show the functionality of the fabrication method and platform, hepatospheres were encapsulated within the gelatin/TG hydrogel having a 2D

channel network and were actively perfused for seven days. We showed that the system and processes used to encapsulate the hepatospheres and structure the gel was biocompatible. Also, the ability of fabricate several perfusable networks suggested the possibility for the engineering of complex and thick tissue constructs with controlled micro-environment.

The concept is further developed in **Chapter 4**. It was possible to create thick and densely populated constructs by encapsulating 15 million HepG2 cells in a 1.5 mL of gelatin/TG hydrogel with a stiffness of 3 kPa. The fabricated construct integrated a 3D perfusable vasculature, and was actively perfused for 15 days. It was showed that the active perfusion was critical for maintaining viable and metabolically active the encapsulated HepG2 cells in the gelatin/TG hydrogel. In fact, the HepG2 cells were capable of proliferating by forming spheroids with different dimensions (diameter of 40-70 µm) and different conformations (round and mass structures) [4]. These results illustrated how important is the control of the in vitro culture conditions. Also, it showed how important is the role of the construct material in creating the relevant ECM matrix environment to guide and to maintain the cells in the correct homeostasis [5,6]. These fabricated constructs could represent a step forward for the fabrication of functional constructs capable of shifting the paradigm of tumor modeling [7] as well as in drug studies [8]. The presented fabrication method could allow the fabrication of constructs with more relevant dimensions and, hopefully, with cell densities able to resemble the minimum number required to simulate a functional organ [9,10].

To further illustrate the versatility of the presented fabrication method, in **Chapter 5** is shown the fabrication of a gelatin/TG device composed by two parallel microfluidic channels (1.2 cm long) separated by a gelatin membrane of 370 µm. The system was designed for the simulation of physiological barriers such as intestine and blood-brain barriers. Guides were used to incorporate electrodes horizontally into channels having 1.7 mm diameter. The integrated electrodes were used to carry on real time impedance measurements across the barrier. These measurements could be used to extrapolate the trans-epithelial electrical resistance (TEER), which is an indication of the status and quality of the formed barrier. The electrical characterization of the sensor was performed by using buffers proving that different conductivities could be measured. Electrical signals varied very little **(**max $\pm$ 3.5 Ω**)** during 48h perfusion with medium, indicating that the device could support long term experiments. The presented model could represent a step forward for the

fabrication of fluidic devices mimicking more closely the physiological barrier microenvironment.

6.2 Future work considerations

In this thesis, we showed the fabrication of densely populated tissue constructs with controlled mechanical properties and a perfusable vasculature. However, the vasculature does not include the presence of endothelial cells, which is characteristic of the human vascular system. The need of creating an epithelial layer is crucial since it modulates the transport of molecules and nutrients throughout the barrier [11,12]. A future work recommendation could be the use of two different population of cells: one encapsulated into the hydrogel, and the second one lining into the conducts to generate a functional epithelium. This thesis demonstrated that an active perfusable 3D vasculature should be sufficient to maintain viable and metabolically active a high density of cells for several days. However, to further increase the dimensions of the construct along with the number of cells, the construct would need to be fully vascularized. At this moment, there are no fabrication techniques capable of creating engineered constructs with a vascular network comparable to the typical one found in the human body. However, It has been shown that endothelial cells encapsulated in the ECM should spontaneously induce the formation of a network in the construct that can naturally anastomose together with the pre-existent vascular network [13,14]. This is known as pre-vascularization and represents one of the possible strategies to create a vascular network guided by the maturation of the cells [15]. The pre-vascularization has been investigated showing promising results [16,17]. Therefore, a future possibility could be (1) the encapsulation of endothelial cells together with another cell line in the gelatin/TG hydrogel to form a vascular network in the construct, and (2) the use of endothelial cells to form a monolayer within the engineered channel network as presented at this thesis. These two considerations are critical for creating fully vascularized tissue constructs [18].

The fabrication method presented in this work allowed the creation of hydrogel-based fluidic devices, with an integrated sensor, capable of simulating barriers. However, a barrier should include different cell lines lining in both sides of the barrier and parenchymal cells in between. Therefore, a future work should include multiple cells lines cultured within the device.

Finally, around the fabrication method presented and with the fluidic platform, we envision the possibility of fabricating tissue engineered constructs capable of simulating

different compartments that are connected in series or in parallel. This could represent a breakthrough and should allow the possibility to study the crosstalk between tissues, understanding as an example how a molecule absorbed through the intestine compartment could influence the liver cells in the liver compartment.

References

[1]   S. Mohanty, K. Kuldeep, A. Heiskanen, J. Trifol Guzman, P. Szabo, M. Dufva, J. Emnéus, A. Wolff, Fabrication of scalable tissue engineering scaffolds with dual-pore microarchitecture by combining 3D printing and particle leaching, Mater. Sci. Eng. C Mater. Biol. Appl. 61 (2016) 180–189. doi:10.1016/j.msec.2015.12.032.

[2]   A.J. Engler, S. Sen, H.L. Sweeney, D.E. Discher, Matrix elasticity directs stem cell lineage specification., Cell. 126 (2006) 677–89. doi:10.1016/j.cell.2006.06.044.

[3]   M.M. Stevens, J.H. George, Exploring and engineering the cell surface interface., Science. 310 (2005) 1135–1138. doi:10.1126/science.1106587.

[4]   R. Edmondson, J.J. Broglie, A.F. Adcock, L. Yang, Three-dimensional cell culture systems and their applications in drug discovery and cell-based biosensors., Assay Drug Dev. Technol. 12 (2014) 207–18. doi:10.1089/adt.2014.573.

[5]   C.M. Magin, D.L. Alge, K.S. Anseth, Bio-inspired 3D microenvironments: a new dimension in tissue engineering., Biomed. Mater. 11 (2016) 22001. doi:10.1088/1748-6041/11/2/022001.

[6]   B.M. Baker, C.S. Chen, Deconstructing the third dimension - how 3D culture microenvironments alter cellular cues, J. Cell Sci. 125 (2012) 3015–3024. doi:10.1242/jcs.079509.

[7]   E.L.S. Fong, D.A. Harrington, M.C. Farach-Carson, H. Yu, Heralding a new paradigm in 3D tumor modeling, Biomaterials. 108 (2016) 197–213. doi:10.1016/j.biomaterials.2016.08.052.

[8]   S. Breslin, L. O'Driscoll, Three-dimensional cell culture: the missing link in drug discovery., Drug Discov. Today. 18 (2013) 240–9. doi:10.1016/j.drudis.2012.10.003.

[9]   J.S. Miller, K.R. Stevens, M.T. Yang, B.M. Baker, D.-H.T. Nguyen, D.M. Cohen, E. Toro, A. a Chen, P. a Galie, X. Yu, R. Chaturvedi, S.N. Bhatia, C.S. Chen, Rapid casting of patterned vascular networks for perfusable engineered three-dimensional tissues., Nat. Mater. 11 (2012) 768–74. doi:10.1038/nmat3357.

[10]   S.J. Paulsen, J.S. Miller, Tissue vascularization through 3D printing: Will technology bring us flow?, Dev. Dyn. 244 (2015) 629–640. doi:10.1002/dvdy.24254.

[11]   H. Bae, A.S. Puranik, R. Gauvin, F. Edalat, B. Carrillo-Conde, N.A. Peppas, A. Khademhosseini, Building Vascular Networks, Sci. Transl. Med. 4 (2012) 160ps23-160ps23. doi:10.1126/scitranslmed.3003688.

[12]   Y. Zheng, J. Chen, M. Craven, N.W. Choi, S. Totorica, A. Diaz-Santana, P. Kermani, B. Hempstead, C. Fischbach-Teschl, J.A. López, A.D. Stroock, In vitro microvessels for the study of angiogenesis and thrombosis., Proc. Natl. Acad. Sci. U. S. A. 109 (2012) 9342–7. doi:10.1073/pnas.1201240109.

[13]   V.K. Lee, A.M. Lanzi, H. Ngo, S.S. Yoo, P.A. Vincent, G. Dai, Generation of multi-scale vascular network system within 3D hydrogel using 3D bio-printing technology, Cell. Mol. Bioeng. 7 (2014) 460–472. doi:10.1007/s12195-014-0340-0.

[14]   M. Lovett, K. Lee, A. Edwards, D.L. Kaplan, Vascularization Strategies for Tissue Engineering, Tissue Eng. Part B Rev. 15 (2009) 353–370. doi:10.1089/ten.TEB.2009.0085.

[15]   J. Rouwkema, N.C. Rivron, C.A. van Blitterswijk, Vascularization in tissue

engineering, Trends Biotechnol. 26 (2008) 434–441.
doi:10.1016/j.tibtech.2008.04.009.

[16]   W. Zhu, X. Qu, J. Zhu, X. Ma, S. Patel, J. Liu, P. Wang, C.S.E. Lai, M. Gou, Y. Xu, K. Zhang, S. Chen, Direct 3D bioprinting of prevascularized tissue constructs with complex microarchitecture, Biomaterials. 124 (2017) 106–115.
doi:10.1016/j.biomaterials.2017.01.042.

[17]   V.K. Lee, D.Y. Kim, H. Ngo, Y. Lee, L. Seo, S.S. Yoo, P.A. Vincent, G. Dai, Creating perfused functional vascular channels using 3D bio-printing technology, Biomaterials. 35 (2014) 8092–8102. doi:10.1016/j.biomaterials.2014.05.083.

[18]   J. Rouwkema, A. Khademhosseini, Vascularization and Angiogenesis in Tissue Engineering: Beyond Creating Static Networks, Trends Biotechnol. 34 (2016) 733–745. doi:10.1016/j.tibtech.2016.03.002.

DTU Nanotech
Department of Micro- and Nanotechnology